PACIFIC EARTHQUAKE ENGINEERING
RESEARCH CENTER

Structural Characterization and Seismic Response Analysis of a Highway Overcrossing Equipped with Elastomeric Bearings and Fluid Dampers: A Case Study

Nicos Makris
University of California, Berkeley

and

Jian Zhang
University of Illinois, Urbana-Champaign

PEER 2002/17
NOV. 2002

Technical Report Documentation Page

1. Report No. 2002/17	2. Government Accession No.	3. Recipient's Catalog No.
4. Title and Subtitle Structural Characterization and Seismic Response Analysis of a Highway Overcrossing Equipped with Elastomeric Bearings and Fluid Dampers: A Case Study		5. Report Date November 2002
		6. Performing Organization Code UCB/ENG-9374
7. Authors Nicos Makris and Jian Zhang		8. Performing Organization Report No. UCB/PEER 2002/17
9. Performing Organization Name and Address Pacific Earthquake Engineering Research Center 1301 South 46th Street Richmond, CA 94804		10. Work Unit No. (TRAIS)
		11. Contract or Grant No. CMS-9696241 and RTA-59A169
12. Sponsoring Agency Name and Address California Department of Transportation Engineering Service Center 1801 30th Street MS#9 Sacramento, CA 95816		13. Type of Report and Period Covered Research Report July 1, 1999 to June 30, 2002
		14. Sponsoring Agency Code National Science Foundation
15. Supplementary Notes		

16. Abstract

This report presents a case study on the seismic response of a newly constructed freeway overcrossing that is equipped with elastomeric bearings and fluid dampers. The 91/5 overcrossing is located in Orange County, California, and is the first reinforced concrete bridge in the United States equipped with fluid dampers.

First, the bridge is decomposed into its main substructural components such as approach embankments, pile foundations, center bent, abutments, deck, and the seismic protection system that consists of isolation bearings and fluid dampers. Subsequently, the mechanical behavior of each substructural component is examined and expressed by macroscopic force-displacement laws represented in the form of equations or graphics. The overcrossing is modeled with a simple stick model that synthesizes the individual mechanical behavior of the various substructural elements. The modal analysis of the overcrossing is conducted within the context of equivalent linear analysis. Seismic response analysis is conducted in the time domain to capture the nonlinear behavior of the protective system. Finally, an in-depth parametric study is presented of the nonlinear seismic response of the isolated bridge accounting for the effects of soil-structure interaction. The various response quantities presented are compared with the corresponding response quantities of a hypothetical bridge with integral abutments. Advantages and challenges in the two design configurations are identified and discussed.

The study concludes that the bridge with sitting abutments results in large displacements and accelerations at the deck ends. Supplemental damping reduces both displacements and accelerations, yet the response of the bridge with integral abutments appears to outperform the response of the bridge with sitting abutments. Soil-structure interaction is responsible for increasing substantially both displacements and forces at the end abutments.

17. Key Words Highway overcrossings, seismic response, soil-structure interaction, elastomeric bearings, fluid dampers		18. Distribution Statement No restrictions	
19. Security Classif. (of this report) Unclassified	20. Security Classif. (of this page) Unclassified	21. No. of Pages 190	22. Price

Form DOT F 1700.7 (2-86)

Structural Characterization and Seismic Response Analysis of a Highway Overcrossing Equipped with Elastomeric Bearings and Fluid Dampers: A Case Study

Nicos Makris
Department of Civil and Environmental Engineering
University of California, Berkeley

and

Jian Zhang
Department of Civil and Environmental Engineering
University of Illinois, Urbana-Champaign

A report on research conducted under
grant CMS-9696241 from the National Science Foundation and
grant RTA-59A169 from the California Department of Transportation

PEER Report 2002/17
Pacific Earthquake Engineering Research Center
College of Engineering
University of California, Berkeley

November 2002

ABSTRACT

This report presents a case study on the seismic response of a newly constructed freeway overcrossing that is equipped with elastomeric bearings and fluid dampers. The 91/5 overcrossing, shown in Figure A, is located in Orange County, California, and is the first reinforced concrete bridge in the United States equipped with fluid dampers.

Figure A. View of 91/5 overcrossing located in Orange County in southern California. The deck is supported at mid-span by an outrigger prestressed beam, while at each abutment it rests on four elastomeric pads and is attached with four fluid dampers.

First, the bridge is decomposed into its main substructural components such as approach embankments, pile foundations, center bent, abutments, deck, and the seismic protection system that consists of isolation bearings and fluid dampers. Subsequently, the mechanical behavior of each substructural component is examined and expressed by macroscopic force-displacement laws represented in the form of equations or graphics. The overcrossing is modeled with a simple stick model that synthesizes the individual mechanical behavior of the various substructural elements. The modal analysis of the overcrossing is conducted within the context of equivalent linear analysis. Seismic response analysis is conducted in the time domain to capture the nonlinear behavior of the protective system. Finally, an in-depth parametric study is presented of the nonlinear seismic response of the isolated bridge accounting for the effects of soil-structure

interaction. The various response quantities presented are compared with the corresponding response quantities of a hypothetical bridge with integral abutments. Advantages and challenges in the two design configurations are identified and discussed.

The study concludes that the bridge with sitting abutments results in large displacements and accelerations at the deck ends. Supplemental damping reduces both displacements and accelerations, yet the response of the bridge with integral abutments appears to outperform the response of the bridge with sitting abutments. Soil-structure interaction is responsible for increasing substantially both displacements and forces at the end abutments.

ACKNOWLEDGMENTS

Partial financial support for this study was provided by the National Science Foundation under Grant CMS-9696241 and the California Department of Transportation under Grant RTA-59A169. Mr. Steven Yuen contributed significantly in assembling the damper testing machine shown in Figure 5.3. Invaluable technical assistance during the design and construction of the damper testing machine was provided by Mr. Don Clyde and Mr. Wes Neighbour at the Richmond Field Station Structural Laboratory, University of California, Berkeley Their services are greatly appreciated. The valuable input and comments of Dr. Tim Delis from Caltrans are also appreciated.

The Pacific Earthquake Engineering Research Center is supported by the Earthquake Engineering Research Centers Program of the National Science Foundation under Award Number EEC-9701568.

CONTENTS

LIST OF FIGURES

LIST OF TABLES

LIST OF SYMBOLS

$a_0 = \omega d / V_s$	dimensionless frequency
A	area
B_b	embankment width at base
B_c	embankment width at crest
$c_x(\omega)$	frequency dependent dashpot constant of a dynamic Winkler model
C_x, C_y, C_z	dashpot constants along transverse, longitudinal and vertical directions
C_1	equivalent damping coefficient
C_α	damping constant of nonlinear viscous damper
$[C]$	damping matrix
d	pile diameter
E, E_s	Young's modulus of soil
E_p	Young's modulus of pile
f	frequency/natural frequency
F_p	hysteretic force
F^Y	yielding force
G	shear modulus
G_1	storage modulus
G_2	loss modulus
G_h	shear modulus of half space
G_{max}	small strain shear modulus of soil
G_s	shear modulus of soil
H	embankment height
$H(\Phi)$	Heaviside function
I	moment of intertia
$I(\omega)$	kinematic response function
I_p	moment of inertia of pile

J_0, J_1	zero- and first-order Bessel function of the first kind
k, k_n	wave number
$k_x(\omega)$	frequency dependent spring constant of dynamic Winkler model
$\hat{k}_x(0)$	transverse static stiffness of a shear wedge
$\hat{k}_z(0)$	vertical static stiffness of a shear wedge
K_1	pre-yield elastic stiffness
K_2	post-yield hardening stiffness
$K_{eff} = \dfrac{G_{eff}A}{t}$	effective stiffness of elastomeric bearing
K_x, K_y, K_z	static stiffness along transverse, longitudinal and vertical directions
K_r	static rocking stiffness of pile group
K_{xr}, K_{yr}	static cross-rocking stiffness of pile group
$[K]$	stiffness matrix
$[K_t]$	tangent stiffness matrix
$\hat{\mathcal{k}}_z(\omega)$	dynamic stiffness of a unit-width shear wedge
$\mathcal{k}_x(\omega)$	dynamic stiffness of a unit-width shear wedge solved by finite element analysis
$\mathcal{K}_x^{[1]}(\omega)$	lateral dynamic stiffness of a single pile
$\mathcal{K}_z^{[1]}(\omega)$	vertical dynamic stiffness of a single pile
$\mathcal{K}_x^{[G]}(\omega)$	lateral dynamic stiffness of a pile group
$\mathcal{K}_z^{[G]}(\omega)$	vertical dynamic stiffness of a pile group
L	length
L_c	critical length of approach embankment
m	mass per length of pile
$[M]$	mass matrix
N_{60}	blow count number measured in SPT test
p_x, p_y	distributed load
P_x, P_y	concentrated load
$P(t)$	piston force

$P = \{P_x, P_y\}^T$	restoring force vector
P^Y	yielding force
$Q(z, t)$	time dependent shear force at depth z
Q_D	zero-displacement force intercept
S	slope
sgn	signum function
t	time variable/thickness of elastomeric pads
$u^b(\omega)$	Fourier transform of base displacement
$u^c(t)$	crest response of embankment
$u_g(t)$	base displacement
u_{g0}	base displacement amplitude
$\ddot{u}_g(t)$	base acceleration
$u_x(z, t)$	horizontal displacement of shear wedge
$\hat{u}_x^c$	representative crest displacement
$u^c_{x, max}$	maximum crest displacement of embankment
$u^Y = \dfrac{Q_D}{(K_1 - K_2)}$	yielding displacement
$\{u\}$	response vector
u	translational deformation
u_p	plastic displacement
$V_{La} = \dfrac{3.4 V_s}{\pi(1 - \nu)}$	Lysmer's analogue velocity
V_s	shear-wave velocity of soil
y_i	horizontal displacement of pile i in a pile group
Y_0, Y_1	zero- and first-order Besseal function of the seconf kind
z	vertical coordinate
$z_0 = B_c H / (B_b - B_c)$	
Z	dimensionless plastic variable of Bouc-Wen model
α	Rayleigh damping coefficient/fractional power of nonlinear viscous damper
$\alpha_x(S, \theta)$	horizontal dynamic interaction factor of pile

β	Rayleigh damping coefficient
$\beta_s = \eta/2$	damping constant of soil
γ	strain/plasticity multiplier
$\hat{\gamma}$	average strain
δ	relative difference
η	damping coefficient
η_h	damping coefficient of half space
μ	friction coefficient
ν	Poisson ratio
ξ_n	damping ratio
ρ_p	density of pile
ρ_s	density of soil
$\bar{\sigma}_v$	effective vertical stress of soil
τ	stress
$\Phi(F_p)$	yielding surface
ϕ_n	mode shape
$\{\phi\}$	characteristic verctor
$\psi(r, \theta)$	attenuation function
ω	frequency
ω_n	natural frequency
$\bar{\omega}_x = \sqrt{k_x(\omega)/m}$	characteristics frequency of pile-soil system
Ω	complex characteristic value

1 Introduction

Earthquake damage in most highway overcrossings is the result of excessive seismic displacements and large force demands that have been substantially underestimated during design. A direct consequence of the underestimated seismic displacements, which are the combined result of poor representation of the kinematic characteristics of the ground, low inertial forces, and overestimated stiffnesses, is that the sitting length at the deck supports is unrealistically short, resulting in loss of support or pounding. In addition to failures that are the result of geometric inconsistencies (limited sitting length, pounding-abutment slumping), bridges also fail due to inadequate strength and ductility of columns, cap-beams, and foundations (Priestley et al. 1996).

In view of the abundance of these failures during the 1971 San Fernando, California, earthquake, many research programs were launched to study the seismic resistance of highway bridges. With the help of strong-motion records, improvements have been achieved in both design and analysis of bridge structures. Extensive retrofit programs have been implemented in California, which include jacketing of columns and the use of composite materials (FHWA 1995).

An alternative strategy that the California Department of Transportation (Caltrans) is currently investigating for the seismic protection of bridges is the implementation of devices such as elastomeric bearings and supplemental dampers.

Traditionally, many conventionally designed bridges use elastomeric bearings (pads) between the deck and its supports to accommodate thermal movements. The long experience with this technology has had a positive role on the implementation of modern seismic protection technologies in bridges. Several bridges worldwide are now equipped with seismic protective bearings that involve some energy-dissipation mechanism (Skinner et al. 1993). The most commonly used seismic isolation system consists of lead-rubber bearings that combine the function of isolation and energy dissipation in a single compact unit, while also supporting the weight of the superstructure and providing restoring force. Sliding bearings allow for appreciable mobility and provide energy dissipation through friction. In this case an additional restoring mechanism is often added to provide the structure with some recentering capacity. Spherical sliding bearings provide **a** restoring mechanism because of their curvature while at the same time dissipating energy.

The traditional non-seismic elastomeric pads used in bridges for thermal movements can provide some limited seismic protection; however their integrity during large displacements might be substantially deteriorated or even destroyed due to shearing of the elastomer or rolling of the entire bearing. Accordingly, elastomeric pads with improved seismic performance have been developed (ATC-17-1 1993, ATC-17-2 2002), while their displacement and stress demands have been established in design specification documents (FHWA 1995, AASHTO 1999). The increasing need for safer bridges in association with the rapid success of energy-dissipation devices in buildings has accelerated the implementation of large-capacity damping devices in bridges. The Vincent Thomas suspension bridge in southern California (Smyth et al. 2000), the Rion-Antirion cable-stayed bridge in western Greece (Papanikolas 2002), the San Francisco-Oakland Bay Bridge in the San Francisco Bay Area (Caltrans 2002), the Coronado Bridge near San Diego, California, and the 91/5 highway overcrossing in southern California (Delis et al. 1996, Zhang and Makris 2000) are examples of bridges that have been or will be equipped with fluid dampers.

The promise of modern seismic protection technologies to operate under strong shaking has directed most of the attention to the performance of bearings and dampers under large displacements and large velocities. The interaction of these devices with the remaining bridge structure is an issue that has either been incorporated in the response analysis indirectly via global finite element analysis of the entire bridge with large computer codes or has merely been neglected, partly because the transmitting forces are assumed relatively small and the reactive substructures are assumed relatively stiff.

In this report the efficiency of modern seismic protection technologies is examined by analyzing the seismic response of a newly constructed highway overcrossing in southern California. The 91/5 overcrossing of interest**,** shown in Figure 1.1, is supported at each end abutment on four traditional (non-seismic) elastomeric pads, while it is attached by four fluid dampers. The deck is supported near the center bent by a prestressed reinforced concrete outrigger. The interesting characteristic of this structure is that its transverse and longitudinal

Figure 1.1 View of 91/5 overcrossing located in Orange County, southern California.

modal periods lie in the range between 0.4 sec and 0.8 sec, a period range for which supplemental damping in a single-degree-of-freedom structure has a beneficial effect. Furthermore, the approach embankments on each side of the bridge have a tendency to amplify the free-field motion and increase the role of soil-structure interaction. Accordingly, the assessment of the efficiency of the seismic protection devices is conducted by accounting in our analysis for the effects of soil-structure interaction at the end abutments/approach embankments and at the foundations of the center columns. In principle, lengthening the period of a structure with mechanical isolation reduces accelerations and increases displacements. Nevertheless, a more flexible configuration offers to the deck additional mobility that may result in an undesirable response. The investigation of these issues and the seismic response analysis of the bridge when excited by various strong earthquakes is the subject of this study.

2 Location, Structural Configuration, and Geotechnical Information

2.1 LOCATION

Figure 2.1 shows the location of the 91/5 overcrossing in the Greater Los Angeles area together with the traces of nearby faults. The Whittier-Elsinore fault is 11.6 km (7.2 miles) to the northeast, while the Newport-Inglewood fault zone is 20 km (12.5 miles) to the southwest.

2.2 STRUCTURAL CONFIGURATION AND DECOMPOSITION TO SUBSTRUCTURE ELEMENTS

The newly constructed 91/5 overcrossing is a continuous two-span, cast-in-place prestressed concrete box-girder bridge supported by an outrigger bent at the center and equipped with four fluid dampers at each end abutment (eight dampers total). The bridge has two spans of 58.5 m (192 ft) long spanning a four-lane highway and has two abutments skewed at $33°$. The width of the deck along the east span is about 12.95 m (42.5 ft), while along the west span about 15 m (49.2 ft). The cross section of the deck consists of three cells. The deck is supported by a 31.4 m (103 ft) long prestressed outrigger which rests on two pile groups, each consisting of 49 driven concrete friction piles. The columns are approximately 6.9 m (22.5 ft) high.

At each abutment the deck rests on four non-seismic elastomeric pads. Figure 2.2 presents the elevation and plan views of the bridge. The total weight of the deck (including outrigger beam) is approximately 25 MN, whereas the weight of each abutment is approximately 5 MN. The distribution of vertical reactions is also shown in Figure 2.2 below the elevation. Since each abutment supports approximately 4 MN, each pad carries a vertical load of approximately

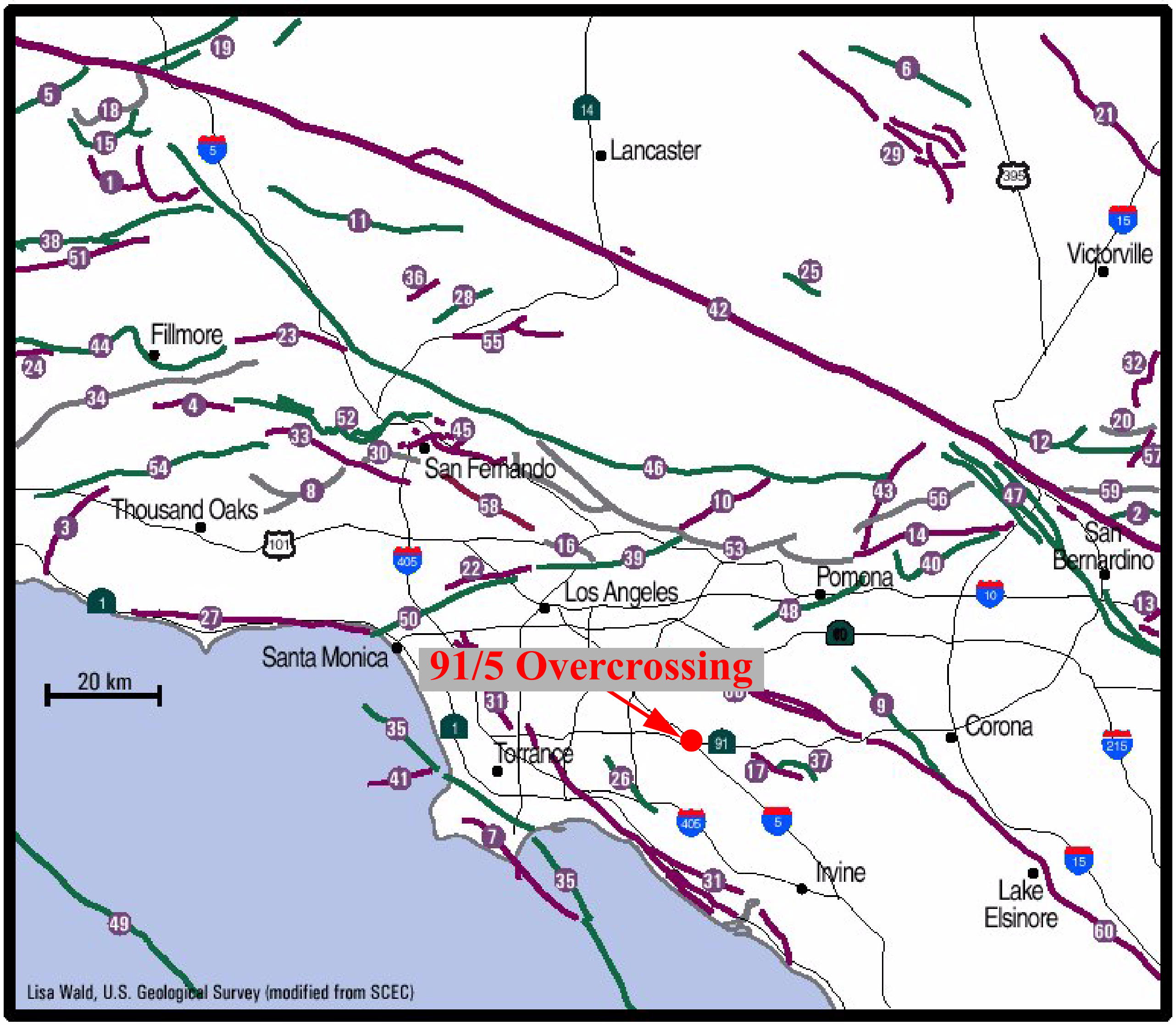

1 Alamo thrust
2 Arrowhead fault
3 Bailey fault
4 Big Mountain fault
5 Big Pine fault
6 Blake Ranch fault
7 Cabrillo fault
8 Chatsworth fault
9 Chino fault
10 Clamshell-Sawpit fault
11 Clearwater fault
12 Cleghorn fault
13 Crafton Hills fault zone
14 Cucamonga fault zone
15 Dry Creek
16 Eagle Rock fault
17 El Modeno
18 Frazier Mountain thrust
19 Garlock fault zone
20 Grass Valley fault
21 Helendale fault
22 Hollywood fault
23 Holser fault
24 Lion Canyon fault
25 Liano fault
26 Los Alamitos fault
27 Malibu Coast fault
28 Mint Canyon fault
29 Mirage Valley fault zone
30 Mission Hills fault
31 Newport Inglewood fault zone
32 North Frontal fault zone
33 Northridge Hills fault
34 Oak Ridge fault
35 Palos Verdes fault zone
36 Pelona fault
37 Peralta Hills fault
38 Pine Mountain fault
39 Raymond fault
40 Red Hill fault
41 Redondo Canyon fault
42 San Andreas fault
43 San Antonio fault
44 San Cayetano fault
45 San Fernando fault zone
46 San Gabriel fault zone
47 San Jacinto fault
48 San Jose fault
49 Santa Cruz fault zone
50 Santa Monica fault
51 Santa Ynez fault
52 Santa Susana fault zone
53 Sierra Madre fault zone
54 Simi fault
55 Soledad Canyon fault
56 Stoddard Canyon fault
57 Tunnel Ridge fault
58 Verdugo fault
59 Waterman Canyon fault
60 Whittier-Elsinore fault

Figure 2.1 Location of 91/5 overcrossing and traces of nearby faults.

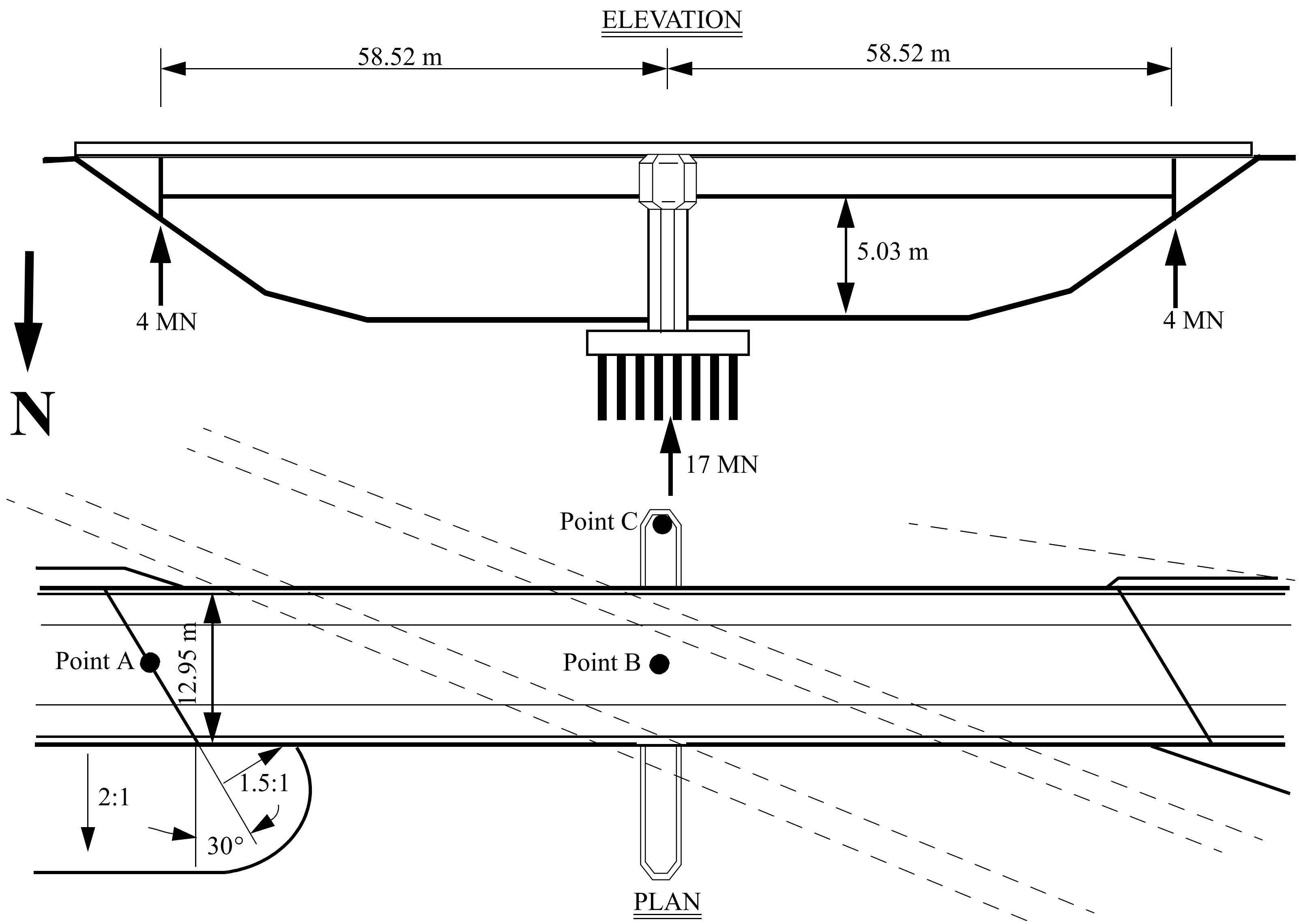

Figure 2.2 Elevation and plan views of 91/5 overcrossing.

$4\ MN/4 = 1\ MN$. The bridge is equipped with eight hydraulic dampers, four at each end, connecting the deck with the abutments as shown in Figure 2.3. With this arrangement the dampers engaged in both longitudinal and transverse motions of the deck. Figure 2.4 shows a photograph of the four fluid dampers installed at the east abutment, while Figure 2.5 shows a close-up view of the first fluid damper installed. The cross section of the bridge along the outrigger and a plan view of the pile group are shown in Figure 2.6.

In the case that the bridge deck is isolated not only at the end-abutments but also at the center bent, the inertia forces transferred at the center columns are relatively small and the columns behave essentially elastic. The 91/5 overcrossing is supported on bearings at the end-abutments but is rigidly connected to the center columns through the outrigger beam. In this case the columns are expected to behave inelastically. Figure 2.7 (top) plots the nonlinear moment-curvature behavior of each of the two center columns of the 91/5 overcrossing. The moment-curvature curve was computed with the recently developed software OpenSees (McKenna 1997) which is available on-line at **http://opensees.berkeley.edu**, after providing the dimensions of the columns, the amount of reinforcement and the associated strength of the concrete and steel. The validity of the OpenSees program in predicting the moment-curvature curve of reinforced concrete columns is confirmed by comparing the numerical predictions of the code against the experimental results from two reinforced concrete columns tested by Lehman (1998).

Figure 2.8 shows an idealization of the 91/5 overcrossing together with its approach embankments and pile foundations. In this study we isolate the main substructure elements of the bridge, such as the approach embankments, pile foundations, end abutments, center bent, and protective devices, in order to characterize their behavior with macroscopic force-displacement constitutive laws. The proposed constitutive laws are sophisticated enough to capture the leading mechanical behavior of the substructure elements, yet simple enough to be incorporated in a stick model that approximates the bridge structure. Table 2.1 shows the schematics of the substructure elements of interest, together with the proposed force-displacement constitutive relations that approximate their behavior. The parameters of the macroscopic constitutive models of these substructure elements have been established in past studies (Zhang and Makris 2001, 2002a). This study examines in depth the relative significance of these substructure elements in governing the seismic response of the bridge.

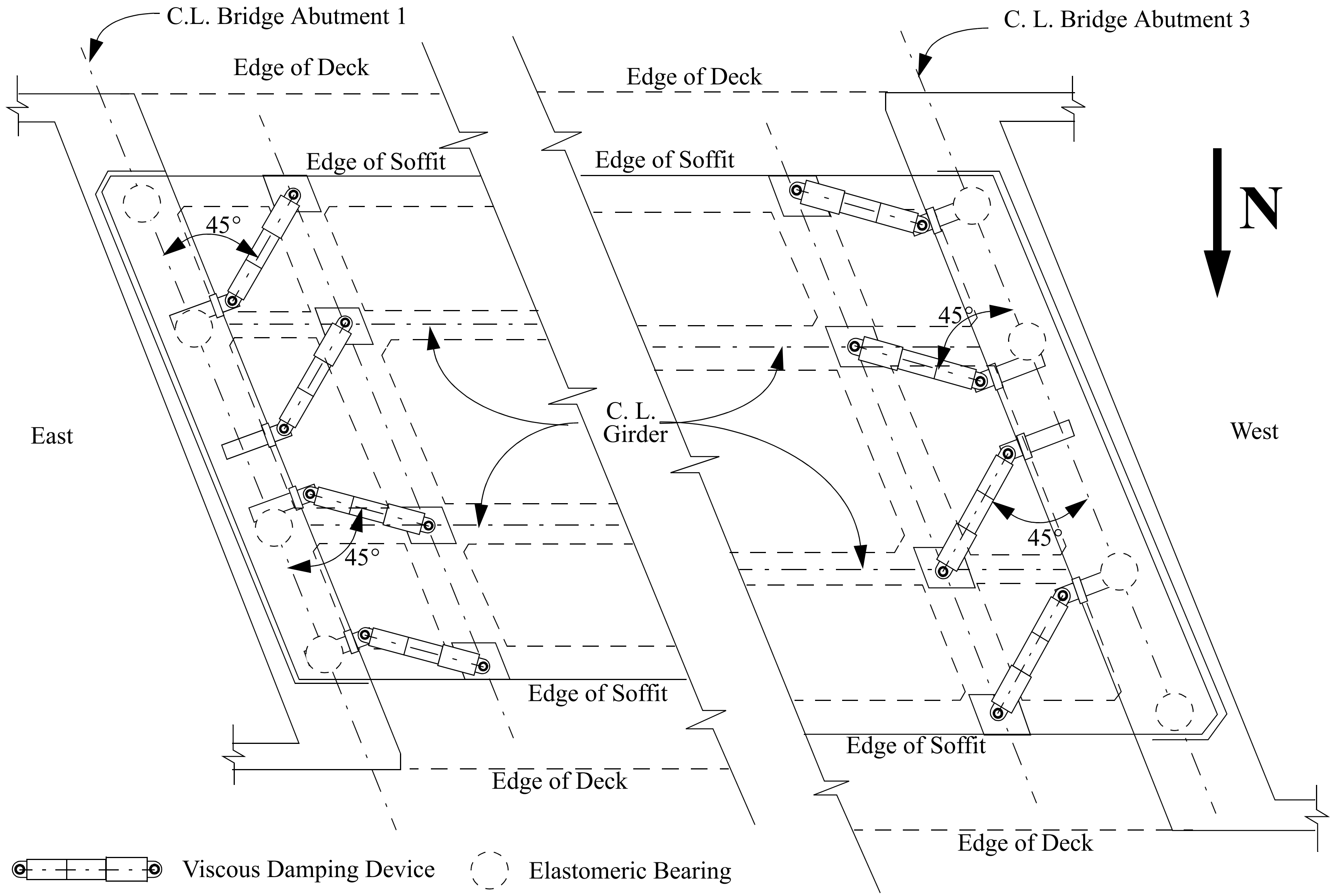

Figure 2.3 Layout of eight fluid dampers installed at end abutments and locations of elastomeric pads.

Figure 2.4 View of four fluid dampers installed at east abutment of 91/5 overcrossing.

Figure 2.5 Close-up view of first fluid damper installed at east abutment of 91/5 overcrossing.

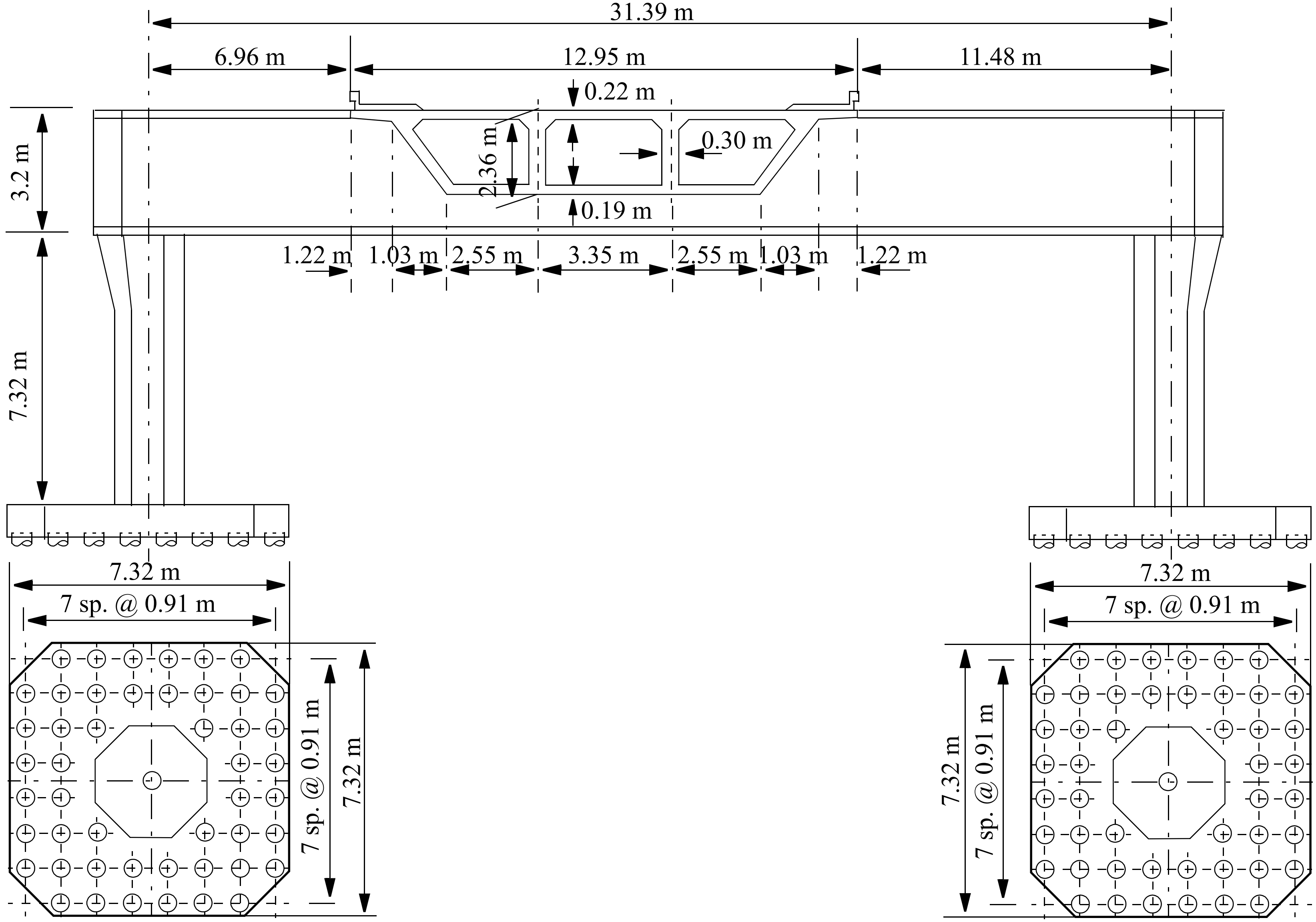

Figure 2.6 Cross section of 91/5 overcrossing and configuration of pile groups at center bent.

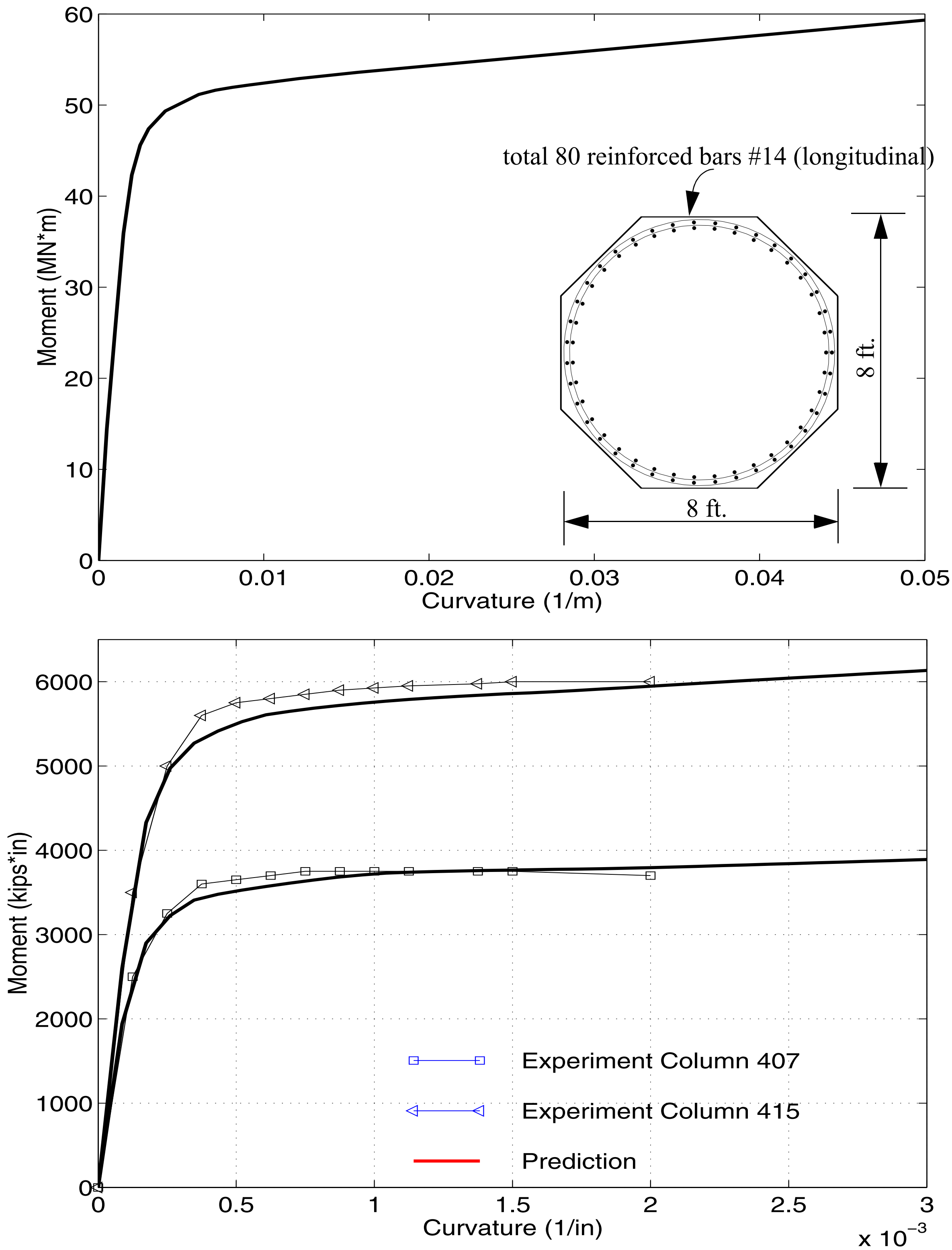

Figure 2.7 Top: computed moment-curvature curve of center columns of 91/5 overcrossing; bottom: comparison of numerical predictions with OpenSees and experimental data by Lehman (1998).

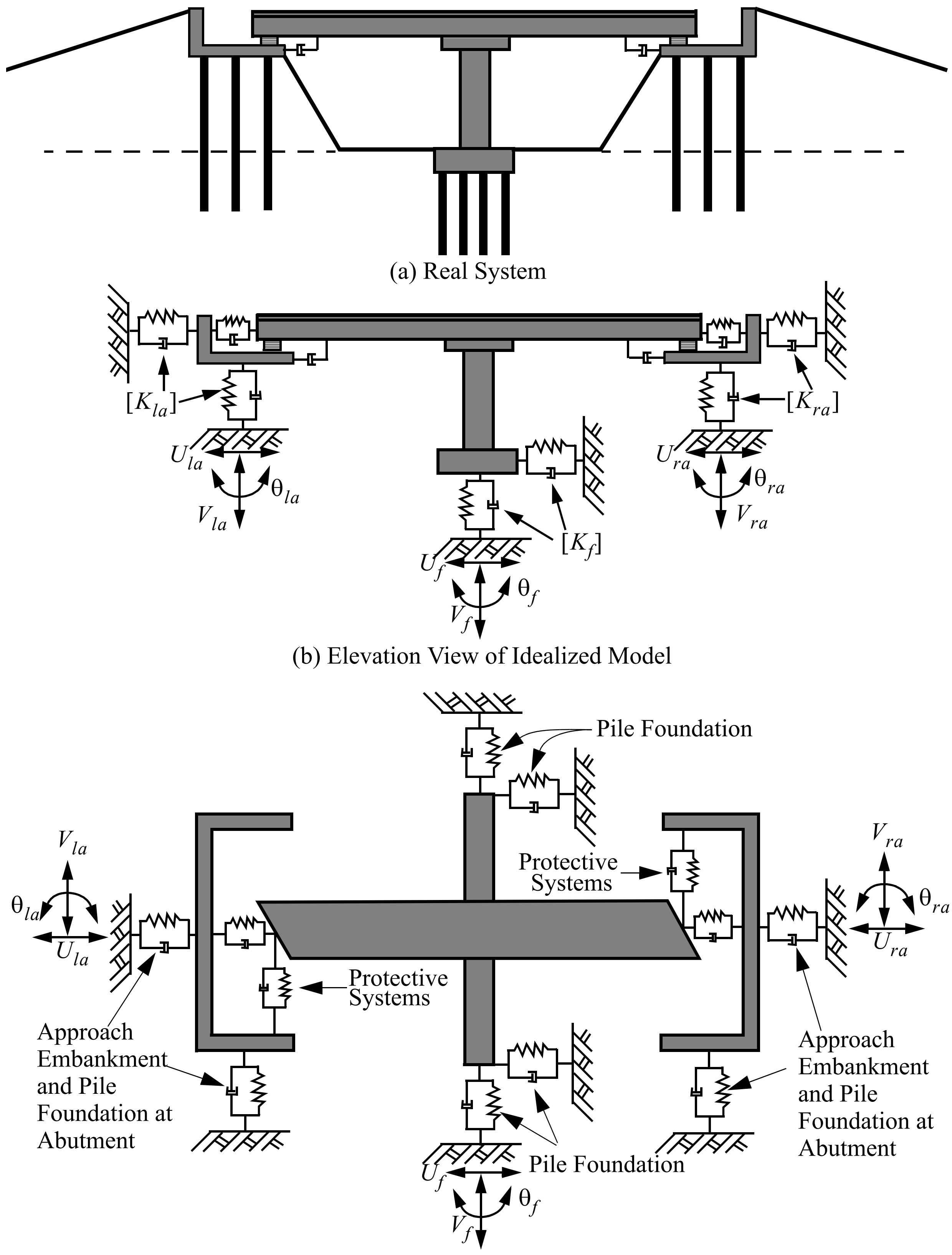

Figure 2.8 Schematic of a highway overcrossing and its idealized model.

Table 2.1 Summary of substructure elements and their constitutive laws

Substructure Elements	Constitutive Laws
Embankment 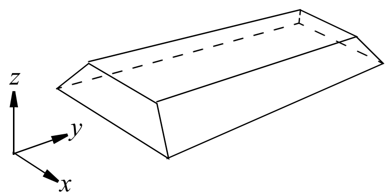	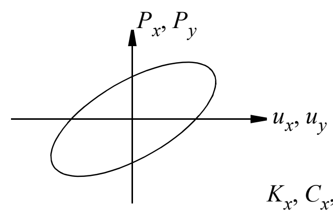 2D Decoupled Equivalent Linear Viscoelastic $P_x(t) = K_x u_x(t) + C_x \dot{u}_x(t)$ $P_y(t) = K_y u_y(t) + C_y \dot{u}_y(t)$ K_x, C_x, K_y, C_y are strain dependent
Pile Foundation 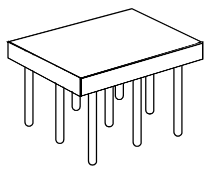	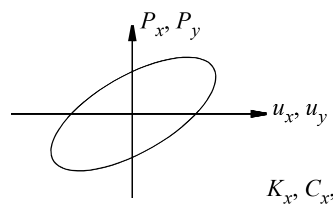 2D Decoupled Equivalent Linear Viscoelastic $P_x(t) = K_x u_x(t) + C_x \dot{u}_x(t)$ $P_y(t) = K_y u_y(t) + C_y \dot{u}_y(t)$ K_x, C_x, K_y, C_y are strain dependent
Center Bent 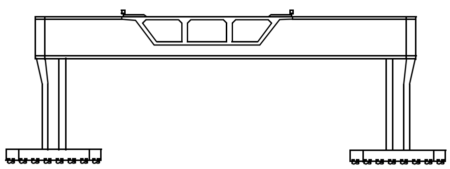	Nonlinear Moment-Curvature Curve of Single Column $M = M(\phi)$ 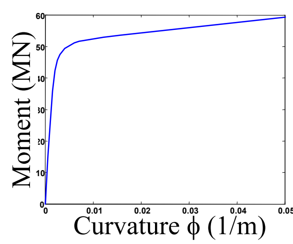 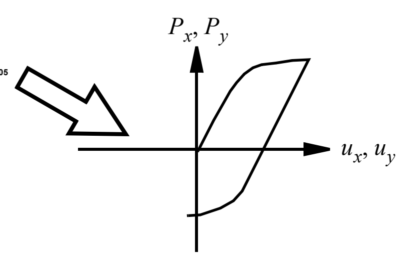
Elastomeric Bearing 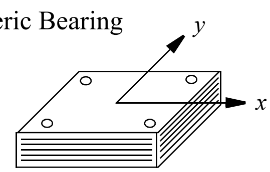	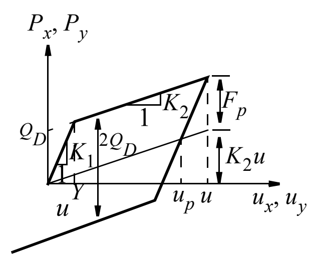 2-D Coupled Bilinear Plastic $\mathbf{P} = K_2\mathbf{u} + \mathbf{F}_p$ $\mathbf{P} = \begin{Bmatrix} P_x \\ P_y \end{Bmatrix}$ $\Phi(\mathbf{F}_p) = \lVert\mathbf{F}_p\rVert - Q_D$ $\mathbf{F}_p = (K_1 - K_2)\cdot(\mathbf{u} - \mathbf{u}_p)$ $\mathbf{u} = \begin{Bmatrix} u_x \\ u_y \end{Bmatrix}$ $\dot{\mathbf{u}}_p = \gamma \cdot \dfrac{\partial\Phi(\mathbf{F}_p)}{\partial\mathbf{F}_p}$ $\gamma \ge 0, \Phi(\mathbf{F}_p) \le 0, \gamma \cdot \Phi(\mathbf{F}_p) = 0$ $\gamma\dot{\Phi}(\mathbf{F}_p) = 0$
Fluid Damper 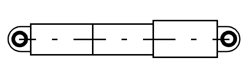	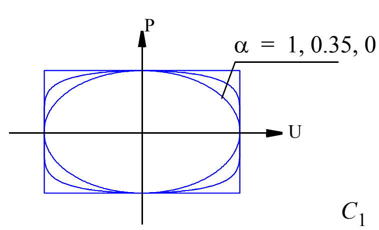 1-D Nonlinear Viscous $P(t) = C_\alpha \lvert\dot{u}(t)\rvert^\alpha \operatorname{sgn}[\dot{u}(t)]$ or Equivalent Linear Viscous $P(t) = C_1 \dot{u}(t)$ $C_1 = C_\alpha \dfrac{2^{2+\alpha}}{\pi}\omega^{\alpha-1}u_0^{\alpha-1}\dfrac{\Gamma^2\left(\frac{\alpha}{2}+1\right)}{\Gamma(\alpha+2)}$ ω: frequency of oscillation u_0: nominal displacement amplitude

Figure 2.9 summarizes the static pushover curves that result from the constitutive models adopted in this study. Each pushover curve extends to the range of deformation that the corresponding element experiences during strong and moderately strong earthquake loading. All substructure elements except the elastomeric bearings exhibit a nearly elastic behavior. This observation is in agreement with observations from the studies on highway overcrossings, such as the Meloland Road and the Painter Street overcrossings that have been shaken by strong earthquakes (Werner et al. 1987, McCallen and Romstad 1994, Goel and Chopra 1997). Even the center bent, which shares a large fraction of the horizontal inertia loading, behaves nearly elastic. This finding is in agreement with recent design practice adopted by Caltrans (Delis 2002).

2.3 GEOTECHNICAL DATA

Before construction, a geotechnical exploration at the location of the piers and near the end abutments was conducted. By using standard penetration test (SPT) measurements from the ground surface down to a depth about 35 m, moderately stiff soil was identified, which consisted of silty and clayey sand, sandy silt to clayey silt and occasionally gravelly sand and gravel. SPT blow counts varied from 8 to 70 blows/ft. The averaged soil density is about $\rho = 1800\ kg/m^3$. Figure 2.10 summarizes the results of the geotechnical exploration along with the SPT blow counts for each soil layer. Empirical formulas have been proposed in the literature in order to correlate the SPT blow counts and the maximum shear modulus of sand, G_{max}. For example,

$$G_{max} \approx 325 N_{60}^{0.68}\ (kips/ft^2) \quad \text{(Imai and Tonouchi 1982)} \tag{2.1}$$

or

$$G_{max} = 35 N_{60}^{0.34} (\bar{\sigma}_v)^{0.4}\ (kips/ft^2) \quad \text{(Seed et al. 1986)} \tag{2.2}$$

where N_{60} is the blow count number measured in an SPT test delivering 60% of the theoretical free-fall energy to the drill rod, and $\bar{\sigma}_v$ is the effective vertical stress (lb/ft^2). These two empirical relationships are widely used within a number of publications that correlate results. The inherent difficulty of correlating a small strain parameter G_{max} with a penetration test that relates to much larger strains is evident from the scatter in the data on which they are based and from the variability of the results obtained by different investigators (Kramer 1996). Therefore, equations (2.1) and (2.2) are used only to give a preliminary estimate of G_{max}. The small strain shear

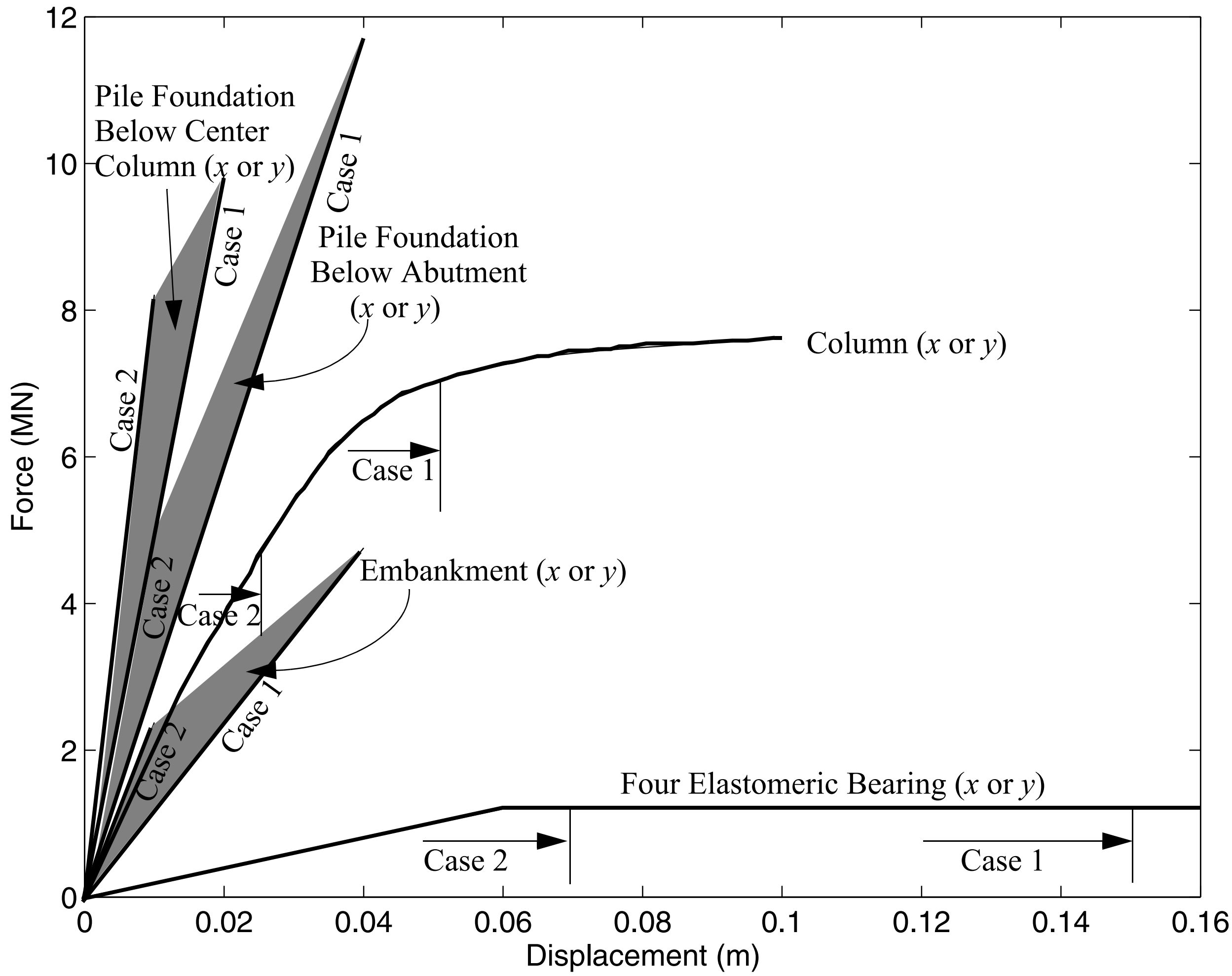

Figure 2.9 Summary of force-displacement (pushover) curves of various substructure elements of interest in this study. Each curve extends to the range of deformation that the corresponding element experiences. Case 1: strong earthquake shaking; Case 2: moderately strong earthquake shaking.

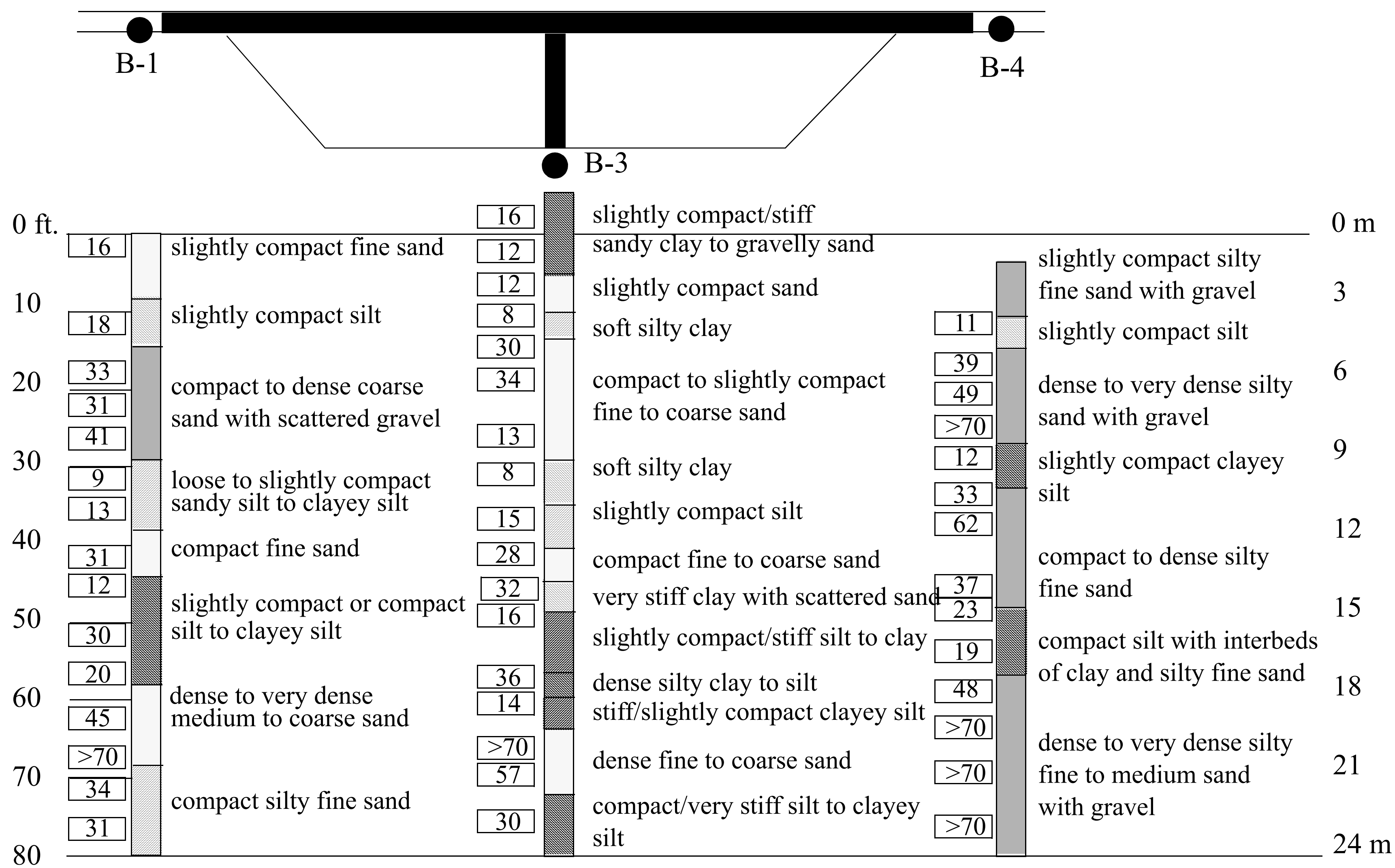

Figure 2.10 Three soil profiles of 91/5 overcrossing site (numerical values in boxes are blow counts by standard penetration test).

modulus G_{max} varies from 64 MPa to 240 MPa. These values were derived from SPT blow counts in the range of 8 to 30 according to equation (2.1), whereas equation (2.2) indicates the shear modulus G_{max} is an increasing function with depth. At a depth of 20 ft, an average blow count of 30 results in G_{max} of 84 MPa. Given the variability of data, the value of $G_{max} = 72\ MPa$ is adopted in this study, which results in a shear wave velocity of 200 m/s. The Poisson ratio of soil is assumed to be 0.4.

3 Ground Motions

Because of the proximity of the bridge to active faults, the thrust of this analysis is on near-source ground motions that exhibit distinguishable strong acceleration and velocity pulses. These relatively long duration pulses assume various shapes; however they often result in a main forward motion (type-A pulse), a forward-and-back motion (type-B pulse), a one main cycle in the displacement history (type-C_1 pulse), or two main cycles in the displacement history (type-C_2 pulse). The response of an isolated structure with various levels of damping when subjected to near-source and pulse-type motions has been investigated analytically by Makris and Chang (1998, 2000), whereas an experimental investigation with the emphasis on short bridges has been presented by Chang et al. (2002). These studies that concentrated on the seismic response of a rigid block supported on a variety of isolators concluded that for all ground motions examined, an increase of the viscous damping ratio from 14% to 50% reduces base displacement by half or even more without appreciably increasing base accelerations.

In this study the structural system of interest is more complicated than the model adopted in the Makris and Chang studies, not only because of the flexibility of the deck, but also because of the effects of soil-structure interaction between the bridge and the approach embankments, which are dramatically altered when the deck is isolated at the abutments. In order to investigate this problem we use 11 strong ground motions recorded in California relatively close to the faults of major earthquakes. Table 3.1 lists in historic order the records of interest, together with the magnitude of the earthquake and distance of the accelerographs from the causative fault.

Figures 3.1 to 3.11 plot the fault-normal and fault-parallel components of these motions, together with selected trigonometric pulses proposed by Makris (1997) and subsequently used by Makris and Chang (1998), Makris and Zhang (1999), and Makris and Roussos (2000). Figures 3.12 to 3.22 plot the acceleration, velocity, and displacement response spectra of these earthquakes for three levels of damping: $\xi = 10\%$, $\xi = 25\%$ and $\xi = 50\%$. These damping levels are approximately the modal damping values of the first transverse and longitudinal modes of the bridge. When the configuration with integral abutments is considered, the first translational mode exhibits a damping ratio, $\xi \approx 12\%$, whereas the longitudinal mode exhibits a damping ratio, $\xi \approx 58\%$. When the configuration with sitting abutments is considered and the bridge is equipped with fluid dampers, the first transverse and the longitudinal modes exhibit a damping ratio of $\xi \approx 24\%$ and $\xi \approx 29\%$, respectively. Therefore the spectra shown in Figures 3.12 to 3.22 are relevant for both configurations (integral and sitting abutments). The thin lines plot the earthquake spectra, whereas the thick lines plot the pulse spectra. The vertical lines on the fault-normal spectra indicate the transverse modal periods of the bridge when integral abutments are considered, $T^x_{int} = \frac{2\pi}{15.21} = 0.40s$, and when sitting abutments are considered, $T^x_{sit} = \frac{2\pi}{10.38} = 0.61s$. The vertical lines on the fault-parallel spectra indicate the longitudinal modal periods of the bridge when integral abutments are considered, $T^y_{int} = \frac{2\pi}{18.31} = 0.37s$, and when sitting abutments are considered, $T^y_{sit} = \frac{2\pi}{7.5} = 0.84s$. The spectral values that correspond to these periods will be used later in this study in an effort to reach response estimates using an approximate response spectrum analysis.

Table 3.1 Earthquake records selected for simulation

Record Station	Earthquake	Magnitude M_w	Distance to Fault (km)	Peak Acceleration (g)	Peak Velocity (m/s)
Pacoima Dam	1971 San Fernando	6.6	8.5	1.17 (1.08)	1.14(0.57)
El Centro Array #5	1979 Imperial Valley	6.4	30.4	0.38 (0.53)	0.99(0.52)
El Centro Array #6	1979 Imperial Valley	6.4	29.8	0.44 (0.34)	1.13(0.68)
El Centro Array #7	1979 Imperial Valley	6.4	29.4	0.46 (0.34)	1.13(0.55)
Parachute Test Site	1987 Superstition Hills	6.6	7.2	0.45(0.38)	1.12(0.44)
Los Gatos	1989 Loma Prieta	7.0	6.1	0.56(0.61)	0.95(0.51)
Cape Mendocino	1992 Petrolia	7.0	3.8	1.50 (1.04)	1.25(0.41)
Lucerne Valley	1992 Landers	7.3	42.0	0.71 (0.80)	1.36(0.70)
Rinaldi	1994 Northridge	6.7	9.9	0.89 (0.39)	1.75(0.60)
Sylmar	1994 Northridge	6.7	12.3	0.73 (0.60)	1.22(0.54)
Newhall	1994 Northridge	6.7	20.2	0.59 (0.58)	0.96(0.75)

* Peak acceleration and velocity values are for the fault-normal component. The values of the fault-parallel component are in parentheses.

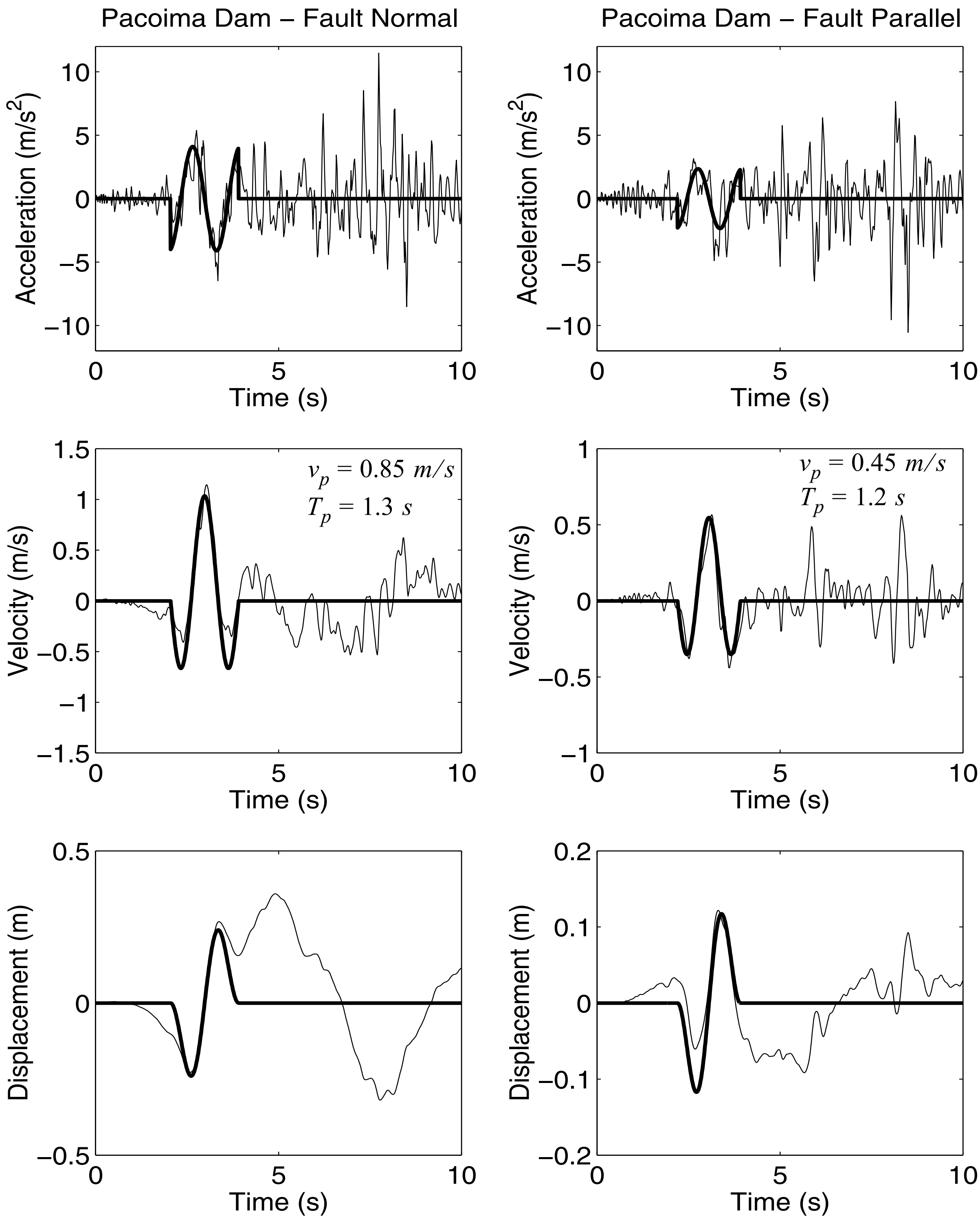

Figure 3.1 Fault-normal (left) and fault-parallel (right) components of the acceleration, velocity, and displacement time histories recorded at the Pacoima Dam station during the 1971 San Fernando, California, earthquake. The heavy lines are approximations with a type-C_1 trigonometric pulse.

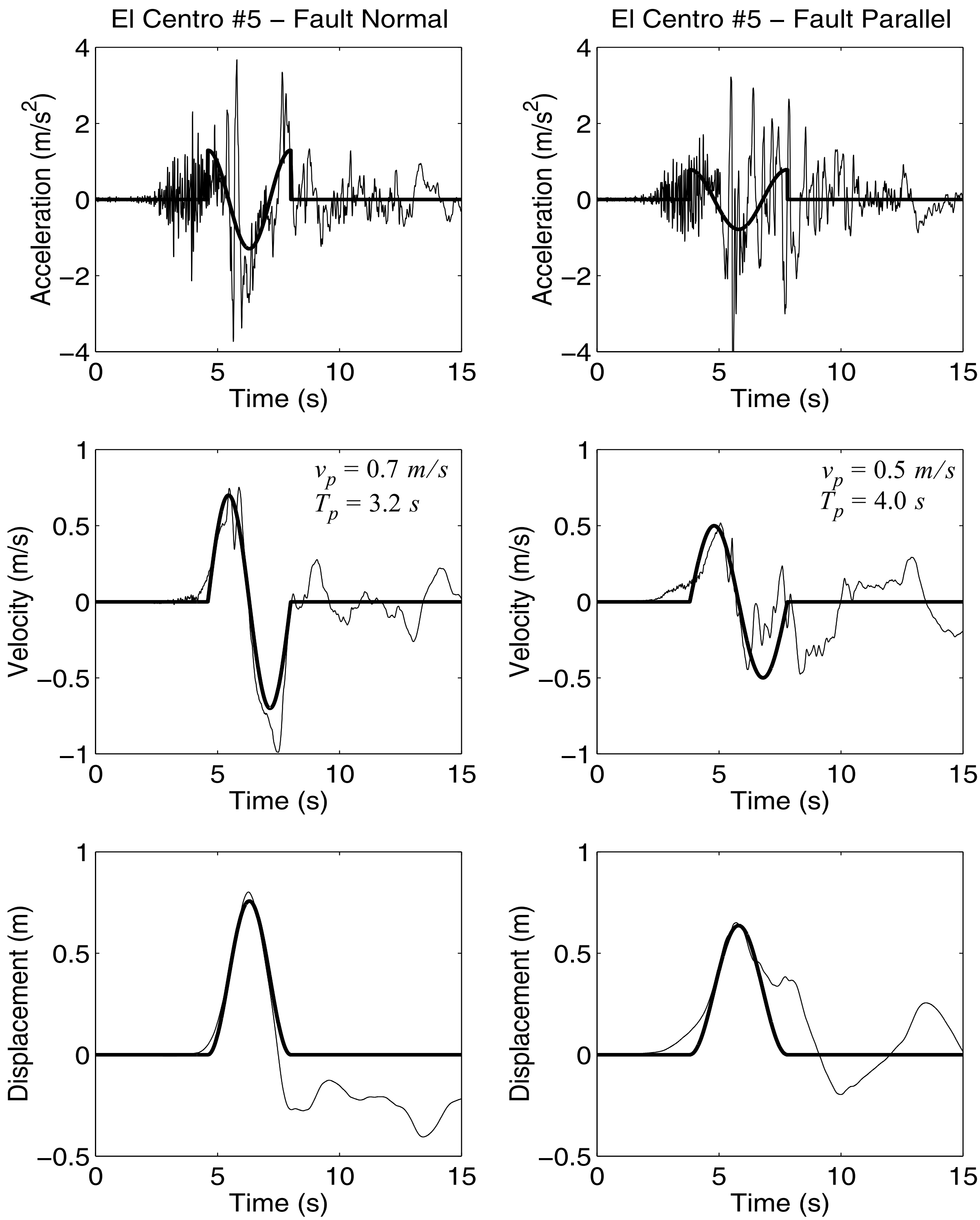

Figure 3.2 Fault-normal (left) and fault-parallel (right) components of the acceleration, velocity, and displacement time histories recorded at the El Centro Array #5 station during the 1979 Imperial Valley, California, earthquake. The heavy lines are approximations with a type-B trigonometric pulse.

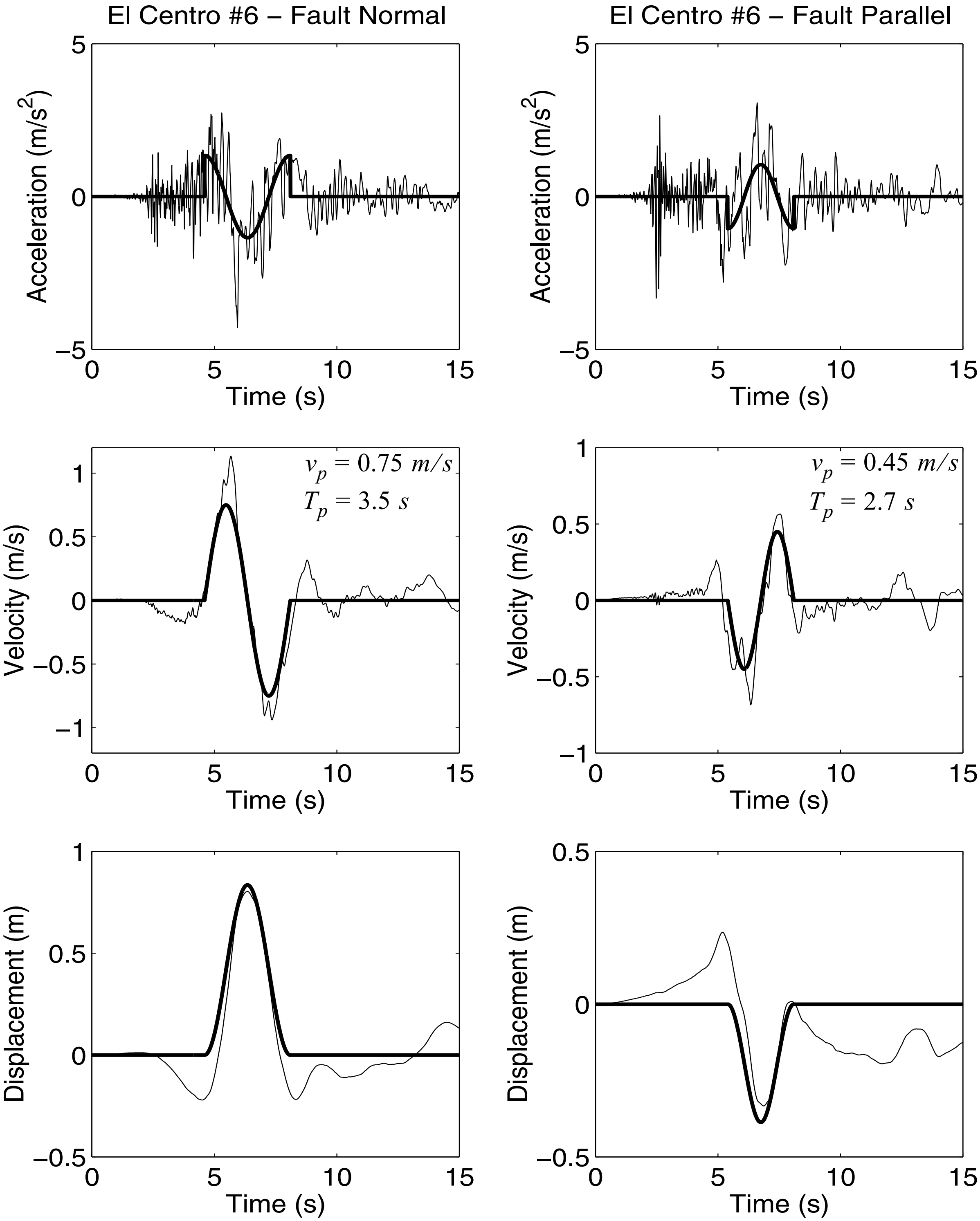

Figure 3.3 Fault-normal (left) and fault-parallel (right) components of the acceleration, velocity, and displacement time histories recorded at the El Centro Array #6 station during the 1979 Imperial Valley, California, earthquake. The heavy lines are approximations with a type-B trigonometric pulse.

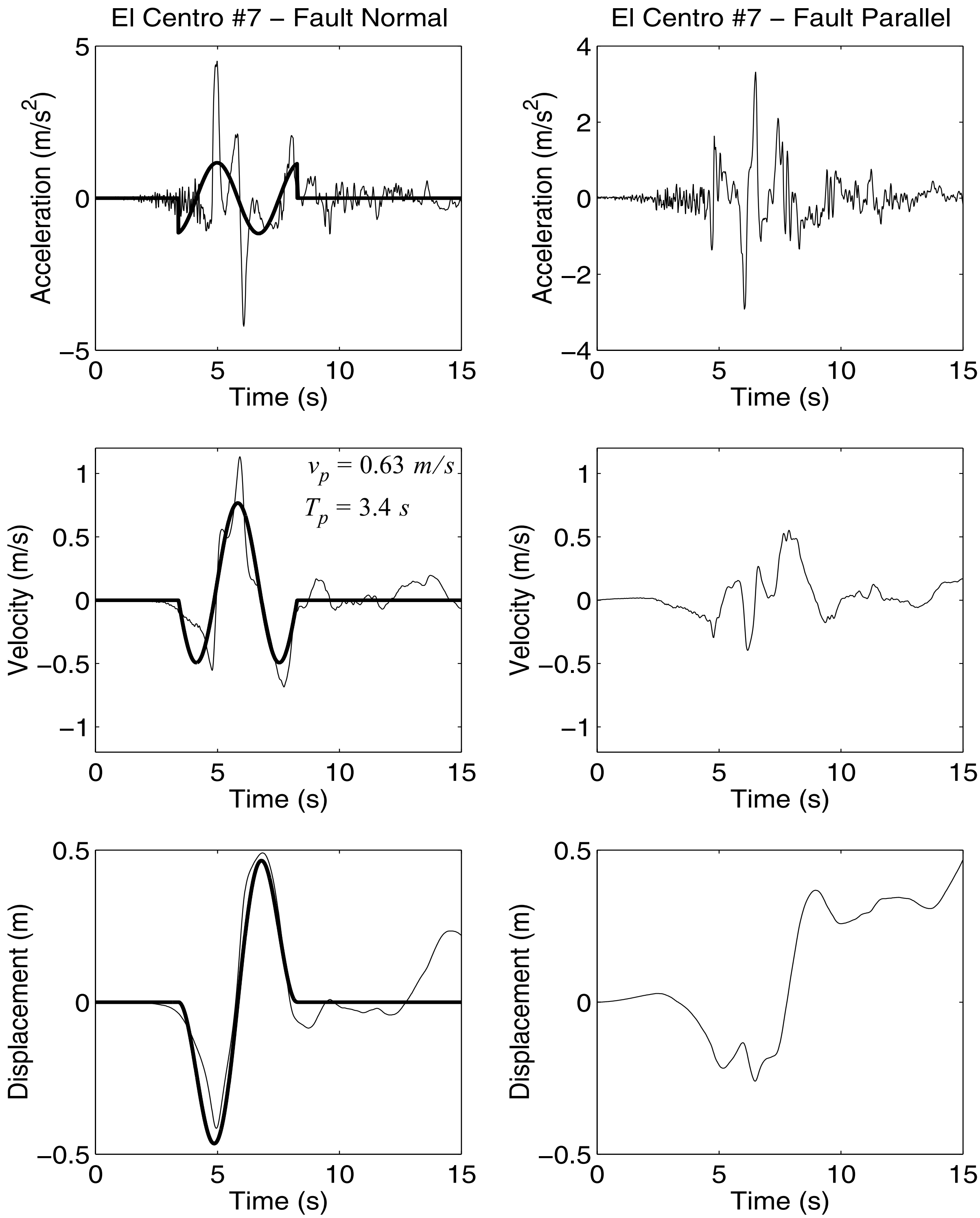

Figure 3.4 Fault-normal (left) and fault-parallel (right) components of the acceleration, velocity, and displacement time histories recorded at the El Centro Array #7 station during the 1979 Imperial Valley, California, earthquake. The heavy lines are approximations with a type-C_1 trigonometric pulse.

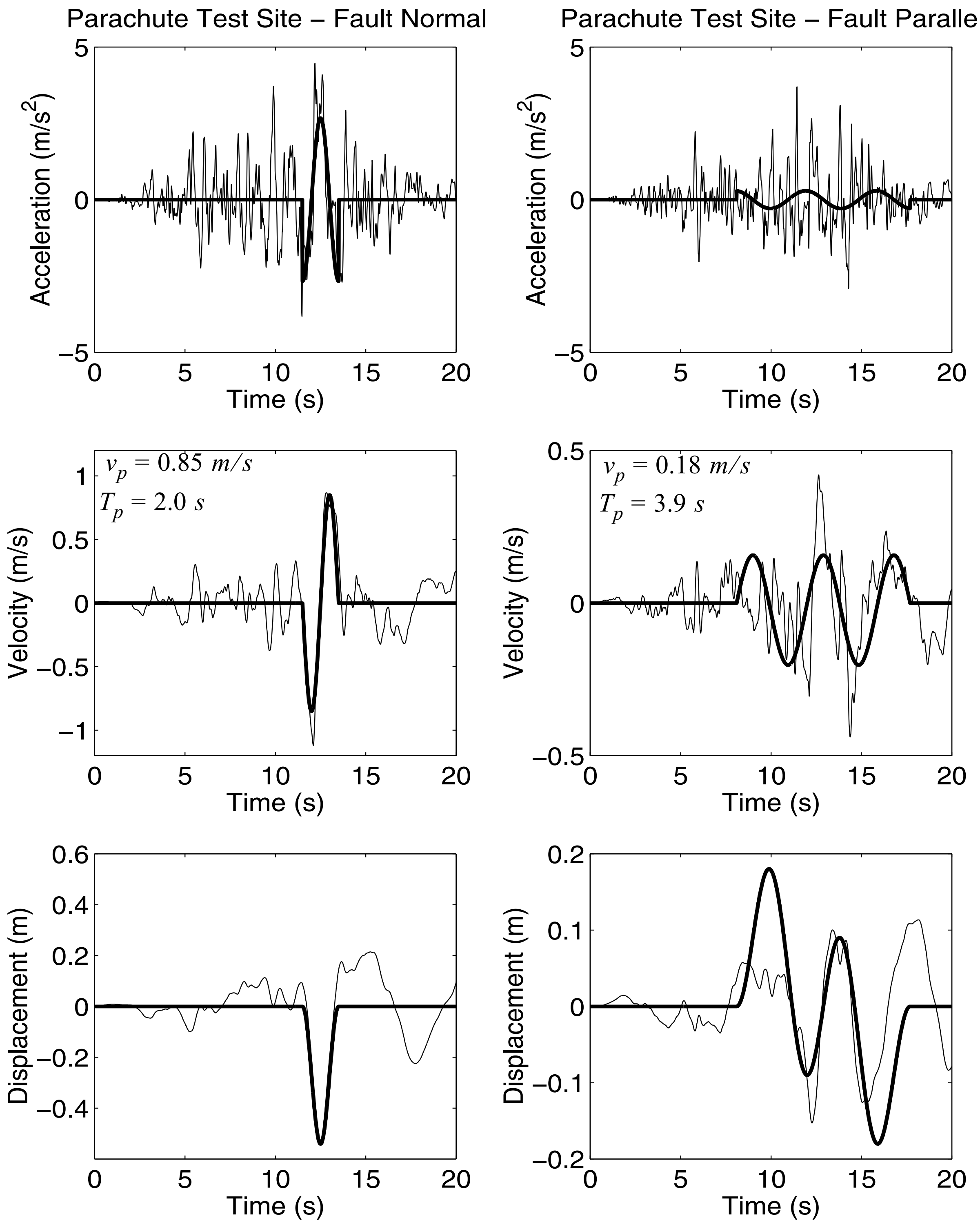

Figure 3.5 Fault-normal (left) and fault-parallel (right) components of the acceleration, velocity, and displacement time histories recorded at the Parachute Test Site during the 1987 Superstition Hills, California, earthquake. The heavy lines are approximations with a type-B (left) and with a type-C_2 (right) pulse.

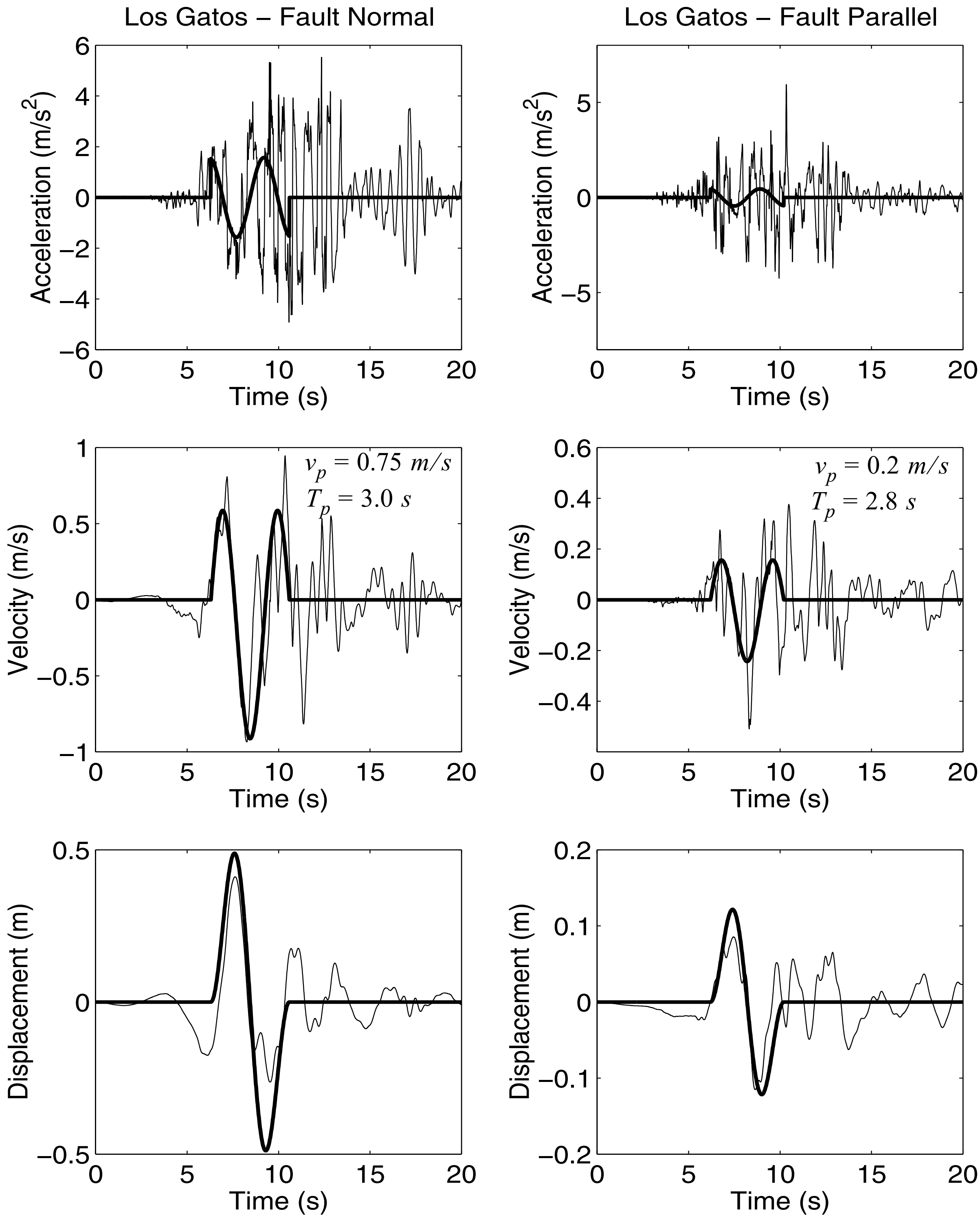

Figure 3.6 Fault-normal (left) and fault-parallel (right) components of the acceleration, velocity, and displacement time histories recorded at the Los Gatos station during the 1989 Loma Prieta, California, earthquake. The heavy lines are approximations with a type-C_1 trigonometric pulse.

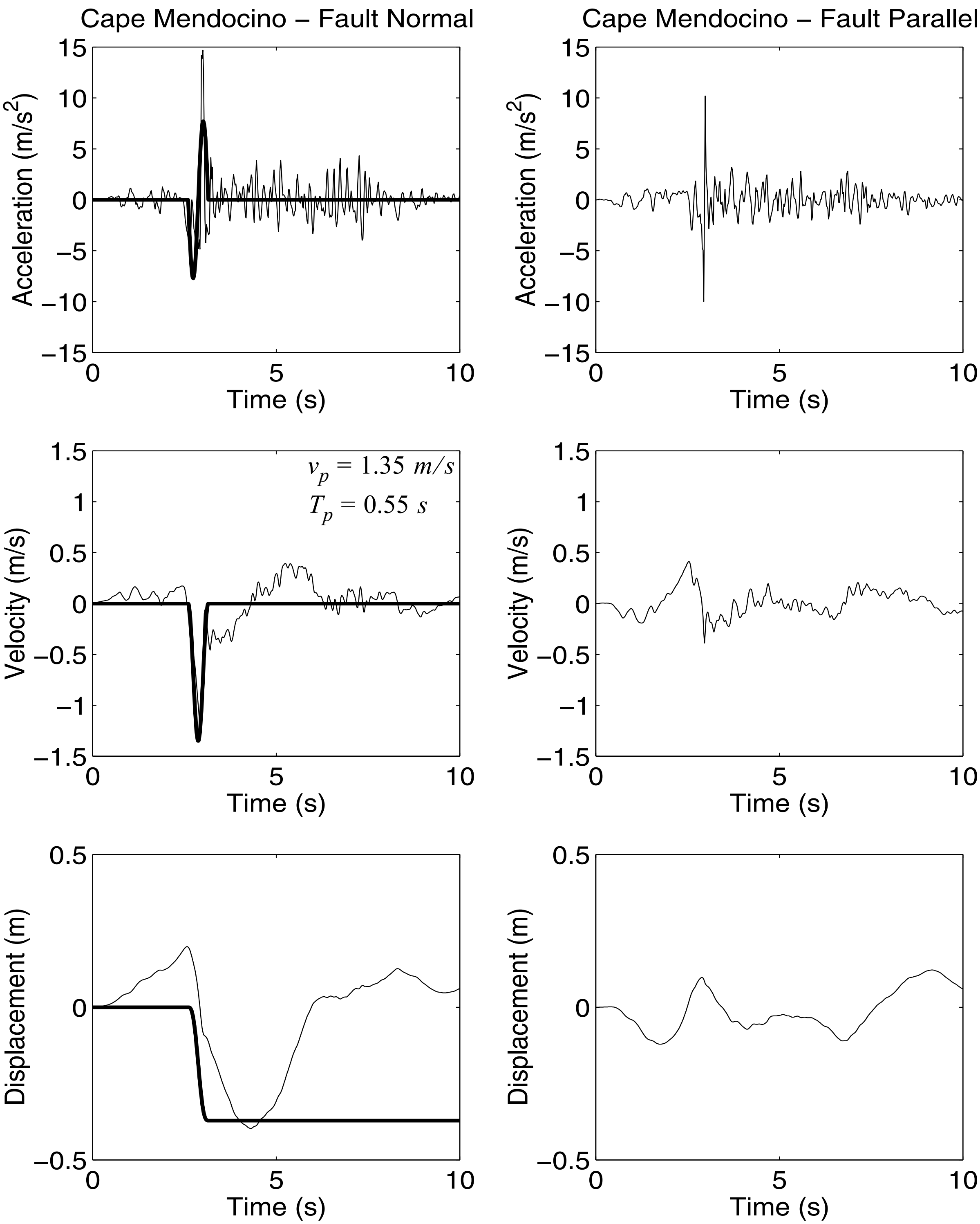

Figure 3.7 Fault-normal (left) and fault-parallel (right) components of the acceleration, velocity, and displacement time histories recorded at the Cape Mendocino station during the 1992 Petrolia, California, earthquake. The heavy lines are approximations with a type-A trigonometric pulse.

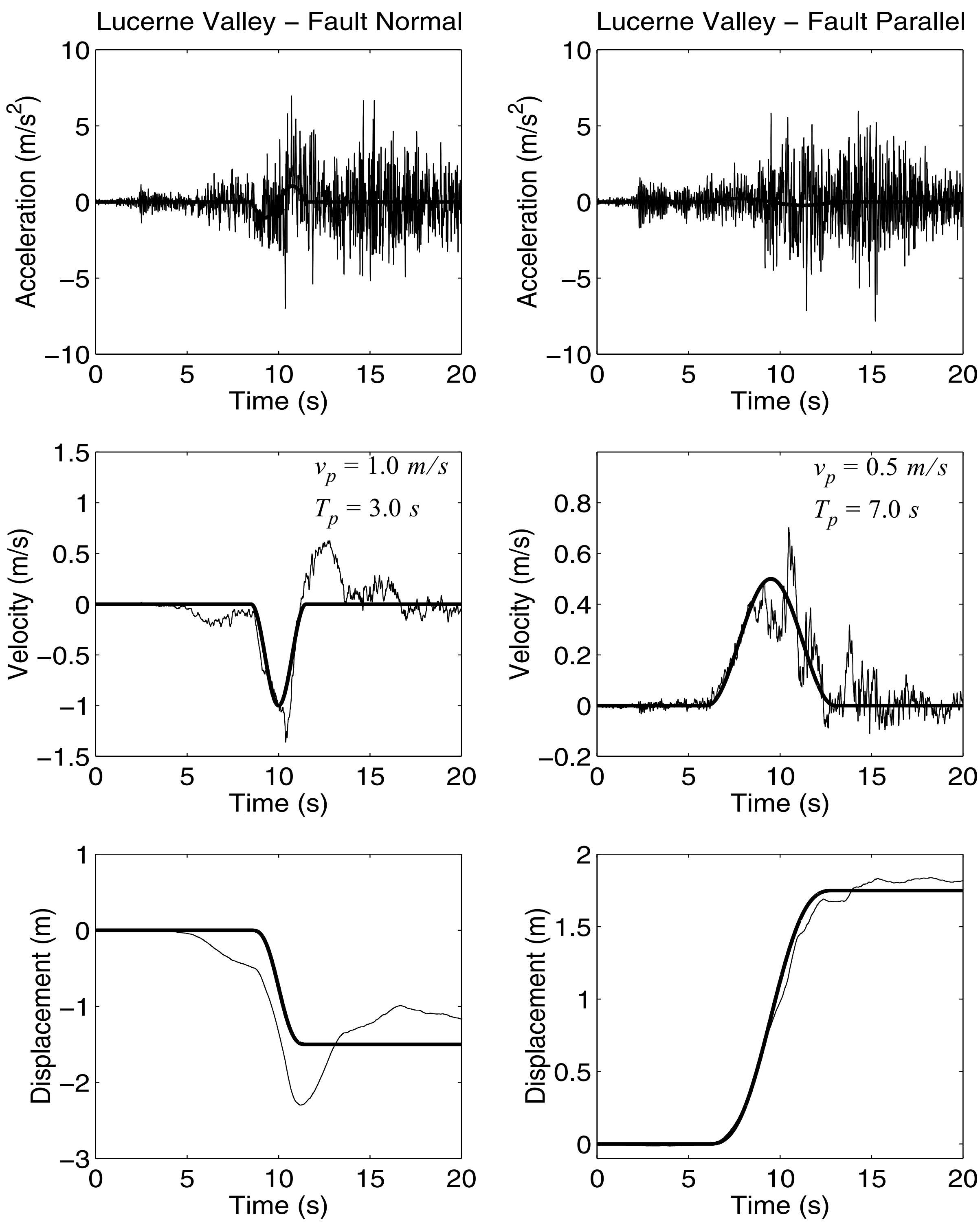

Figure 3.8 Fault-normal (left) and fault-parallel (right) components of the acceleration, velocity, and displacement time histories recorded at the Lucerne Valley station during the 1992 Landers, California, earthquake. The heavy lines are the approximations with a type-A trigonometric pulse.

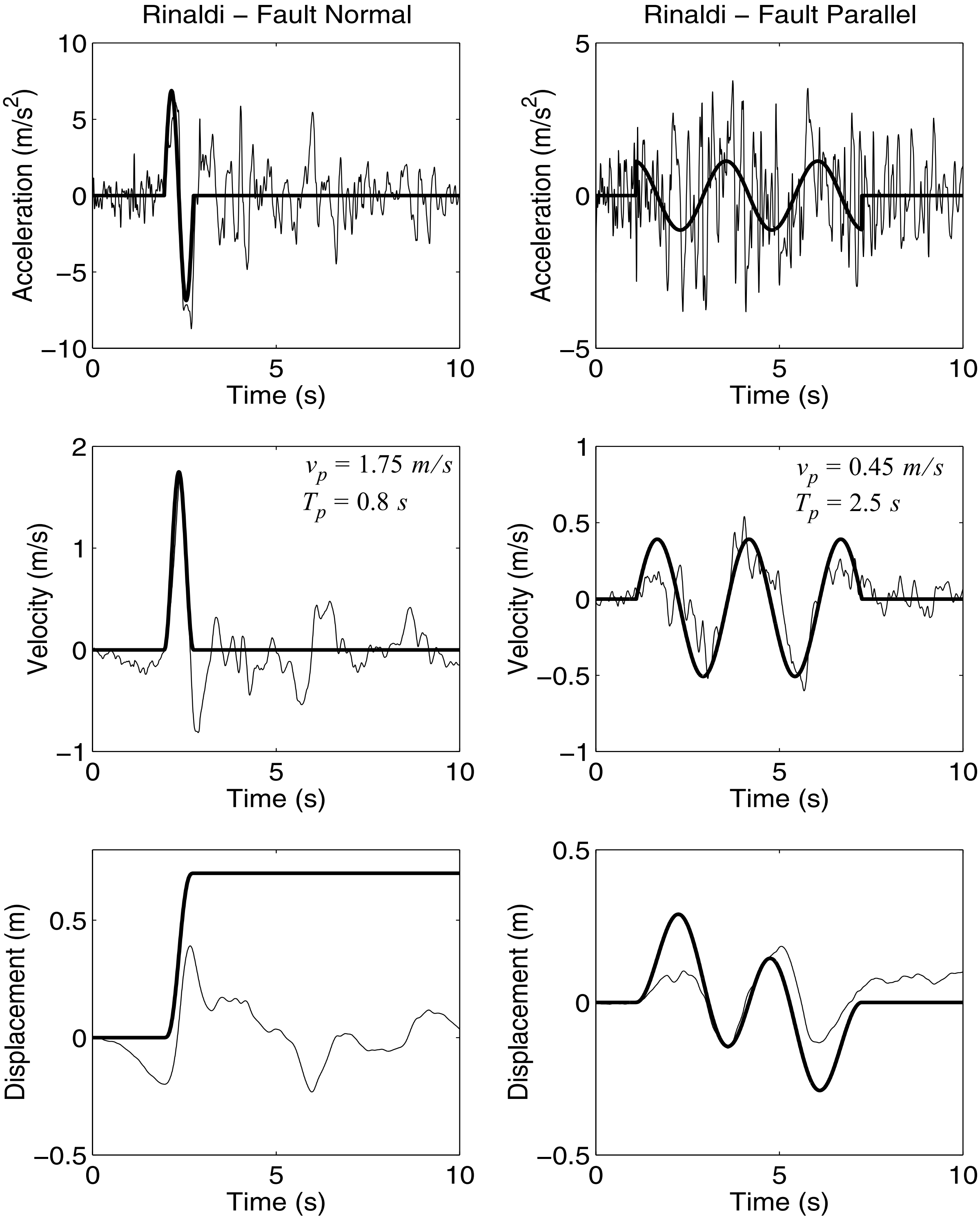

Figure 3.9 Fault-normal (left) and fault-parallel (right) components of the acceleration, velocity, and displacement time histories recorded at the Rinaldi station during the 1994 Northridge, California, earthquake. The heavy lines are approximations with type-A (left) and type-C_2 (right) trigonometric pulses.

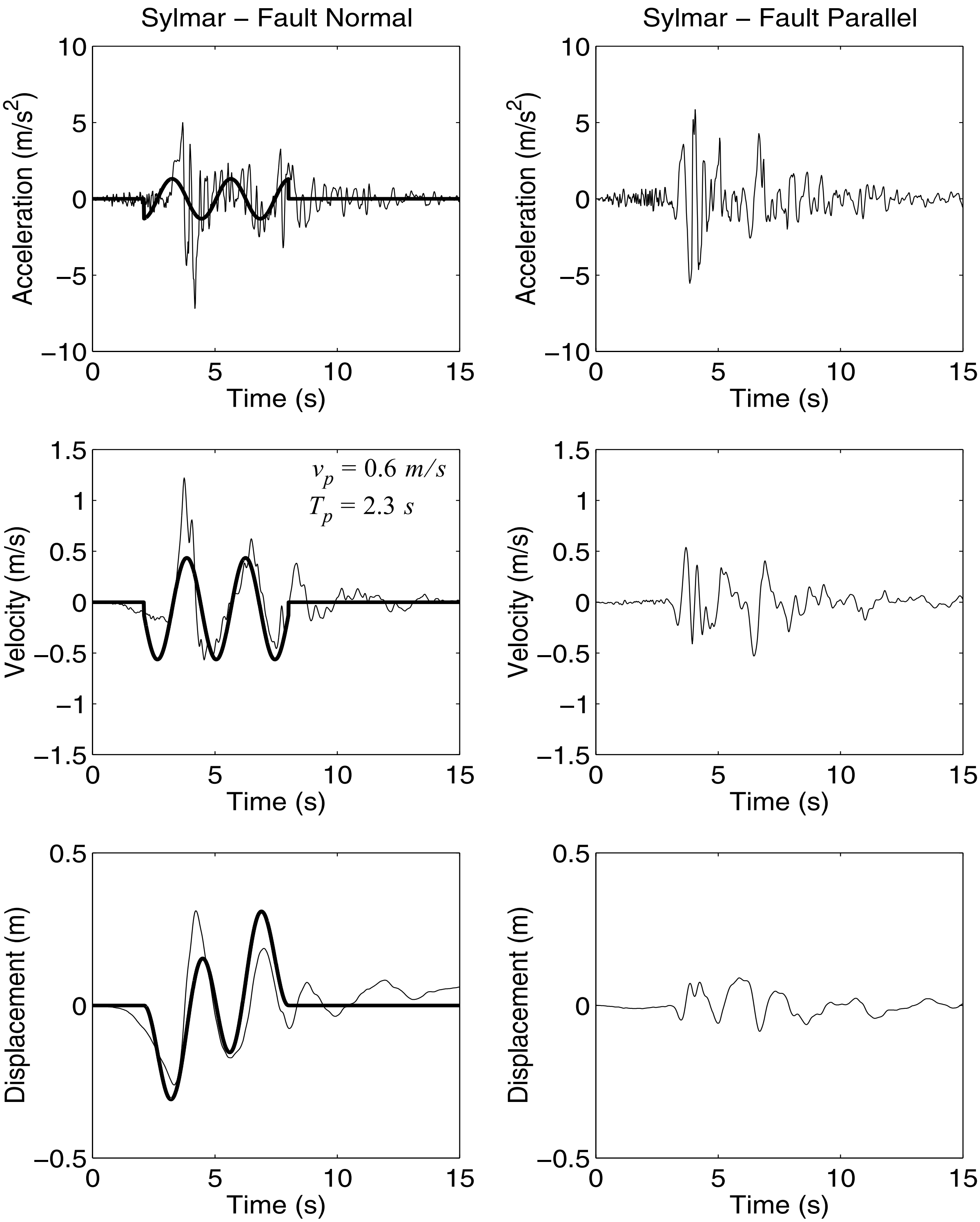

Figure 3.10 Fault-normal (left) and fault-parallel (right) components of the acceleration, velocity, and displacement time histories recorded at the Sylmar station during the 1994 Northridge, California, earthquake. The heavy lines are approximations with a type-C_2 trigonometric pulse.

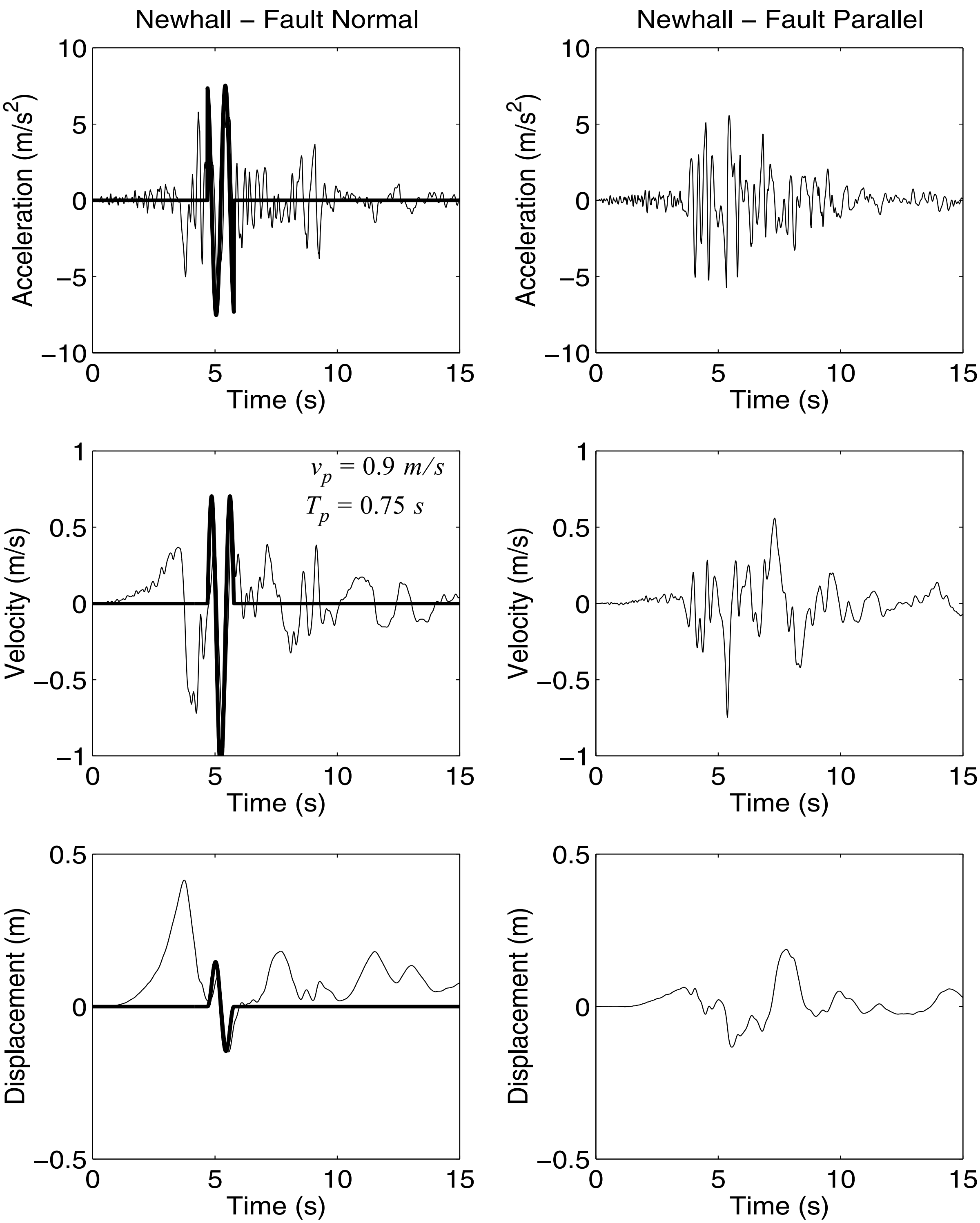

Figure 3.11 Fault-normal (left) and fault-parallel (right) components of the acceleration, velocity, and displacement time histories recorded at the Newhall station during the 1994 Northridge, California, earthquake. The heavy lines are approximations with a type-C_1 trigonometric pulse.

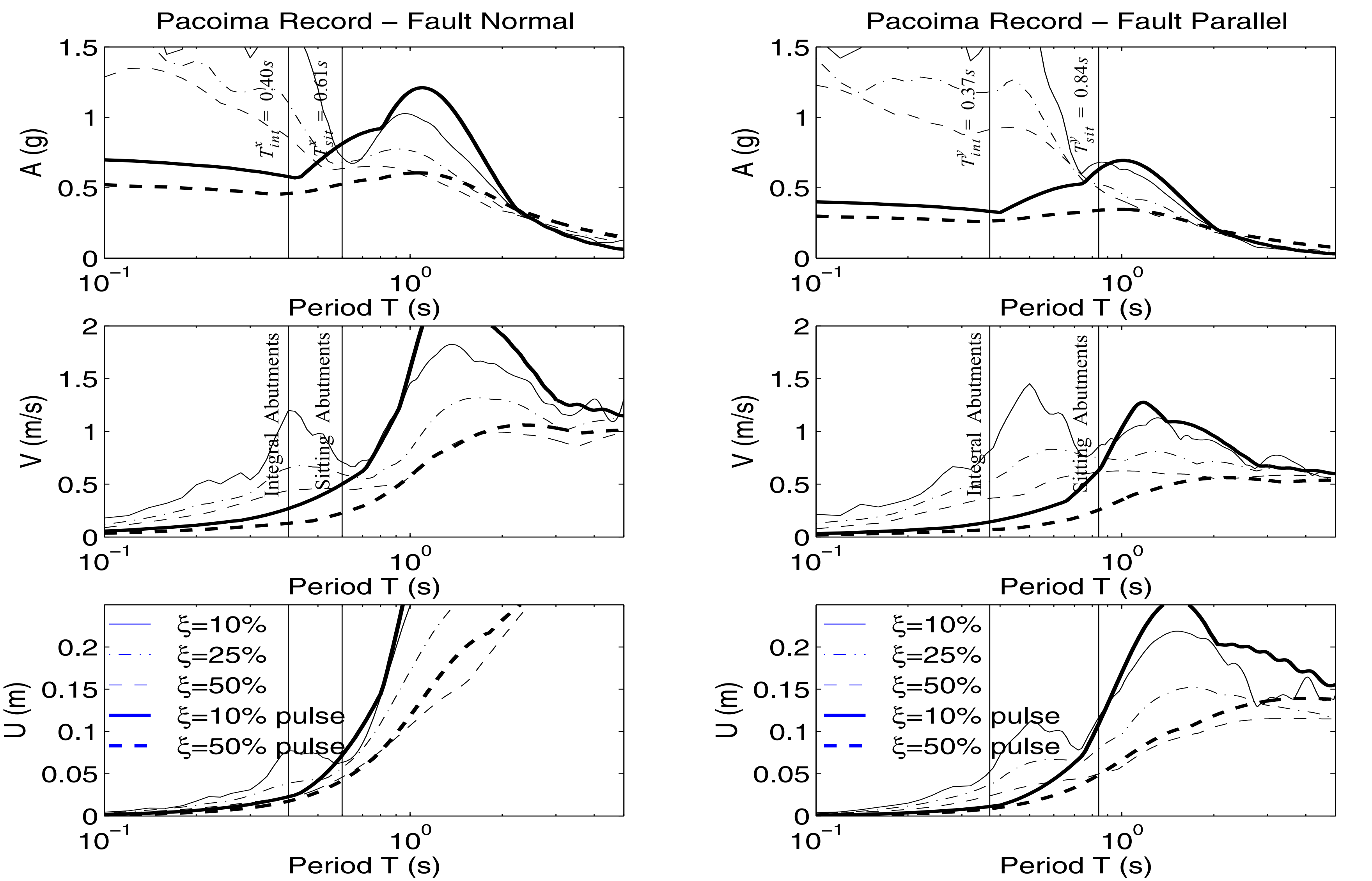

Figure 3.12 Acceleration, velocity, and displacement spectra of fault-normal (left) and fault-parallel (right) components of motions recorded at the Pacoima Dam station during the 1971 San Fernando, California, earthquake.

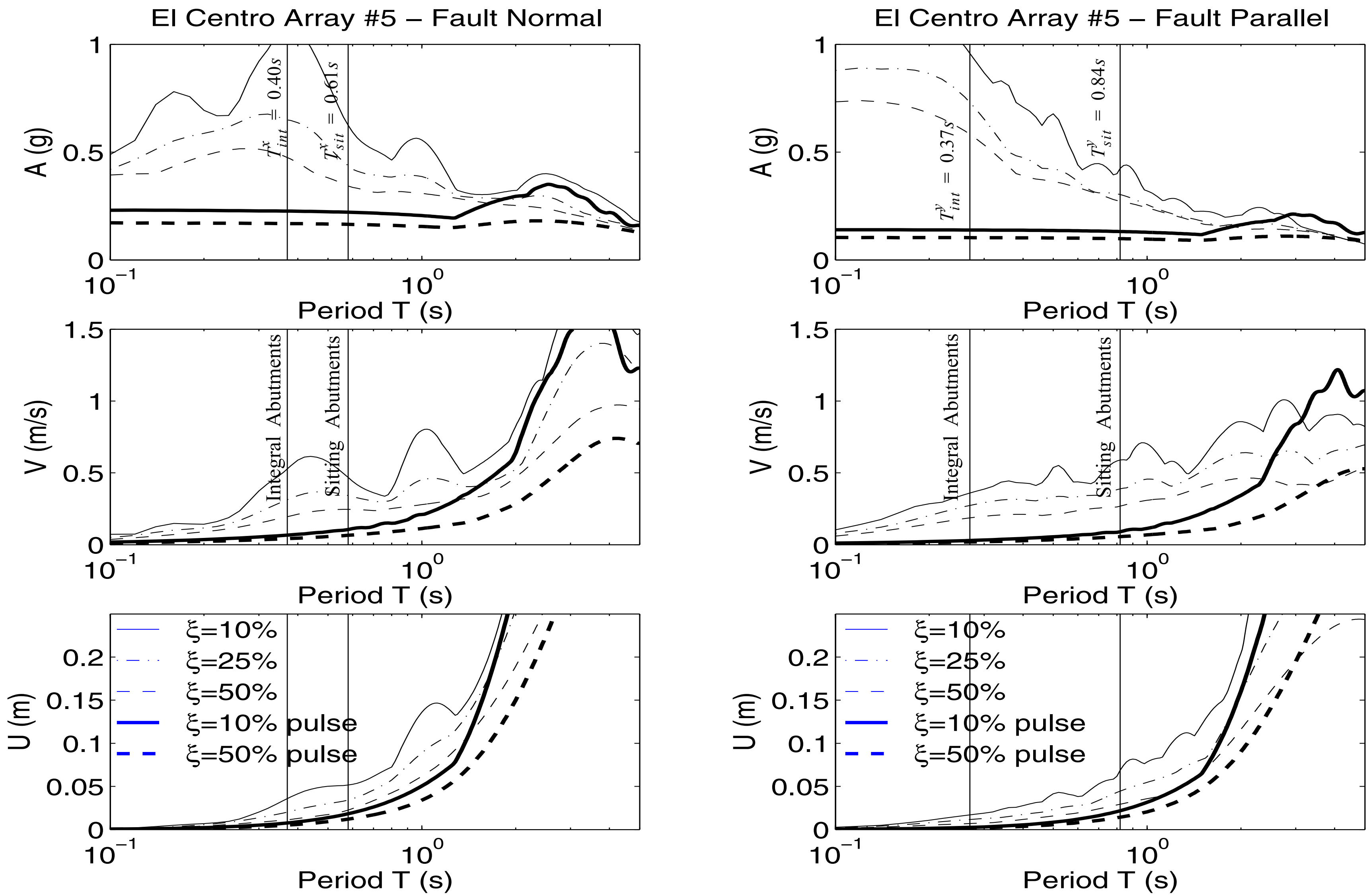

Figure 3.13 Acceleration, velocity, and displacement spectra of fault-normal (left) and fault-parallel (right) components of motions recorded at El Centro Array #5 station during the 1979 Imperial Valley, California, earthquake.

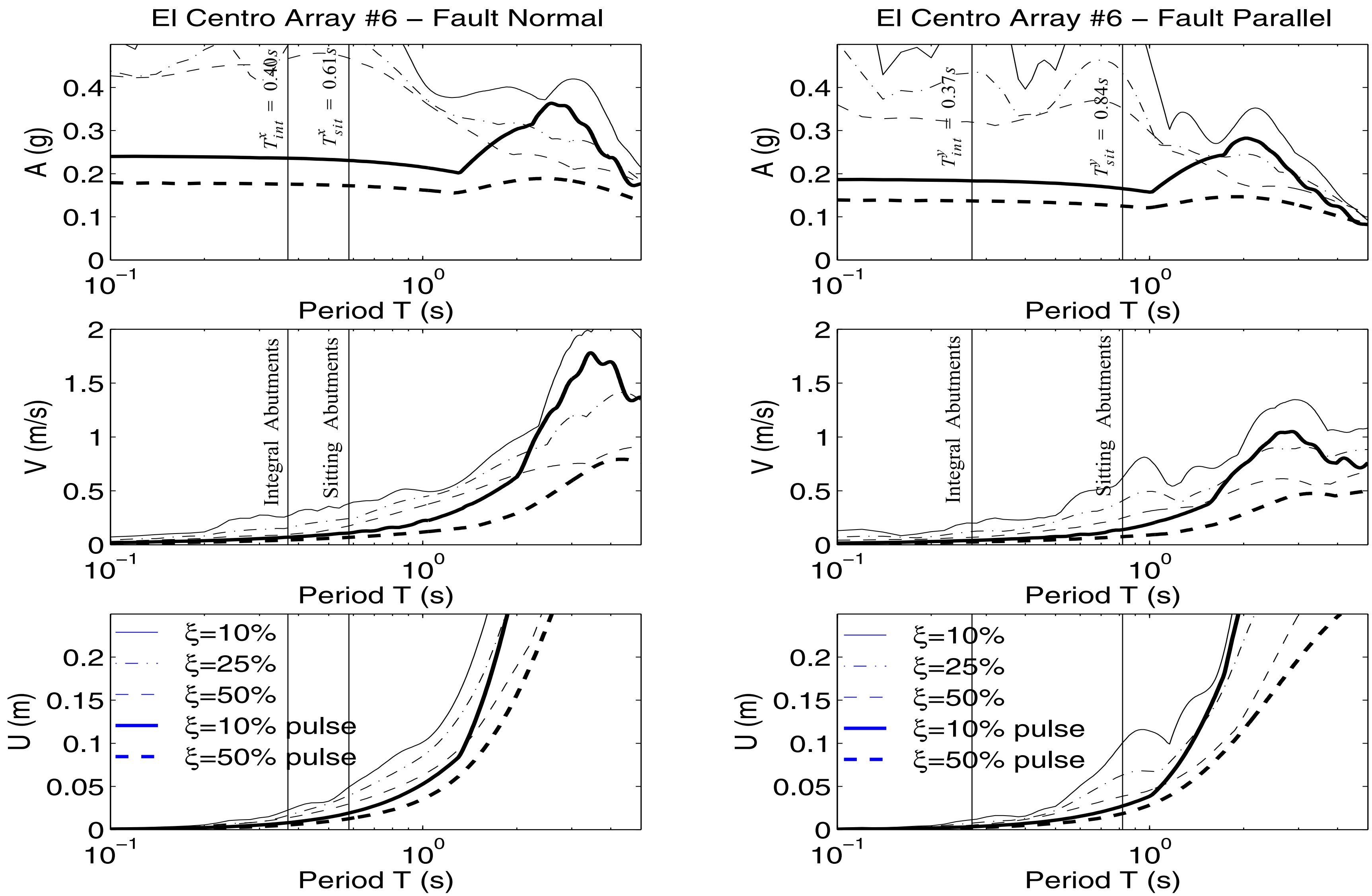

Figure 3.14 Acceleration, velocity, and displacement spectra of fault-normal (left) and fault-parallel (right) components of motions recorded at El Centro Array #6 station during the 1979 Imperial Valley, California, earthquake.

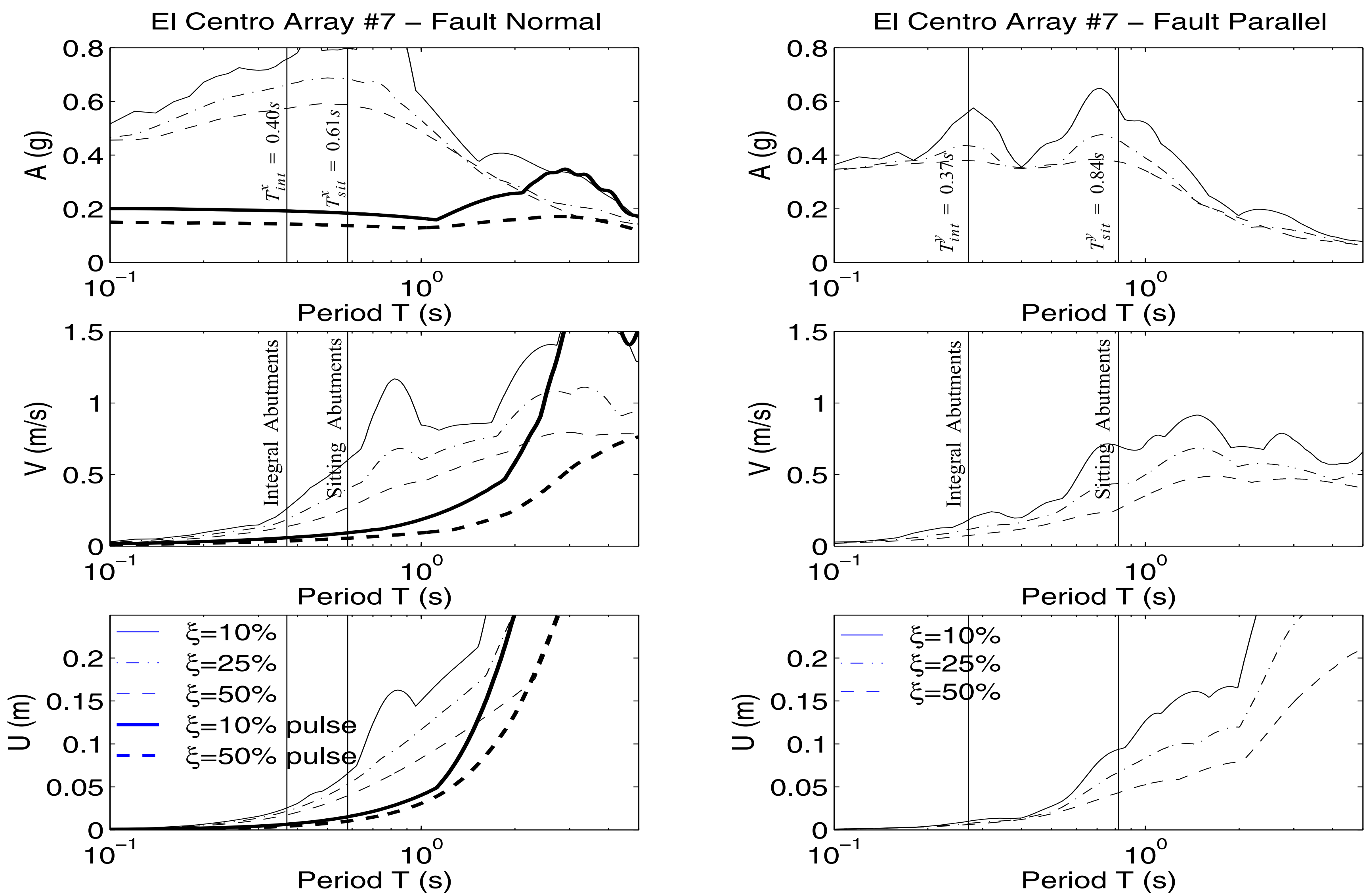

Figure 3.15 Acceleration, velocity, and displacement spectra of fault-normal (left) and fault-parallel (right) components of motions recorded at El Centro Array #7 station during the 1979 Imperial Valley, California, earthquake.

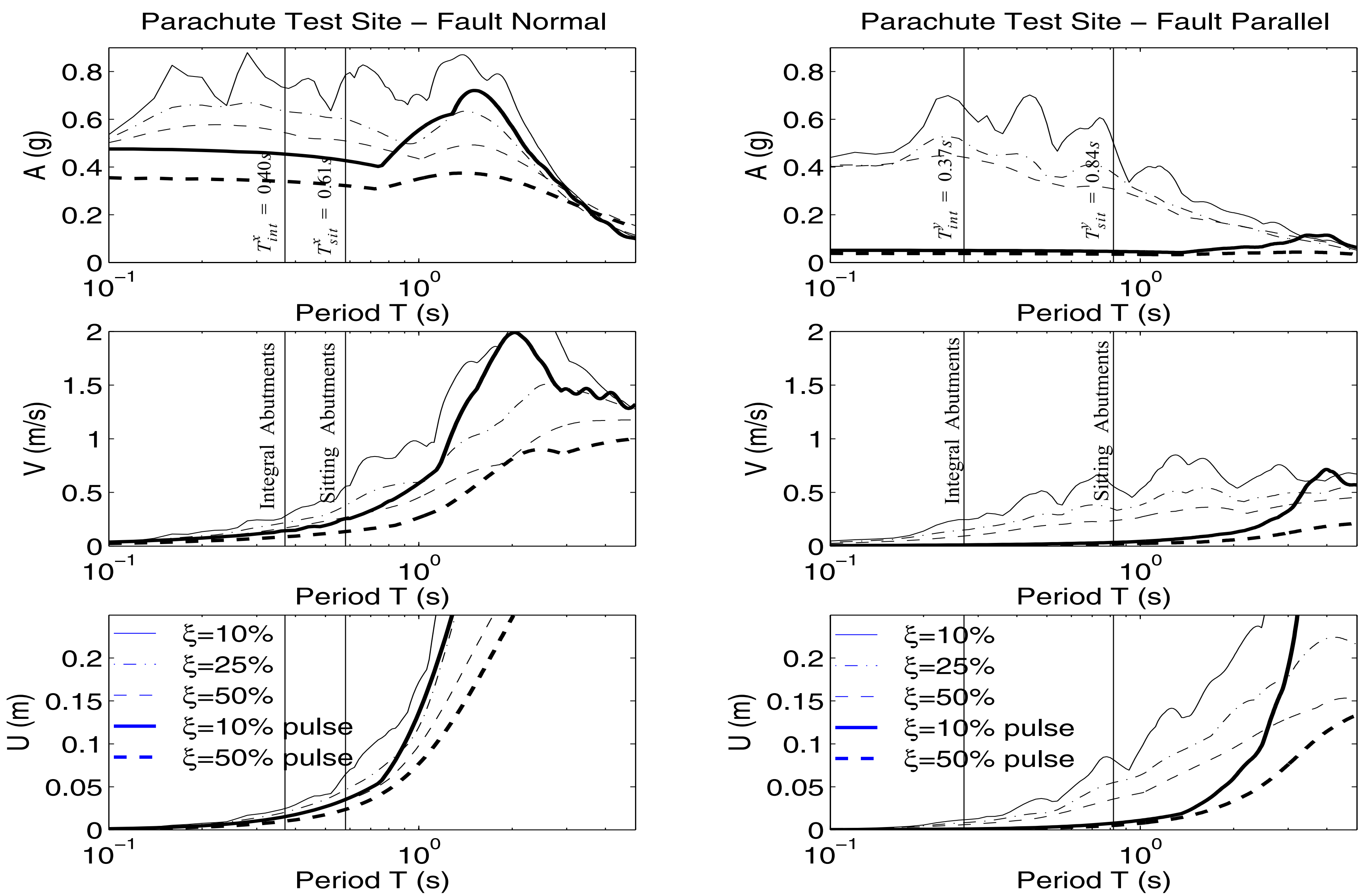

Figure 3.16 Acceleration, velocity, and displacement spectra of fault-normal (left) and fault-parallel (right) components of motions recorded at Parachute Test Site during the 1987 Superstition Hills, California, earthquake.

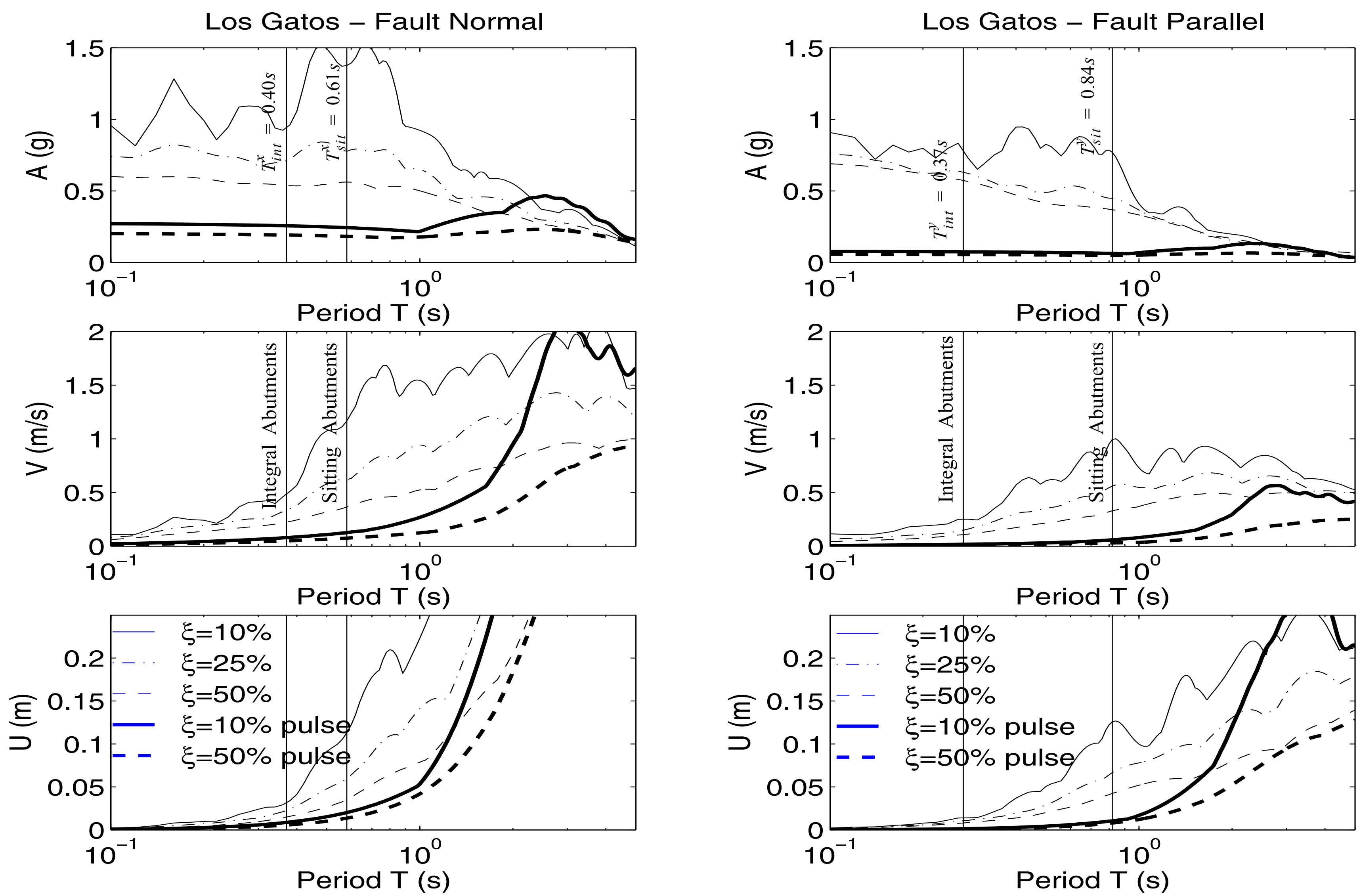

Figure 3.17 Acceleration, velocity, and displacement spectra of fault-normal (left) and fault-parallel (right) components of motions recorded at Los Gatos station during the 1989 Loma Prieta, California, earthquake.

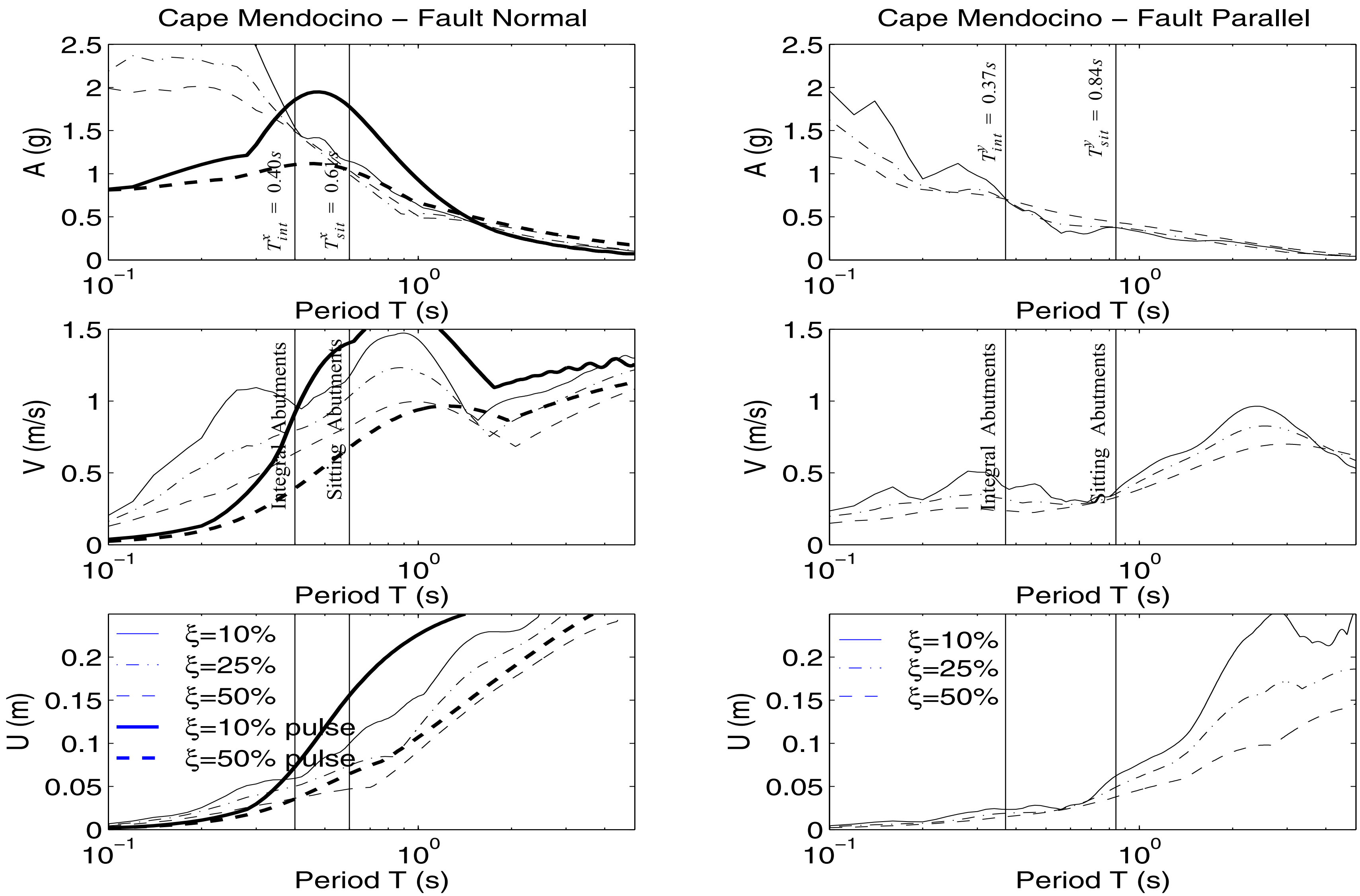

Figure 3.18 Acceleration, velocity, and displacement spectra of fault-normal (left) and fault-parallel (right) components of motions recorded at Cape Mendocino station during the 1992 Petrolia, California, earthquake.

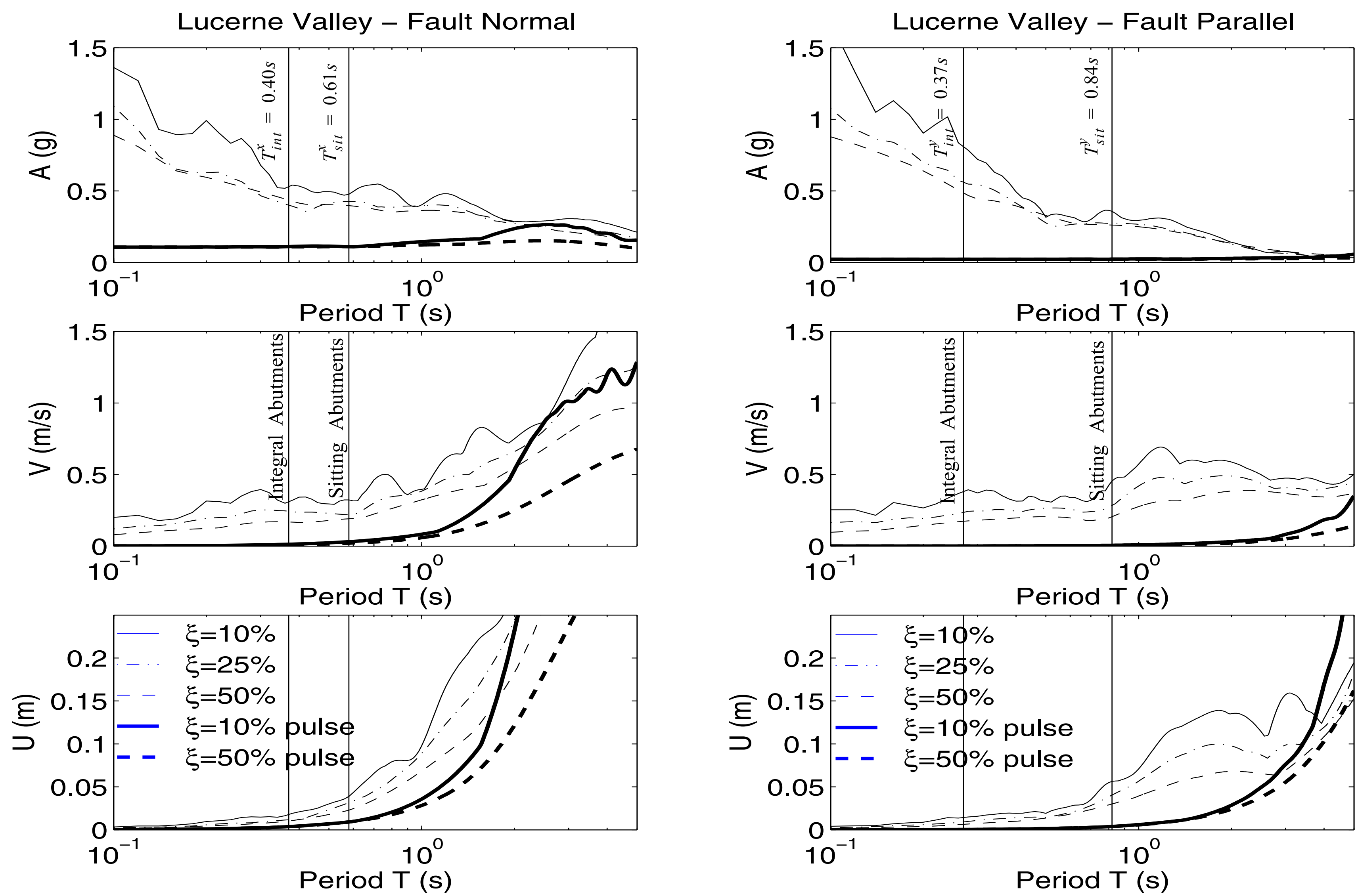

Figure 3.19 Acceleration, velocity, and displacement spectra of fault-normal (left) and fault-parallel (right) components of motions recorded at Lucerne Valley station during the 1992 Landers, California, earthquake.

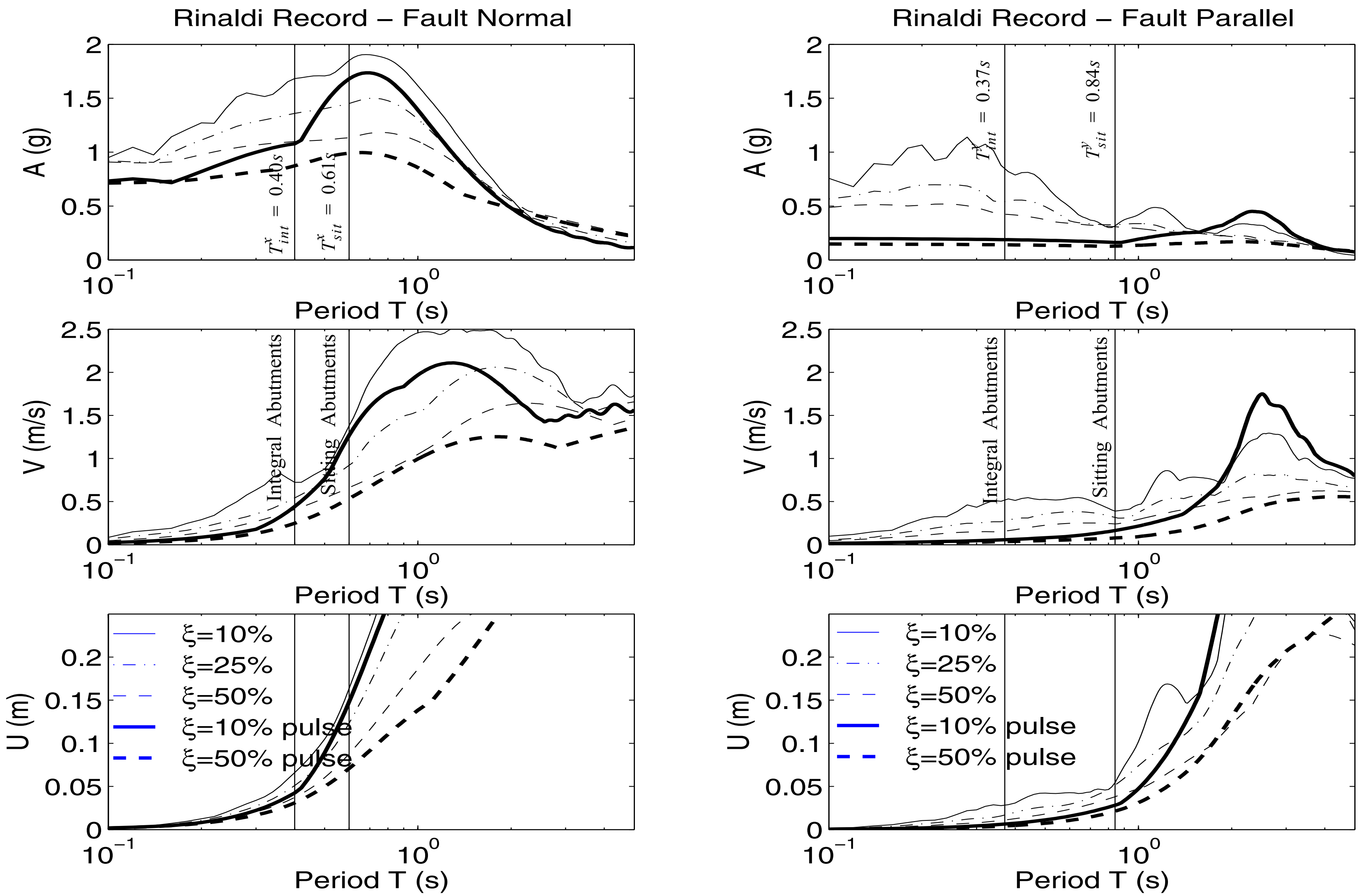

Figure 3.20 Acceleration, velocity, and displacement spectra of fault-normal (left) and fault-parallel (right) components of motions recorded at Rinaldi station during the 1994 Northridge, California, earthquake.

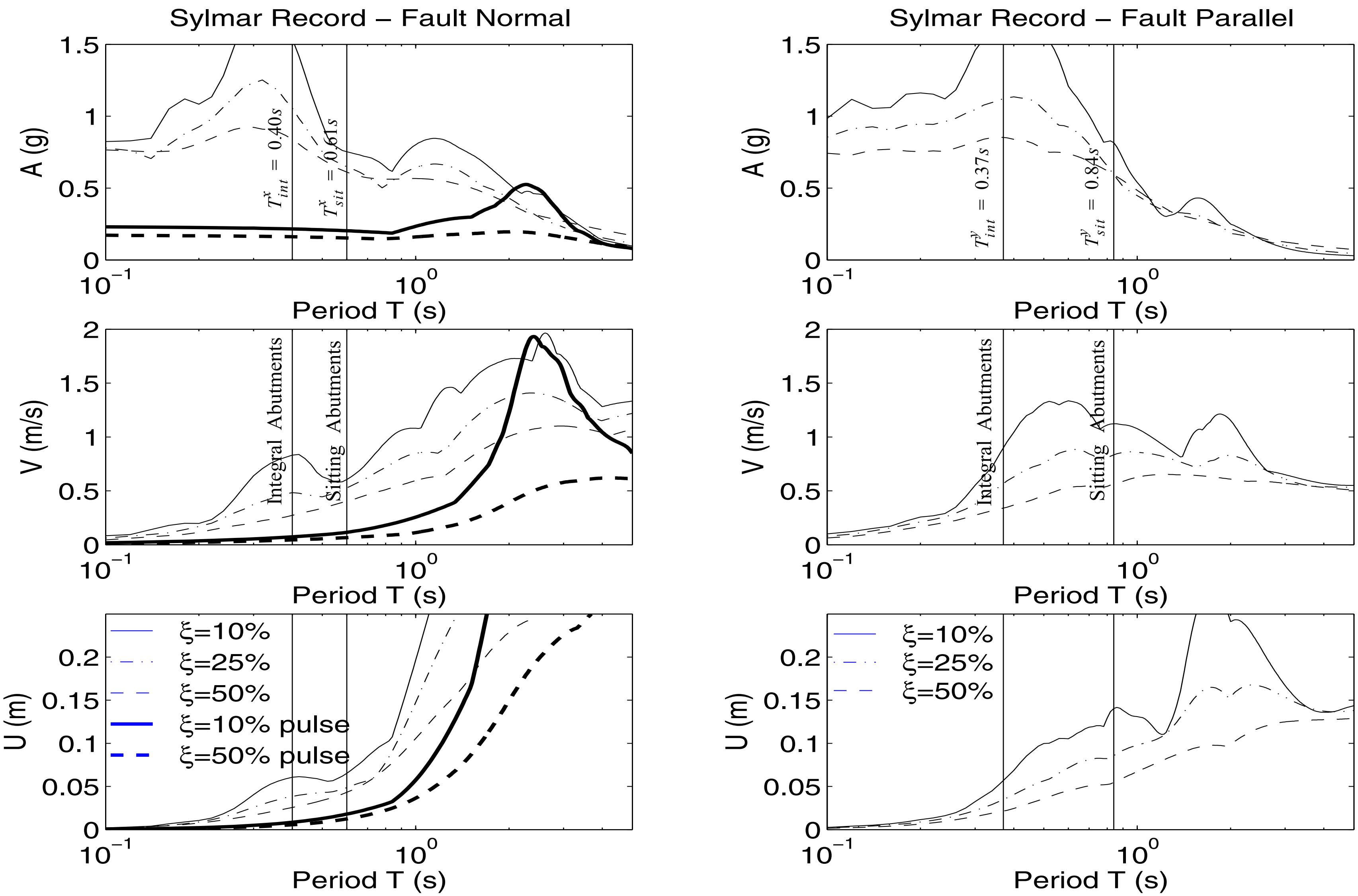

Figure 3.21 Acceleration, velocity, and displacement spectra of fault-normal (left) and fault-parallel (right) components of motions recorded at Sylmar station during the 1994 Northridge, California, earthquake.

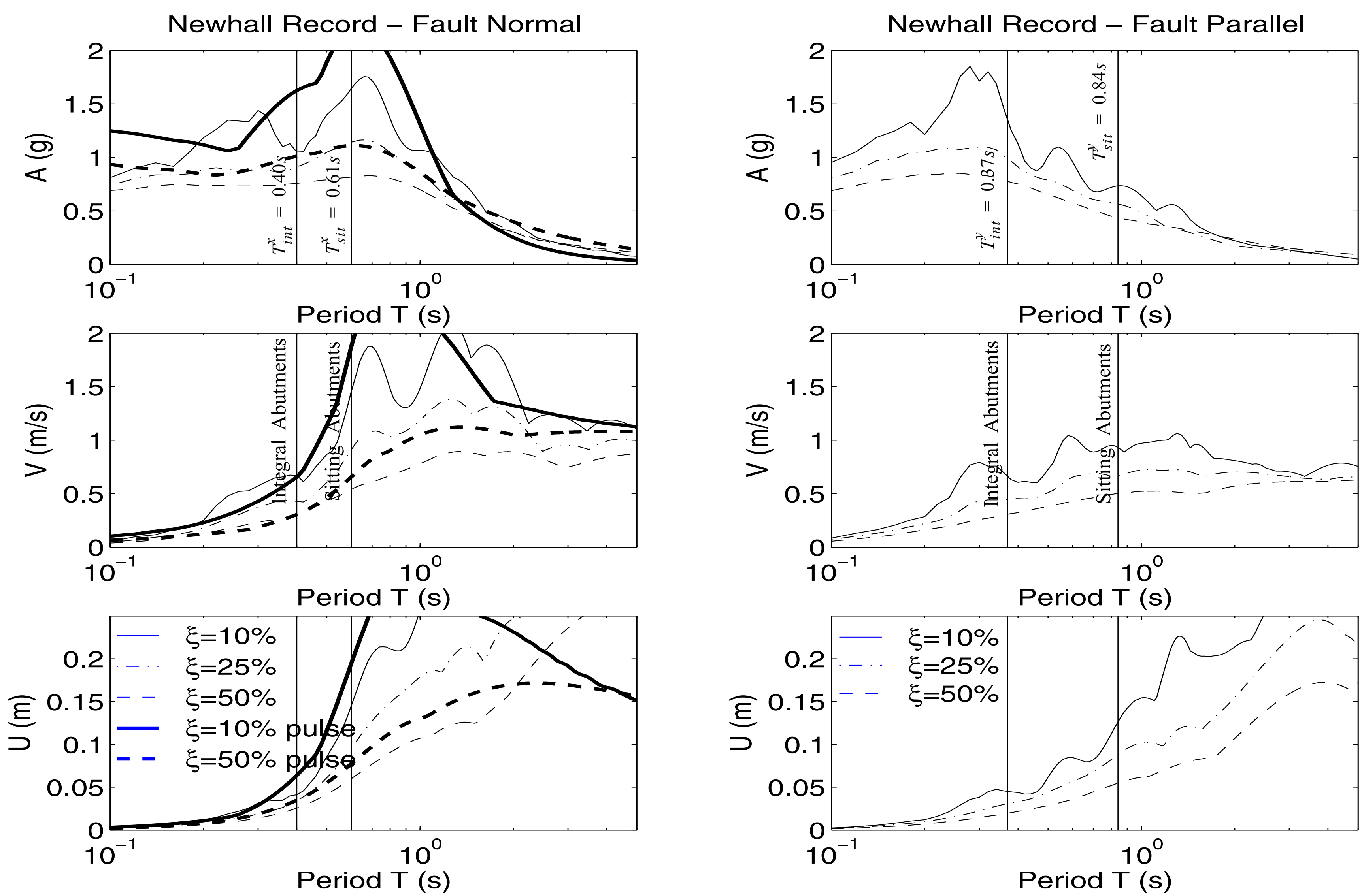

Figure 3.22 Acceleration, velocity, and displacement spectra of fault-normal (left) and fault-parallel (right) components of motions recorded at Newhall station during the 1994 Northridge, California, earthquake.

4 Kinematic Response Functions and Dynamic Stiffnesses of Embankments and Pile Foundations

4.1 KINEMATIC RESPONSE FUNCTIONS AND DYNAMIC STIFFNESSES OF EMBANKMENTS

Approach embankments are massive, long deformable bodies that amplify considerably the free-field earthquake motions and interact strongly with the bridge structure. During the last two decades a considerable amount of published research has focused on refining, expanding, and verifying the basic dynamic models developed in the 1960s for predicting the seismic response of approach embankments. A comprehensive critical review of past studies together with an in-depth investigation on the ability of the shear beam to capture the recorded response on bridge embankments has been presented by Zhang and Makris (2001, 2002a). In this study the validity of the approximate procedure proposed by Zhang and Makris (2001, 2002a) to estimate the kinematic response functions and the dynamic stiffnesses of approach embankments is examined for the case of the 91/5 overcrossing. First the values of the shear modulus, G , and damping ratio η , are estimated with the shear wedge model. Since this involves a one-dimensional (1-D) analysis, each component of the ground motions shown in Figures 3.1 to 3.11 was induced separately. The converged values for the shear modulus, G, the damping coefficient, η , and the average shear strain, γ, that result from the shear wedge analysis are shown in Table 4.1.

The finite element analysis is conducted with the computer software ABAQUS (1997). The seismic response of the approach embankment is computed in the time domain where damping is represented with the Rayleigh approximation. The damping matrix, $[C]$, of the soil

Table 4.1 Converged values of the shear modulus, G, and the damping coefficient, η, under selected strong motion records

Earthquakes	G (MPa)		η		γ	
	SB	**FEM**	**SB**	**FEM**	**SB**	**FEM**
Pacoima Dam (FN), 1971 San Fernando	9.4	8.8	0.50	0.51	4.6×10^{-3}	5.2×10^{-3}
Pacoima Dam (FP), 1971 San Fernando	7.1		0.53		6.8×10^{-3}	
El Centro #5 (FN), 1979 Imperial Valley	14.1	17.8	0.45	0.42	2.6×10^{-3}	1.8×10^{-3}
El Centro #5 (FP), 1979 Imperial Valley	18.5		0.41		1.7×10^{-3}	
El Centro #6 (FN), 1979 Imperial Valley	24.1	23.6	0.36	0.36	1.1×10^{-3}	1.1×10^{-3}
El Centro #6 (FP), 1979 Imperial Valley	22.6		0.37		1.2×10^{-3}	
El Centro #7 (FN), 1979 Imperial Valley	15.1	23.1	0.44	0.36	2.3×10^{-3}	1.2×10^{-3}
El Centro #7 (FP), 1979 Imperial Valley	23.8		0.36		1.1×10^{-3}	
Parachute Test Site (FN), 1987 Superstition Hills	18.0	19.9	0.41	0.39	1.8×10^{-3}	1.5×10^{-3}
Parachute Test Site (FP), 1987 Superstition Hills	22.3		0.37		1.5×10^{-3}	
Los Gatos (FN), 1989 Loma Prieta	8.9	15.7	0.51	0.44	4.9×10^{-3}	2.2×10^{-3}
Los Gatos (FP), 1989 Loma Prieta	17.6		0.42		1.8×10^{-3}	
Cape Mendocino (FN), 1992 Petrolia	6.9	8.7	0.53	0.51	7.0×10^{-3}	5.1×10^{-3}
Cape Mendocino (FP), 1992 Petrolia	17.0		0.42		1.9×10^{-3}	
Lucerne Valley (FN), 1992 Landers	22.2	19.3	0.37	0.40	1.2×10^{-3}	1.6×10^{-3}
Lucerne Valley (FP), 1992 Landers	19.6		0.40		1.5×10^{-3}	
Rinaldi (FN), 1994 Northridge	4.2	9.5	0.59	0.50	1.7×10^{-2}	4.5×10^{-3}
Rinaldi (FP), 1994 Northridge	18.8		0.41		1.7×10^{-3}	
Sylmar (FN), 1994 Northridge	9.7	9.5	0.50	0.50	4.4×10^{-3}	4.5×10^{-3}
Sylmar (FP), 1994 Northridge	7.6		0.52		6.1×10^{-3}	
Newhall (N-S), 1994 Northridge	5.6	8.2	0.56	0.52	9.8×10^{-3}	5.6×10^{-3}
Newhall (E-W), 1994 Northridge	11.3		0.48		3.7×10^{-3}	

structure is assumed to be a linear combination of the mass matrix, $[M]$, and the stiffness matrix, $[K]$:

$$[C] = \alpha[M] + \beta[K] \tag{4.1}$$

where parameters α and β are determined by $\xi_1 = \xi_2 = \eta/2$.

Figure 4.1 plots the computed time histories of the converged strains at the base, mid-height, and crest of the east embankment of the 91/5 overcrossing subjected simultaneously to the fault-normal and fault-parallel components of the motion recorded at the Pacoima Dam station during the 1971 San Fernando earthquake. The left column plots the time history of the strains due to transverse shearing (γ_{xz}), the center column plots the time history of strains due to longitudinal shearing (γ_{yz}), whereas the right column plots the amplitude of the maximum shear strains γ_{max} as a function of time. Following a suggestion by Seed and Idriss (1969), Figure 4.1 indicates that an approximate value for the converged strain is 5.2×10^{-3}. This corresponds to $G = 8.8\ MPa$ ($G/G_{max} = 0.12$) and $\eta = 0.51$. These values are indeed very close to the values computed with the shear-wedge approximation.

Figure 4.2 plots the computed time histories of the converged strains at the base, mid-height, and crest of the east embankment of the 91/5 overcrossing subjected simultaneously to the fault-normal and fault-parallel components of the motion recorded at Array #5 during the 1979 Imperial Valley earthquake. Figure 4.2 indicates that an approximate value for the converged strain is 1.8×10^{-3}. This corresponds to $G = 17.8\ MPa$ ($G/G_{max} = 0.25$) and $\eta = 0.42$. These values are also very close to the values computed with the shear-wedge approximation. Figure 4.3 plots the computed time histories of the converged strains at the base, mid-height, and crest of the east embankment of the 91/5 overcrossing subjected simultaneously to the fault-normal and fault-parallel components of the motion recorded at the Array #6 during the 1979 Imperial Valley earthquake. Figure 4.3 indicates a converged strain that is close to the values computed with the shear-wedge approximation when the fault-parallel component is used. Figures 4.4 to 4.11 plot the computed time histories of the converged strains of the east embankment subjected simultaneously to the fault-normal and fault-parallel components of the remaining motions listed in Table 4.1. The associated values of the converged strains, shear moduli, and damping coefficients under the three-dimensional (3-D) finite element are also shown in Table 4.1, and it is concluded that the 3-D finite element analysis yields converged strain values close to the values predicted by the shear-wedge approximation. Figure 4.12 plots the variation of soil shear modulus

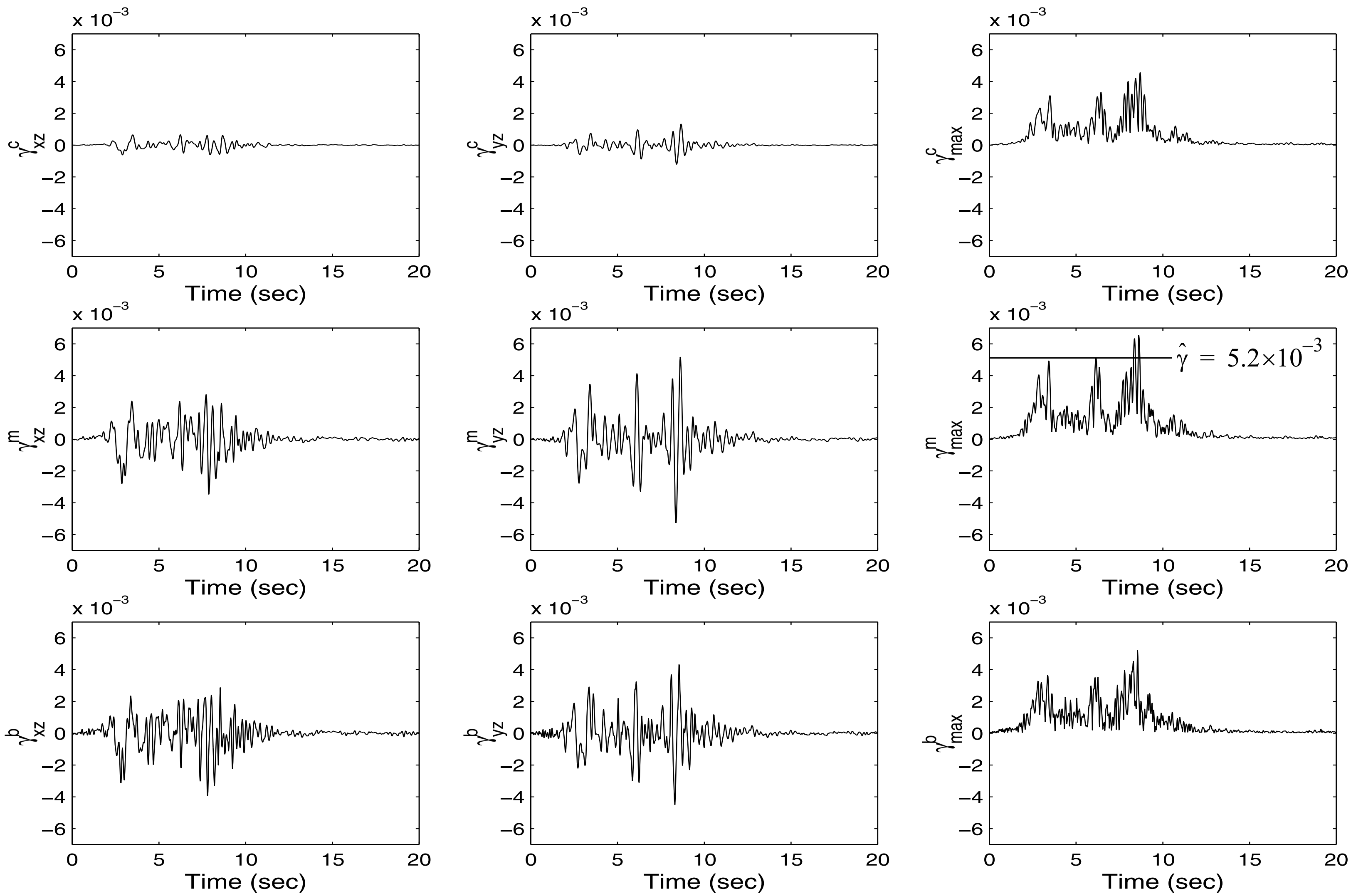

Figure 4.1 Converged strain time histories at base, center, and near top of 91/5 overcrossing embankment under Pacoima Dam record, 1971 San Fernando earthquake, computed with Rayleigh damping approximation ($G = 8.8\ MPa$, $\eta = 0.51$, $\alpha = 2.77$, and $\beta = 2.36\times10^{-2}$).

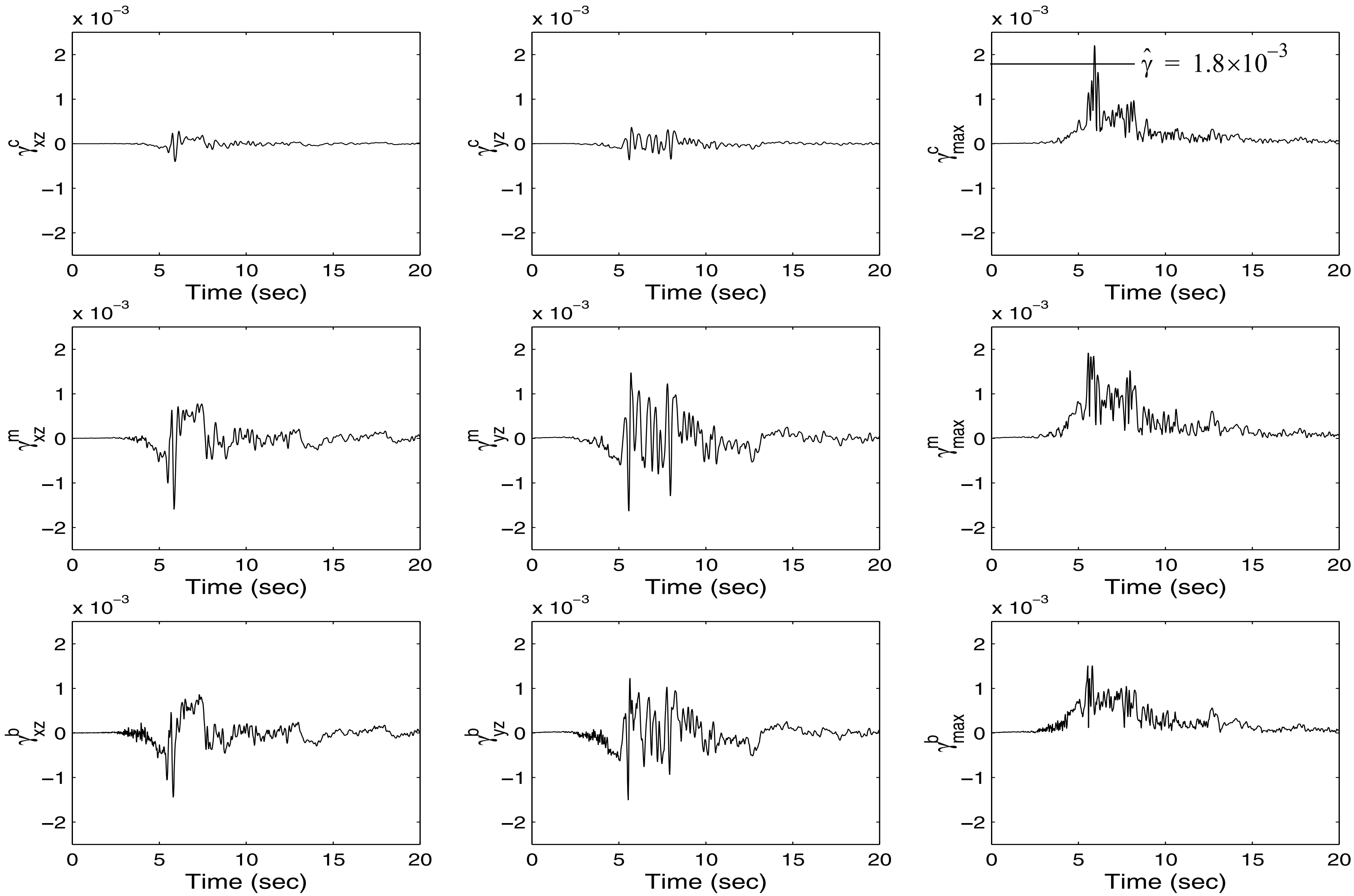

Figure 4.2 Converged strain time histories at base, center, and near top of 91/5 overcrossing embankment under El Centro Array #5 record, 1979 Imperial Valley earthquake, computed with Rayleigh damping approximation ($G = 17.8\ MPa$**,** $\eta = 0.42$**,** $\alpha = 3.24$**, and** $\beta = 1.33\times10^{-2}$**).**

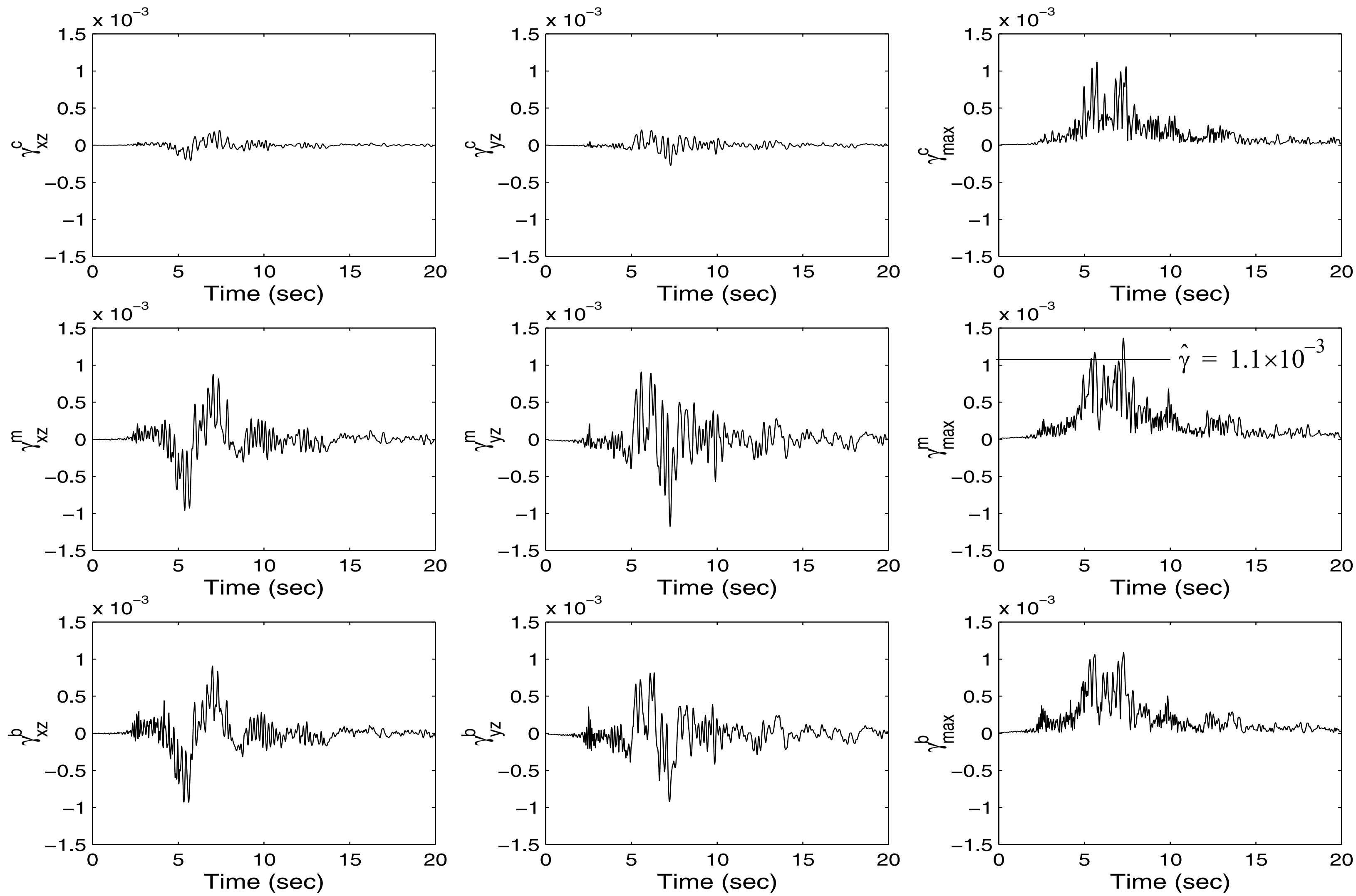

Figure 4.3 Converged strain time histories at base, center, and near top of 91/5 overcrossing embankment under El Centro Array #6 record, 1979 Imperial Valley earthquake, computed with Rayleigh damping approximation ($G = 23.6\ MPa$, $\eta = 0.36$, $\alpha = 3.23$, and $\beta = 9.94\times10^{-3}$).

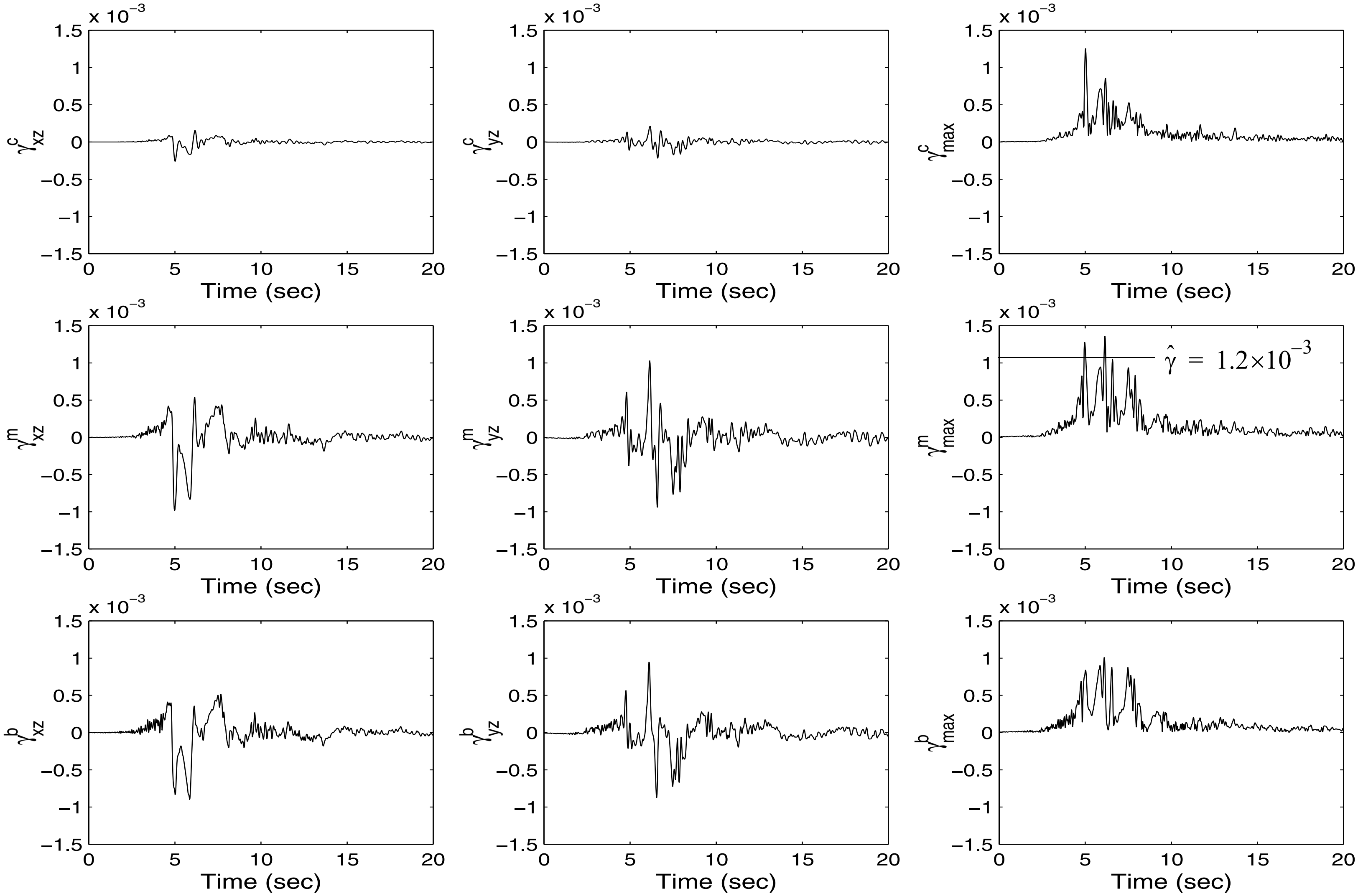

Figure 4.4 Converged strain time histories at base, center, and near top of 91/5 overcrossing embankment under El Centro Array #7 record, 1979 Imperial Valley earthquake, computed with Rayleigh damping approximation ($G = 23.1\ MPa$, $\eta = 0.36$, $\alpha = 3.24$, and $\beta = 1.02\times10^{-2}$).

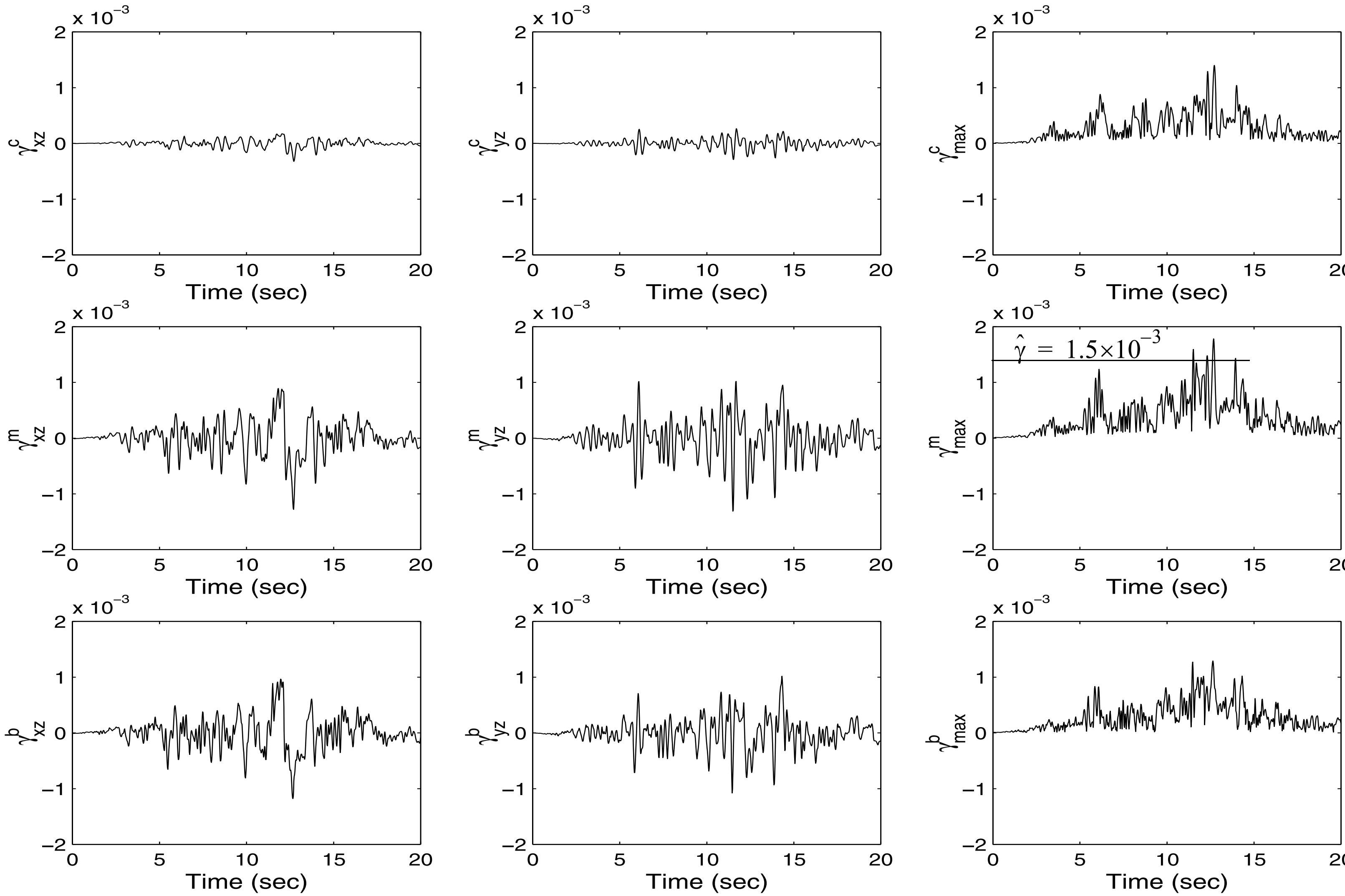

Figure 4.5 Converged strain time histories at base, center, and near top of 91/5 overcrossing embankment under Parachute Test Site record, 1987 Superstition Hills earthquake, computed with Rayleigh damping approximation ($G = 19.9\ MPa$**,** $\eta = 0.39$**,** $\alpha = 3.26$**, and** $\beta = 1.15\times10^{-2}$**).**

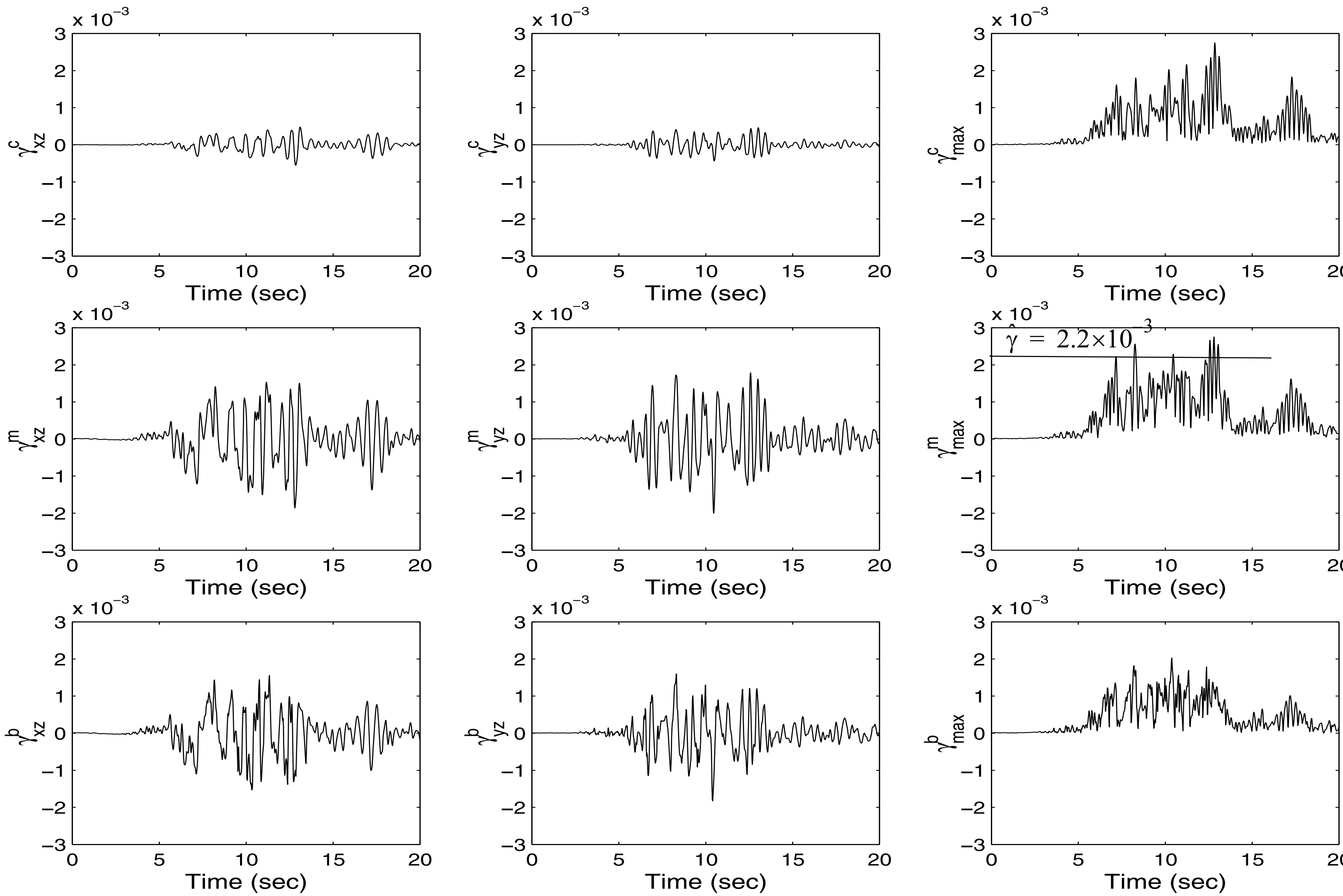

Figure 4.6 Converged strain time histories at base, center, and near top of 91/5 overcrossing embankment under Los Gatos record, 1989 Loma Prieta earthquake, computed with Rayleigh damping approximation ($G = 15.7\ MPa$, $\eta = 0.44$, $\alpha = 3.18$, and $\beta = 1.53 \times 10^{-2}$).

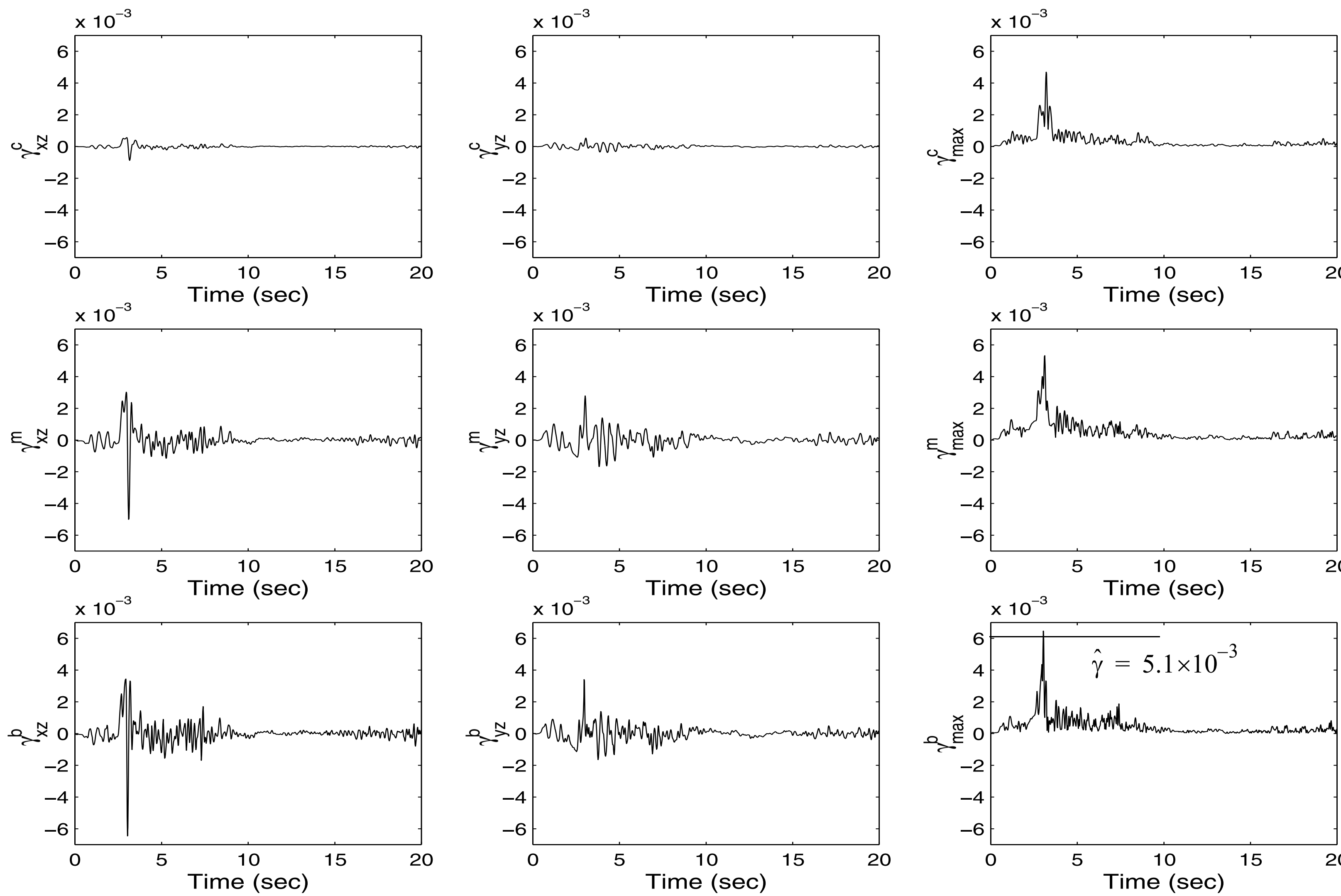

Figure 4.7 Converged strain time histories at base, center, and near top of 91/5 overcrossing embankment under Cape Mendocino record, 1992 Petrolia earthquake, computed with Rayleigh damping approximation ($G = 8.7\ MPa$**,** $\eta = 0.51$**,** $\alpha = 2.78$**, and** $\beta = 2.32\times10^{-2}$**).**

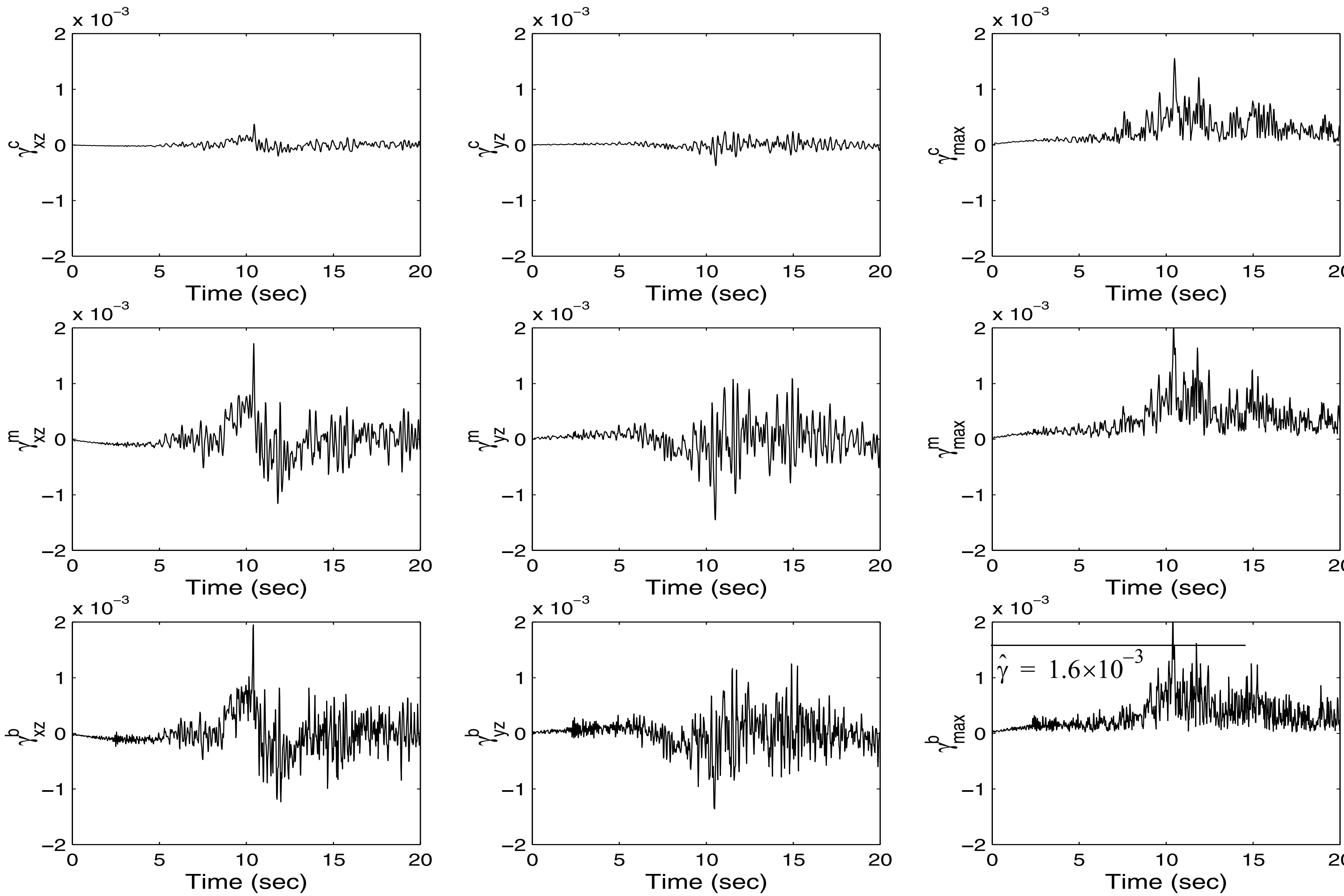

Figure 4.8 Converged strain time histories at base, center, and near top of 91/5 overcrossing embankment under Lucerne Valley record, 1992 Landers earthquake, computed with Rayleigh damping approximation ($G = 19.3\ MPa$**,** $\eta = 0.40$**,** $\alpha = 3.25$**, and** $\beta = 1.23\times10^{-2}$**).**

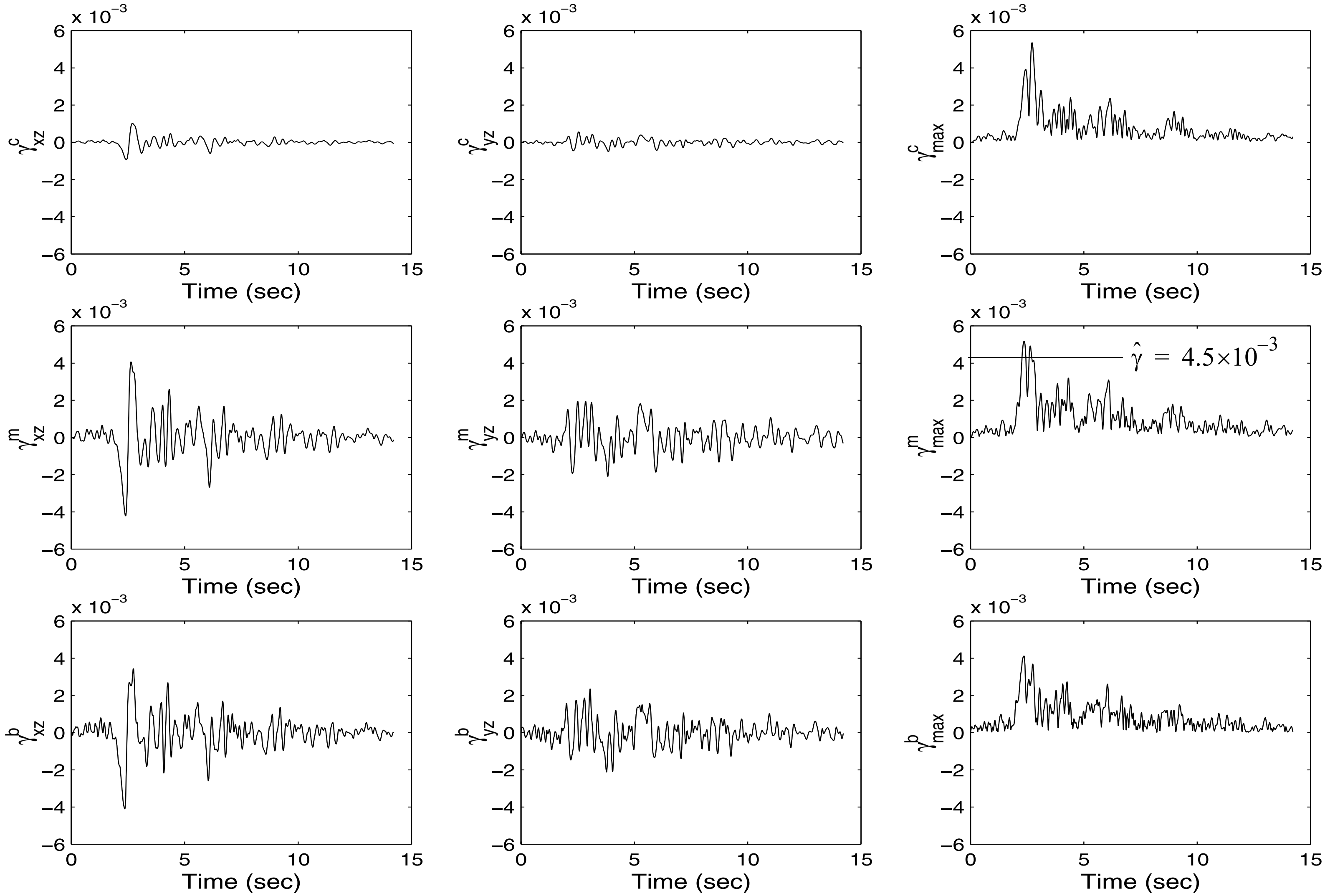

Figure 4.9 Converged strain time histories at base, center, and near top of 91/5 overcrossing embankment under Rinaldi record, 1994 Northridge earthquake, computed with Rayleigh damping approximation ($G = 9.5\ MPa$, $\eta = 0.50$, $\alpha = 2.76$, and $\beta = 2.26\times10^{-2}$).

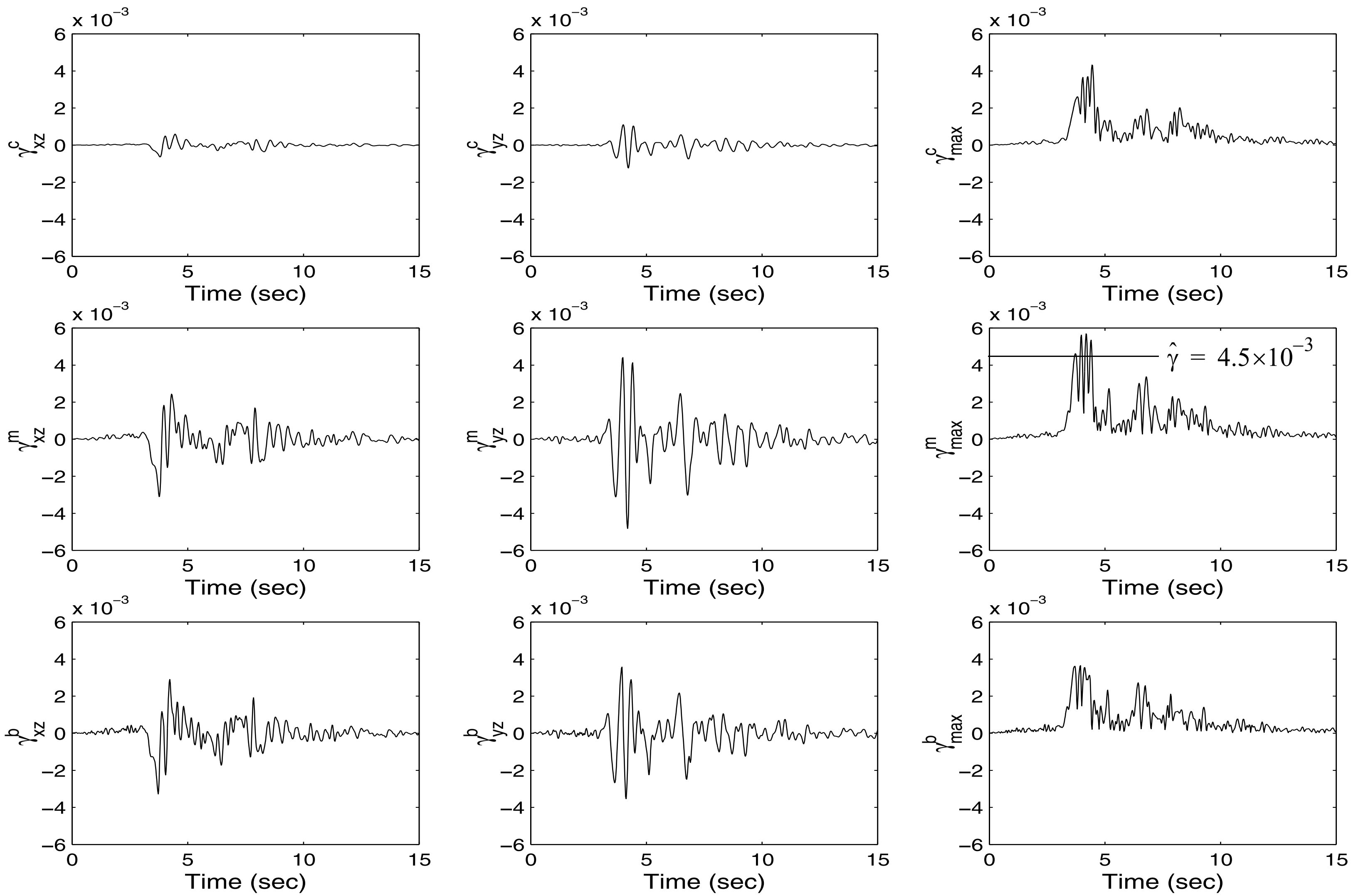

Figure 4.10 Converged strain time histories at base, center, and near top of 91/5 overcrossing embankment under Sylmar record, 1994 Northridge earthquake, computed with Rayleigh damping approximation ($G = 9.5\ MPa$, $\eta = 0.50$, $\alpha = 2.86$, and $\beta = 2.19\times10^{-2}$).

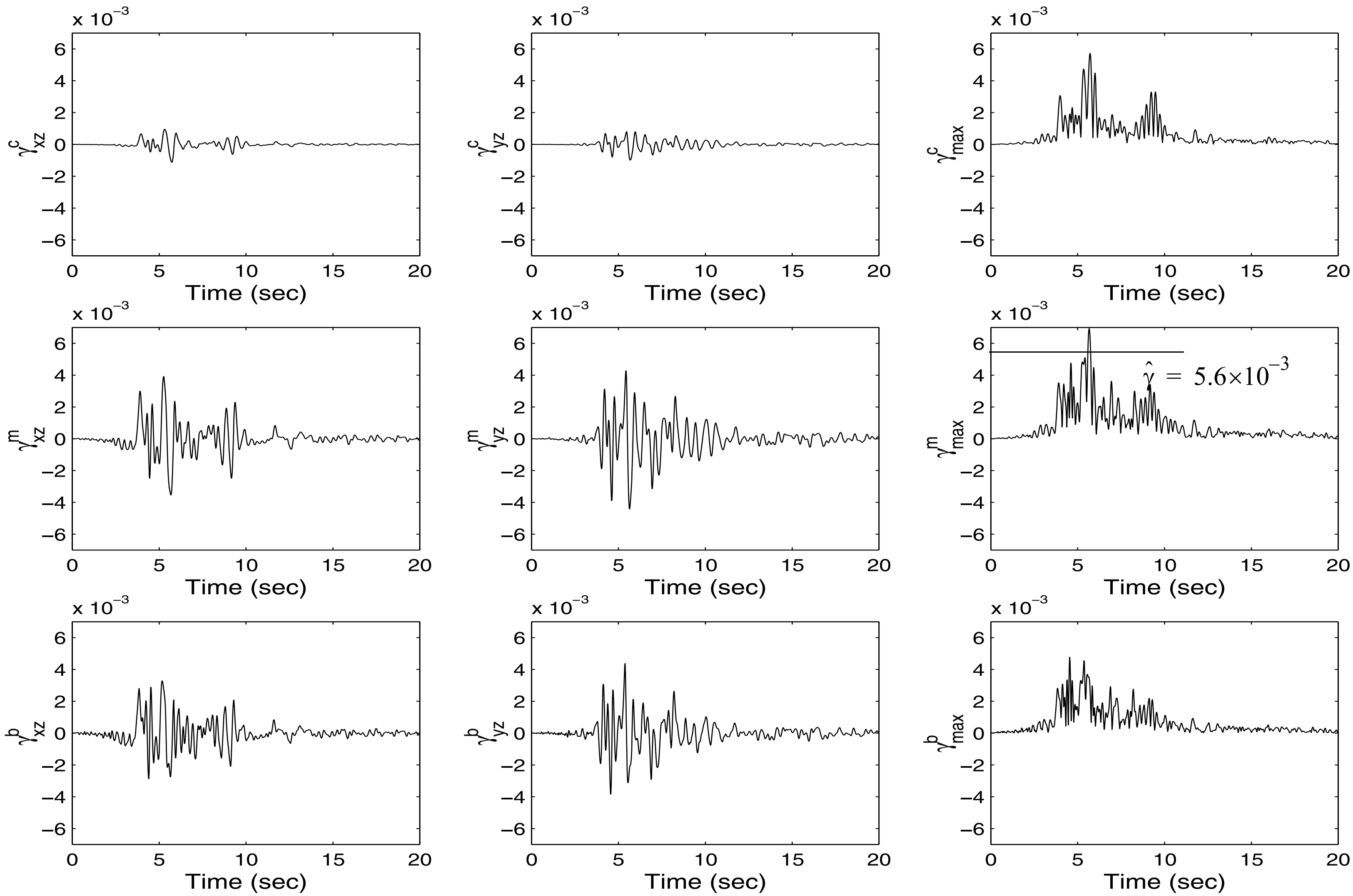

Figure 4.11 Converged strain time histories at base, center, and near top of 91/5 overcrossing embankment under Newhall record, 1994 Northridge earthquake, computed with Rayleigh damping approximation ($G = 8.2\ MPa$, $\eta = 0.52$, $\alpha = 2.73$, and $\beta = 2.45\times10^{-2}$).

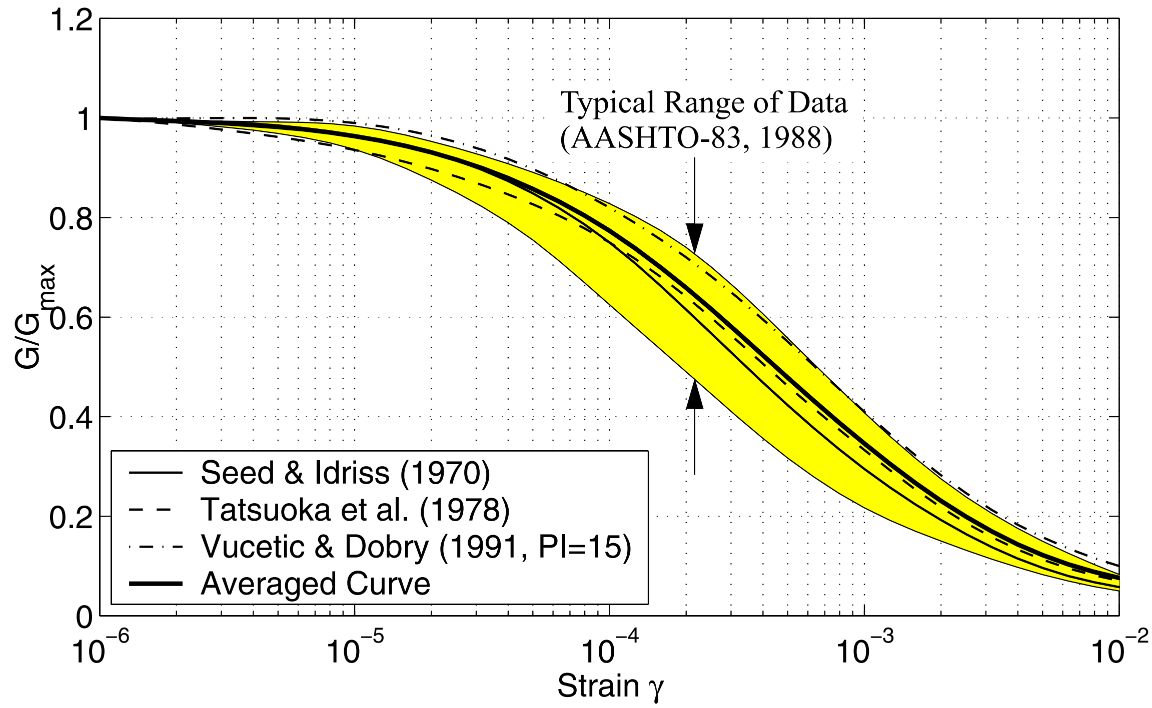

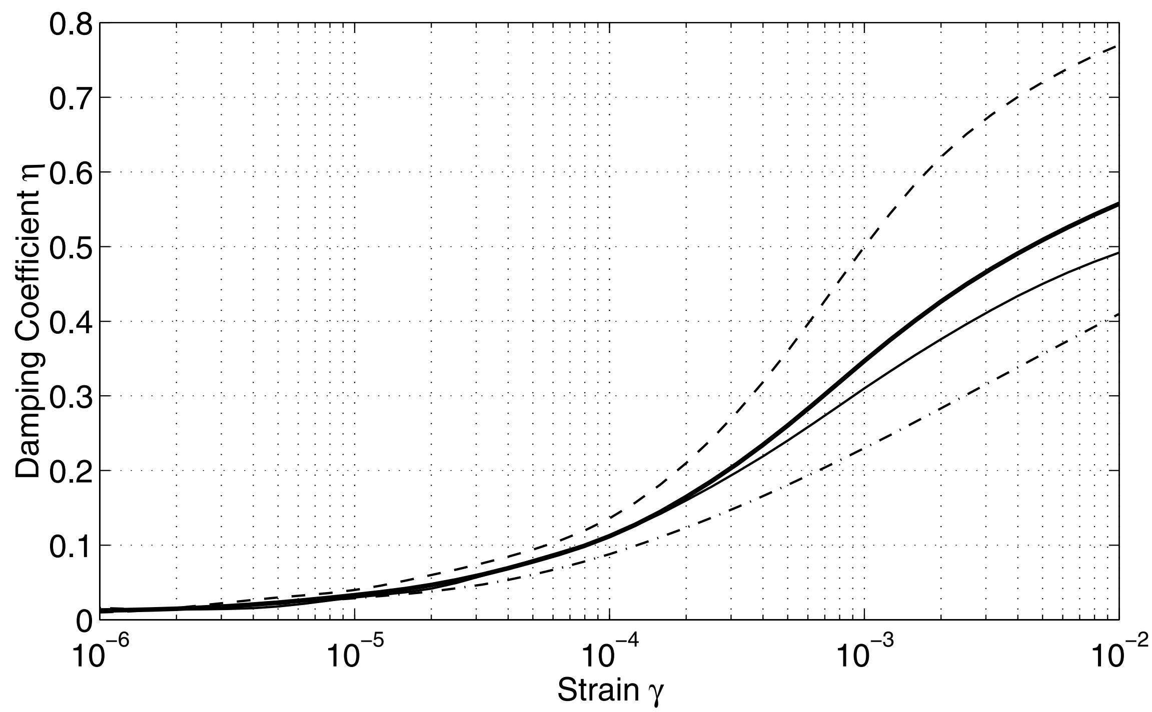

Figure 4.12 Normalized soil shear modulus, G, and damping coefficient, $\eta = 2\xi$, as a function of shear strain.

and damping coefficient with shear strain and the range of maximum shear strains of the embankments that have been computed with the 3-D finite element analysis. Because of the appreciable variability in the converged values of the soil characteristics shown in Table 4.1, two sets of shear modulus and damping coefficient values are identified for the forthcoming parametric analysis: $G = 10\ MPa$, $\eta = 0.50$ and $G = 20\ MPa$, $\eta = 0.40$, corresponding to strong, and moderately strong earthquakes, respectively.

Figure 4.13 plots the kinematic response functions along the transverse direction (top) and longitudinal direction (bottom) of the east embankment of the 91/5 overcrossing computed with values of $G = 10\ MPa$ and $\eta = 0.50$ (left column) and $G = 20\ MPa$ and $\eta = 0.4$ (right column). The results are obtained with the shear-beam approximation and a 3D finite element analysis. Even though the east embankment of the 91/5 overcrossing has asymmetrical geometry, a hypothetical case where the embankment is symmetric is also presented for comparison. The asymmetric and symmetric geometries yield very close results. The results shown on Figure 4.13 indicate the same trends observed from the analysis of the Meloland Road overcrossing and the Painter Street bridge embankments presented in earlier studies by Zhang and Makris (2001, 2002a).

Figure 4.14 plots the real and imaginary parts of the dynamic stiffnesses of a unit-width wedge that has the same cross section as the 91/5 overcrossing soil embankment. The continuous lines are obtained with the shear-wedge model, whereas the interrupted lines are the results from the finite element analysis. The dashed lines are the results from a 2-D finite element analysis whereas the chain lines are the finite element solution that are obtained by restraining the vertical degree of freedom. The real part of the solutions given by the shear-wedge model at the static limit agrees with the solution of Wilson and Tan (1990). A practical spring and dashpot value can be obtained by passing a line through the real and imaginary parts as indicated by the darker lines in Figure 4.14. To translate the spring and dashpot values resulting from the unit-width wedge to the spring and dashpot values representing the dynamic stiffness of the entire embankment, multiply the unit-width wedge values with a critical length, L_c. The critical length, L_c , is approximated by $0.7\sqrt{SB_cH}$ for the case of a symmetric embankment, and $L_c = 0.7\sqrt{z_0H}$ for the case of an asymmetric embankment that has one slope perpendicular to ground, as is the case of the east embankment of the 91/5 overcrossing (Zhang and Makris 2001, 2002a).

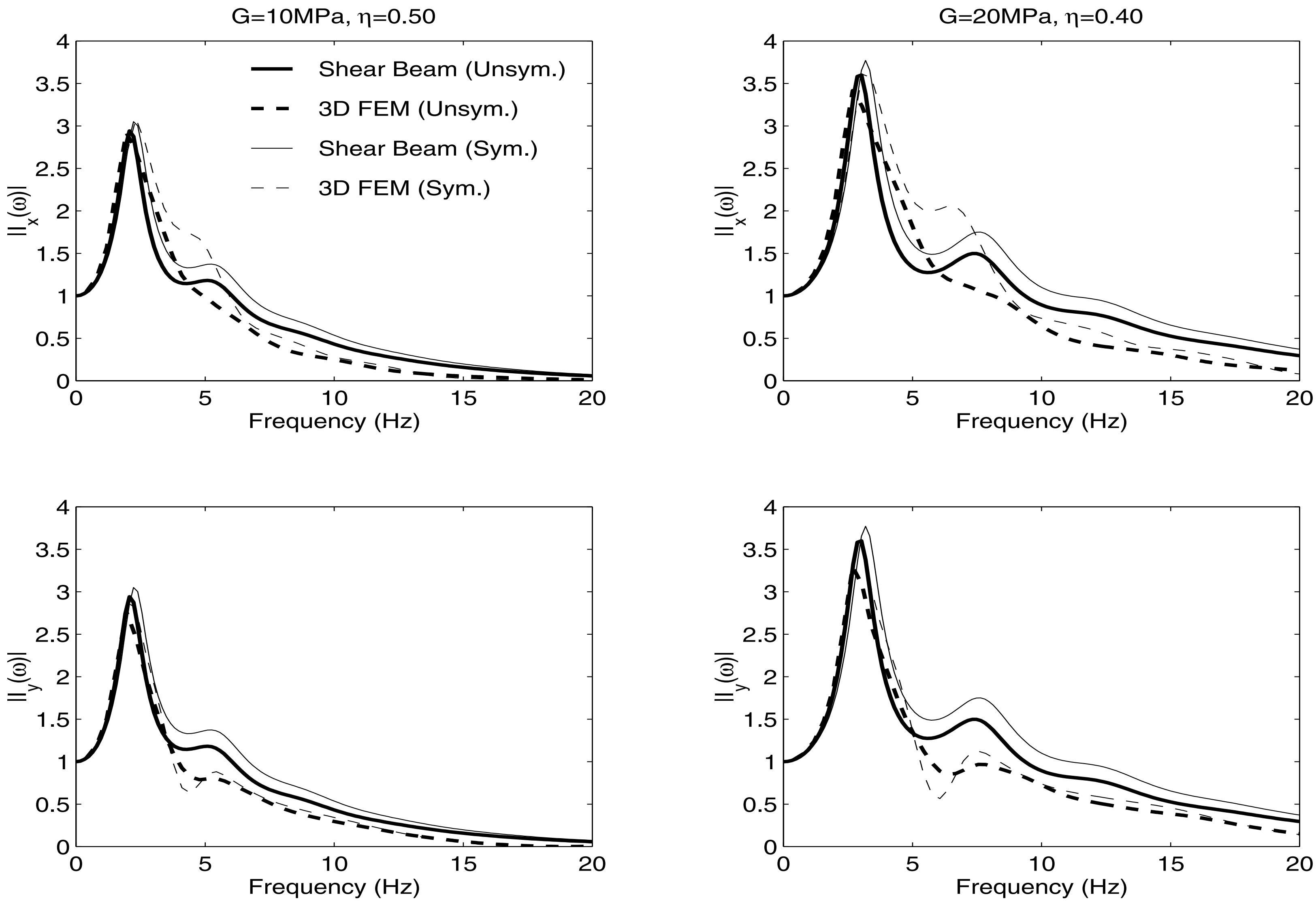

Figure 4.13 Kinematic response functions of 91/5 overcrossing embankment with $G = 10MPa$ **and** $\eta = 0.50$ **(left), and** $G = 20MPa$ **and** $\eta = 0.40$ **(right).**

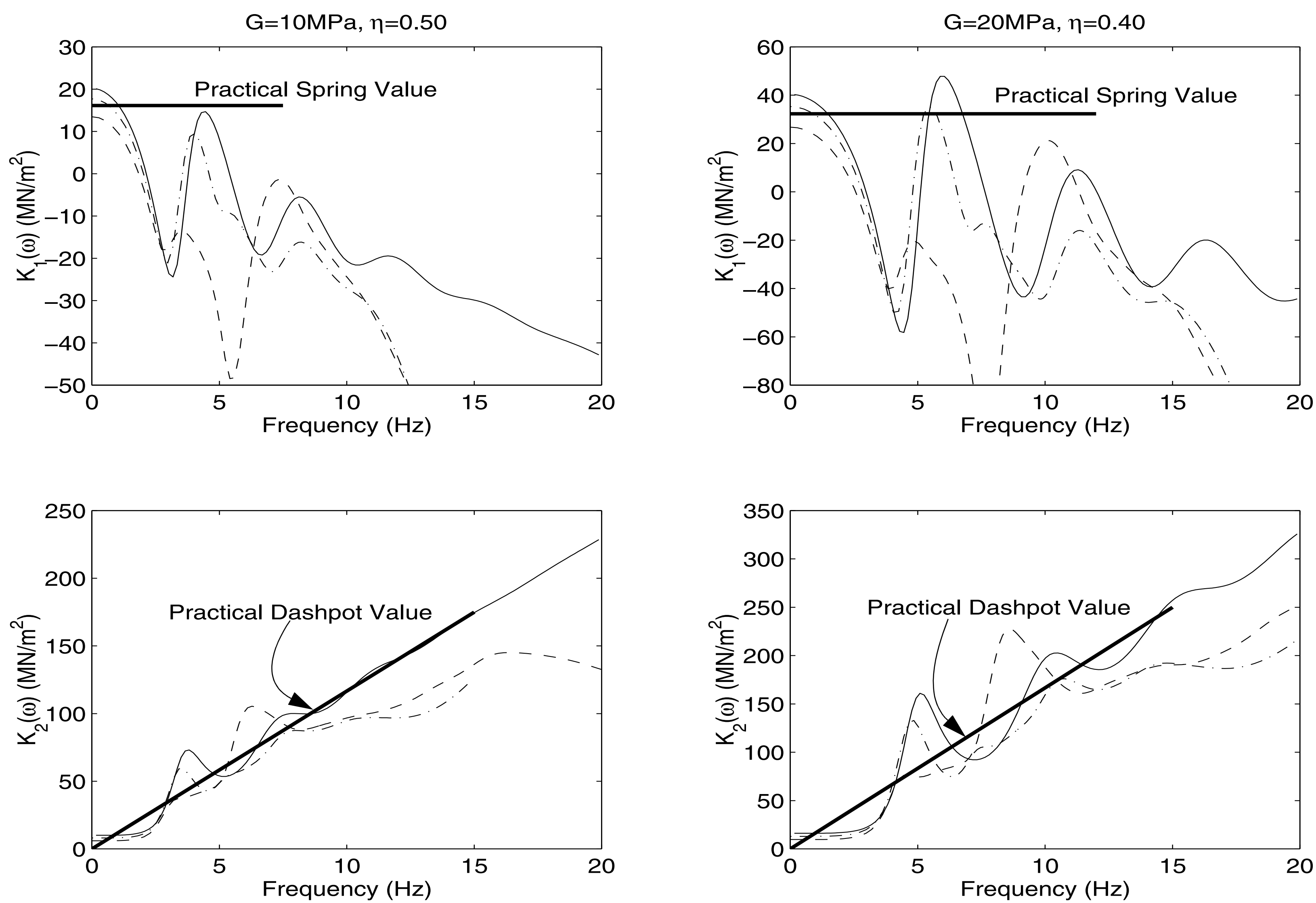

Figure 4.14 Transverse dynamic stiffnesses of shear-wedge model and solution of 2-D finite element formulation for 91/5 over-crossing embankment.

Figure 4.15 plots the computed real and imaginary part of the distributed transverse and longitudinal dynamic stiffnesses of the east embankment of the 91/5 overcrossing by using the 3-D finite element analysis. The values of shear modulus, G, and damping coefficient, η, are the two sets of values determined in the previous section, namely $G = 10\ MPa$ and $\eta = 0.50$ (left), and $G = 20\ MPa$ and $\eta = 0.40$ (right), respectively. The darker lines in these figures are the spring and dashpot values of the practical spring or dashpot value identified in Figure 4.14 multiplied by critical length, L_c, and divided by the embankment width, B_c. The spring and dashpot value can be extracted by multiplying the values shown in Figure 4.15 with the embankment width, B_c. For the case of $G = 10\ MPa$ and $\eta = 0.50$, the representative distributed stiffness along both transverse and longitudinal directions is approximately $k_x = k_y = 9.2\ MN/m^2$. This value is approximately one third of the value used by Caltrans along the longitudinal direction. As frequency increases, the real part of the dynamic stiffness fluctuates around the practical value and subsequently decreases monotonically due to the inertia effects of the soil mass. In view of the variability in soil strains and frequency content during ground shaking, the macroscopic value of the horizontal and transverse spring that approximates the presence of the embankment is assumed to be $K_x = K_y = kB_c = 119\ MN/m$. The loss stiffness also fluctuates with frequency; however its upward trend can be approximated with a slope $c_x = c_y = 0.85\ MN \cdot s/m^2$. The damping constant of the embankment along the transverse and longitudinal directions is $C_x = C_y = cB_c \approx 11\ MN \cdot s/m$.

4.2 INPUT MOTION AT PILE CAPS AND DYNAMIC STIFFNESSES OF PILE FOUNDATIONS

The difference between the free-field motion and the motion at the cap of a pile foundation is due to the scattered wave field generated from the difference between the pile and soil rigidities. Nevertheless, for motions that are not rich in high frequencies, the scattered field is weak, and the support motion can be considered to be approximately equal to that of the free field (Fan et al. 1991; Gazetas 1984; Kaynia and Novak 1992; Makris and Gazetas 1992; Mamoon and Banerjee 1990; Tajimi 1977). For instance, for the Painter Street bridge the soil deposit has an average shear velocity, V_s, of about $200\ m/s$ (Heuze and Swift 1991); the pile diameter, d, is 0.36 m. Accordingly, even for the high-frequency content of the input motion ($f \approx 10\ Hz$), the

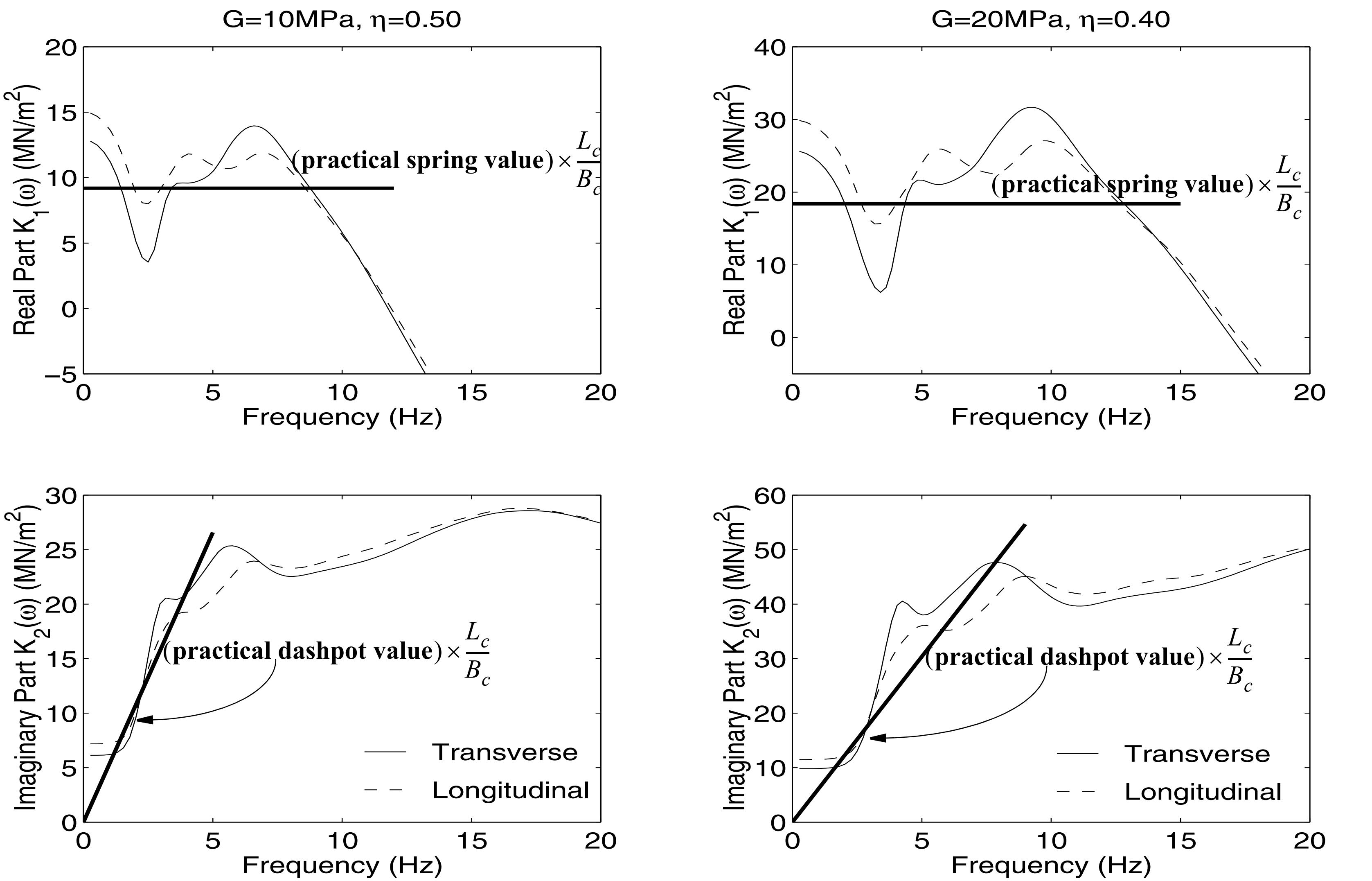

Figure 4.15 Transverse and longitudinal dynamic stiffnesses of approach embankment of 91/5 overcrossing (left: $G = 10MPa$, $\eta = 0.50$; right: $G = 20MPa$, $\eta = 0.40$). Spring and dashpot values are extracted by multiplying values shown above with width of embankment, B_c.

dimensionless frequency, $a_0 = 2\pi fd/V_s$, is of the order of only 0.1. From studies on vertically propagating shear waves in homogeneous soil deposits (Fan et al. 1991), the kinematic-seismic response factors (head-group displacement over free-field displacement) are very close to unity, even at values of the dimensionless frequency, $a_0 > 0.1$.

Waves other than vertical S-waves also participate in ground shaking. The seismic-kinematic response factors for SV waves, P waves, and Rayleigh surface waves are given by Mamoon and Banerjee (1990), Kaynia and Novak (1992), Makris (1994), and Makris and Badoni (1995). For all these types of waves that produce a vertical component of the seismic input motion, the kinematic response factors are also close to unity. Only in some cases do SV waves with a high angle of incidence result in kinematic response factors of the order of 0.90. Based on such supporting analytical evidence, in most cases the excitation input motion at the level of the pile foundation can be assumed to be equal to that of the free-field motion. Only at very high frequencies or for very soft soils will a reduction be needed. Moreover, in the case of Rayleigh waves and SV waves, a pile group produces an effective rocking input motion, whereas for oblique incidence SH waves the foundation experiences torsional excitation. These motions are the result of phase differences that the seismic input has at the locations of different piles in the group (wave passage effect); their intensity depends on the frequency content of the seismic input and the geometry of the pile group.

The dynamic stiffnesses of pile groups along the various vibration mode are computed by the method outlined by Makris et al. (1994), which has also been presented in a report by Zhang and Makris (2001). Figure 4.16 shows the pile group configuration at the east and west end abutments. Both pile groups consist of vertical and battered piles. While a limited number of studies are available to analyze the dynamic response of battered piles (Guin and Banerjee 1998), in this study the effect of battered pile is neglected in order to take advantage of the simple superposition procedure that has been verified only for vertical piles.

Figure 4.17 plots the normalized group dynamic stiffnesses as a function of the dimensionless frequency, $a_0 = \omega d/V_s$ of the 49-pile group at the center bent of the 91/5 overcrossing. The soil properties used are $G = 28MPa$ and $\eta = 0.35$. The static group stiffness is only a fraction of the sum of the individual pile static stiffnesses as a result of interaction between piles. Figures 4.18 and 4.19 plot the normalized dynamic stiffnesses of the pile group at

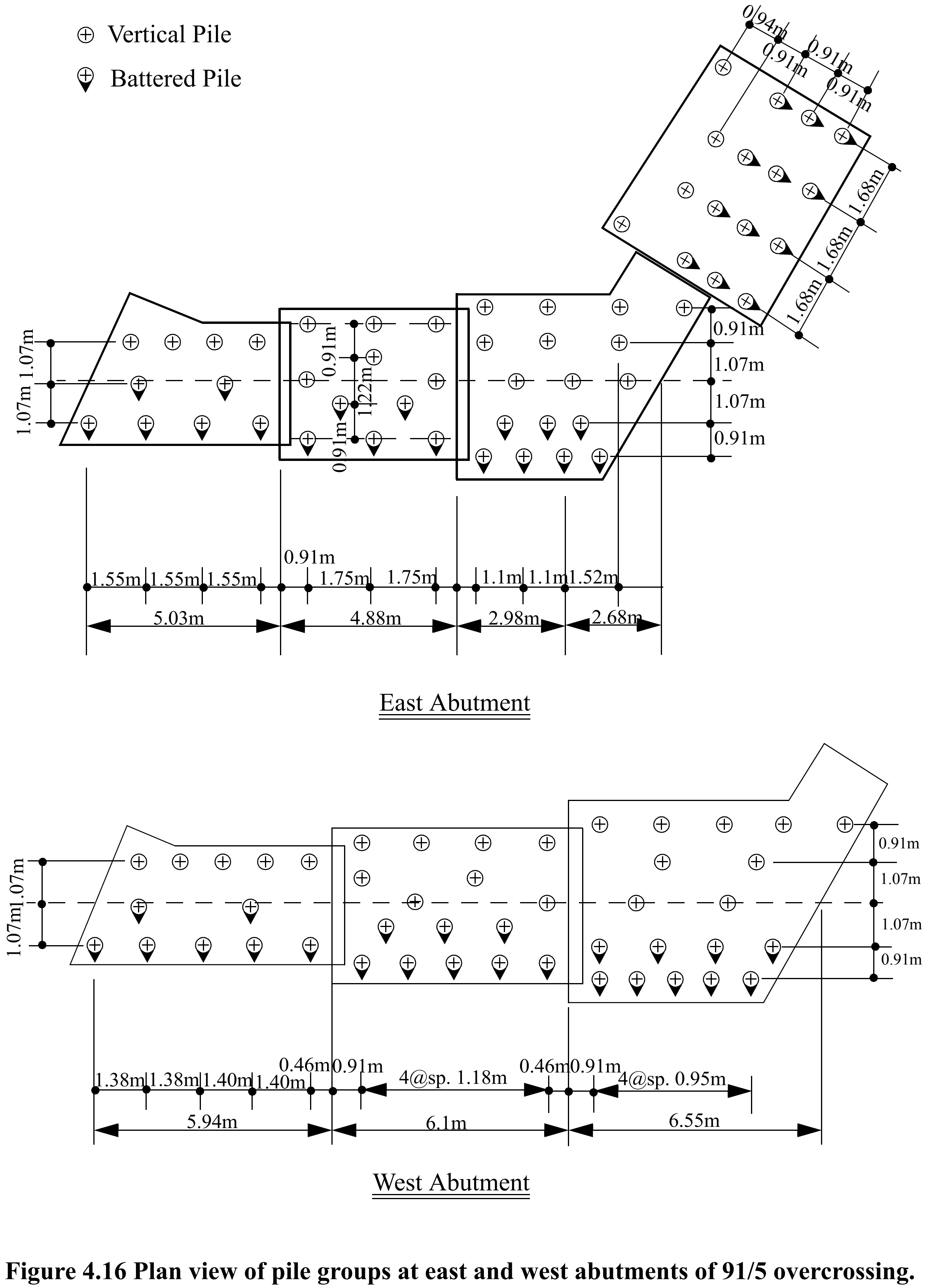

Figure 4.16 Plan view of pile groups at east and west abutments of 91/5 overcrossing.

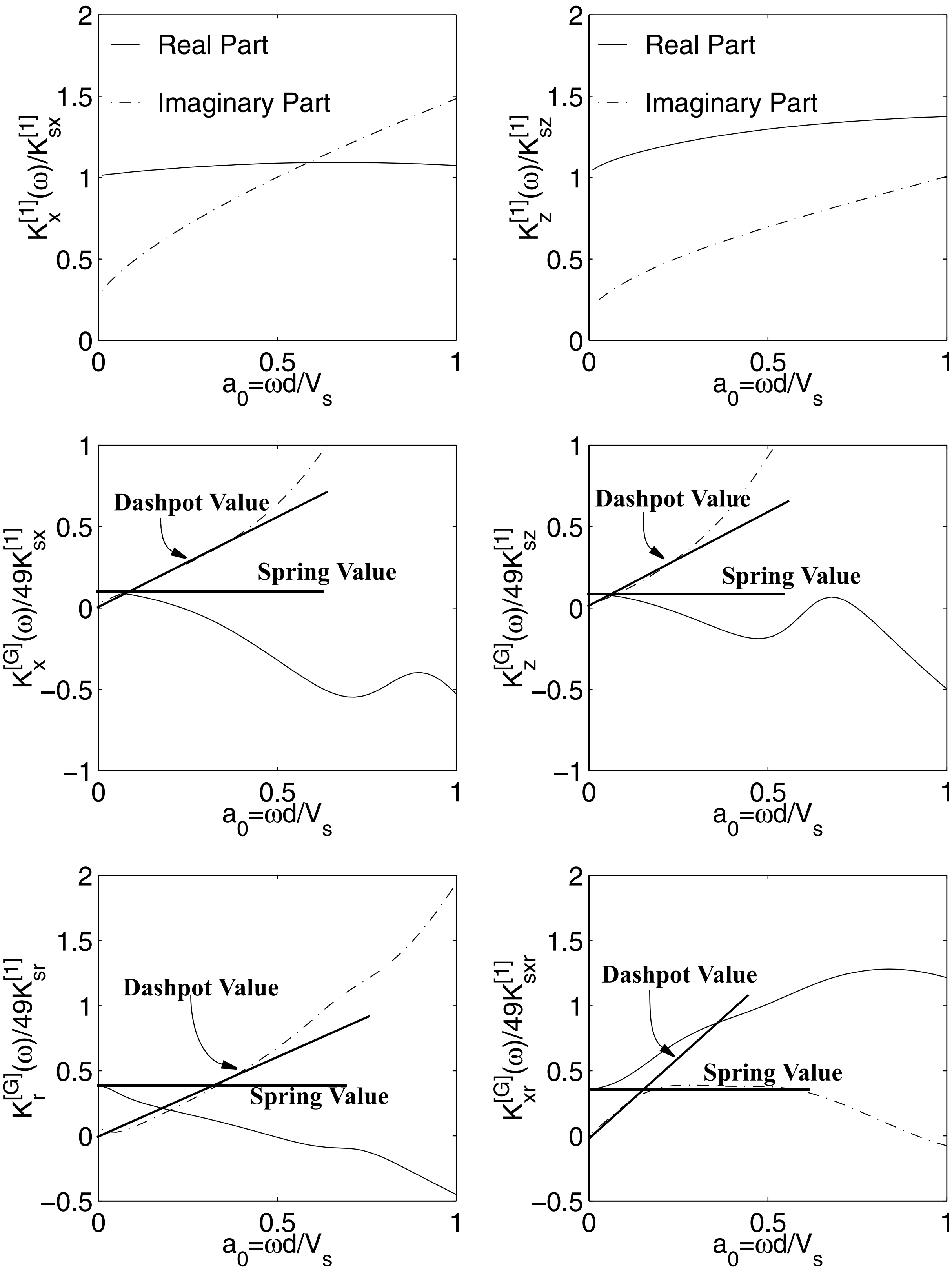

Figure 4.17 Dynamic stiffnesses of single pile and pile group at center bent of 91/5 overcrossing.

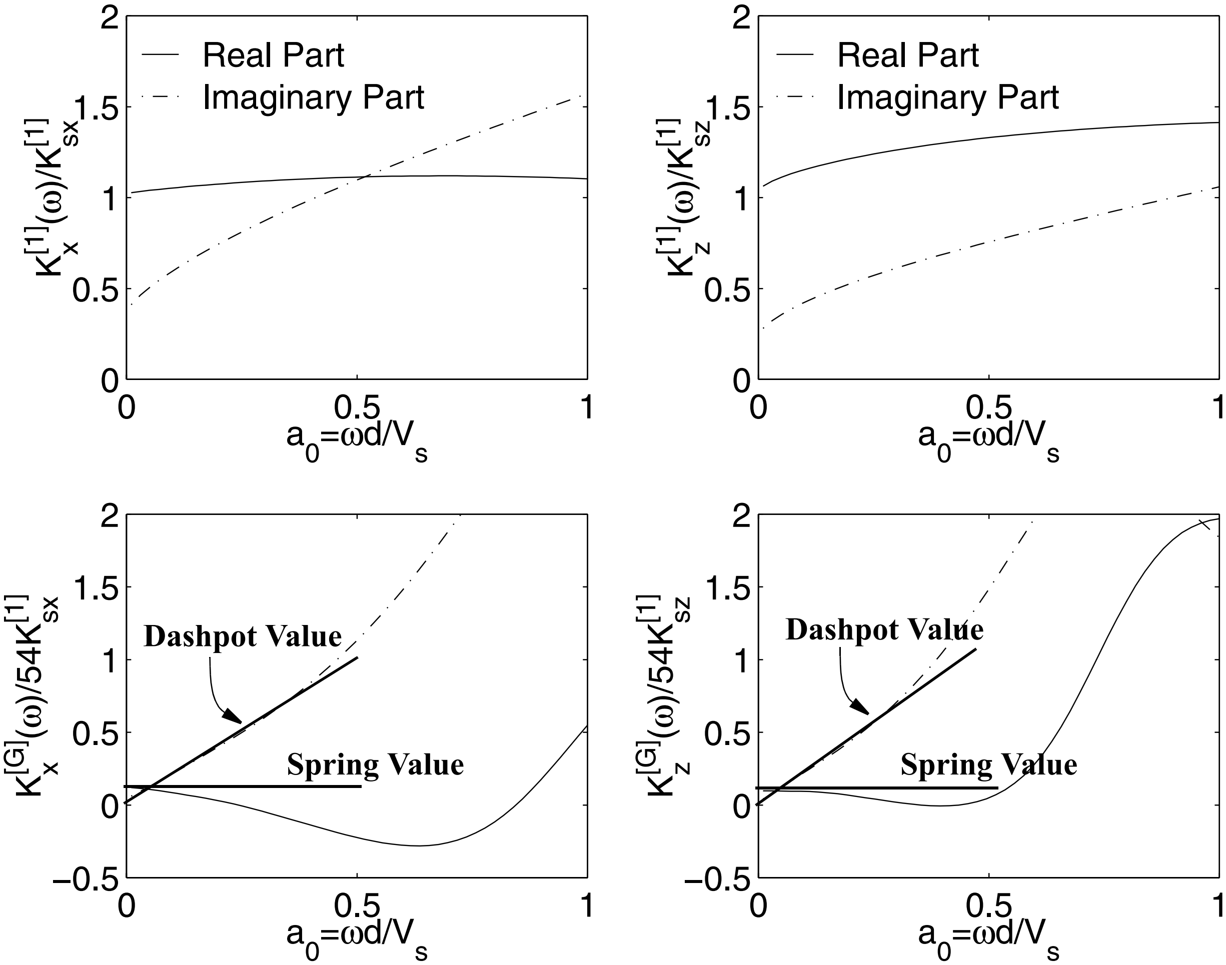

Figure 4.18 Dynamic stiffnesses of single pile and pile group at east abutment of 91/5 overcrossing.

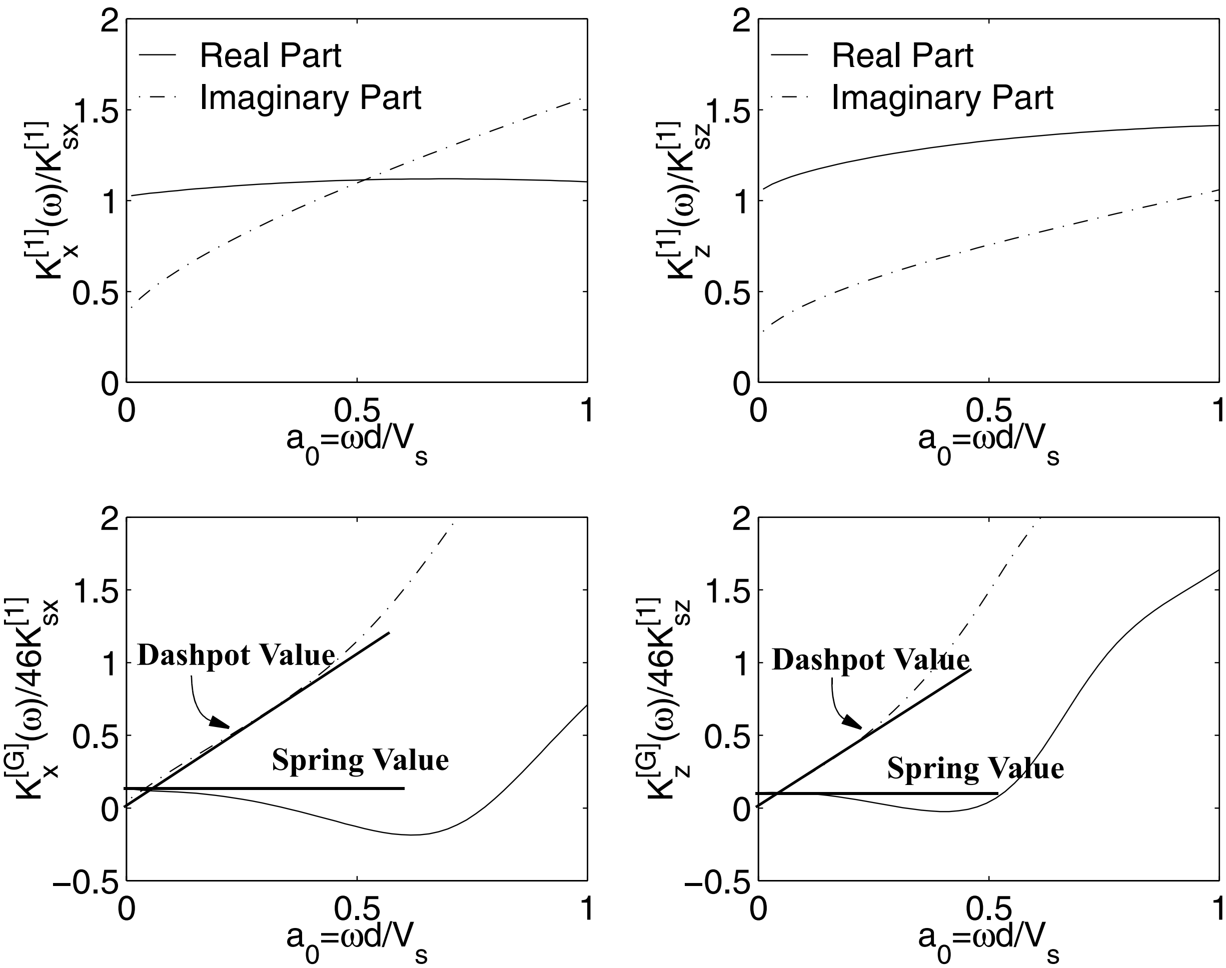

Figure 4.19 Dynamic stiffnesses of single pile and pile group at west abutment of 91/5 overcrossing.

the east and west abutments, respectively, where $G = 10MPa$ and $\eta = 0.50$ for the soil are used.

Table 4.2 summarizes the spring and dashpot values that approximate the stiffnesses and damping at the overcrossing center bent and at each end of the superstructure. Two sets of soil properties (namely shear modulus, G , and damping coefficient, η), that correspond to strong and moderatley strong earthquakes, respectively, are used to obtain the combined spring and dashpot values at end abutments. Similarly, the soil properties for the pile group at the center bent are also chosen to correspond to the severity of the earthquake. They are $G = 28\ MPa$ and $\eta = 0.35$, and $G = 56\ MPa$ and $\eta = 0.12$ for strong and moderately strong earthquakes, respectively. The spring and dashpot values of the east and west abutments differ only slightly from each other due to the different pile group configurations. For simplicity, it is assumed that both abutments adopt the spring and dashpot values of the east abutment.

Table 4.2 Spring and dashpot values that approximate the presence of the approach embankments and pile foundation of the 91/5 overcrossing

Parameters		Case 1	Case 2
Embankment + Pile Foundations	$K_x\ (MN/m)$	119+292 (119+271)	238+488 (238+453)
	$K_y\ (MN/m)$	119+293 (119+272)	238+490 (238+456)
	$K_z\ (MN/m)$	451+1135 (451+1058)	892+1586(892+1478)
	$C_x\ (MN \cdot s/m)$	11+28 (11+24)	13+32 (13+28)
	$C_y\ (MN \cdot s/m)$	11+22 (11+17)	13+26 (13+19)
	$C_z\ (MN \cdot s/m)$	14+128 (14+101)	27+124 (27+98)
Pile Foundation of Center Bent	$K_x, K_y\ (MN/m)$	492	821
	$K_r\ (MN \cdot m/rad)$	31739	44187
	$K_{xr}, K_{yr}\ (MN/rad)$	-811	-1138
	$K_z\ (MN/m)$	1452	2020
	$C_x, C_y\ (MN \cdot s/m)$	14.5	16.2
	$C_z\ (MN \cdot s/m)$	54.3	50.2
Note	Case 1: $G = 10MPa$, $\eta = 0.5$ at abutment; $G = 28MPa$, $\eta = 0.35$ at center bent. Case 2: $G = 20MPa$, $\eta = 0.4$ at abutment; $G = 56MPa$, $\eta = 0.12$ at center bent Numbers in parenthesis are the values for west abutment		

5 Mechanical Modeling of Seismic Protective Devices

At each end abutment the deck rests on four elastomeric pads and is attached to the abutments with four fluid dampers. The mechanical behavior of these protective devices is nonlinear, since the elastomeric pads allow for sliding beyond a threshold elastic deformation, while the dampers deliver forces that depend on a fractional power of the piston velocity. In this chapter the macroscopic constitutive laws of the elastomeric pads and hydraulic dampers are presented at the force-displacement level.

5.1 ELASTOMERIC PADS

The elastomeric pads consist of neoprene, have a square plan view $(24" \times 24")$ and are $3"$ tall without any steel reinforcement. Their effective shear modulus, $G_{eff} \approx 150\ psi(1\ MN/m^2)$, and the resulting elastic stiffness of each pad is approximately

$$K_{eff} = \frac{G_{eff}A}{t} \approx 5\ MN/m \tag{5.1}$$

where $A = 24" \times 24" = 576\ in^2(0.37\ m^2)$ is the plan area and t is the height of the elastomers. Under shear deformation the elastomeric pads deform nearly elastically until they develop a threshold force $F^Y = \mu N$, where $\mu \approx 0.3$ is the friction coefficient of the pad-deck interface and N is the normal force on the pad. Figure 5.1 (top) illustrates schematically the force-deformation loop of the elastomeric pad in one direction. Static analysis yields that the vertical reaction at each abutment is $4.0 MN$, so the normal force at each elastomeric pad is approximately $1.0 MN$. Accordingly, the force when sliding initiates is $F^Y = 0.3 \times 1.0 = 0.30 MN$, and the yield displacement is $u^Y = F^Y/K_{eff} \approx 0.06 m$. The mechanical behavior of the elastomeric bearings can

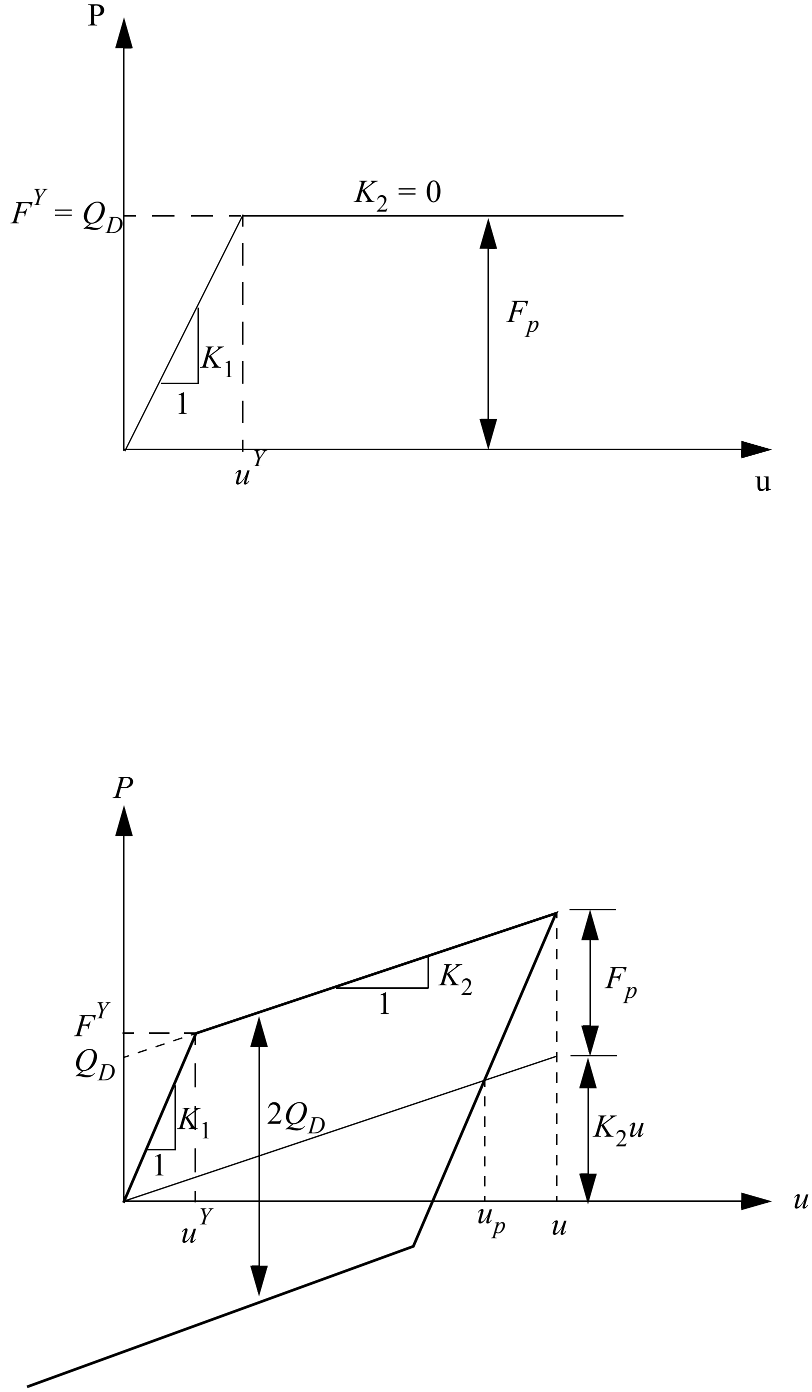

Figure 5.1 1-D force-displacement relation of the elastomeric pads (top) and 1-D force-displacement relationship of the more general bilinear plasticity model (bottom).

be best approximated with a bilinear plasticity model (Simo and Hughes 1998) or a 2-D Bouc-Wen model (Nagarajaiah et al. 1990 and references reported therein).

5.1.1 Bilinear Plasticity Model

This model is based on classical rate-independent plasticity assuming isotropic behavior. Figure 5.1 (bottom) presents a schematic sketch of the idealized uniaxial force-displacement relation of the bilinear plasticity model. The restoring force, $\mathbf{P}=\begin{bmatrix} P_x & P_y \end{bmatrix}^T$ consists of an elastic-hardening component and a hysteretic component, given by

$$\mathbf{P} = K_2\mathbf{u}+\mathbf{F}_p \tag{5.2}$$

where K_2 is the post-yield hardening stiffness, $\mathbf{F}_p$ is the hysteretic force and $\mathbf{u}=\begin{bmatrix} u_x & u_y \end{bmatrix}^T$ is the translational deformation. In our specific application, $K_2 = 0$; however, the general formulation is presented here for $K_2 \neq 0$. The yielding surface, $\Phi(\mathbf{F}_p)$ is assumed to be a circular interaction surface, i.e.,

$$\Phi(\mathbf{F}_p) = \|\mathbf{F}_p\| - Q_D \tag{5.3}$$

where Q_D is the zero-displacement force intercept and K_1 is the pre-yield elastic stiffness, as shown in Figure 5.1. Variable Q_D represents one half the size of the hysteresis loops. The plastic displacement, $\mathbf{u}_p$, is governed by the associative plastic flow rule:

$$\dot{\mathbf{u}}_p = \gamma \cdot \frac{\partial\Phi(\mathbf{F}_p)}{\partial\mathbf{F}_p} = \gamma \cdot \frac{\mathbf{F}_p}{\|\mathbf{F}_p\|} \tag{5.4}$$

where $\gamma \geq 0$ is the plasticity multiplier. The Kuhn-Tucker loading/unloading condition (Simo and Hughes 1998) is

$$\gamma \geq 0, \quad \Phi(\mathbf{F}_p) \leq 0, \quad \gamma \cdot \Phi(\mathbf{F}_p) = 0 \tag{5.5}$$

and the consistency condition is

$$\gamma \cdot \dot{\Phi}(\mathbf{F}_p) = 0 \tag{5.6}$$

The hysteretic force $\mathbf{F}_p$ is computed by

$$\mathbf{F}_p = (K_1 - K_2) \cdot (\mathbf{u}\text{-}\mathbf{u}_p) \tag{5.7}$$

The return-mapping algorithm for plasticity proposed by Simo and Hughes (1998) is used to compute the restoring force $\mathbf{P}$ for a given displacement history $\mathbf{u}$. Figure 5.2 illustrates the return mapping algorithm of a uniaxial bilinear plasticity model. Given the solution ($\mathbf{P}^n$, $\mathbf{F}_p^n$, $\mathbf{u}_p^n$,

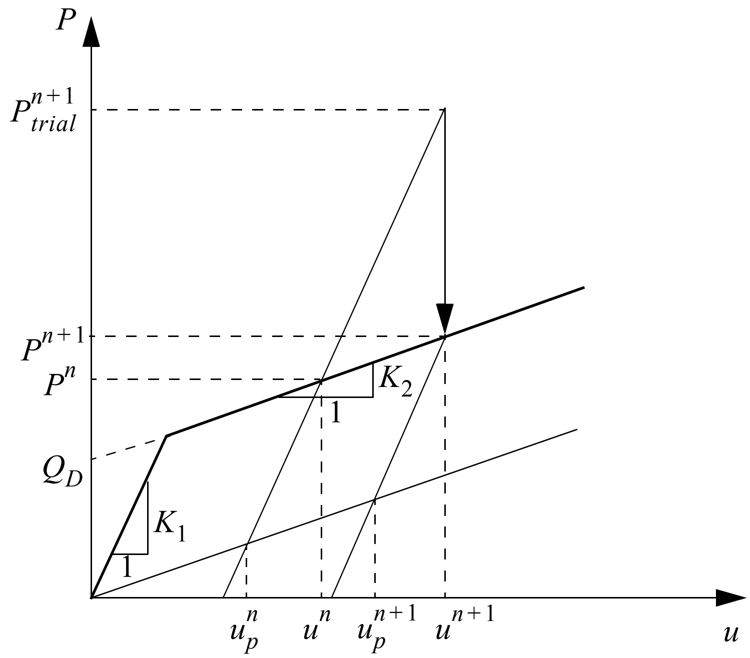

Figure 5.2 Return mapping algorithm of the uniaxial bilinear plasticity model.

and $\mathbf{u}^n$) at time increment n and displacement at time increment $n+1$ ($\mathbf{u}^{n+1}$), a trial state corresponding to a purely elastic step can be obtained as

$$\begin{aligned} \mathbf{F}_p^{n+1, trial} &= (K_1 - K_2) \cdot (\mathbf{u}^{n+1} - \mathbf{u}_p^n) \\ \mathbf{u}_p^{n+1, trial} &= \mathbf{u}_p^n \\ \Phi^{n+1, trial} &= \left\| \mathbf{F}_p^{n+1, trial} \right\| - Q_D \end{aligned} \tag{5.8}$$

The trial state is determined solely in terms of the solution at time increment n and given displacement $\mathbf{u}^{n+1}$. This state may not, and in general will not, correspond to any actual, physically admissible state unless the incremental process is elastic, i.e., $\Phi^{n+1, trial} \leq 0$. Otherwise, we need to find the real solutions at increment $n+1$ which satisfy the condition

$$\Phi(\mathbf{F}_p^{n+1}) = 0 \text{ and } \Delta\gamma > 0 \tag{5.9}$$

According to the flow rule

$$\mathbf{u}_p^{n+1} = \mathbf{u}_p^n + \Delta\gamma \cdot \frac{\mathbf{F}_p^{n+1}}{\left\| \mathbf{F}_p^{n+1} \right\|} \tag{5.10}$$

Thus

$$\mathbf{F}_p^{n+1} = (K_1 - K_2) \cdot (\mathbf{u}^{n+1} - \mathbf{u}_p^{n+1}) = (K_1 - K_2) \cdot \left(\mathbf{u}^{n+1} - \mathbf{u}_p^n - \Delta\gamma \cdot \frac{\mathbf{F}_p^{n+1}}{\left\| \mathbf{F}_p^{n+1} \right\|} \right) \tag{5.11}$$

Equation (5.11) can be written in terms of $\mathbf{F}_p^{n+1, trial}$

$$\left\| \mathbf{F}_p^{n+1} \right\| \cdot \frac{\mathbf{F}_p^{n+1}}{\left\| \mathbf{F}_p^{n+1} \right\|} = \left\| \mathbf{F}_p^{n+1, trial} \right\| \cdot \frac{\mathbf{F}_p^{n+1, trial}}{\left\| \mathbf{F}_p^{n+1, trial} \right\|} - \Delta\gamma \cdot (K_1 - K_2) \frac{\mathbf{F}_p^{n+1}}{\left\| \mathbf{F}_p^{n+1} \right\|} \tag{5.12}$$

Moving the second term in the right-hand side to the left-hand side results in

$$\{ \left\| \mathbf{F}_p^{n+1} \right\| + \Delta\gamma \cdot (K_1 - K_2) \} \cdot \frac{\mathbf{F}_p^{n+1}}{\left\| \mathbf{F}_p^{n+1} \right\|} = \left\| \mathbf{F}_p^{n+1, trial} \right\| \cdot \frac{\mathbf{F}_p^{n+1, trial}}{\left\| \mathbf{F}_p^{n+1, trial} \right\|} \tag{5.13}$$

Therefore

$$\left\| \mathbf{F}_p^{n+1, trial} \right\| = \left\| \mathbf{F}_p^{n+1} \right\| + \Delta\gamma \cdot (K_1 - K_2) \tag{5.14}$$

and

$$\frac{\mathbf{F}_p^{n+1}}{\left\| \mathbf{F}_p^{n+1} \right\|} = \frac{\mathbf{F}_p^{n+1, trial}}{\left\| \mathbf{F}_p^{n+1, trial} \right\|} \tag{5.15}$$

Substituting Eq. (5.14) into the first equation of (5.9) obtains

$$\Phi(\mathbf{F}_p^{n+1}) = \left\|\mathbf{F}_p^{n+1}\right\| - Q_D = \left\|\mathbf{F}_p^{n+1,\,trial}\right\| - \Delta\gamma \cdot (K_1 - K_2) - Q_D = 0 \tag{5.16}$$

The incremental plasticity multiplier $\Delta\gamma$ is then obtained as

$$\Delta\gamma = \frac{\left\|\mathbf{F}_p^{n+1,\,trial}\right\| - Q_D}{(K_1 - K_2)} = \frac{\Phi^{n+1,\,trial}}{(K_1 - K_2)} \tag{5.17}$$

The solution at increment $n + 1$ can be easily calculated as

$$\begin{aligned} \mathbf{u}_p^{n+1} &= \mathbf{u}_p^n + \Delta\gamma \cdot \frac{\mathbf{F}_p^{n+1,\,trial}}{\left\|\mathbf{F}_p^{n+1,\,trial}\right\|} \\ \mathbf{F}_p^{n+1} &= \mathbf{F}_p^{n+1,\,trial} - \Delta\gamma \cdot (K_1 - K_2) \cdot \frac{\mathbf{F}_p^{n+1,\,trial}}{\left\|\mathbf{F}_p^{n+1,\,trial}\right\|} \end{aligned} \tag{5.18}$$

In order to incorporate the bilinear plasticity model into the earthquake analysis, the tangent stiffness matrix needs to be obtained. During an elastic regime, the tangent stiffness is merely

$$\mathbf{K}_t = K_1 \begin{bmatrix} \mathbf{I} & -\mathbf{I} \\ -\mathbf{I} & \mathbf{I} \end{bmatrix} \tag{5.19}$$

where $\mathbf{I}$ is a two by two identity matrix. As for a plastic regime, the rate of plastic force is (from equation (5.7)):

$$\dot{\mathbf{F}}_p = (K_1 - K_2) \cdot (\dot{\mathbf{u}} - \dot{\mathbf{u}}_p) = (K_1 - K_2) \cdot \left(\dot{\mathbf{u}} - \gamma \frac{\mathbf{F}_p}{\left\|\mathbf{F}_p\right\|}\right) \tag{5.20}$$

where γ is obtained from $\dot{\Phi}(\mathbf{F}_p) = 0$, i.e.,

$$\gamma = \frac{\mathbf{F}_p^T \cdot \dot{\mathbf{u}}}{\left\|\mathbf{F}_p\right\|} \tag{5.21}$$

Substituting (5.21) into (5.20), one obtains

$$\dot{\mathbf{F}}_p = (K_1 - K_2) \cdot \dot{\mathbf{u}} - \left((K_1 - K_2) \cdot \frac{\mathbf{F}_p \mathbf{F}_p^T}{\left\|\mathbf{F}_p\right\|^2}\right) \dot{\mathbf{u}} \tag{5.22}$$

The rate of the restoring force is then

$$\dot{\mathbf{F}} = K_2 \dot{\mathbf{u}} + \dot{\mathbf{F}}_p = \left(K_1 \mathbf{I} - \frac{(K_1 - K_2) \mathbf{F}_p \mathbf{F}_p^T}{\left\|\mathbf{F}_p\right\|^2}\right) \dot{\mathbf{u}} \tag{5.23}$$

Therefore, the tangent stiffness matrix during a plastic step is

$$\mathbf{K}_t = \begin{bmatrix} K_1\mathbf{I} - (K_1 - K_2)\dfrac{\mathbf{F}_p\mathbf{F}_p^T}{\|\mathbf{F}_p\|^2} & -\left(K_1\mathbf{I} - (K_1 - K_2)\dfrac{\mathbf{F}_p\mathbf{F}_p^T}{\|\mathbf{F}_p\|^2}\right) \\ -\left(K_1\mathbf{I} - (K_1 - K_2)\dfrac{\mathbf{F}_p\mathbf{F}_p^T}{\|\mathbf{F}_p\|^2}\right) & K_1\mathbf{I} - (K_1 - K_2)\dfrac{\mathbf{F}_p\mathbf{F}_p^T}{\|\mathbf{F}_p\|^2} \end{bmatrix}. \tag{5.24}$$

5.1.2 Bidirectional Bouc-Wen Model

The uniaxial Bouc-Wen model, originally proposed by Bouc (1971) and subsequently extended by Wen (1975, 1976), is used extensively in random vibration studies of inelastic systems. Casciati (1989) considered the Bouc-Wen model as a smoothed form of the rate independent plasticity model and generalized it to a bidirectional case. Equation (5.22) can be written as

$$\dot{\mathbf{F}}_p = (K_1 - K_2)\cdot\dot{\mathbf{u}} - \left((K_1 - K_2)\cdot\frac{\mathbf{F}_p^T\cdot\dot{\mathbf{u}}}{\|\mathbf{F}_p\|^2}\right)\mathbf{F}_p\cdot H(\Phi)\cdot H(\dot{\Phi}) \tag{5.25}$$

where $H(\Phi)$ is the Heaviside function. $H(\Phi)$ can be approximated with a smoothed function

$$H(\Phi) = H(\|\mathbf{F}_p\| - Q_D) \approx \frac{\|\mathbf{F}_p\|^\eta}{Q_D^\eta} \tag{5.26}$$

where $\eta \geq 0$. $H(\dot{\Phi})$ is defined as

$$H(\dot{\Phi}) = H(\mathbf{F}_p^T\mathbf{F}_p) = \frac{1 + \operatorname{sgn}(\mathbf{F}_p^T\dot{\mathbf{u}})}{2} \tag{5.27}$$

Therefore, the rate of plastic force is approximated with

$$\dot{\mathbf{F}}_p = (K_1 - K_2)\cdot\dot{\mathbf{u}} - \frac{\|\mathbf{F}_p\|^{\eta-2}}{Q_D}\cdot(K_1 - K_2)\cdot(\mathbf{F}_p^T\cdot\dot{\mathbf{u}})\cdot\frac{1 + \operatorname{sgn}(\mathbf{F}_p^T\dot{\mathbf{u}})}{2}\mathbf{F}_p \tag{5.28}$$

Defining a dimensionless plastic variable $\mathbf{Z}$ such that $\mathbf{F}_p = Q_D\mathbf{Z}$ and uniaxial “yield”: displacement, $u^Y = Q_D/(K_1 - K_2)$, equation (5.28) becomes

$$\dot{\mathbf{Z}}u^Y = \dot{\mathbf{u}} - \|\mathbf{Z}\|^{\eta-2}\cdot(\mathbf{Z}^T\dot{\mathbf{u}})\cdot\left(\frac{1}{2} + \frac{1}{2}\operatorname{sgn}(\mathbf{Z}^T\dot{\mathbf{u}})\right)\mathbf{Z} \tag{5.29}$$

Equation (5.29) can be written in a more general form

$$\dot{\mathbf{Z}}u^Y = A\dot{\mathbf{u}} - \|\mathbf{Z}\|^{\eta-2}\cdot(\mathbf{Z}^T\dot{\mathbf{u}})\cdot[\gamma + \beta\operatorname{sgn}(\mathbf{Z}^T\dot{\mathbf{u}})]\mathbf{Z} \tag{5.30}$$

where γ, β, and η are dimensionless quantities that control the shape of the hysteretic loop. In this study, $A = 1$ and $\gamma = \beta = 0.5$. This results in the bound of variable $\mathbf{Z}$ as $\|\mathbf{Z}\| \le 1$. By using equation (5.28) and $Q_D/U_Y = K_1 - K_2$, the rate of restoring force can be written as

$$\dot{\mathbf{P}} = K_2\dot{\mathbf{u}} + \dot{\mathbf{F}}_p = \{K_2 + A(K_1 - K_2) - (K_1 - K_2)\|\mathbf{Z}\|^{\eta-2}[\gamma + \beta \operatorname{sgn}(\mathbf{Z}^T\dot{\mathbf{u}})](\mathbf{Z}\mathbf{Z}^T)\}\dot{\mathbf{u}} \tag{5.31}$$

i.e.,

$$\frac{\partial \mathbf{P}}{\partial \mathbf{u}} = K_2 + A(K_1 - K_2) - (K_1 - K_2)\|\mathbf{Z}\|^{\eta-2}[\gamma + \beta \operatorname{sgn}(\mathbf{Z}^T\dot{\mathbf{u}})](\mathbf{Z}\mathbf{Z}^T) \tag{5.32}$$

Therefore, the tangent stiffness matrix is

$$\mathbf{K}_t = \begin{bmatrix} \dfrac{\partial \mathbf{P}}{\partial \mathbf{u}} & -\dfrac{\partial \mathbf{P}}{\partial \mathbf{u}} \\ -\dfrac{\partial \mathbf{P}}{\partial \mathbf{u}} & \dfrac{\partial \mathbf{P}}{\partial \mathbf{u}} \end{bmatrix} \tag{5.33}$$

The Bouc-Wen model is very versatile for modeling various seismic protection devices, such as sliding, elastomeric, or lead-rubber bearings.

5.2 FLUID DAMPERS

Fluid dampers have been accepted as a promising alternative to dissipate the energy that earthquakes and wind induce in structures. Several major retrofitting projects of buildings, such as San Bernardino County Hospital, Los Angeles City Hall, Hayward City Hall, and the Rockwell building in Newport Beach, California, among others, have adopted fluid dampers to suppress seismic-induced shaking. Theoretical and experimental studies on the implementability of hydraulic fluid dampers in bridges have also been conducted (Tsopelas 1994; Delis et al. 1996; Aiken and Kelly 1995). Examples of actual implementation of fluid dampers as protection devices are the Vincent Thomas suspension bridge in southern California (Symth et al. 2000), the Rion-Antirion cable-stayed bridge in Greece (Papanikolas 2002), and the 91/5 highway overcrossing in Orange County, California, the bridge of interest in this study. The implementation of dampers for the seismic upgrade of the Coronado and the Oakland-San Francisco Bay bridges in California are also under way.

Hydraulic dampers designed for seismic protection applications have specially shaped orifices that yield a nonlinear force-velocity relationship of the form

$$P(t) = C_\alpha |\dot{u}(t)|^\alpha \operatorname{sgn}[\dot{u}(t)] \tag{5.34}$$

where $P(t)$ is piston force, $u(t)$ is piston velocity, α is fractional exponent, and $0 \le \alpha \le 1$, C_α is the damping constant with units of $(force) \cdot \left(\frac{time}{length}\right)^\alpha$ and sgn( ) is the signum function. When $\alpha = 1$, equation (5.34) reduces to the linear viscous case

$$P(t) = C_1 \dot{u}(t) \tag{5.35}$$

When $\alpha < 1$ damper forces are less dependent on velocity compared to the viscous case, and at the limit where $\alpha = 0$, equation (5.34) represents a hysteretic law of dissipation (rigid-plastic behavior) where the resulting force is velocity independent

$$P(t) = C_0 \mathrm{sgn}[\dot{u}(t)] = P^Y \mathrm{sgn}[\dot{u}(t)] \tag{5.36}$$

where $P^Y = C_0 = yield\ force$.

Each fluid damper installed in the 91/5 overcrossing was designed to produce 250 kips at a piston velocity of 42 in/sec. The fractional exponent in equation (5.34) was estimated $0.3 < \alpha < 0.4$, and all the analysis during the design of the bridge and in this study was conducted with $\alpha = 0.35$. The stroke capacity of the dampers is ±8.0 in.

Upon the installation of the dampers and the completion of this study, the California Department of Transportation (Caltrans) funded the construction of a large damper testing machine under the supervision of the senior author. Figure 5.3 shows the view of the large damper testing machine at the University of California, Berkeley, with one of the dampers installed from the 91/5 overcrossing. The machine shown in Figure 5.3 has ±12.0 in stroke capacities and is powered by a 115 in^2 bore dynamic (double-ended) actuator. It is capable of achieving 20 in/sec under 200 $kips$ load. Figures 5.4 and 5.5 show recorded force-displacement loops from one of the dampers of the 91/5 overcrossing.

The theoretical loops are produced by assuming that the exponent $\alpha = 0.35$ and by back-figuring the value of $C_\alpha = 67.6\ kips(s/in)^\alpha$ from equation (5.34) given that the maximum load $P_{max} = 250\ kips$ occurs at $v_{max} = 42\ in/sec$. With the value of $C_\alpha = 67.6\ kips(s/in)^\alpha$ established, Figures 5.4 and 5.5 plot the prediction of equation (5.34) for the velocity histories for which that the damper was tested. The good agreement between the theoretical prediction and experimental results demonstrates that the dampers are indeed characterized with fidelity by equation (5.34), where $\alpha = 0.35$ and $C_\alpha = 67.6\ kips(s/in)^\alpha$. In Figure 5.4 the peak piston velocity is $v_{max} = 3.77\ in/sec$ and the resulting force history is nearly sinusoidal. In Figure 5.5 the peak piston velocity is $v_{max} = 18.85\ in/sec$ and the nonlinear behavior is apparent in the force history.

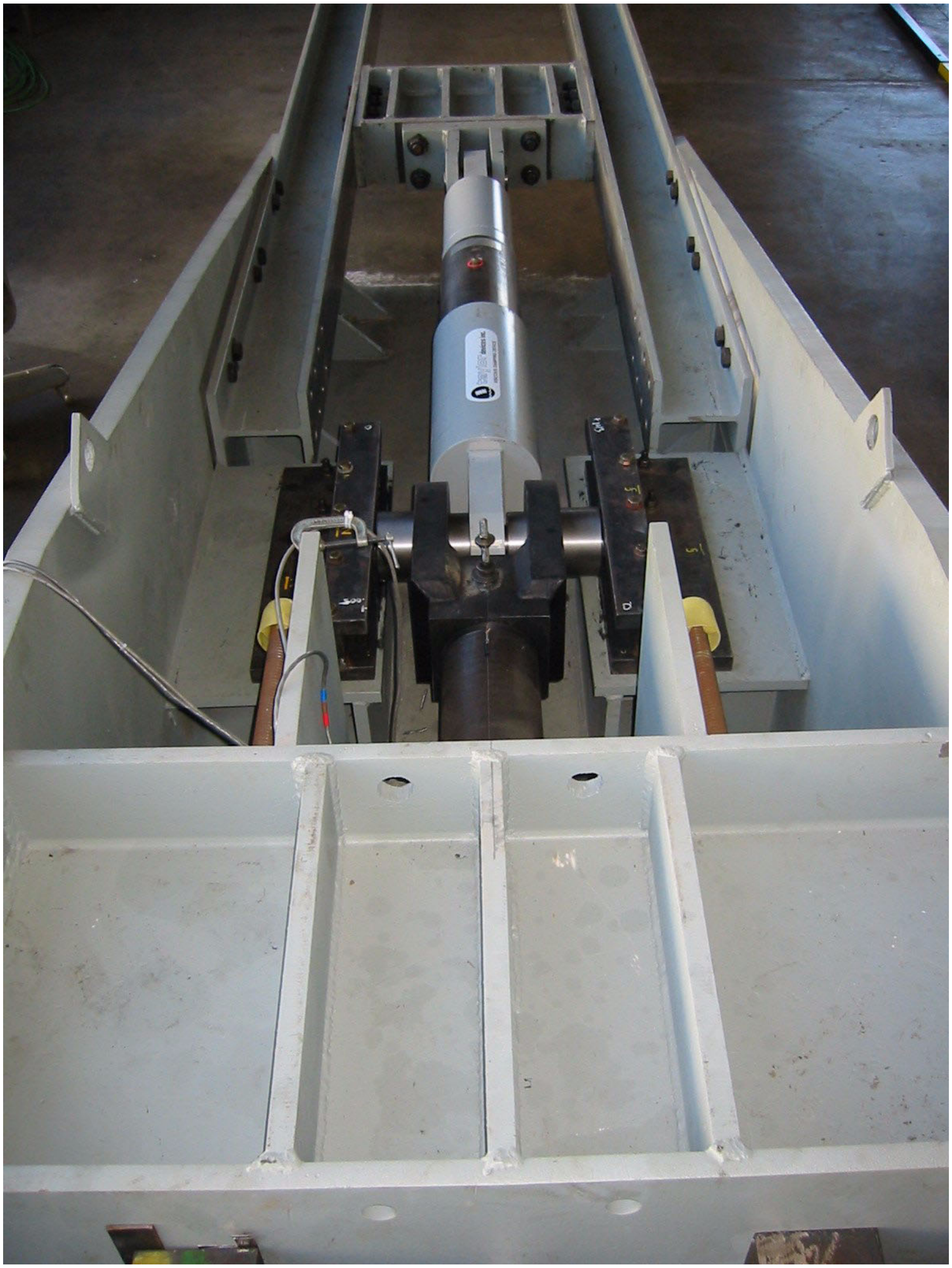

Figure 5.3 Top view of the UC Berkeley damper testing machine.

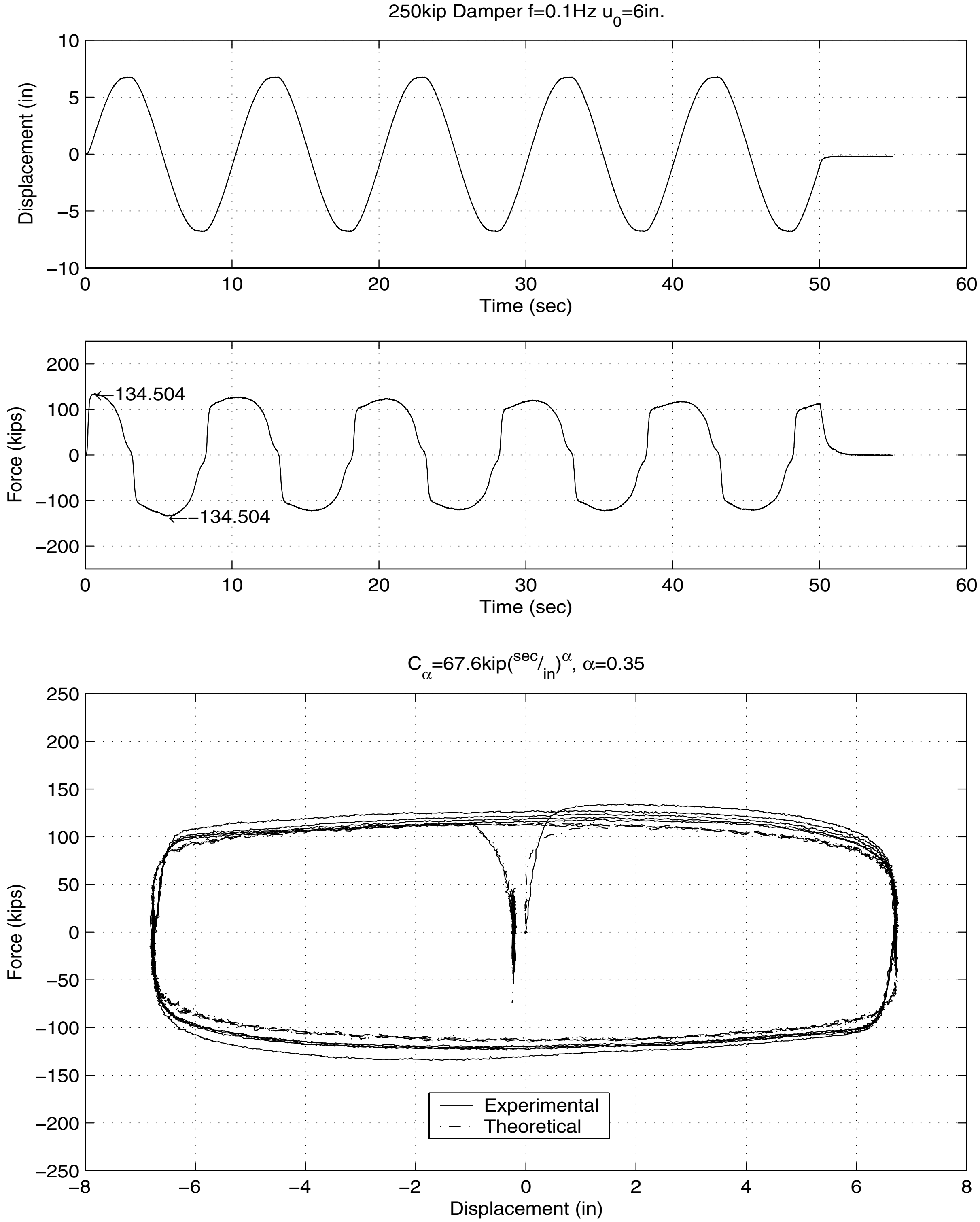

Figure 5.4 Imposed displacement history (top), recorded force history (center), and recorded force-displacement loop (bottom), from one of the dampers installed at the 91/5 overcrossing under testing frequency $f = 0.1Hz$. The nonlinear behavior is captured satisfactorily with $C_\alpha = 67.6kip(s/in)^\alpha$ and $\alpha = 0.35$.

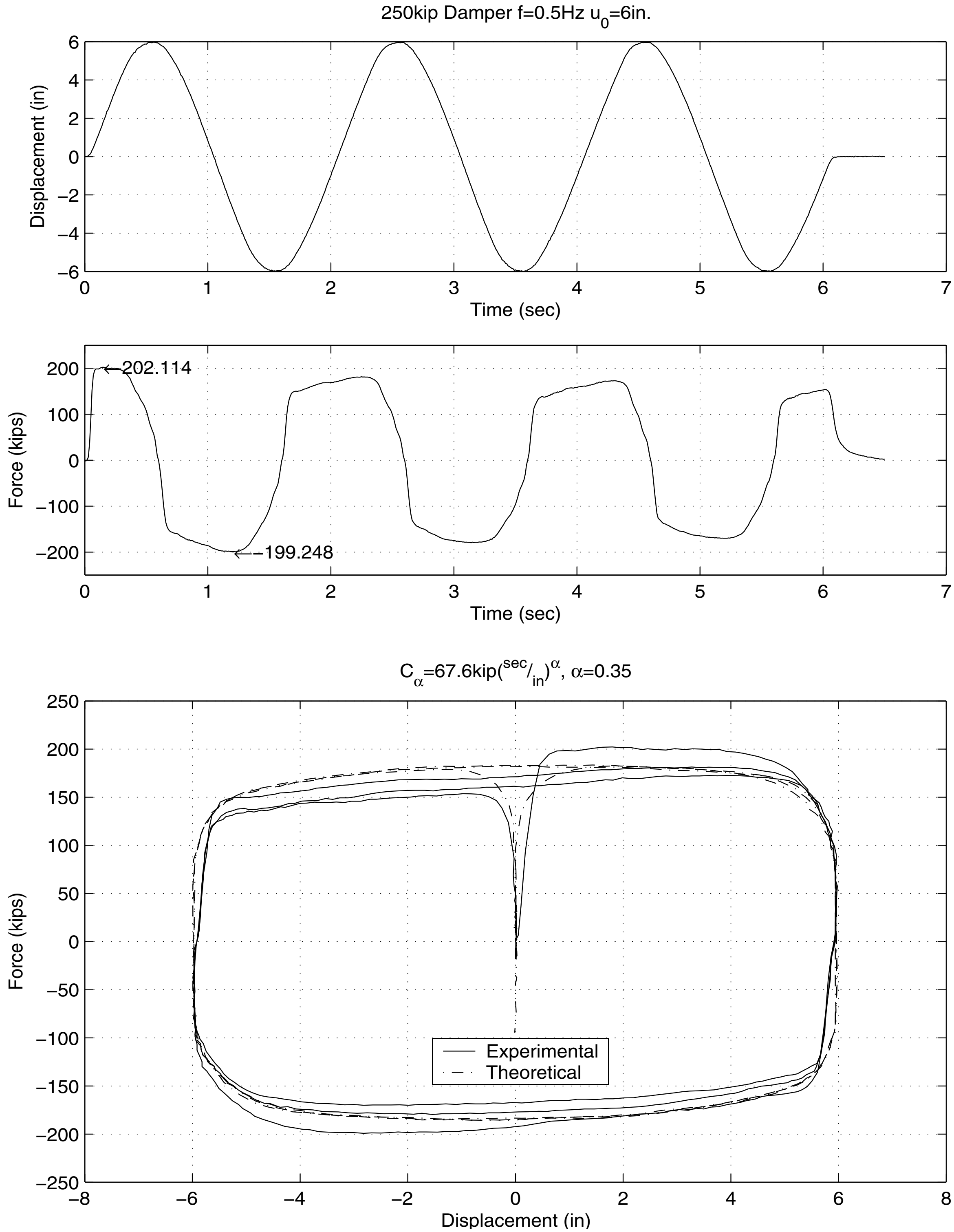

Figure 5.5 Imposed displacement history (top), recorded force history (center), and recorded force-displacement loop (bottom), from one of the dampers installed at the 91/5 overcrossing under testing frequency $f = 0.5Hz$. The nonlinear behavior is captured satisfactorily with $C_{\alpha} = 67.6kip(s/in)^{\alpha}$ and $\alpha = 0.35$.

When a nonlinear time domain analysis is conducted, equation (5.34) can be used directly in conjunction with the nonlinear force that originates from the bearings (eq. (5.31)). Despite the nonlinear nature of fluid dampers ($\alpha < 1$), modal analysis is possible with the introduction of equivalent linear quantities. The equivalent linear damping coefficient, C_1, for each nonlinear damper with damping constant, C_α, is calculated by equating the energy dissipated during one cycle by the two dampers. This idea was apparently first introduced by Jacobsen (1930) and subsequently used in several other studies (Fabunmi 1985, Symans and Constantinou 1998, Pekcan et al. 1999, among others).

The energy dissipated by any device during one cycle of motion $u(t) = u_0\sin(\omega t)$ is

$$E_D = \oint P(t)du = \int_0^{\frac{2\pi}{\omega}} P(t)\dot{u}(t)dt \tag{5.37}$$

where $P(t)$ is the force at the attachment of the damper that is given by (5.34) in the case of the nonlinear damper ($\alpha < 1$) or by (5.35) in the case of a linear damper ($\alpha = 1$). When $\alpha < 1$ equation (5.37) becomes

$$E_D^\alpha = \int_0^{\frac{2\pi}{\omega}} C_\alpha \omega^{\alpha+1} u_0^{\alpha+1} |\cos(\omega t)|^\alpha \mathrm{sgn}[\cos(\omega t)]\cos(\omega t)dt. \tag{5.38}$$

Now since the function $|\cos(\omega t)|^\alpha \mathrm{sgn}[\cos(\omega t)]$ has the same sign as $\cos(\omega t)$, equation (5.38) is integrated only over one quadrant:

$$E_D^\alpha = 4C_\alpha \omega^\alpha u_0^{\alpha+1}\int_0^{\frac{\pi}{2}} \cos^{\alpha+1}(\omega t)d(\omega t) \tag{5.39}$$

The integral appearing in (5.39) is known to be (Abramowitz and Stegun 1970)

$$\int_0^{\frac{\pi}{2}} \cos^{\alpha+1}\eta d\eta = 2^\alpha \frac{\Gamma\left(\frac{\alpha}{2}+1\right)\Gamma\left(\frac{\alpha}{2}+1\right)}{\Gamma(\alpha+2)} \tag{5.40}$$

and equation (5.39) gives

$$E_D^\alpha = C_\alpha 2^{2+\alpha}\omega^\alpha u_0^{\alpha+1}\frac{\Gamma^2\left(\frac{\alpha}{2}+1\right)}{\Gamma(\alpha+2)} \tag{5.41}$$

On the other hand when $\alpha = 1$ equation (5.37) gives

$$E_D^1 = C_1 \pi\omega u_0^2 \tag{5.42}$$

which is the result of (5.41) when $\alpha = 1$ ($\Gamma\left(\frac{1}{2}+1\right) = \frac{\sqrt{\pi}}{2}$, $\Gamma(3) = 2$). Equating the results from (5.41) and (5.42) yields

$$C_1 = C_\alpha \frac{2^{2+\alpha}}{\pi}\omega^{\alpha-1}u_0^{\alpha-1}\frac{\Gamma^2\left(\frac{\alpha}{2}+1\right)}{\Gamma(\alpha+2)} \tag{5.43}$$

Equation (5.43) indicates that the equivalent damping constant C_1 of a linear damper that dissipates the same amount of energy per cycles as the nonlinear damper is a function of the amplitude of the motion u_0. This amplitude dependence requires iteration in the equivalent linear analysis. A recent study that followed this approach has been presented by Lin and Chopra (2001).

Figure 5.6 plots the force-displacement loops of one of the dampers installed at the 91/5 overcrossing when cycled at frequencies $f = 0.5\ Hz$ and $1.0\ Hz$. The dashed lines plot the loops of an equivalent linear viscous dashpot with C_1 given by equation (5.43) when evaluated at $u_0 = 0.075\ m \approx 3\ in$. Although the corresponding loops from the nonlinear and linear dampers dissipate the same energy per cycle, the linear (viscous) damper results in a higher force.

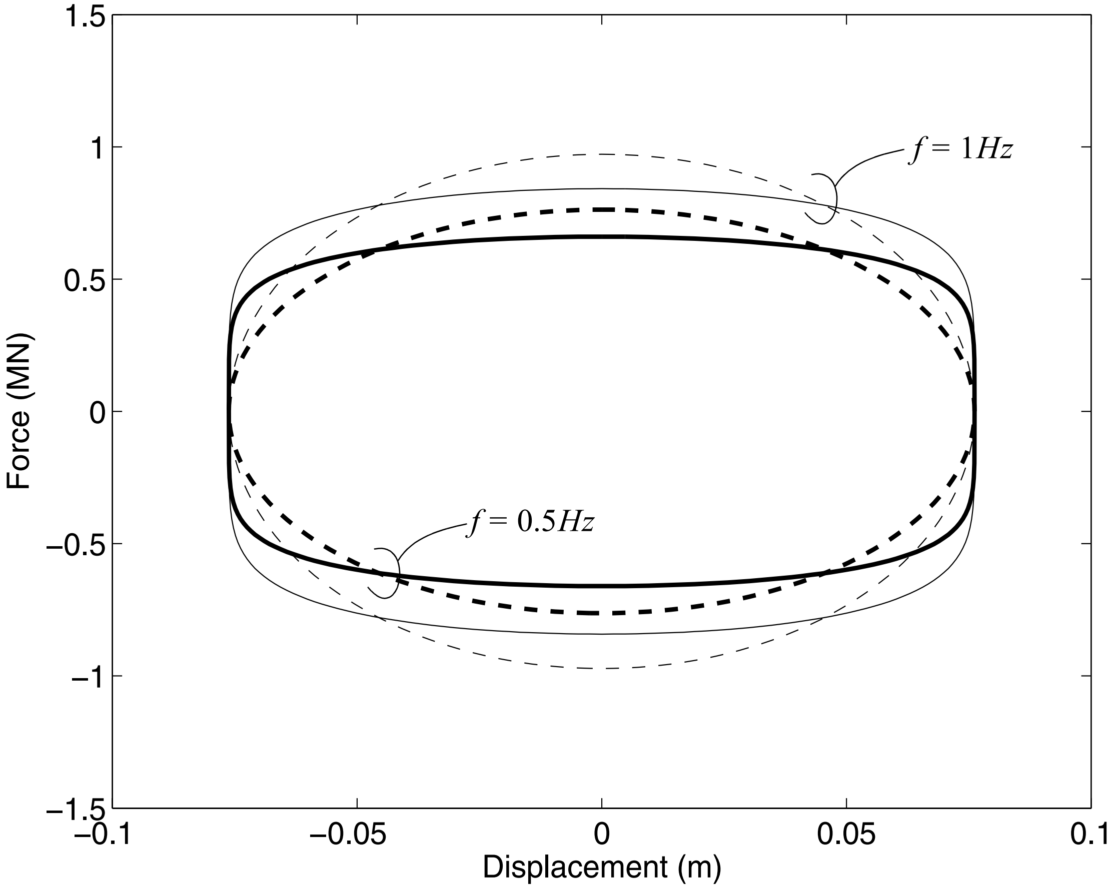

Figure 5.6 Force-displacement relation of the nonlinear fluid damper ($\alpha = 0.35$, solid lines) and its equivalent linear damper ($\alpha = 1.0$, dashed lines) evaluated at frequencies $f = 0.5Hz$ and $f = 1.0Hz$, respectively.

6 Seismic Response Analysis

6.1 EIGENVALUE ANALYSIS

With the validity of the stick model being established in past studies (McCallen and Romstad 1994, Zhang and Makris 2001, 2002b), the eigensolutions of the 91/5 overcrossing are computed for the stick model, shown in Figure 6.1, by using the commercially available software ABAQUS. The bridge superstructure consists of beam elements with massless links at each end that preserve the skewed geometry and serve as the connecting elements between the bridge deck and the end abutments. The elastomeric bearings are modeled with the 2-D plasticity model presented in Chapter 5; however, in the eigenvalue analysis it is assumed that the amplitude is small enough ($u_{deck} < u_y$) to keep the deformation of the bearing elastic. The nonlinear fluid dampers are replaced with linear dashpots that dissipate the same amount of energy at some nominal amplitude, u_0, that is discussed later. Each abutment is connected with the "springs" and "dashpots" that were established earlier to represent the stiffness and damping of the approach embankments along the longitudinal and transverse directions. The pile foundations at the center bent and end abutments are represented with equivalent flexural beams with the appropriate length and cross section that yield the correct static translational and rotational stiffnesses. Dashpots have been also appended at the location of the pile caps to represent the energy dissipated by the pile groups. The cross-section properties of the bridge superstructure are obtained from geometric data without considering any cracked section reduction. The damping of the bridge superstructure is approximated with the Rayleigh damping approximation, where the parameters α and β are computed by assuming a 5% modal damping ratio in the first and second modes. The Young's modulus of the concrete is assumed to be $22\ MPa$. This value is

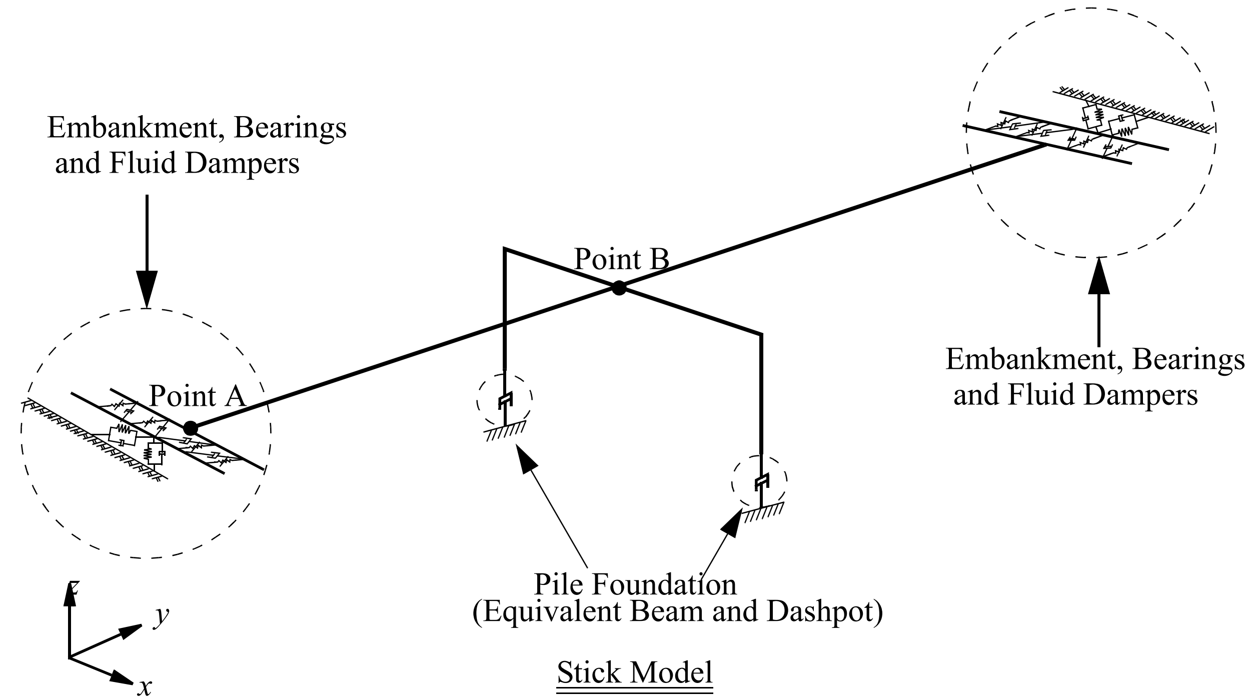

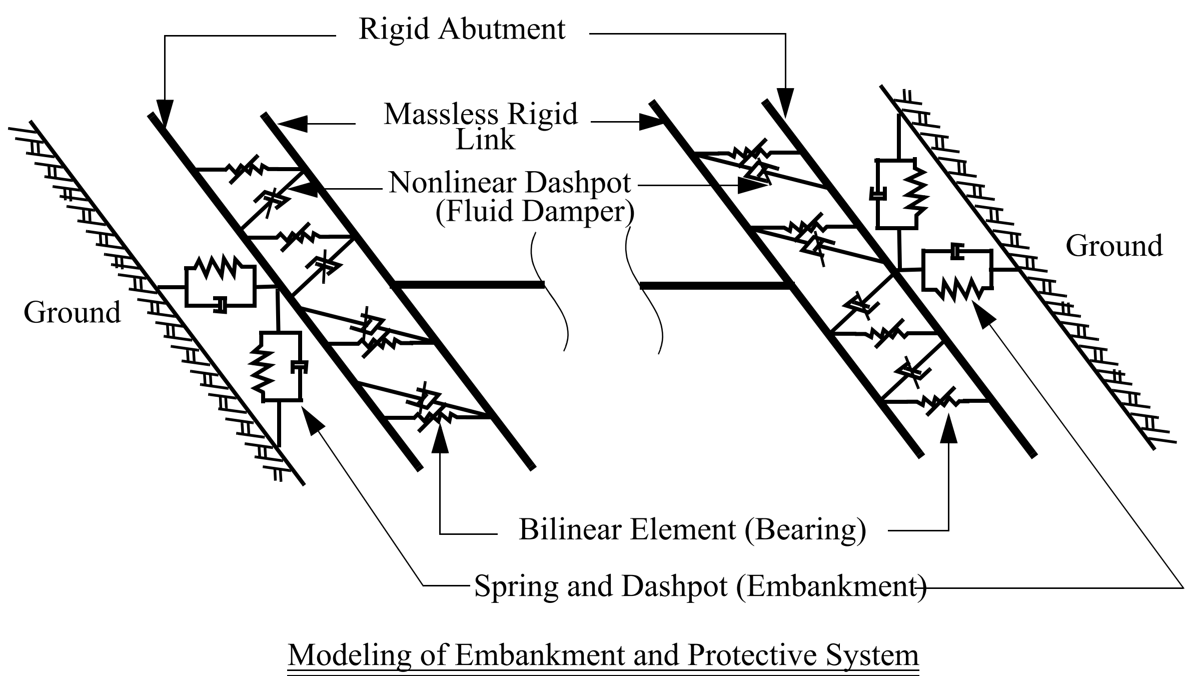

Figure 6.1 Top: structural idealization of the 91/5 overcrossing with beam elements and frequency-independent springs and dashpots; bottom: detail of the mechanical model that transfers forces from the deck to the surrounding soil.

approximately 80% of the value obtained from empirical expressions to account for the cracking that is expected during a strong earthquake. The density of concrete is $2400\ kg/m^3$.

Eigensolutions are performed for the bridge with integral abutments and the bridge with protective devices (elastomeric pads and fluid dampers) by using the commercially available software ABAQUS. Since the fluid dampers do not provide any stiffness, the bridge with pads essentially yields only the same modes and modal frequencies as those of the bridge equipped with both pads and fluid dampers. Figure 6.2 depicts the first six mode shapes as well as the natural frequencies of the bridge equipped with integral abutments (left) and those of the bridge with pads and fluid dampers (right), where the soil properties are taken as $G = 20MPa$ and $\eta = 0.40$ at the abutments and $G = 56MPa$ and $\eta = 0.12$ at the center bent.

For the bridge with integral abutments, the first modeshape is antisymmetric vertical, while the second modeshape is symmetric vertical. The third is the first transverse mode that indicates lateral flexure of the deck. When the bridge is sitting on elastomeric pads at each end, the structural configuration is more flexible. Accordingly, the modal frequencies of the bridge sitting on elastomeric pads at each end are smaller than the modal frequencies of the bridge with integral abutments. As a result, the first mode is longitudinal, the second mode is torsional about the vertical axis while the third mode is antisymmetric vertical. The first transverse mode of the sitting abutment configuration is the fourth mode that indicates more of a rigid body translation of the deck rather than flexure which is observed in the third mode of the bridge with integral abutment. Table 6.1 compares the first six natural frequencies of the bridge with integral abutment and the bridge with protective devices when soil properties are taken as: $G = 10MPa$, $\eta = 0.50$ at abutment and $G = 28MPa$, $\eta = 0.35$ at center bent (Case 1); and $G = 20MPa$, $\eta = 0.40$ at abutment and $G = 56MPa$, $\eta = 0.12$ at center bent (Case 2). These two sets of soil properties correspond to the foundation response under different levels of earthquake.

Modal damping ratios are estimated with the complex eigenvalue procedure presented by Zhang and Makris (2001). A reduced-order stick model was developed with fewer degrees of freedom in order to bypass the problem of computing and interpreting the large number of complex eigenvalues resulting from the original stick model. For simplicity, the reduced-order stick model lumped the four fluid dampers into two orthogonal nonlinear dashpots rather than preserving the exact layout as shown in Figure 6.1. Similarly, the presence of the embankment

Bridge with Integral Abutments **Bridge with Sitting Abutments**

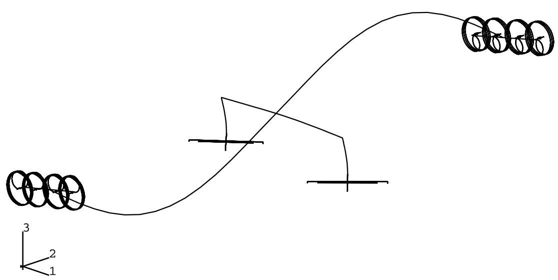

Case 2: $f_1 = 1.44\ Hz$ $\xi_1 = 5.3\%$

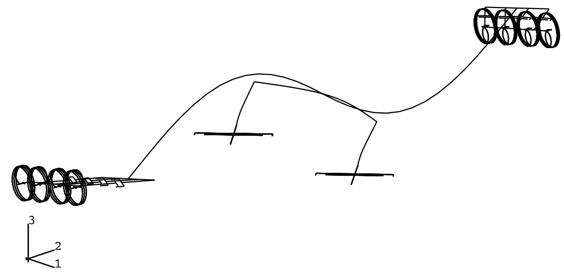

Case 2: $f_1 = 1.21\ Hz$ $\xi_1 = 28.9\%\ (5.6\%)$

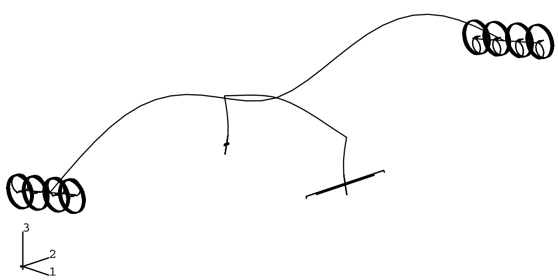

Case 2: $f_2 = 1.79\ Hz$ $\xi_2 = 5.8\%$

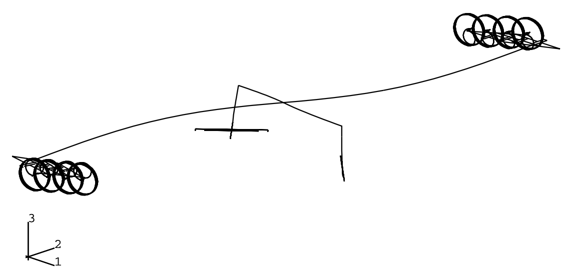

Case 2: $f_2 = 1.27\ Hz$ $\xi_2 = 84.4\%\ (5.7\%)$

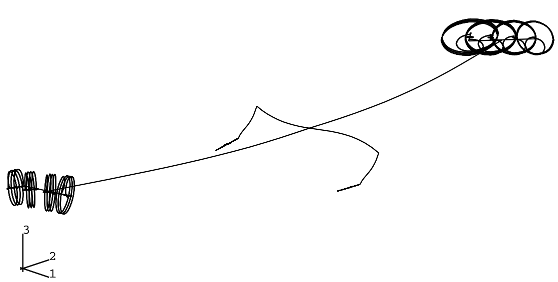

Case 2: $f_3 = 2.93\ Hz$ $\xi_3 = 12.3\%$

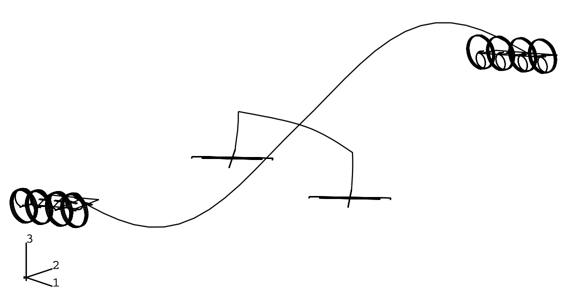

Case 2: $f_3 = 1.52\ Hz$ $\xi_3 = 9.8\%\ (5.7\%)$

Figure 6.2 First six modal frequencies, damping ratios, and modeshapes computed with stick model of 91/5 overcrossing (left: bridge with integral abutments; right: bridge with sitting abutments). The damping ratios in parentheses are for the bridge with pads only (continued).

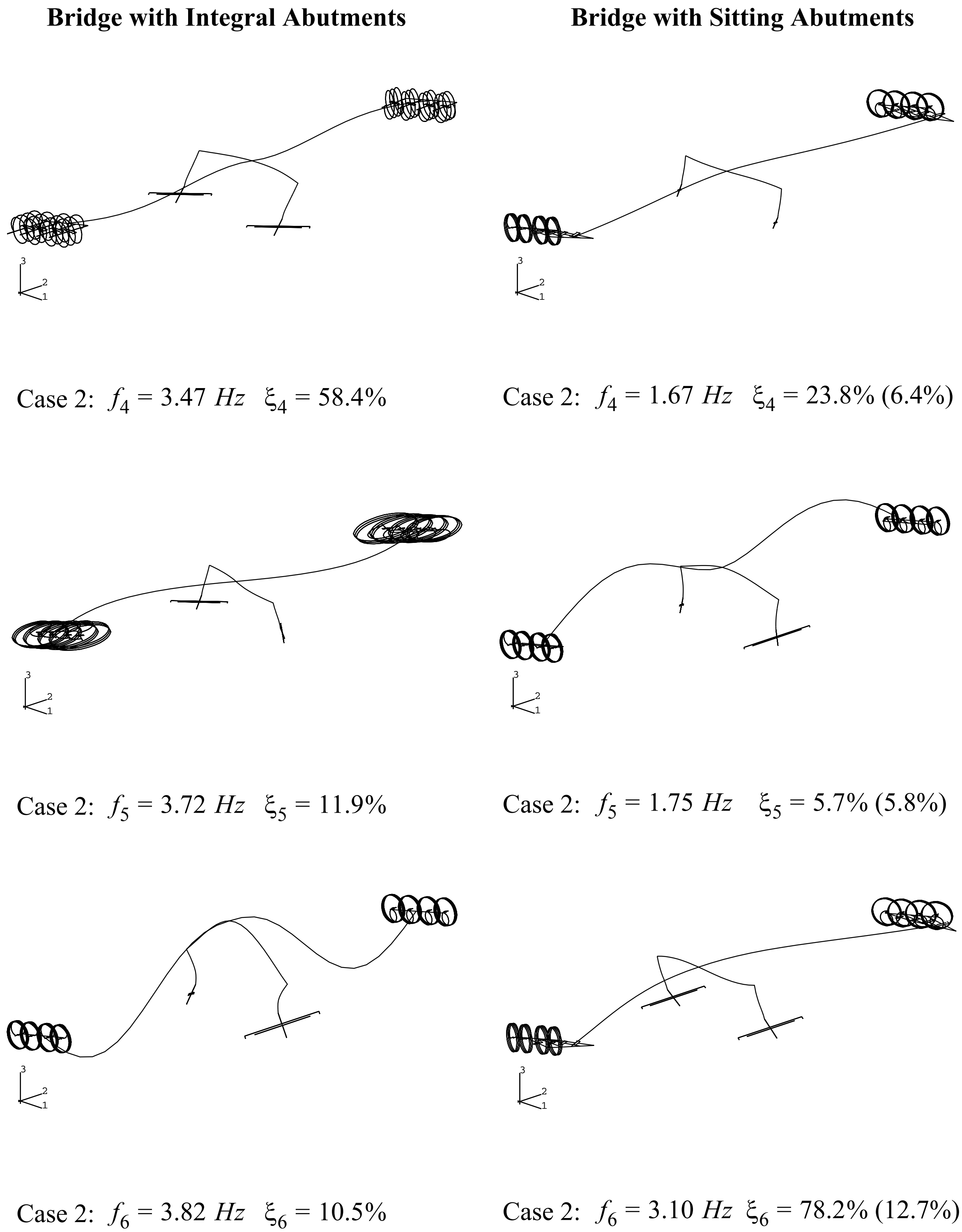

Figure 6.2 First six modal frequencies, damping ratios, and modeshapes computed with stick model of 91/5 overcrossing (left: bridge with integral abutments; right: bridge with sitting abutments). The damping ratios in parentheses are for the bridge with pads only.

and elastomeric pads are represented by two orthogonal springs and dashpots respectively, as shown in Figure 6.1.

To the same extent that the modal characteristics of the bridge depend on the level of shaking because of the strain-dependent behavior of the soil, they also depend on the level of shaking because of the amplitude-dependent behavior of fluid dampers with exponent $\alpha < 1$. The nominal amplitudes for the two levels of excitation considered are $u_0 \approx 2$ in and $u_0 \approx 4.5$ in, respectively, and the damping constant of the equivalent linear dashpot is given by (Jacobsen 1930).

$$C_1 = C_\alpha \frac{2^{2+\alpha}}{\pi} \omega^{\alpha-1} u_0^{\alpha-1} \frac{\Gamma^2\left(\frac{\alpha}{2}+1\right)}{\Gamma(\alpha+2)} \tag{6.1}$$

The frequency ω appearing in equation (6.1) is taken to be equal to the first modal frequency ($\omega = \omega_1$).

Table 6.1 compares the first six modal frequencies and modal damping ratios of the bridge with integral abutment, the bridge with pads, and the bridge with pads and nonlinear fluid dampers under different levels of earthquake. It worth mentioning that the natural modes of the bridge with integral abutments are different from that of the bridge with elastomeric pads and/or nonlinear fluid dampers. Therefore, a one-to-one comparison of modal damping ratios between these two cases is not meaningful. A more meaningful comparison is the case with pads only and the case with pads and nonlinear dampers. Several key observations from Table 6.1 are

- The behavior of the bridge with integral abutments is essentially very close to that of the Meloland Road overcrossing and the Painter Street bridge (Zhang and Makris 2001 and 2002b), where high modal damping ratios are associated with the longitudinal and transverse modes that mobilize a large volume of soil with high damping.
- The first transverse mode of the deck with integral abutment is a flexural mode whereas the first transverse mode of the deck with pads is essentially a translational mode.
- Because of the flexibility introduced by elastomeric pads at the deck ends, the modal damping ratios associated with the longitudinal or transverse modes of the bridge with sitting abutments are appreciably smaller than the modal damping ratios of the bridge with integral abutments,

Table 6.1 Modal frequencies, ω_j (rad/s) and damping ratios, ξ_j (%), of bridge under different levels of earthquake

Bridge Structure		Modes	Case 1 Undamped ω_j (rad/s)	Case 1 Damped ω_j (rad/s)	Case 1 ξ_j (%)	Case 2 Undamped ω_j (rad/s)	Case 2 Damped ω_j (rad/s)	Case 2 ξ_j (%)
Bridge With Integral Abutment	1	1st vertical (antisymmetric)	8.6897	$8.7045 + 0.4824i$	5.53	8.7366	$8.7353 + 0.4624i$	5.29
	2	2nd vertical (symmetric)	10.735	$10.774 + 0.6949i$	6.44	10.897	$10.904 + 0.6343i$	5.81
	3	1st transverse	15.218	$15.614 + 2.7763i$	17.51	17.154	$17.548 + 2.1811i$	12.34
	4	longitudinal	18.310	$15.734 + 11.237i$	58.12	22.988	$20.801 + 14.963i$	58.39
	5	torsional/vertical	21.656	$24.437 + 3.5534i$	14.39	23.526	$24.686 + 2.9479i$	11.86
	6	3rd vertical (symmetric)	22.508	$23.011 + 2.7880i$	12.03	23.275	$23.492 + 2.4673i$	10.45
Bridge With Pads Only	1	longitudinal	7.4960	$7.5083 + 0.5884i$	6.36	7.6837	$7.6803 + 0.4313i$	5.61
	2	torsional	7.8492	$7.8898 + 0.6089i$	6.46	7.9938	$7.9989 + 0.4557i$	5.69
	3	1st vertical (symmetric)	9.3974	$9.4020 + 0.5832i$	6.19	9.6029	$9.5987 + 0.5442i$	5.66
	4	1st transverse	10.325	$10.428 + 0.8812i$	8.42	10.806	$10.836 + 0.6947i$	6.40
	5	2nd vertical (symmetric)	10.782	$10.802 + 0.6775i$	6.26	10.940	$10.934 + 0.6324i$	5.77
	6	2nd transverse	19.149	$19.410 + 3.086i$	15.70	20.942	$21.108 + 2.6958i$	12.67
Bridge With Pads & Fluid Dampers	1	longitudinal	7.4960	$7.6955 + 1.4542i$	18.57	7.6837	$8.1866 + 2.4706i$	28.89
	2	torsional	7.8492	$6.4342 + 5.5283i$	65.17	7.9938	$8.8755 + 13.983i$	84.43
	3	1st vertical (symmetric)	9.3974	$9.0575 + 0.9042i$	9.93	9.6029	$8.7969 + 0.8466i$	9.78
	4	1st transverse	10.325	$10.161 + 5.3303i$	46.45	10.806	$17.835 + 4.3610i$	23.75
	5	2nd vertical (symmetric)	10.782	$10.800 + 0.6753i$	6.24	10.940	$10.926 + 0.6223i$	5.69
	6	2nd transverse	19.149	$17.630 + 5.7330i$	30.92	20.942	$11.550 + 14.506i$	78.23
Notes	Case 1: $G = 10MPa$, $\eta = 0.50$ (abutment); $G = 28MPa$, $\eta = 0.35$ (center bent); $u_0 = 4.5$ in (nominal amplitude of fluid dampers) Case 2: $G = 20MPa$, $\eta = 0.40$ (abutment); $G = 56MPa$, $\eta = 0.12$ (center bent); $u_0 = 2.0$ in (nominal amplitude of fluid dampers)							

since the bridge superstructure can move substantially without mobilizing large volumes of soil. At the same time, the modal frequencies of the bridge with pads are lower than that of the bridge with integral abutments.

- When integral abutments are considered the modal damping along the longitudinal direction is 58% and along the transverse direction is 18%. When pads and dampers are added the situation reverses. Because of the flexibility of the pads the bridge moves appreciably both in the longitudinal and transverse directions. Along the longitudinal direction the modal damping of the bridge with pads and dampers is approximately 18%, whereas along the transverse direction the modal damping is 50%.
- When nonlinear fluid dampers are added, the modal damping ratios of modes that involve large movement of the fluid dampers increase substantially (longitudinal, torsional, and transversal modes).

6.2 TIME HISTORY RESPONSE ANALYSIS

The bridge response is computed by inducing as support motions along the transverse and longitudinal directions the recorded acceleration time histories at the free field and the amplified acceleration time histories at the crest of the embankment to the idealized model shown on Figure 6.1. The fault-normal component is applied to the transverse direction, while the fault-parallel component is applied simultaneously to the longitudinal direction. The time history response analysis is conducted on the bridge with integral abutment, the bridge with elastomeric pads, and the bridge with elastomeric pads and nonlinear fluid dampers, subjected to the ground motions listed in Table 3.1. The macroscopic force-displacement laws of the various substructure elements of the bridge appearing in Table 2.1 have been presented and discussed in the previous chapters.

The Appendix offers computed time histories of response quantities at various points, as well as displacement and force signatures and force-displacement loops at various locations. The results of our investigations are presented in summary plots where peak response values are presented for all 11 earthquake motions used in this study. Figure 6.3 shows the peak total accelerations and relative displacements along the transverse and longitudinal directions near the east end of the deck (point A). The same quantities normalized to the response of the configuration with integral abutments are shown in Figure 6.4. The longitudinal response of the bridge is in accordance with what one expects intuitively. The bridge with sitting abutment is more flexible than that with integral abutments, so accelerations are smaller and displacements are larger. Damping reduces both displacements and accelerations of the flexible configuration. Figures 6.3 and 6.4 (left) show that the transverse response of the bridge with integral abutments yields not only smaller relative displacements but also smaller accelerations. This can be explained by concentrating on the transverse modes of the two configurations that is the third mode (3rd) when integral abutments are considered and the fourth mode (4th) when sitting abutments are considered. In the case of integral abutments the transverse mode is primarily a flexural mode, whereas in the case of sitting abutment the transverse mode is primarily a translational mode where the entire deck translates sideways without flexing appreciably. This causes larger displacements at the deck ends but also larger accelerations. Supplemental damping reduces both displacements and accelerations but the response of the bridge with sitting abutments appears to underperform compared to the response of the bridge with integral abutments. Figure 6.5 plots the normalized response of the bridge computed without soil-structure interaction to the response of the bridge computed with soil-structure interaction. For the configuration with pads and dampers this ratio is below unity, indicating that soil-structure interaction increases both accelerations and displacements.

Figures 6.6 to 6.8 plot total accelerations and relative-to-the-ground displacements at the mid-span (point B). The trend of accelerations and displacements along the longitudinal directions resemble the trend at point A (east of the deck near the abutment). Along the transverse direction the results for accelerations and displacements of the two configurations are mixed. This is because the mid-span moves sideways approximately the same amount regardless of whether the transverse movement is the result of a primarily flexural mode or of a primarily translational mode. Figure 6.8 indicates that an analysis of the bridge response that neglects the effect of soil-structure interaction underestimates considerably the transverse and longitudinal displacements at mid-span.

The results of Figures 6.3 to 6.8 indicate that lengthening of the period of an overcrossing by introducing sitting abutments reduces the longitudinal accelerations of the deck but increases the translational accelerations. Introduction of damping is beneficial; but the configuration with integral abutment is shown to yield the most favorable response. Soil-structure interaction is responsible for increasing displacements, while having mixed effect on accelerations.

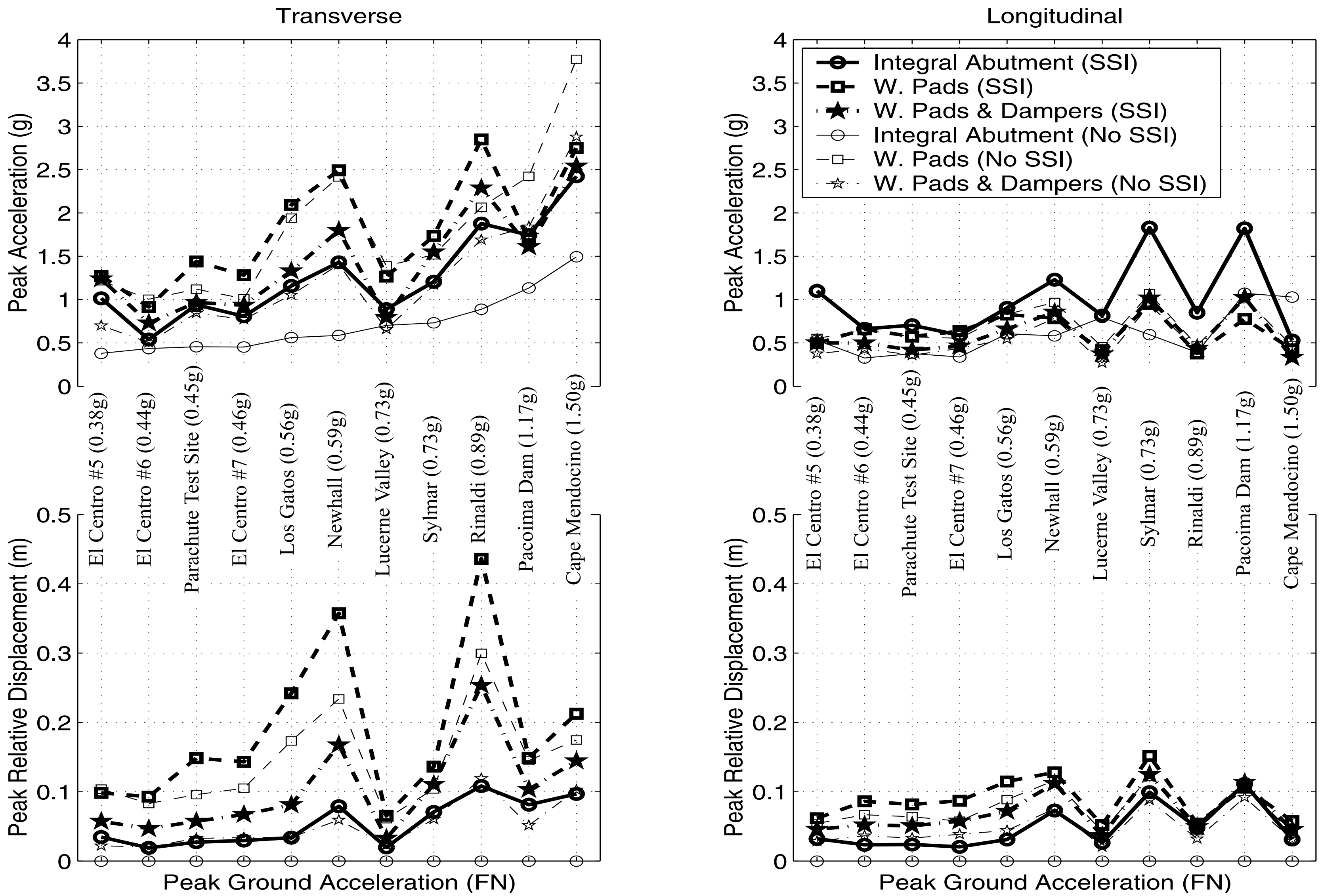

Figure 6.3 Peak total accelerations (top) and peak relative displacements (bottom) near east end of deck (point A) due to various earthquake motions ordered with increasing peak ground acceleration of the fault-normal component.

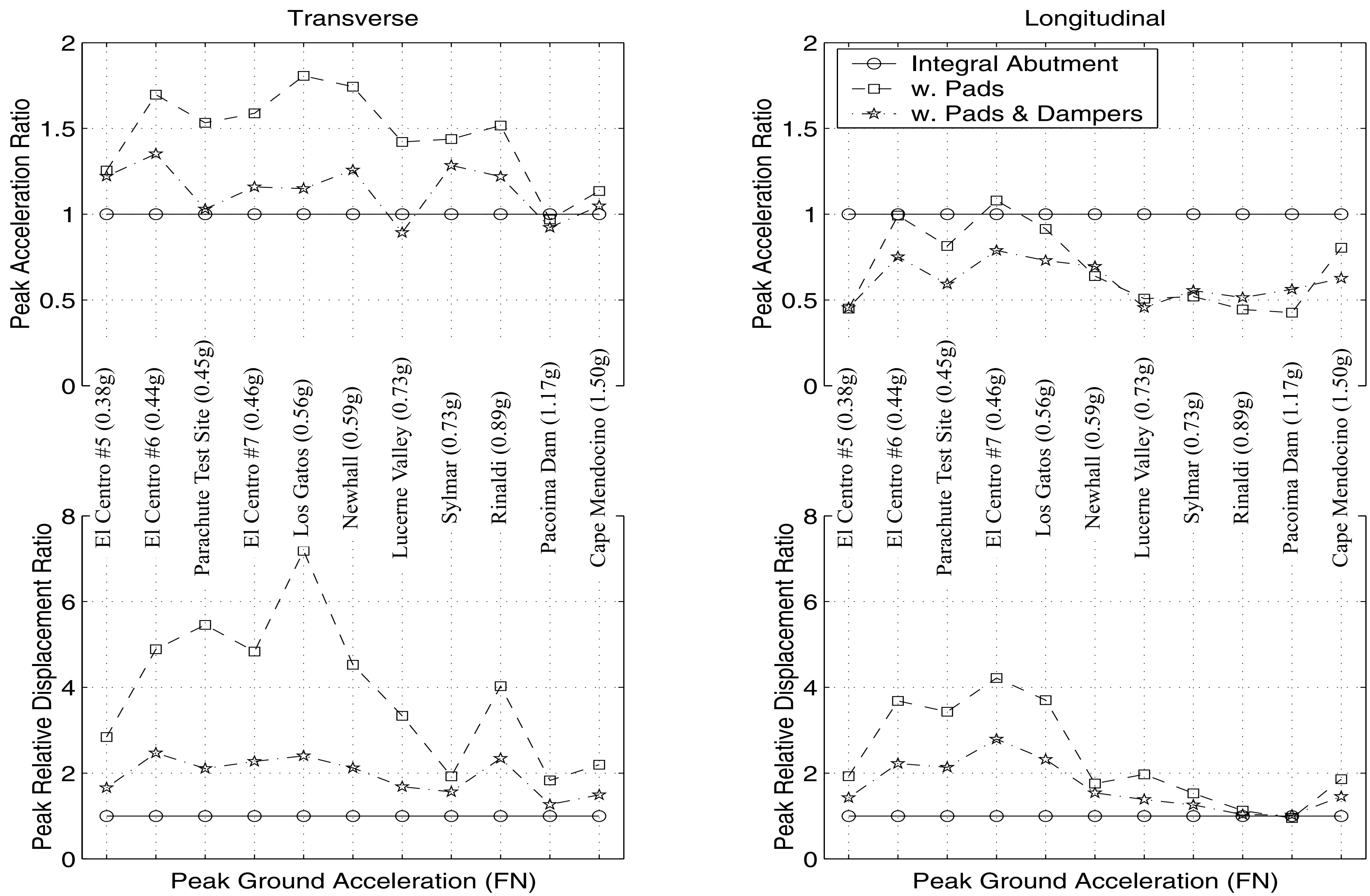

Figure 6.4 Normalized bridge response quantities near east end of deck (point A) to the corresponding response quantities of bridge with integral abutments due to various earthquake motions ordered with increasing peak ground acceleration of the fault-normal component.

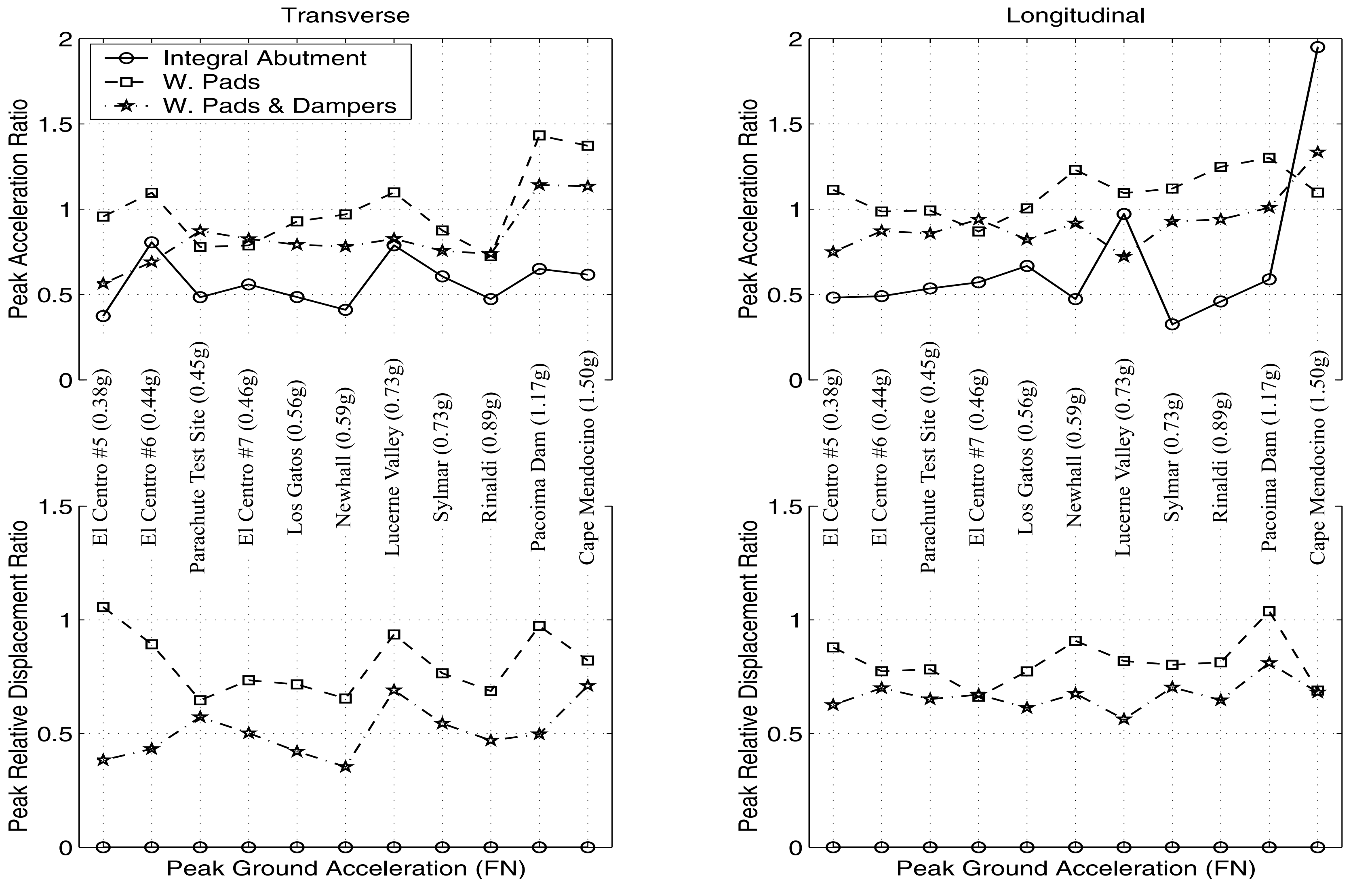

Figure 6.5 **Normalized bridge response quantities near east end of deck (point A) computed without soil-structure interaction to the corresponding response quantities computed with soil-structure interaction due to various earthquake motions ordered with increasing peak ground acceleration of the fault-normal component.**

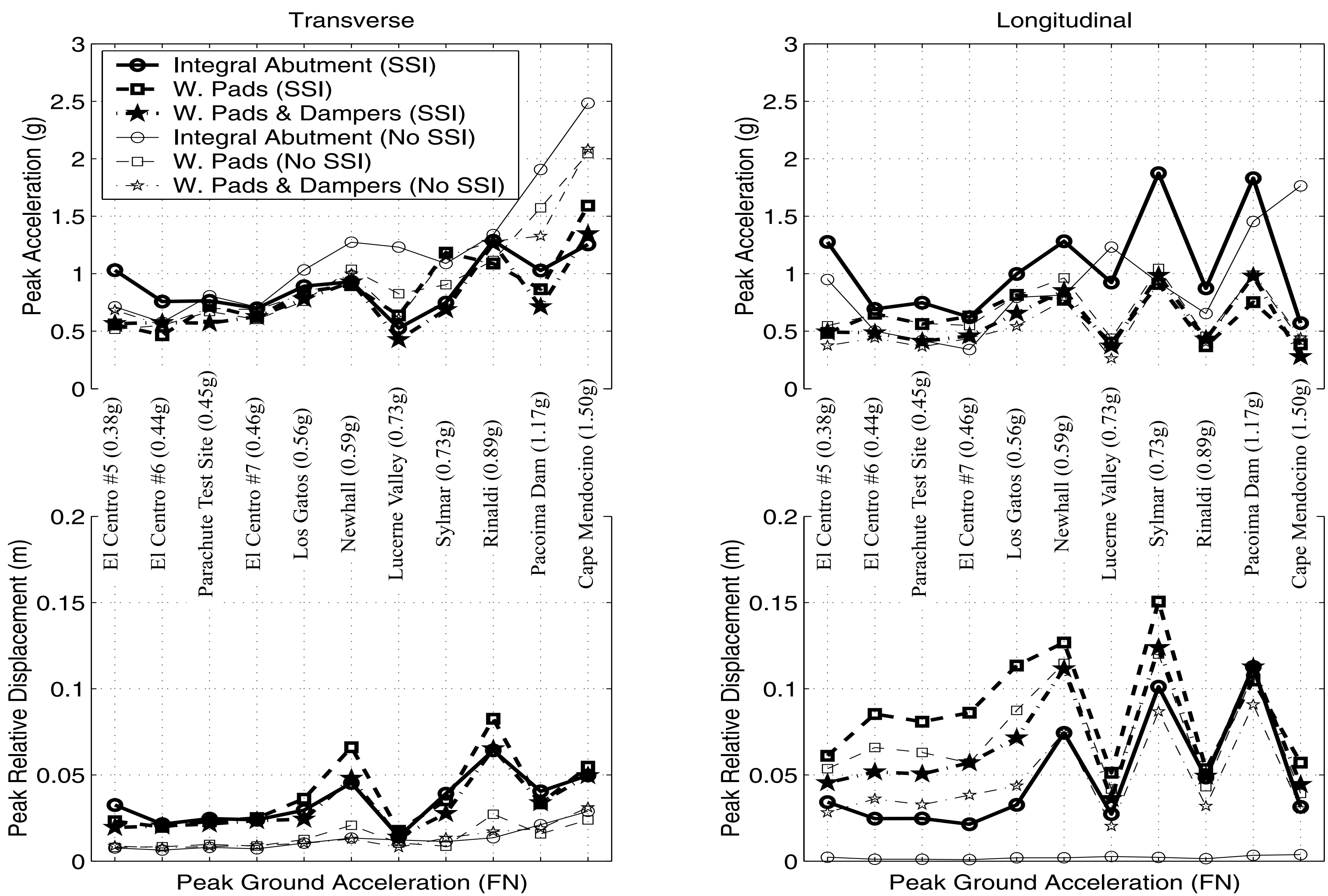

Figure 6.6 Peak total accelerations (top) and peak relative displacements (bottom) at mid-span (point B) due to various earthquake motions ordered with increasing peak ground acceleration of the fault-normal component.

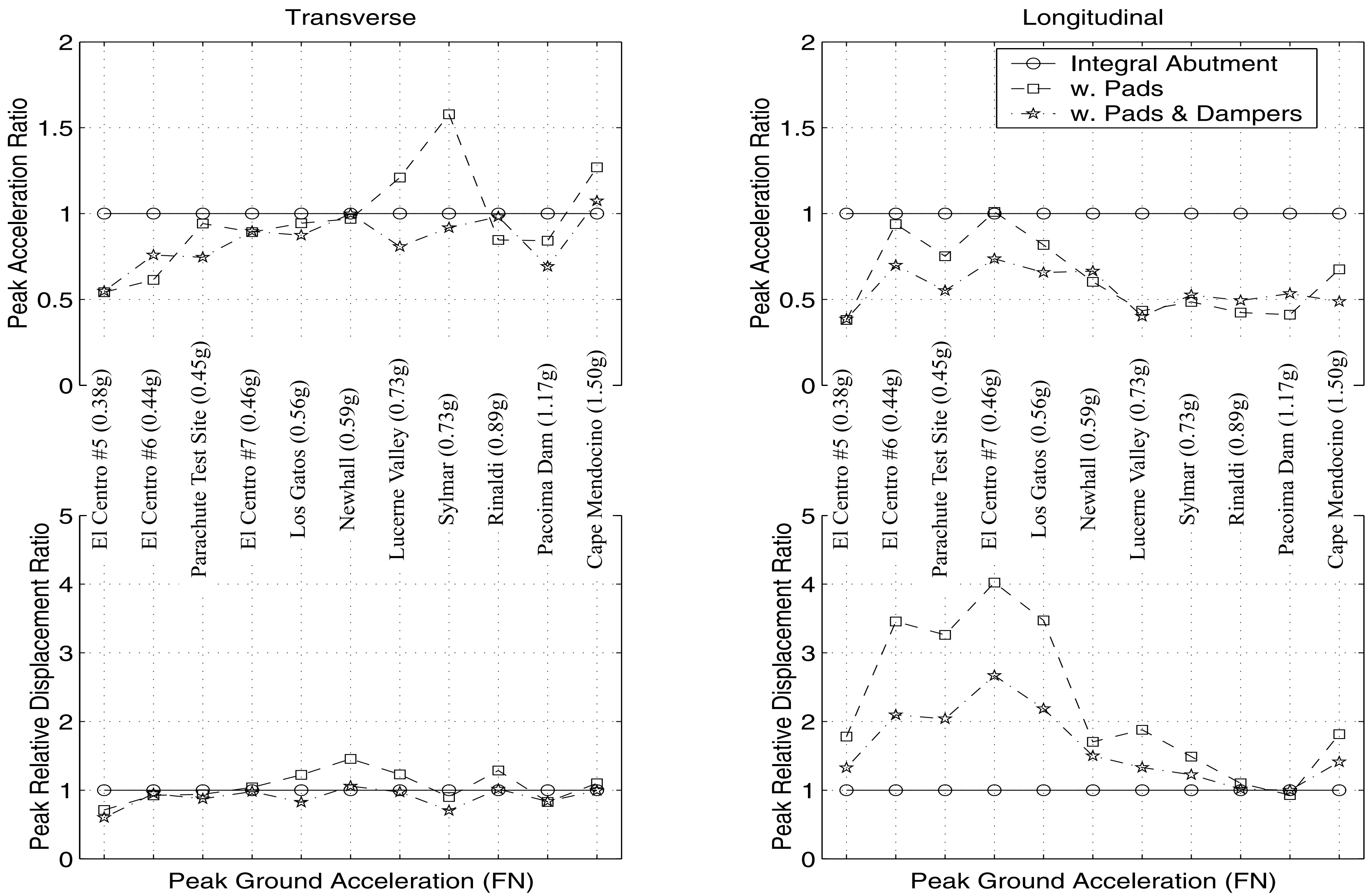

Figure 6.7 Normalized bridge response quantities at mid-span (point B) to the corresponding response quantities of bridge with integral abutments due to various earthquake motions ordered with increasing peak ground acceleration of the fault-normal component.

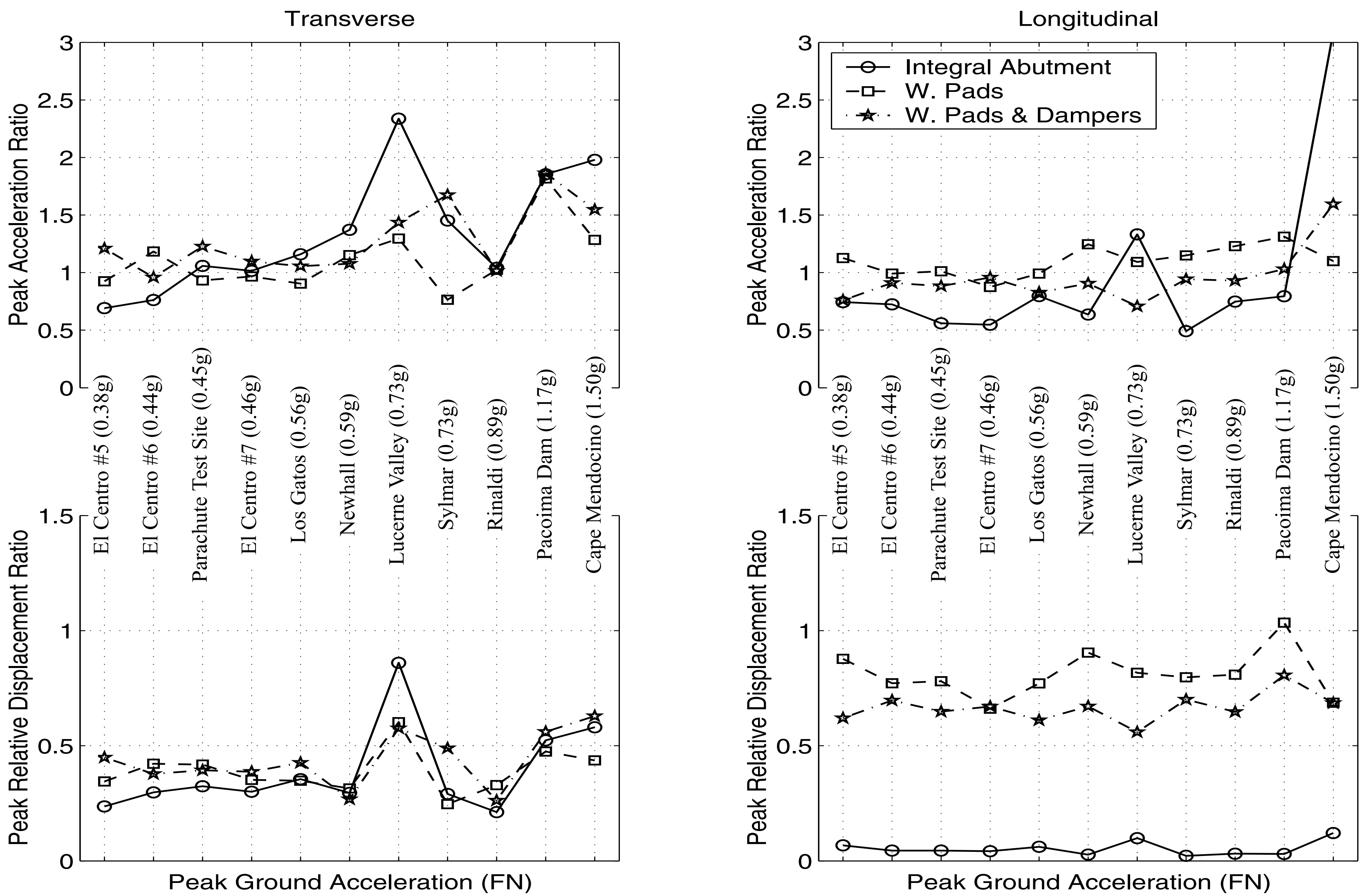

Figure 6.8 Normalized bridge response quantities at mid-span (point B) computed without soil-structure interaction to the corresponding response quantities computed with soil-structure interaction due to various earthquake motions ordered with increasing peak ground acceleration of the fault-normal component.

Figure 6.9 plots peak forces that develop at the deck ends due to various earthquake motions. Clearly the configuration with integral abutments results in higher forces that, in some cases, are as high as half (1/2) the deck weight. The configuration with pads alone results in the smaller forces that are approximately 5% of the deck weight. This result is expected, since the $4MN$ of the vertical reaction at each deck-end is approximately $0.16W$ and with a coefficient of friction, $\mu = 0.3$, the maximum horizontal force is $0.3 \times 0.16W \approx 0.05W$. The forces normalized to the forces of the configuration with integral abutments are shown in Figure 6.10.

Figure 6.11 plots the transverse and longitudinal forces behind the end abutments for the three configurations of interest and the two cases with and without soil-structure interaction. The forces normalized to the forces of the bridge with integral abutments when soil-structure interaction is considered are shown in Figure 6.12. Clearly the configuration of the bridge with sitting abutments reduces the longitudinal forces but not the transverse forces. The presence of fluid dampers yield transverse forces that are higher than the forces when the bridge has integral abutments.

Figure 6.13 shows the normalized forces behind the abutments computed without soil-structure interaction compared to the corresponding forces computed with soil-structure interaction. For all but the Cape Mendocino record, the forces without soil-structure interaction are smaller than the forces with soil-structure interaction. In some cases, such as the El Centro Array #5 record or the Newhall and Sylmar records, the force ratio is as low as 0.5. This observation indicates that soil-structure interaction has an important effect and should be included in the dynamic analysis.

Figure 6.14 plots the transverse and longitudinal shear forces at the bases of columns of the center bent for the three configurations of interest and the two cases with and without soil-structure interaction. The forces normalized to the corresponding forces of the bridge with integral abutments when soil-structure interaction is considered are shown in Figure 6.15. Along the transverse direction the bridge with sitting abutments transmits approximately the same forces to the column bases as the bridge with integral abutment transmits. Along the longitudinal direction the differences are dramatic, since in some earthquakes the column forces of the bridge with sitting abutments are more than two times the column forces of the bridge with integral abutments. Nevertheless, our analysis indicated that even when the bridge is isolated, the center columns remain practically elastic. Figure 6.16 shows the normalized column forces computed

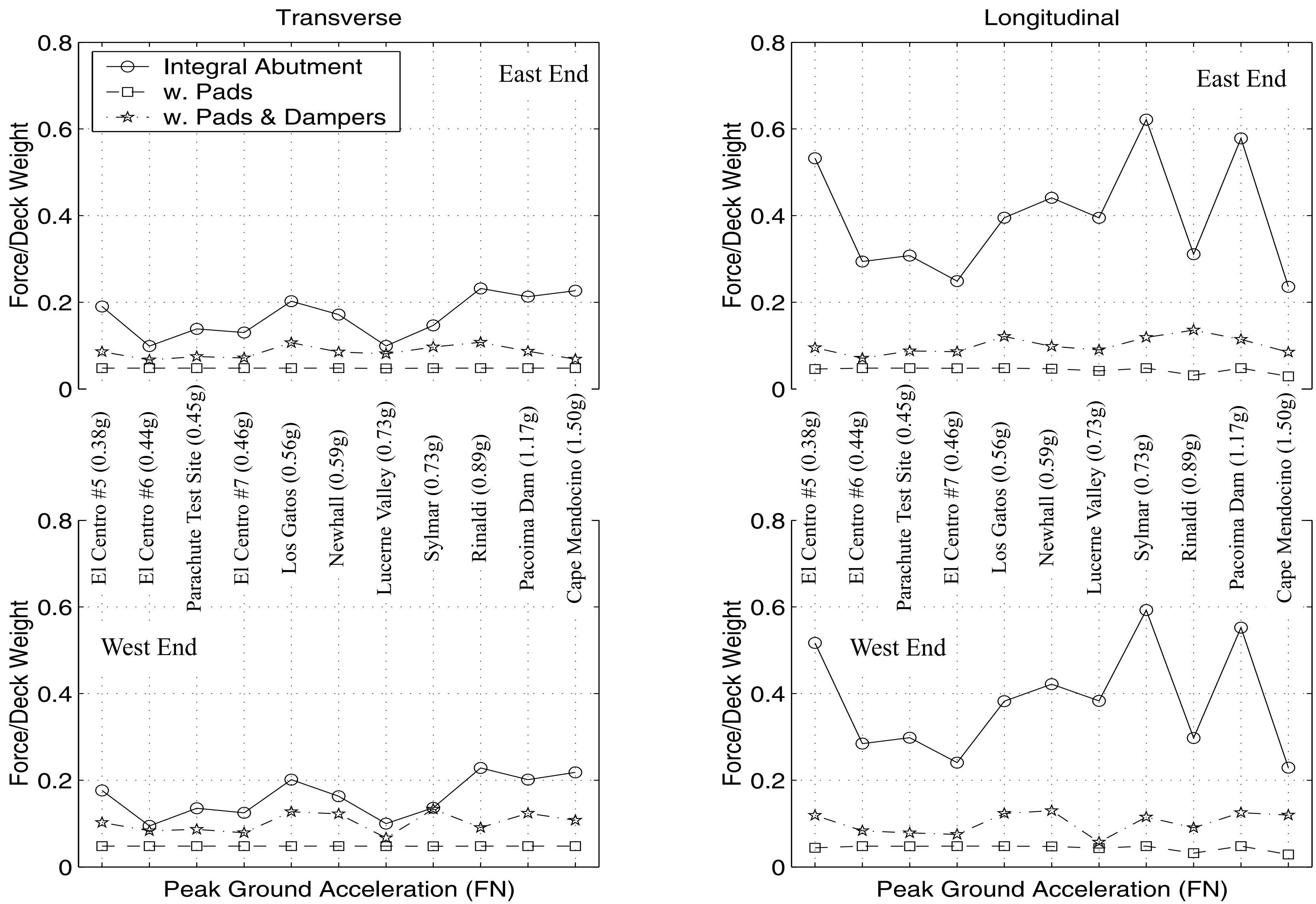

Figure 6.9 Peak forces at deck ends due to various earthquake motions ordered with increasing peak ground acceleration of the fault-normal component.

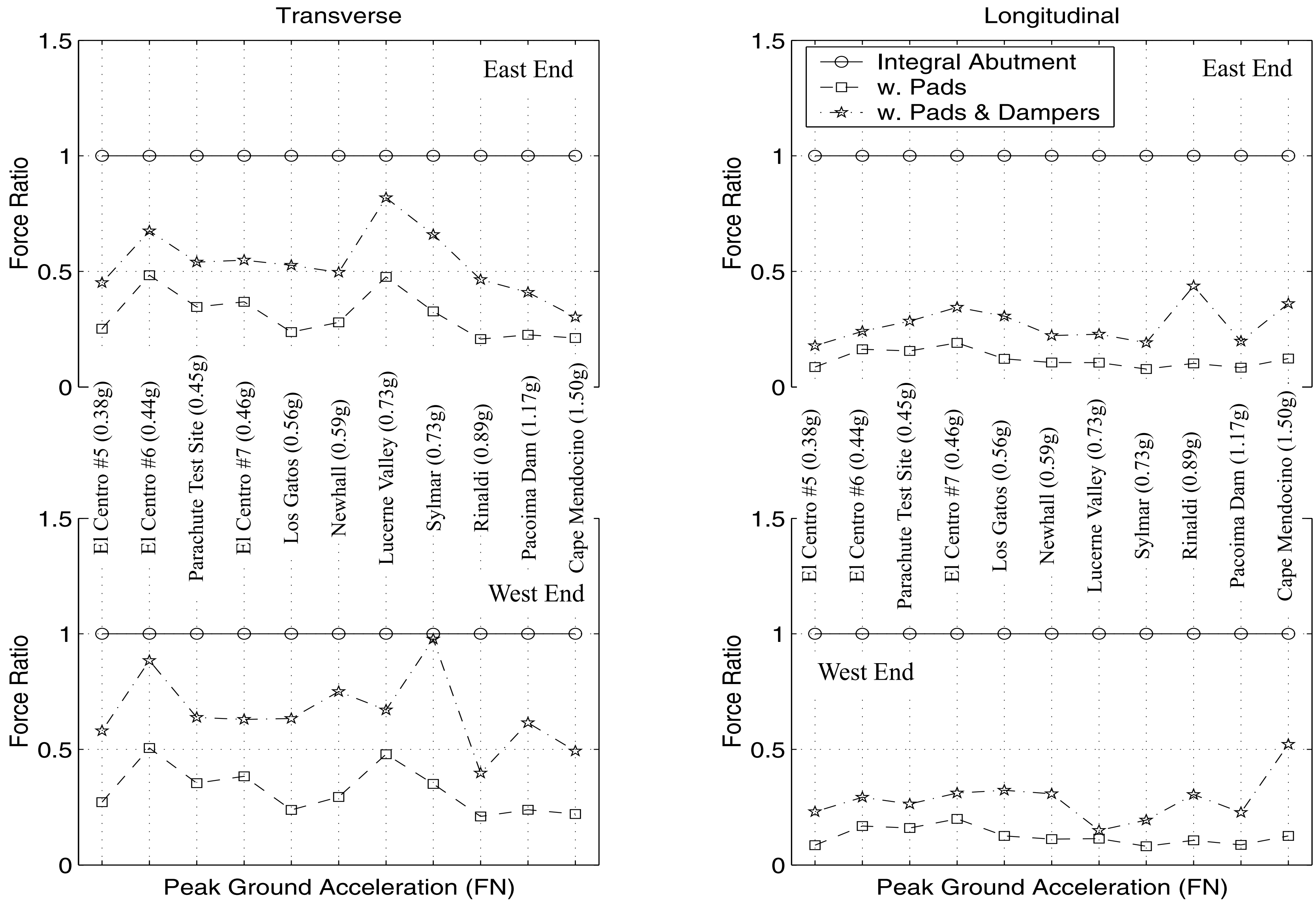

Figure 6.10 Normalized forces at deck ends and the corresponding forces of bridge with integral abutments due to various earthquake motions ordered with increasing peak ground acceleration of the fault-normal component.

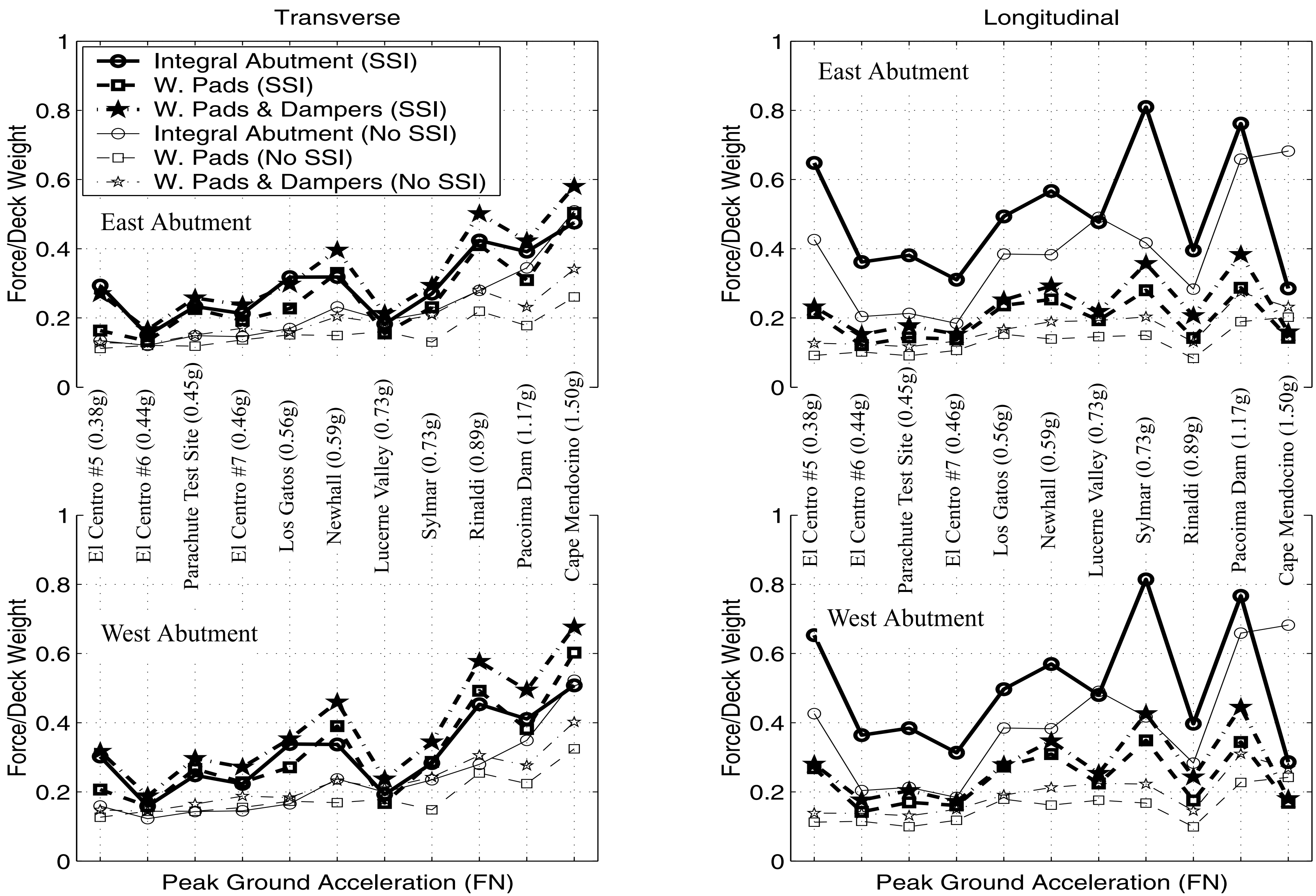

Figure 6.11 Peak forces behind end abutments due to various earthquake motions ordered with increasing peak ground acceleration of the fault-normal component.

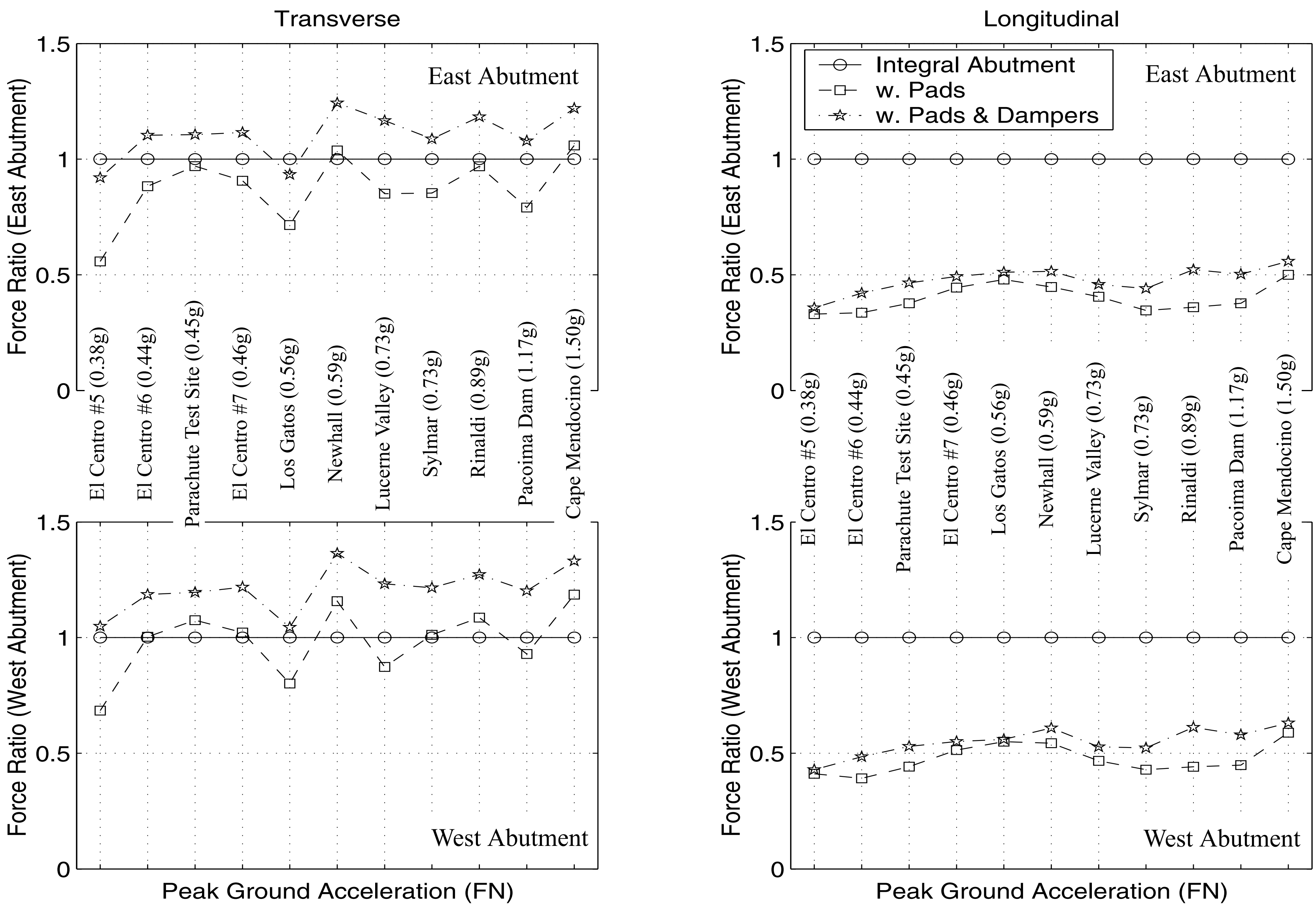

Figure 6.12 Normalized forces behind end abutments and the corresponding forces of bridge with integral abutments due to various earthquake motions ordered with increasing peak ground acceleration of the fault-normal component.

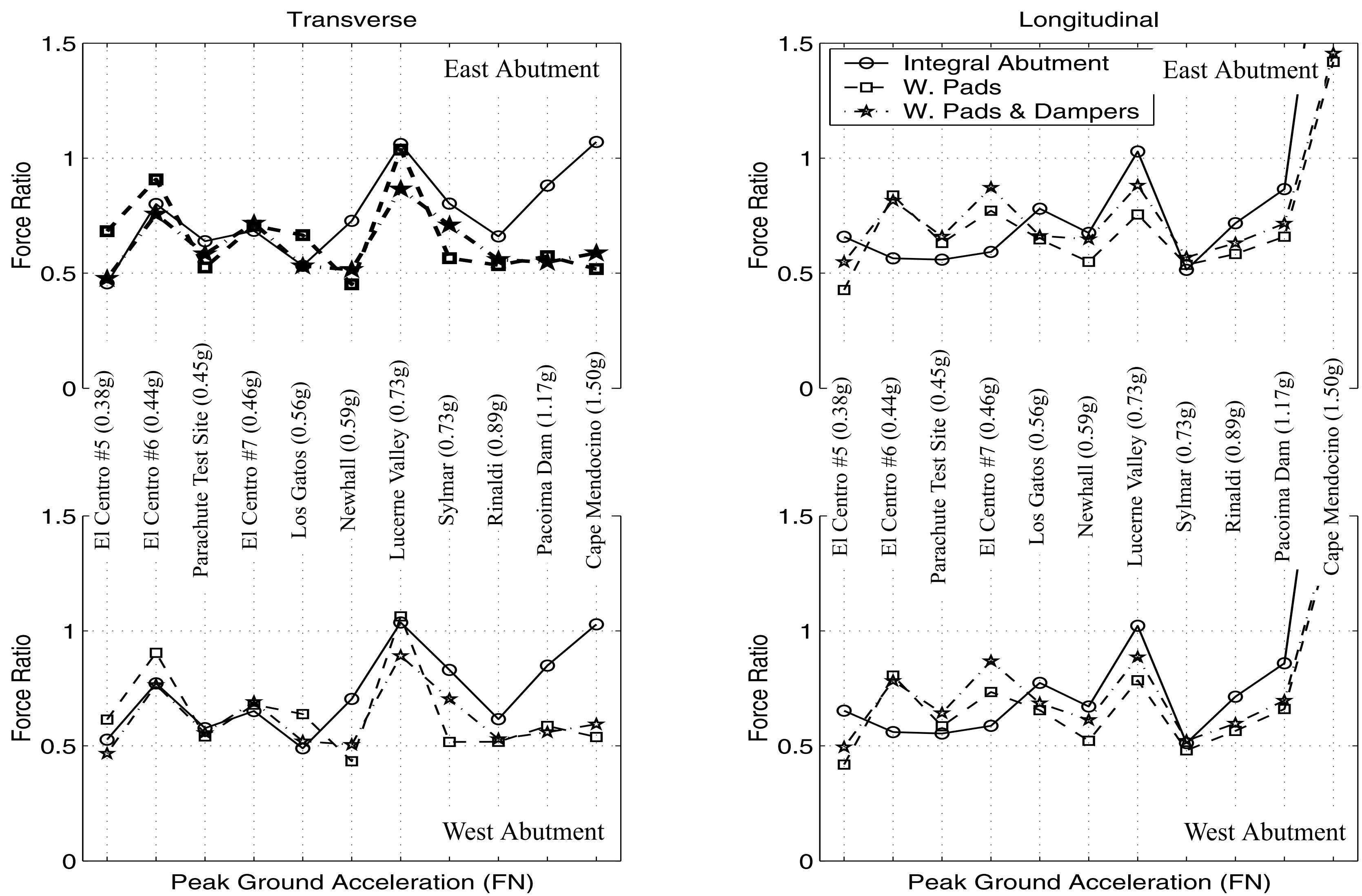

Figure 6.13 Normalized forces behind end abutments computed without soil-structure interaction and the corresponding forces computed with soil-structure interaction due to various earthquake motions ordered with increasing peak ground acceleration of the fault-normal component.

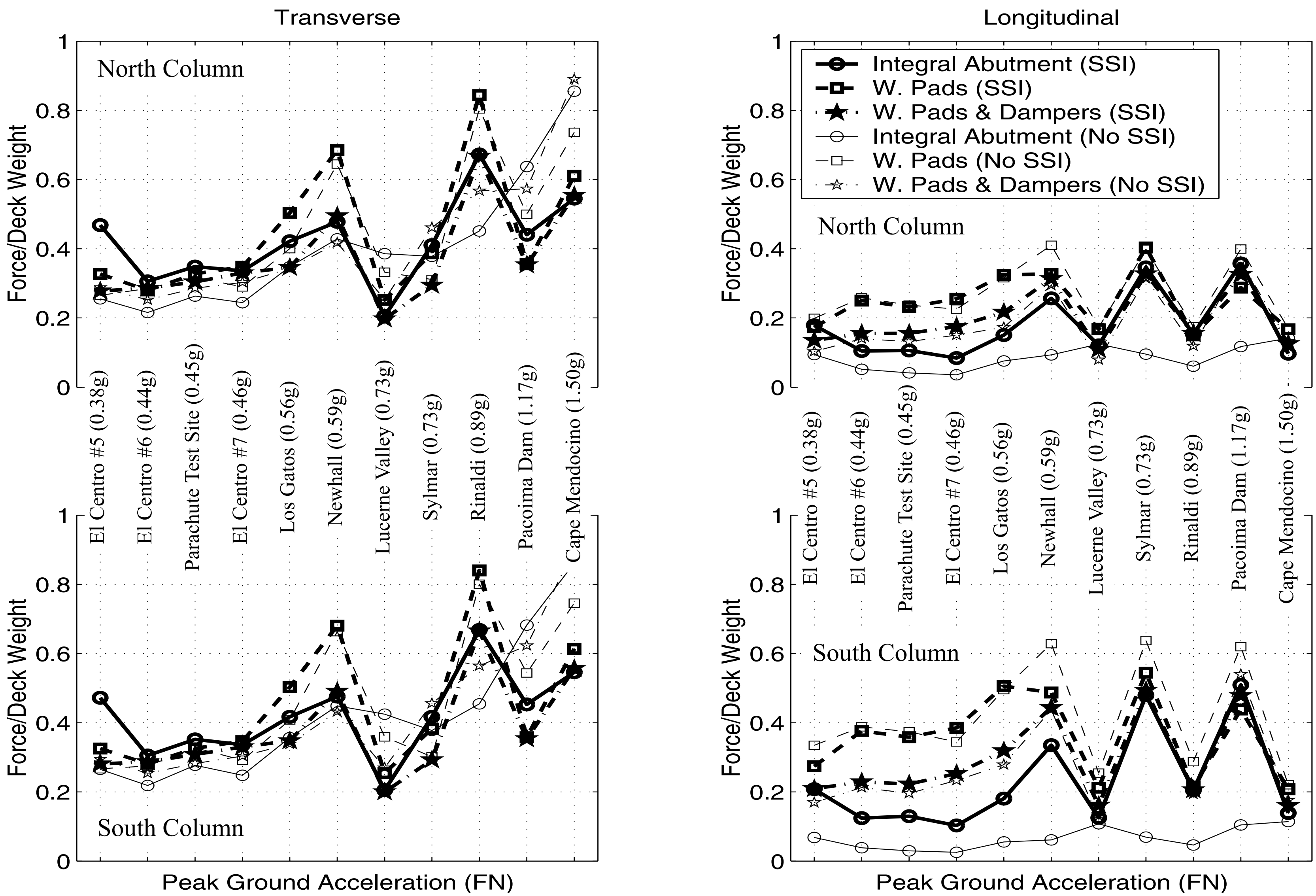

Figure 6.14 Peak forces at bases of center columns due to various earthquake motions ordered with increasing peak ground acceleration of the fault-normal component.

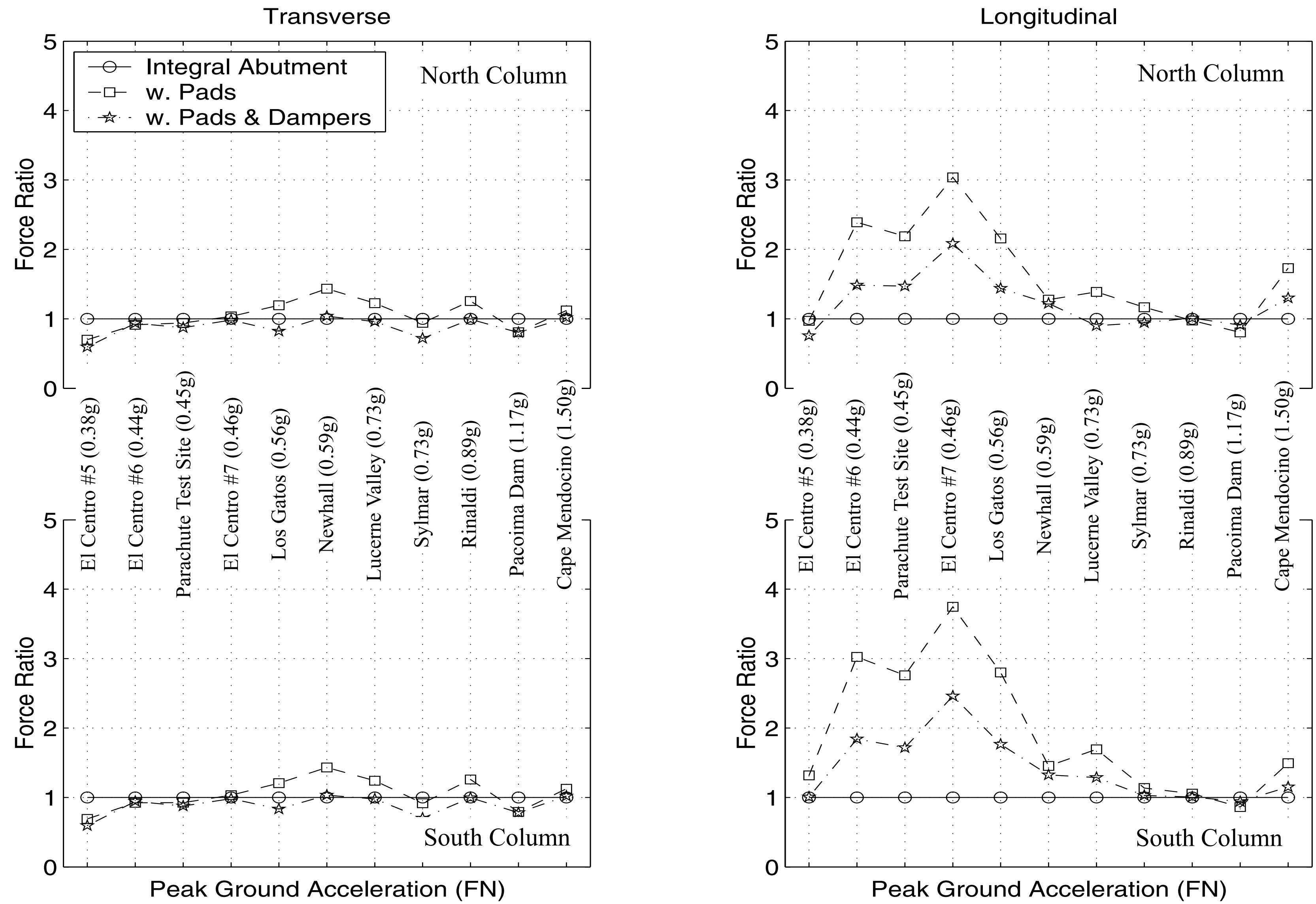

Figure 6.15 Normalized forces at bases of center columns and the corresponding forces of bridge with integral abutments due to various earthquake motions ordered with increasing peak ground acceleration of the fault-normal component.

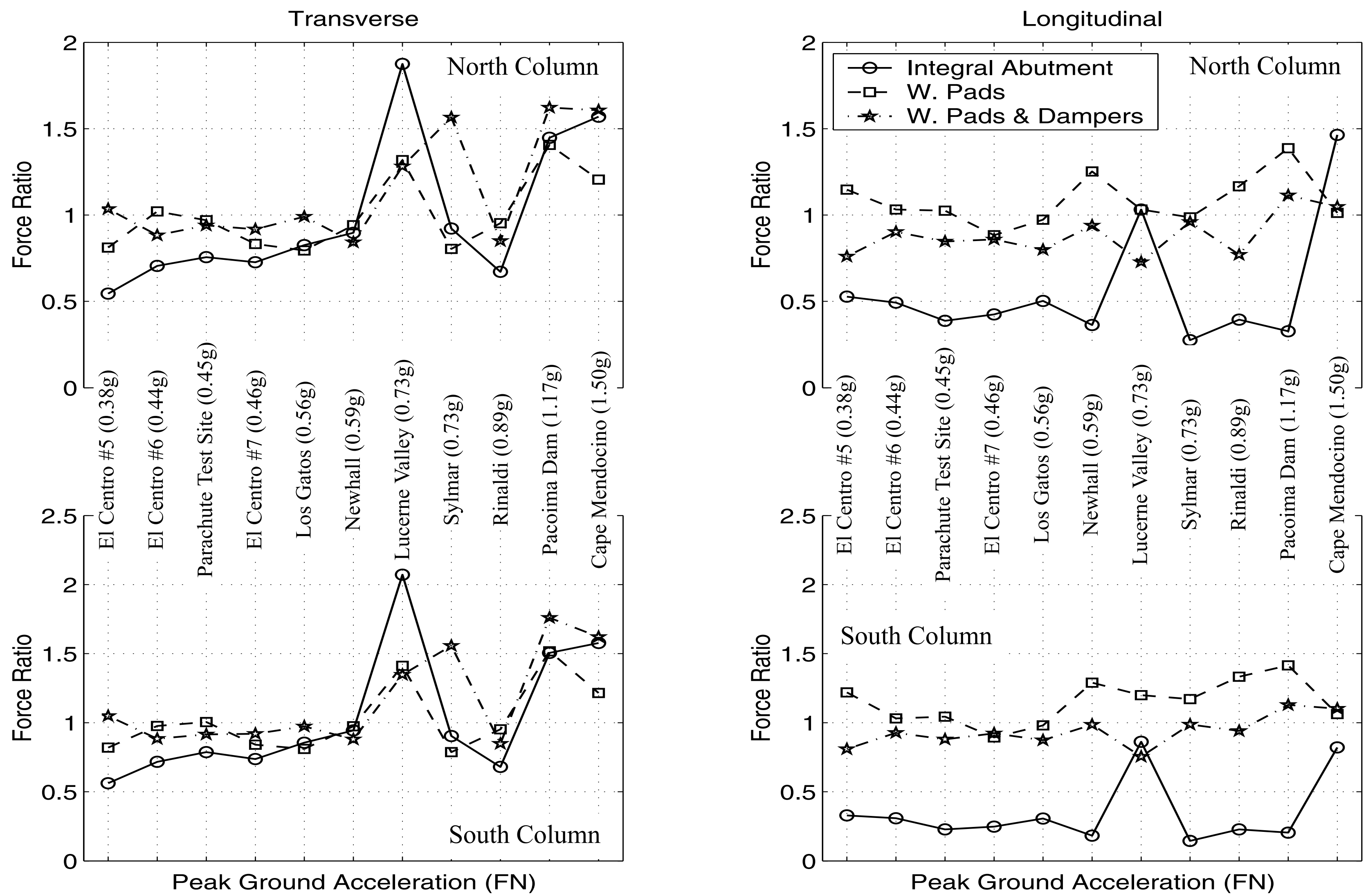

Figure 6.16 Normalized forces at bases of center columns computed without soil-structure interaction and the corresponding forces computed with soil-structure interaction due to various earthquake motions ordered with increasing peak ground acceleration of the fault-normal component.

without soil-structure interaction to the corresponding forces computed with soil-structure interaction. Other than the Lucerne Valley and Cape Mendocino records the base shears of the center columns of the bridge with integral abutments are significantly underestimated when soil-structure interaction is neglected. When the bridge is sitting on elastomeric pads at the deck ends the value of the base shears of the columns is relatively insensitive to the effect of soil-structure interaction.

6.3 APPROXIMATE RESPONSE SPECTRUM ANALYSIS

The eigenvalue analysis of this chapter indicates that the transverse and longitudinal modes of the bridge are well separated while the coupling of the vibrational modes of interest is not strong. Given that in the analysis presented herein the fault-normal excitation is induced along the transverse direction of the bridge while the fault-parallel excitation is induced along the longitudinal direction it is worth examining the results that one obtains for the bridge response using the response spectra offered in Chapter 3 and assuming that along each direction the bridge behaves as a decoupled single-degree-of-freedom (SDOF) oscillator.

Figure 6.17 compares peak total accelerations (top) and peak relative displacements (bottom) at mid-span (point B) of the bridge with sitting abutments computed with the exact time history analysis and the response spectrum analysis using the response spectra shown in Figures 3.12 to 3.22. Along each direction (transverse and longitudinal) the bridge is assumed to be a single-degree-of-freedom (SDOF) oscillator with frequency and damping equal to the modal quantities that were computed for the corresponding mode with the “rigorous” eigenvalue analysis presented in Section 6.1 ($T_x^{sit} = 0.61\ sec$, $\xi_x^{sit} = 20\%$ and $T_y^{sit} = 0.84\ sec$, $\xi_y^{sit} = 46\%$).

Along the transverse (x) direction the decoupled SDOF idealization yields good estimates for the peak accelerations while the displacements are overpredicted in some cases by a factor of two. Along the longitudinal (y) direction the decoupled SDOF idealization underpredicts the peak acceleration but yields good estimates of the peak relative displacements. Figure 6.17 indicates that given the “rigorous” modal values of the bridge for the transverse and longitudinal modes of vibration the decoupled SDOF idealization in association with the response spectrum method gives reasonable estimates of the peak accelerations and peak relative displacements.

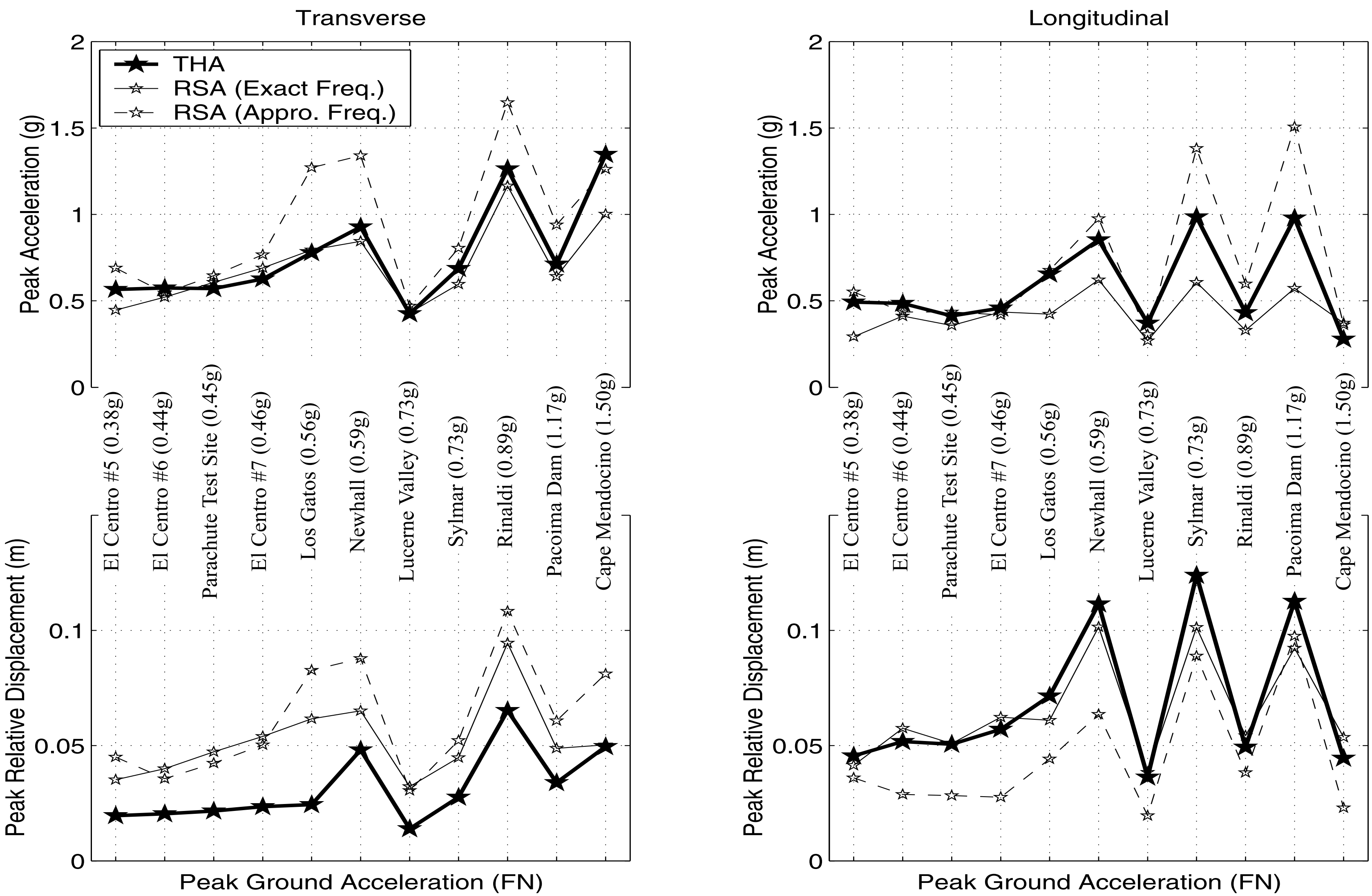

Figure 6.17 Comparison of peak total accelerations (top) and peak relative displacements (bottom) at mid-span (point B) of the bridge with sitting abutments computed with the exact time history analysis and with a SDOF response spectrum analysis. The response spectra for damping ratios, $\xi = 10\%$ and 50% are shown in Figures 3.12 to 3.22.

Nevertheless, the "rigorous" modal values result from the eigenvalue analysis of the 2-D model shown in Figure 6.1 — which is the same model used in the time history analysis.

The relatively good agreement between the 2-D time history analysis and the 1-D response spectrum analysis motivated the investigation of an elementary analysis prediction that assumes that the bridge behaves along the transverse and longitudinal direction as a SDOF oscillator with stiffness equal to the sum of the stiffnesses of the center columns and the stiffnesses of the bearings at the end abutments. This approach ignores the effects of soil-structure interaction. Therefore, the stiffnesses are

$$K_x^{APR} = K_y^{APR} = 2K_x^{COL} + 8K_x^{BRG} = 440\ MN/m \tag{6.2}$$

The mass of the SDOF oscillator is taken to be equal to the mass of the deck ($M^{DCK} \approx 2500\ Mg$) and two times the mass of the abutments ($M^{ABT} \approx 250\ Mg$), i.e., $M^{APR} = M^{DCK} + 2M^{ABT} = 3000\ Mg$. With these values the natural periods along each direction are

$$T_x^{APR} = T_y^{APR} = 2\pi\sqrt{\frac{M^{APR}}{K^{APR}}} = 0.52\ sec \tag{6.3}$$

The damping constants of the SDOF oscillator are

$$C_x^{APR} = C_y^{APR} = 8C^{DMP} + 8C^{BRG} = 9.6\ MN \cdot s/m \tag{6.4}$$

By using that $\xi^{APR} = C^{APR}/(2M^{APR}\omega^{APR})$, the damping ratio along each direction is

$$\xi_x^{APR} = \xi_y^{APR} = 13.2\% \tag{6.5}$$

The dashed line in Figure 6.17 plots the results of the approximate response spectrum analysis using the period value $T_x^{APR} = T_y^{APR} = 0.52\ sec$ and the damping value $\xi_x^{APR} = \xi_y^{APR} = 13.2\%$. The results from the elementary model capture the general trend of the response maxima, but in several occasions are more than 100% off the results from the "rigorous" time history analysis. This comparison illustrates the combined effects of soil-structure interaction and 2-D response.

Figure 6.18 compares peak total accelerations (top) and peak relative displacements (bottom) at mid-span (point B) of the bridge with integral abutments computed with the exact time history analysis and the response spectrum analysis using the response spectra shown in Figures 3.12 to 3.22. Along the transverse direction, the response spectrum analysis yields accurate estimates of the bridge response. However, along the longitudinal direction, the response spectrum analysis yields significantly lower estimates of the bridge response.

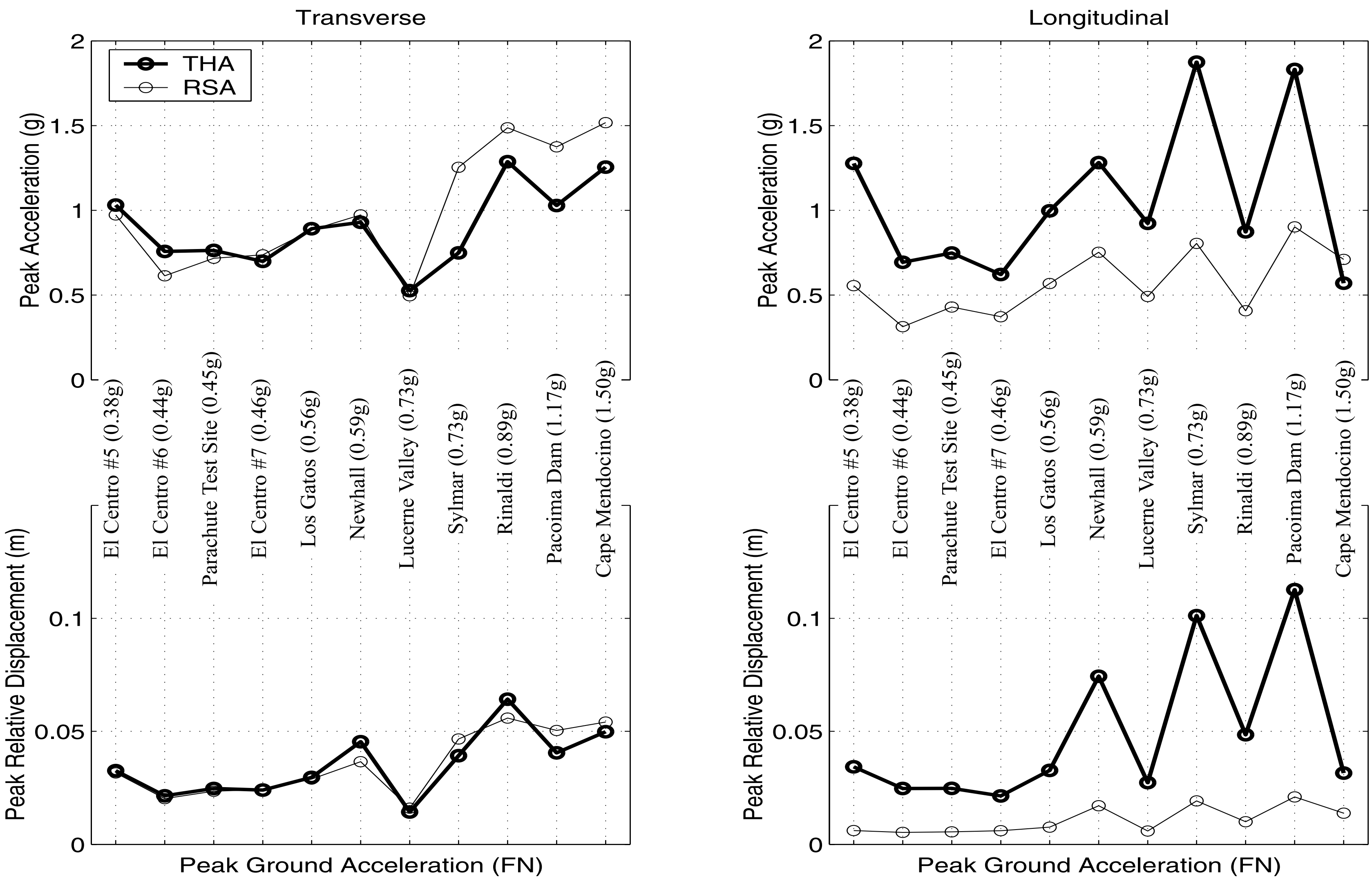

Figure 6.18 Comparison of peak total accelerations (top) and peak relative displacements (bottom) at mid-span (point B) of the bridge with integral abutments computed with the exact time history analysis and with a SDOF response spectrum analysis. The response spectra for damping ratios, $\xi = 10\%$ and 50% , are shown in Figures 3.12 to 3.22.

7 Conclusions

This report presented a case study on the seismic response of a recently constructed highway overcrossing equipped with elastomeric bearings and fluid dampers. The role of this study was to develop a dependable methodology to compute the seismic response of seismically protected bridges accounting for soil-structure interaction and to assess the efficiency of modern technologies in enhancing the response of short bridges. The conclusions of this study are relevant to bridges which are rigidly connected at mid-span to their center bent and supported on elastomeric bearings at the end abutments.

The report first decomposed the bridge into its main substructure elements in an effort to reach a more balanced perspective on the significance of soil-structure interaction together with practical formulas that can be used with a simple stick model to estimate its seismic response. The macroscopic constitutive laws used to describe the behavior of approach embankments, pile foundations, abutments, center columns, elastomeric bearings, and fluid dampers capture satisfactorily the restoring and energy dissipation mechanisms of these substructure elements.

The study presented herein suggests that an equivalent linear viscoelastic analysis can provide valuable estimates on the response of conventional highway overcrossings provided that the significant effects of soil-structure interaction are accounted for (Zhang and Makris 2001, 2002a,b). The nonlinear behavior of protective devices is distinguishable and should be captured with nonlinear time-domain analysis, in particular when the deck experiences large displacements and large velocities.

The seismic response analysis of the bridge is conducted using the substructure method and a reduced-order stick model that have been established elsewhere. Our 2-D nonlinear dynamic analysis revealed distinguishable trends that lead to the following conclusions:

- The first transverse mode of a bridge with integral abutments is a flexural mode, whereas the first transverse mode of a bridge that is supported at the end abutments on bearings is essentially a translational mode.
- The increased mobility of the deck ends due to the seismic protection system results **in** high accelerations which can be suppressed with supplemental damping. The response at the end abutments of a bridge with sitting abutments appears to underperform the response of the same bridge with integral abutments.
- When soil-structure interaction is neglected, the displacements of the bridge with sitting abutments are underestimated, in some cases by a factor of two.
- The longitudinal forces at the backwall are reduced by half when the bridge is on sitting abutments. The presence of elastomeric bearings does not appear to have an effect in reducing backwall forces along the transverse direction. In contrast, the addition of fluid dampers in the bridge with sitting abutments yields transverse forces that exceed the forces transmitted when the bridge has integral abutments.
- When soil-structure interaction is neglected both transverse and longitudinal forces at the backwall are underestimated. In some cases the forces at the backwall when calculated by including the effects of soil-structure interaction can be more than two times larger.
- When the bridge is on sitting abutments, the base shears at the center columns are larger than the corresponding forces of the bridge with integral abutment. This two to three times increase occurs primarily along the longitudinal direction. Despite this considerable increase the center columns of the 91/5 overcrossing remained nearly elastic even under the strongest shaking studied herein.
- When soil-structure interaction is neglected, the base shears of the center columns are in generally significantly underestimated.

In summary the reduced-order stick model in association with concentrated springs and dashpots that represent realistically the behavior of the main substructure elements can generate valuable results on the response of short bridges.

References

AASHTO (1999), *Guide Specifications for Seismic Isolation Design*, American Association of State Highway and Transportation officials.

ABAQUS (1997), *User's Manual V5.7*, Hibbitt, Karlsson & Sorensen, Inc.

ATC-17-1 (1993), *Seminar on Seismic Isolation, Passive Energy Dissipation, and Active Control*, Applied Technology Council, Redwood City, CA.

ATC-17-2 (2002), *Seminar on response modification technologies for performance-based seismic design*, Applied Technology Council, Los Angeles, CA.

Abramowitz, M. and Stegun, I.A. (1970), *Handbook of Mathematical Functions With Formulas, Graphs, and Mathematical Tables*, Dover Publications, Inc., New York, NY.

Aiken, I.D. and Kelly, J.M. (1995), "Prequalification testing of viscous dampers for the Golden Gate Bridge Seismic Rehabilitation Project", *Report No. EERC-STI/95-02*, Earthquake Engineering Research Center, University of California, Berkeley, Richmond, CA.

Bouc, R. (1971), "Modele mathematique d'hysteresis", *Acustica*, 24:16-25.

Caltrans (2002), Personal communication.

Casciati, F. (1989), "Stochastic dynamics of hysteretic media", *Structural Safety*, 6:259-269.

Chang, S.P., Makris, N., Whittaker, A.S., and Thompson, A.C.T. (2002), "Experimental and analytical studies on the performance of hybrid isolation system", *Earthquake Engineering and Structural Dynamics,* 31(2):421-43.

Delis, E.A., Malla, R.B., Madani, M. and Thompson, K.J. (1996), "Energy dissipation devices in bridges using hydraulic dampers", *Proc. Structures Congress XIV,* Chicago, IL, Vol. 2, pp. 188-1196.

Delis, E.A. (2002), Personal communication.

Fabunmi, J.A. (1985), “Extended damping models for vibration data analysis”, *Journal of Sound and Vibration*, 10(2):181-92.

Fan, K., Gazetas, G., Kaynia, A., Kausel, E., and Ahmad, S. (1991), “Kinematic seismic response of single piles and pile groups”, *Journal of Geotechnical Engineering,* ASCE, 117(12):1860-79.

FHWA (1995), Seismic Retrofitting Manual for Highway Bridges, *Publication No. FHWA-RD-94-052*, McLeon, VA.

Gazetas, G. (1984), “Seismic response of endbearing piles”, *Soil Dynamics and Earthquake Engineering,* 3(2):82-93.

Goel, R. K., and Chopra, A. K. (1997), “Evaluation of bridge abutment capacity and stiffness during earthquakes”, *Earthquake Spectra,* 13(1):1-23.

Guin, J. and Banerjee, P.K. (1998), “Coupled soil-pile-structure interaction analysis under seismic excitation”, *J. of Structural Engineering,* 124(4):434-444.

Heuze, F.E., and Swift, R.P. (1991), “Seismic refraction studies at the Painter Street Bridge site, Rio Dell, California”, *Rep. UCRL-ID-108595,* Lawrence Livermore National Laboratory, Oak Ridge, TN.

Imai, T. and Tonouchi, K. (1982), “Correlations among seismic motion, ground conditions and damage: data on the Miyagiken-oki earthquake of 1978”, *Proc. Third International Earthquake Microzonation Conference*, University of Washington, Seattle, WA, Vol. 2, pp. 649-660.

Jacobsen, L.S. (1930), “Steady forced vibration as influenced by damping”, *Trans. A.S.M.E.*, APM-52-15:169-81.

Kaynia, A..M., and Novak, M. (1992),“Response of pile foundations to Rayleigh waves and to obliquely incident body waves”, *Earthquake Engineering and Structural Dynamics*, 21(4):115-32.

Kramer, S.L. (1996), *Geotechnical Earthquake Engineering*, Prentice Hall, Upper Saddle River, NJ.

Lehman, D.E. (1998), “Seismic performance of well-confined concrete bridge columns”, Ph.D Dissertation, University of California, Berkeley, CA.

Lin, W.-H. and Chopra, A. (2001), “Understanding and predicting effects of supplemental viscous damping on seismic response of asymmetric one-storey systems”, *Earthquake Engineering and Structural Dynamics*, 30(10):1475-94.

Makris, N. (1994), “Soil-pile interaction during the passage of Rayleigh waves: an analytical solution”, *Earthquake Engineering and Structural Dynamics,* 23(2):153-67.

Makris, N. (1997), “Causal Hysteretic Element”, *J. of Engineering Mechanics*, ASCE, 123(11):1209-14.

Makris, N. and Gazetas, G. (1992),“Dynamic pile-soil-pile interaction Part II: Lateral and seismic response”, *Earthquake Engineering and Structural Dynamics*, 21(2):145-62.

Makris, N., and Badoni, D. (1995), “Seismic response of pile-groups during the passage of oblique-shear and Rayleigh waves”, *Earthquake Engineering and Structural Dynamics,* 24(4):517-32.

Makris, N. and Chang, S.P. (1998), “Effect of damping mechanisms on the response of seismic isolated structures”, *Report No. PEER-98/06*, University of California, Berkeley, CA.

Makris, N. and Chang, S.P. (2000), “Response of damped oscillators to cycloidal pulses”, *J. of Engineering Mechanics*, 126(2):123-31.

Makris, N. and Chang, S.P. (2000), “Effect of viscous, viscoplastic and friction damping on the response of seismic isolated structures”, *Earthquake Engineering and Structural Dynamics*, 29(1):86-107.

Makris, N. and Roussos, Y.S. (2000), “Rocking response of rigid blocks under near-source ground motions”, *Geotechnique*, L(3):243-62.

Makris, N. and Zhang, J. (1999), “Rocking response and overturning of anchored equipment under seismic excitation”, *Report No. PEER-99/06*, University of California, Berkeley, CA.

Makris, N., Badoni, D., Delis, E. and Gazetas, G. (1994),“Prediction of observed bridge response with soil-pile-structure interaction”, *Journal of Structural Engineering*, 120(10):2992-3011.

Mamoon, S.M., and Banerjee, P.K. (1990), “Response of piles and pile groups to travelling SH-waves”, *Earthquake Engineering and Structural Dynamics,* 19(4):579-610.

McCallen, D.B., and Romstad, K.M. (1994), “Analysis of a skewed short-span, box-girder overpass”, *Earthquake Spectra,* 10(4):729-55.

McKenna, F.T. (1997), “Object-oriented finite element programming: frameworks for analysis, algorithms and parallel computing”, Ph.D Dissertation, University of California, Berkeley, CA.

Nagarajaiah, S., Reinhorn, A.M., and Constantinou, M. (1990), “Analytical modeling of three-dimensional behavior of base isolation devices”, *Proc. Fourth U.S. National Conference on Earthquake Engineering, Proceedings*, Vol. 3, pp. 579-588, Earthquake Engineering Research Institute, El Cerrito, CA.

Pekcan, G., Mander, J.B., and Chen, S.S. (1999), “Fundamental considerations for the design of non-linear viscous dampers”, *Earthquake Engineering and Structural Dynamics*, 28(11):1405-25.

Papanikolas, P.K. (2002), “Deck superstructure and cable stays of the Rion-Antirion bridge”, *Proc. 4th National Conference on Steel Structures,* Patros, Greece.

Priestley, M. J. N., Seible, F., and Calvi, G. M. (1996), *Seismic Design and Retrofit of Bridges*, John Wiley, New York, NY.

Seed, H.B., Wong, R.T., Idriss, I.M., Tokimatsu, K. (1986), “Moduli and damping factors for dynamic analyses of cohesionless soils”, *J. of Geotechnical Engineering*, 112(11):1016-32.

Seed, H.B., Idriss, I.M. (1969), “Influence of soil conditions on motions during earthquakes, “ *J. Soil Mechanics and Foundations,* ASCE 1969, 95:(SMI): 99-137.

Simo, J.C. and Hughes, T.J.R. (1998), *Computational Inelasticity*, Springer, New York, NY.

Skinner, R.I., Robinson, W.H., and McVerry, G.H. (1993), *An introduction to seismic isolation*, John Wiley & Sons, Chichester, U. K. and New York, NY.

Symans, M.D. and Constantinou, M.C. (1998), “Passive fluid viscous damping systems for seismic energy dissipation”, ISET Journal of Earthquake Technology, 35(4):185-206.

Symth A.W., Masri, A.F., Abdel-Ghaffar, A.M., and Nigbor, R.N. (2000), “Development of a nonlinear multi-input.multi-output model for the Vincent Thomas Bridge under earthquake excitations”, *Proc. 12th World Conference on Earthquake Engineering,* Paper No. 2211, Upper Hutt, New Zealand.

Tajimi, H. (1977), “Seismic effects on piles, state-of-the-art report No.2”, *Int. Conf. Soil Mech. Found. Engrg.,* Proc. Specialty Session 10, pp. 15-27.

Tsopelas, P. (1994), “Testing and modeling of a class of bridge seismic isolation systems”, Ph.D Dissertation, State University of New York at Buffalo, NY.

Wen, Y.K. (1975), “Approximate method for nonlinear random vibration”, *Journal of Engineering Mechanics*, ASCE, 101(EM4):389-401.

Wen, Y.K. (1976), “Method for random vibration of hysteretic systems”, *Journal of Engineering Mechanics*, ASCE, 102(EM2):249-63.

Werner, S. D., Beck, J. L., and Levine, M. B. (1987), “Seismic response evaluation of Meloland road overpass using 1979 Imperial valley earthquake records”, *Earthquake Engineering and Structural Dynamics,* 15(2):249-74.

Wilson, J.C., and Tan, B.S. (1990), “Bridge abutments: formulation of simple model for earthquake response analysis”, *Journal of Engineering Mechanics,* 116(8):,1828-37.

Zhang, J. and Makris, N. (2000), “Seismic protection of highway overcrossings using modern technologies”, *Proc. Bridge Engineering Conference*, Sharm El-Sheikh, Egypt.

Zhang, J. and Makris, N. (2001), “Seismic response analysis of highway overcrossings including soil-structure interaction”, *Report No. PEER-01/02*, University of California, Berkeley, CA.

Zhang, J. and Makris, N. (2002a), “Kinematic response functions and dynamic stiffnesses of bridge embankments”, *Earthquake Engineering and Structural Dynamics*, 31:1933-66.

Zhang, J. and Makris, N. (2002b), “Seismic response analysis of highway overcrossings including soil-structure interaction”, *Earthquake Engineering and Structural Dynamics*, 31:1967-91.

Appendix

The maximum values presented in Figures 6.3 to 6.16 were obtained from a nonlinear time history analysis. Figures A.1 to A.9 present the corresponding time histories and bidirectional signatures of the response computed for the Pacoima Dam ground motions recorded during the 1971 San Fernando earthquake when soil-structure interaction is included. Figures A.10 to A.18 present the corresponding time histories and bidirectional signatures of the response computed for the Pacoima Dam records of the 1971 San Fernando earthquake when soil-structure interaction is neglected. Similarly, Figures A.19 to A.36 present the corresponding time histories and bidirectional signatures of the response computed for the Newhall records of the 1994 Northridge earthquake.

The overall bridge response was discussed in Chapter 6. The focus of interest in this appendix is the behavior of the seismic protection elements. As an example Figure A.8 shows the computed displacement and force signatures of the elastomeric bearings when the bridge is subjected to the Pacoima Dam records. When the bearings reach their yield force, F^Y, the plasticity model reaches the yield surface. The second row of plots in Figure A.8 indicates that when the bridge rests on pads only (no dampers), the yield surface is reached very often and most of the yield locus is generated. The last row of plots in Figure A.8 indicates that when in addition to pads, dampers are also added, the displacements are substantially suppressed in all directions and the yield surface is reached only occasionally. The same trend is observed in Figures A.17, A.26, and A.35.

Figures A.9, A.18, A.27, and A.36 plot the force-displacement loops of the nonlinear fluid dampers as they engage under seismic excitation. The maximum computed displacement, u_{max}, approaches 0.15 m (6.0 in). It is worth mentioning that the stroke capacity of the dampers installed at the 91/5 overcrossing is $u_{max} = \pm 8.0\ in$, which offers a safety factor $SF = \frac{8.0}{6.0} = \frac{4}{3}$

under the strongest earthquake motions considered in this study. This finding is credited to Caltrans engineers.

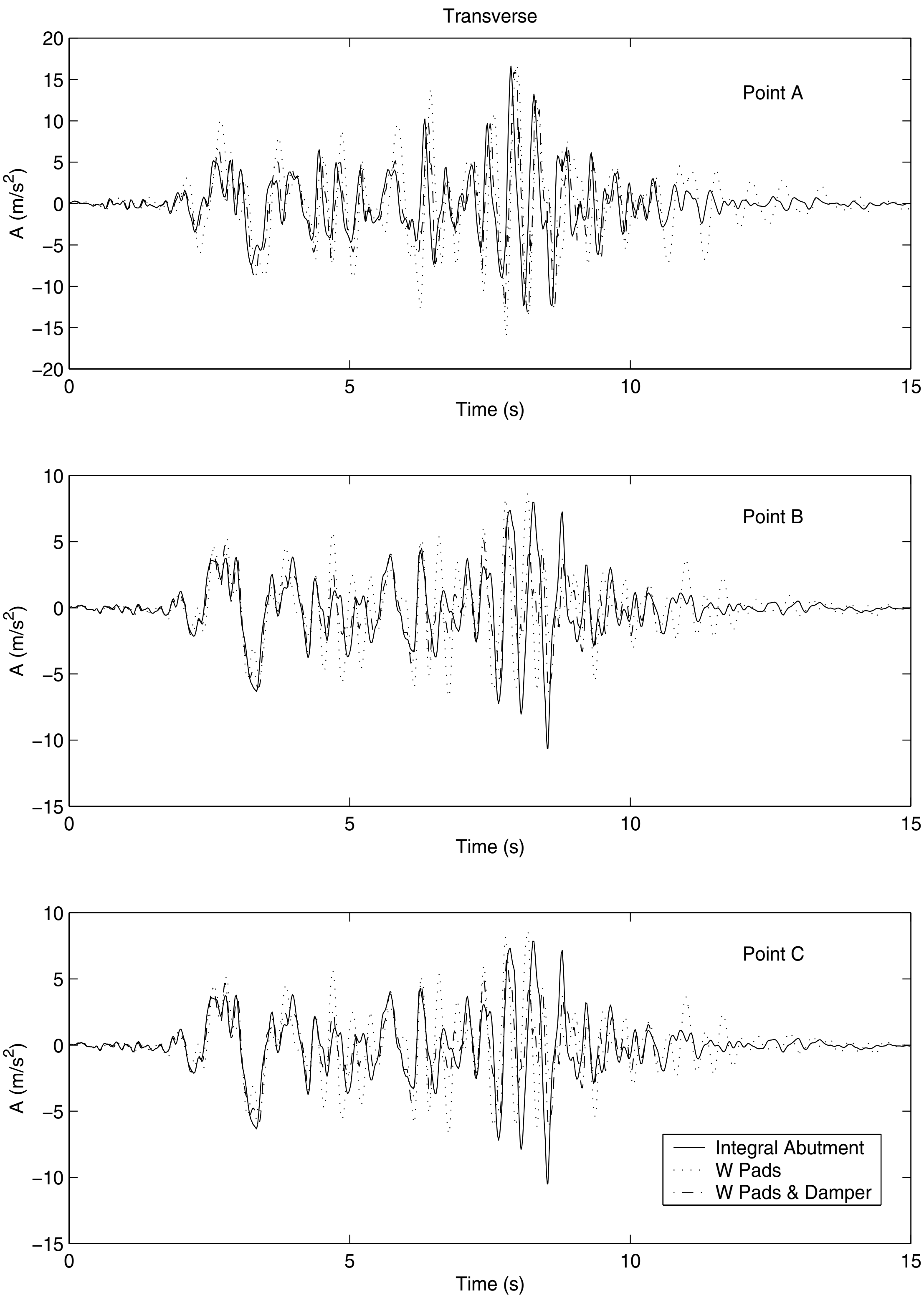

Figure A.1 Transverse acceleration time histories at various locations along bridge subjected to Pacoima Dam records from 1971 San Fernando, California, earthquake. Soil-structure interaction is included.

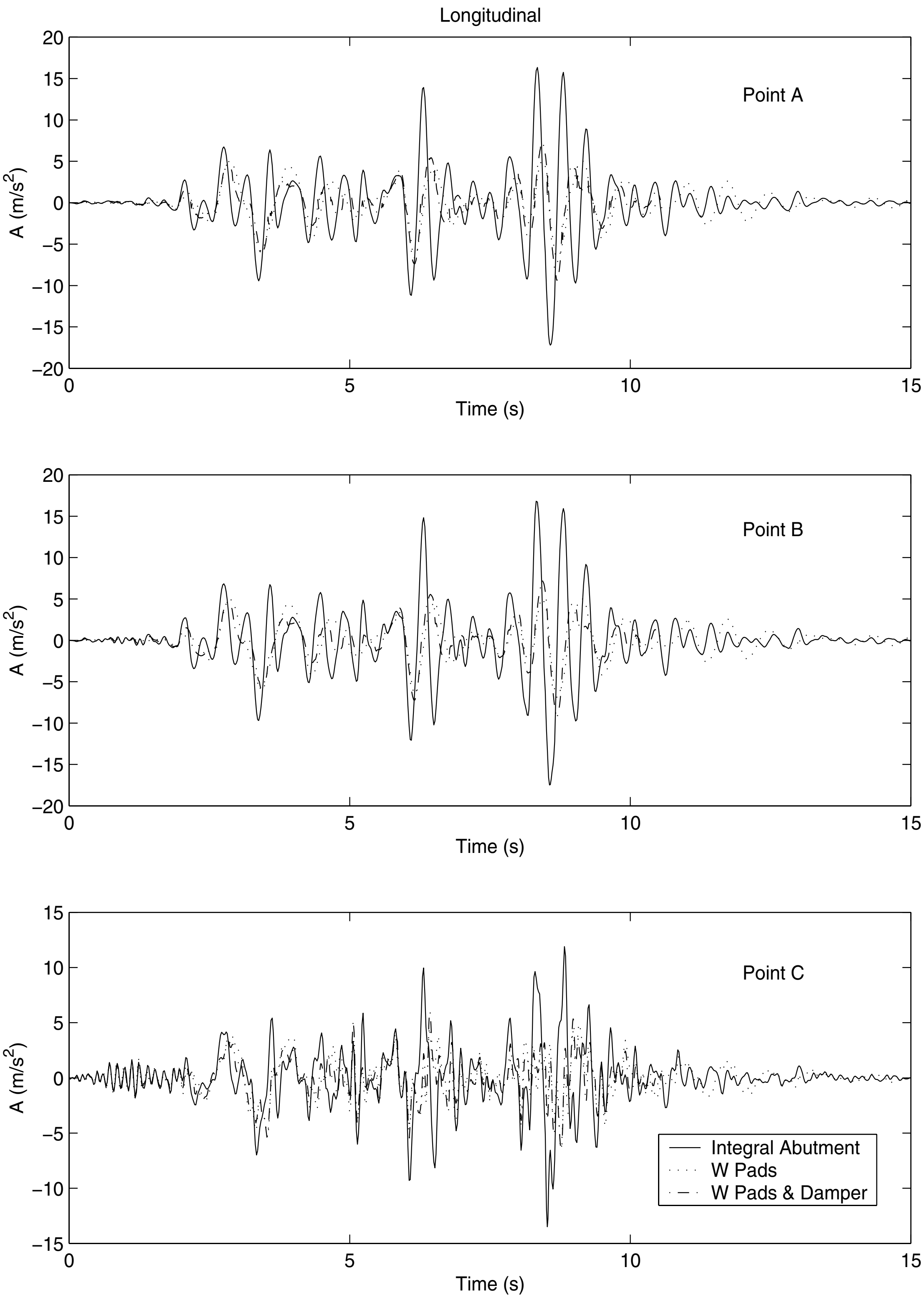

Figure A.2 Longitudinal acceleration time histories at various locations along bridge subjected to Pacoima Dam records from 1971 San Fernando, California, earthquake. Soil-structure interaction is included.

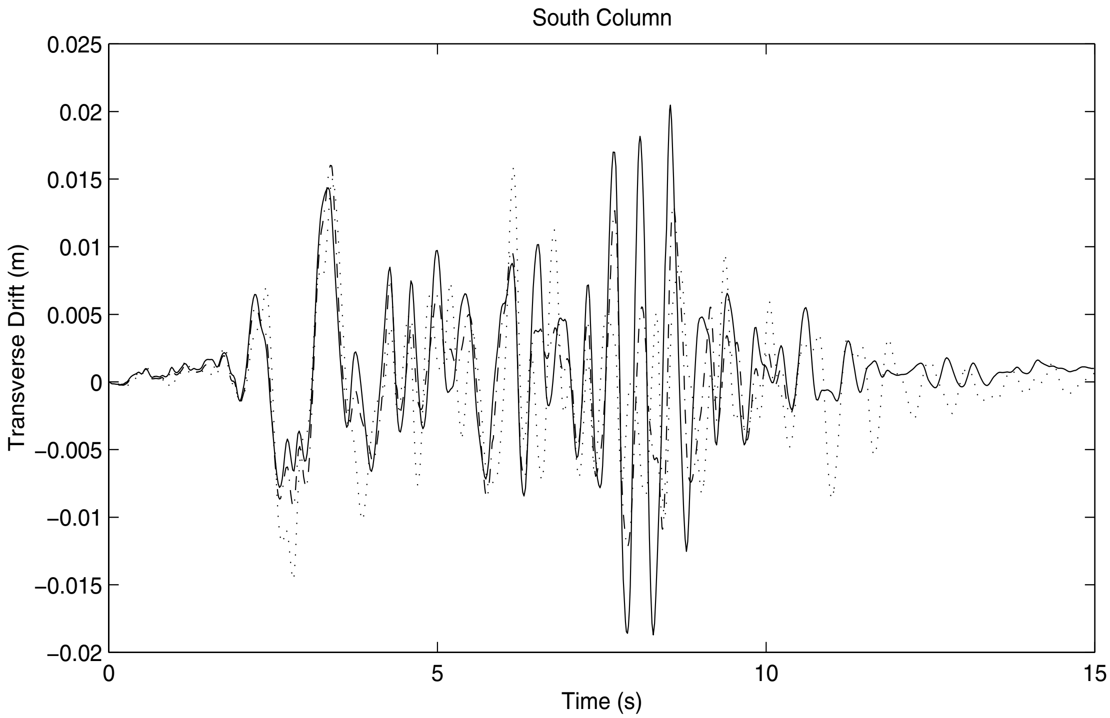

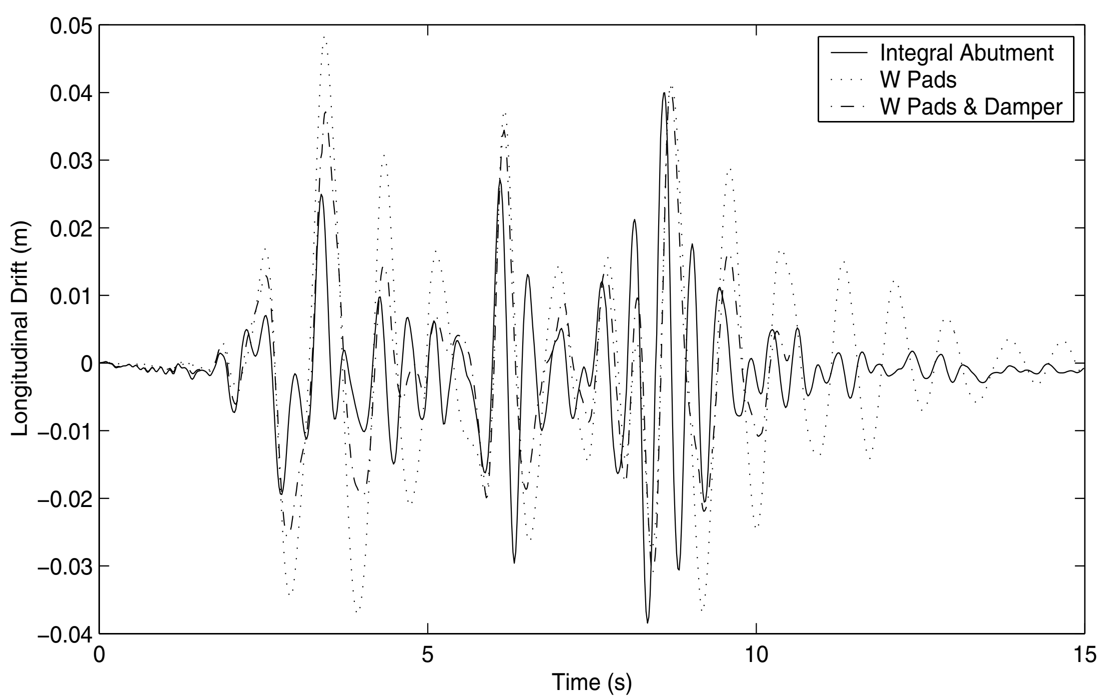

Figure A.3 Drift time histories of south column of 91/5 bridge subjected to Pacoima Dam records from 1971 San Fernando, California, earthquake. Soil-structure interaction is included.

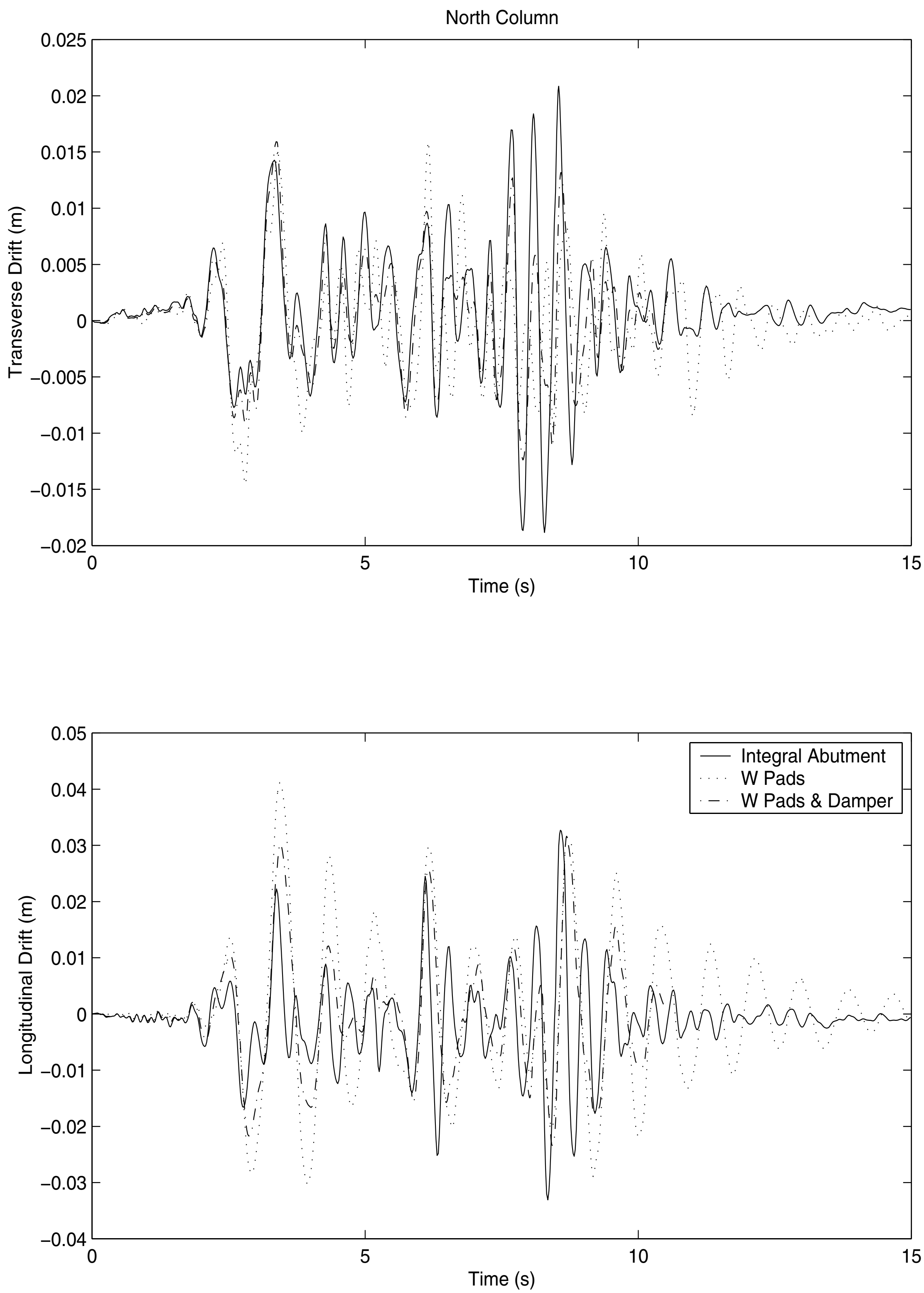

Figure A.4 Drift time histories of north column of 91/5 bridge subjected to Pacoima Dam records from 1971 San Fernando, California, earthquake. Soil-structure interaction is included.

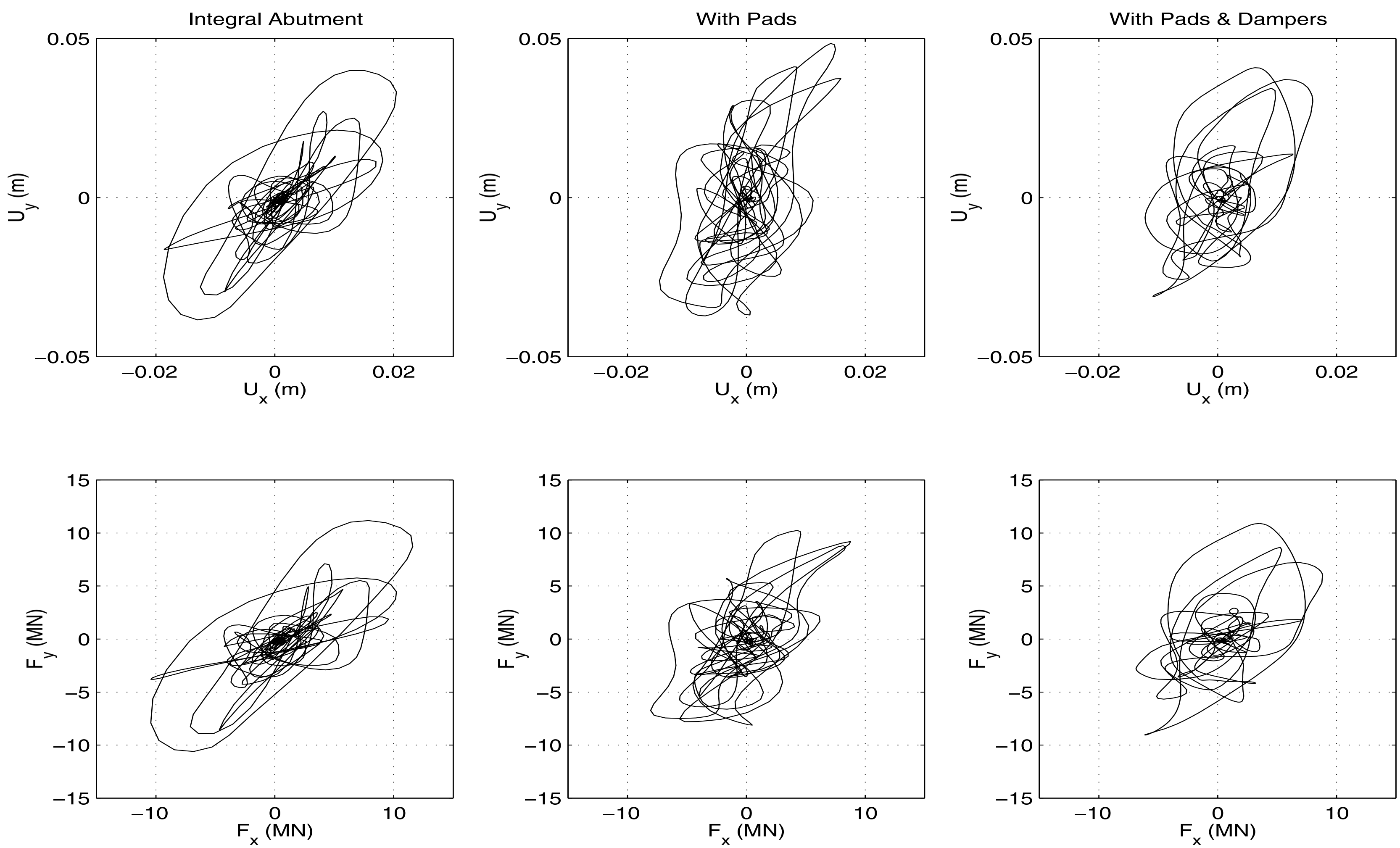

Figure A.5 Displacement and force signatures of south column of 91/5 bridge subjected to Pacoima Dam records from 1971 San Fernando, California, earthquake. Soil-structure interaction is included.

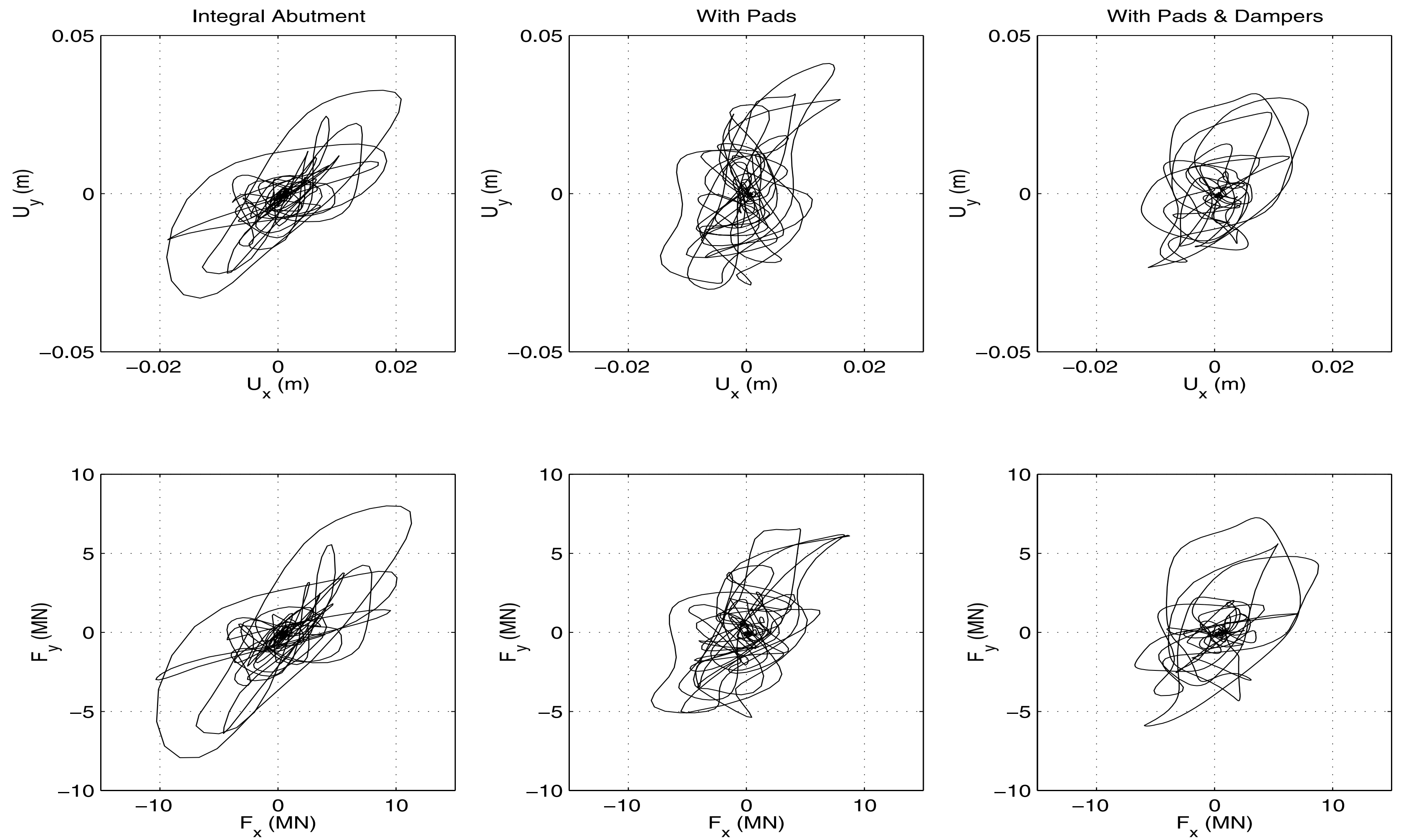

Figure A.6 Displacement and force signatures of the north column of 91/5 bridge subjected to the Pacoima Dam records from the 1971 San Fernando, California, earthquake. Soil-structure interaction is included.

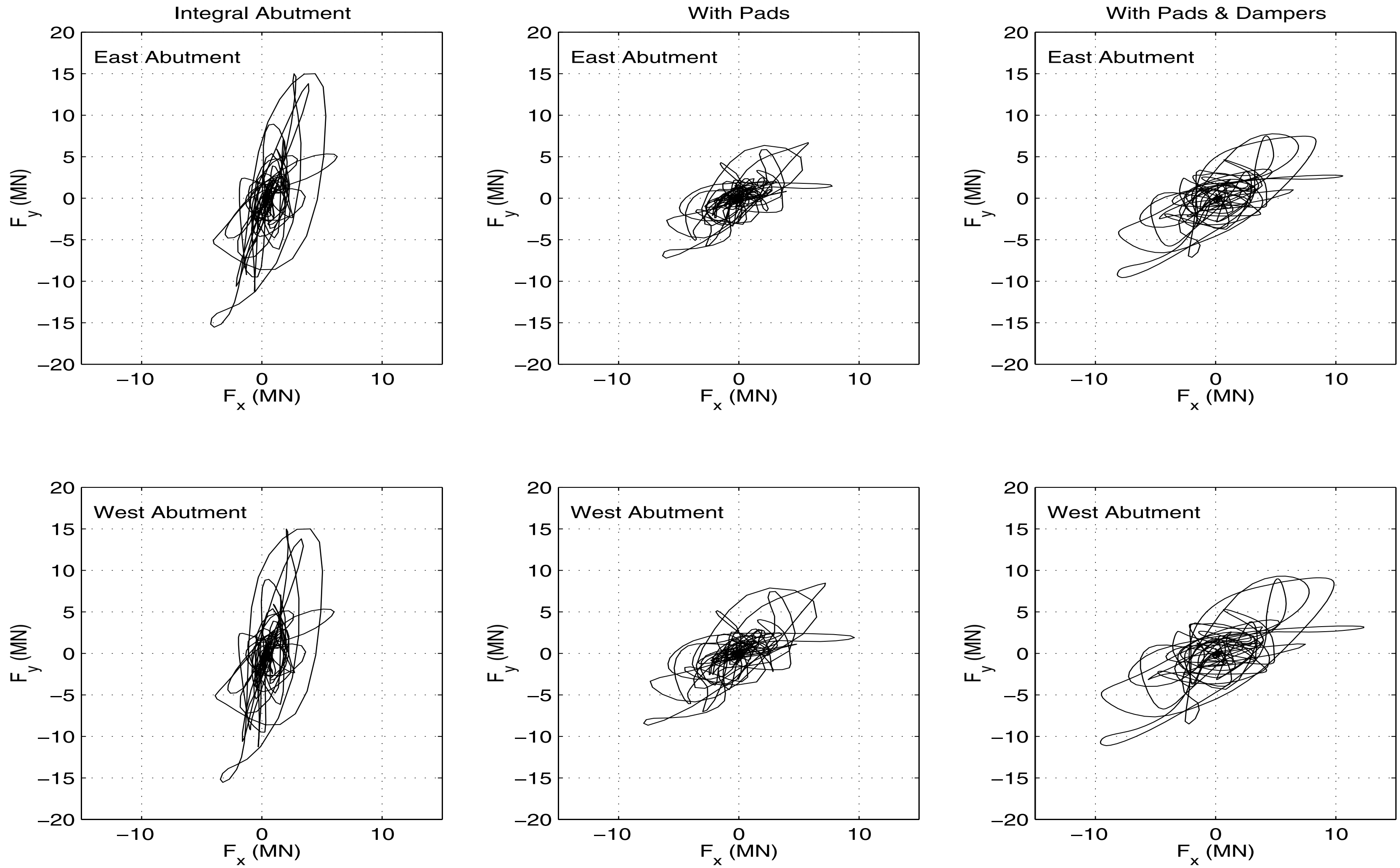

Figure A.7 Displacement and force signatures of end abutments of 91/5 bridge subjected to Pacoima Dam records from the 1971 San Fernando, California, earthquake. Soil-structure interaction is included.

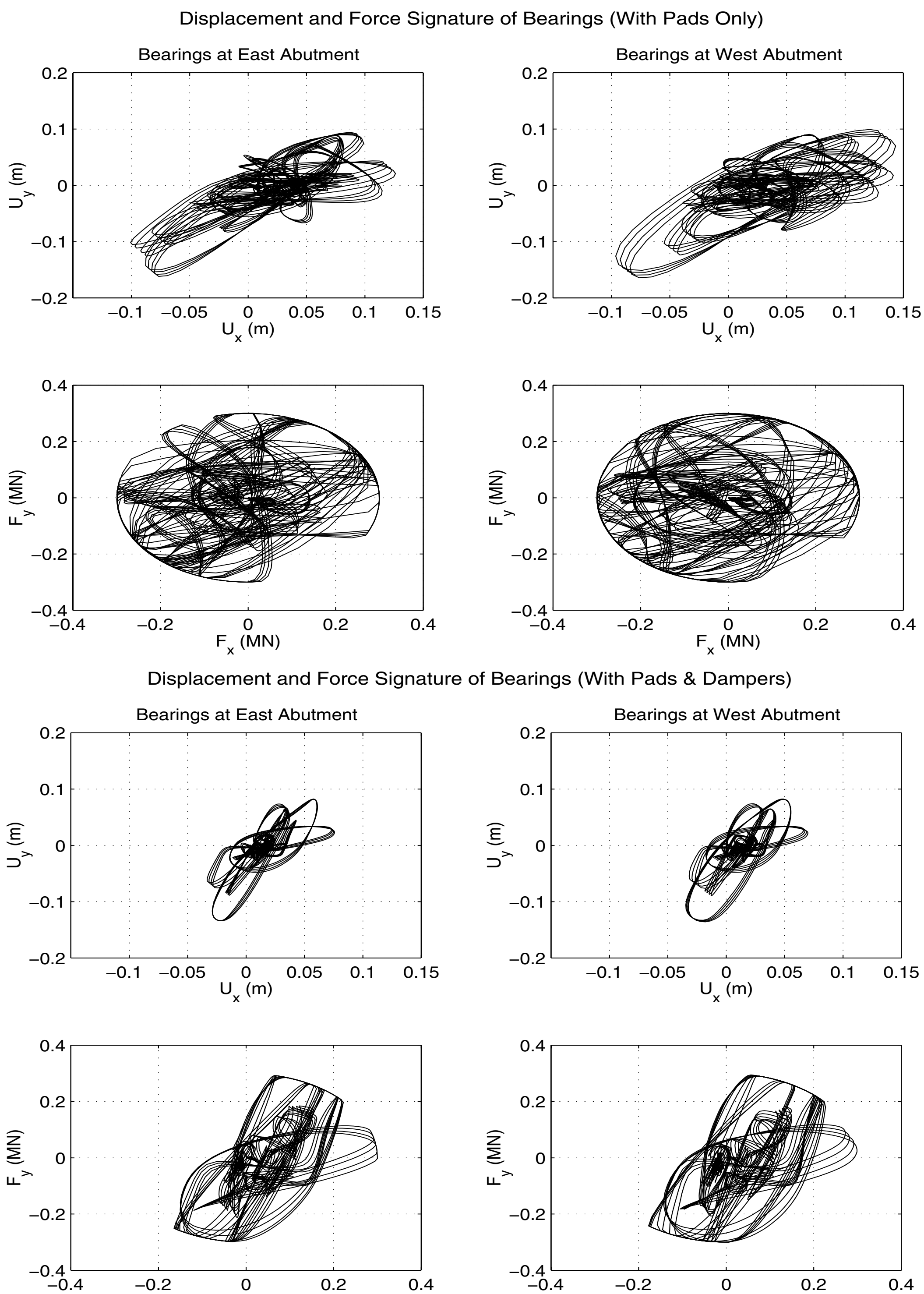

Figure A.8 Displacement and force signatures of elastomeric bearings of 91/5 bridge subjected to Pacoima Dam records from 1971 San Fernando, California, earthquake. Soil-structure interaction is included. Top: with pads only; bottom: with pads and dampers.

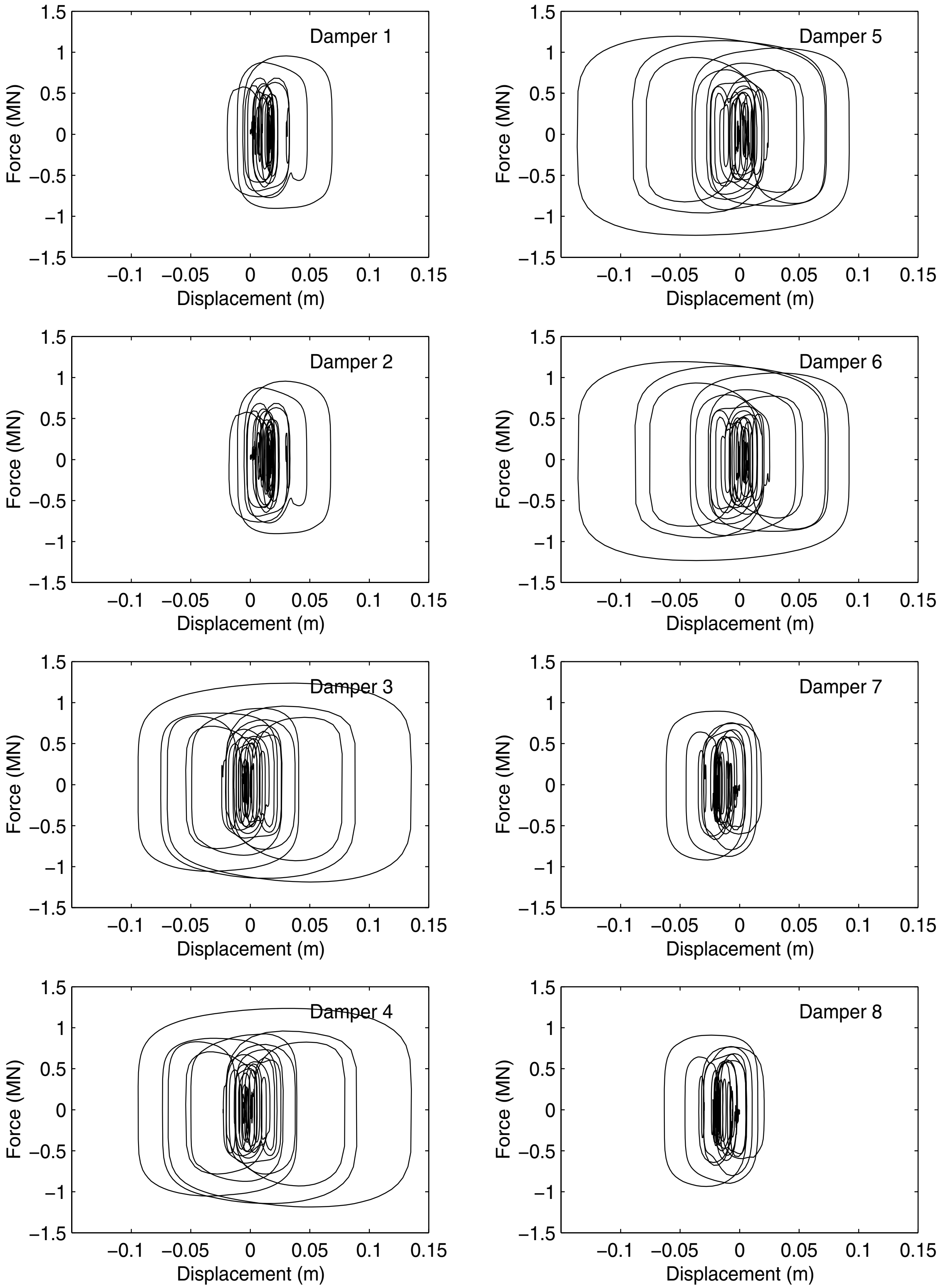

Figure A.9 Force-displacement loops of nonlinear fluid dampers subjected to Pacoima Dam records from the 1971 San Fernando, California, earthquake. Soil-structure interaction is included.

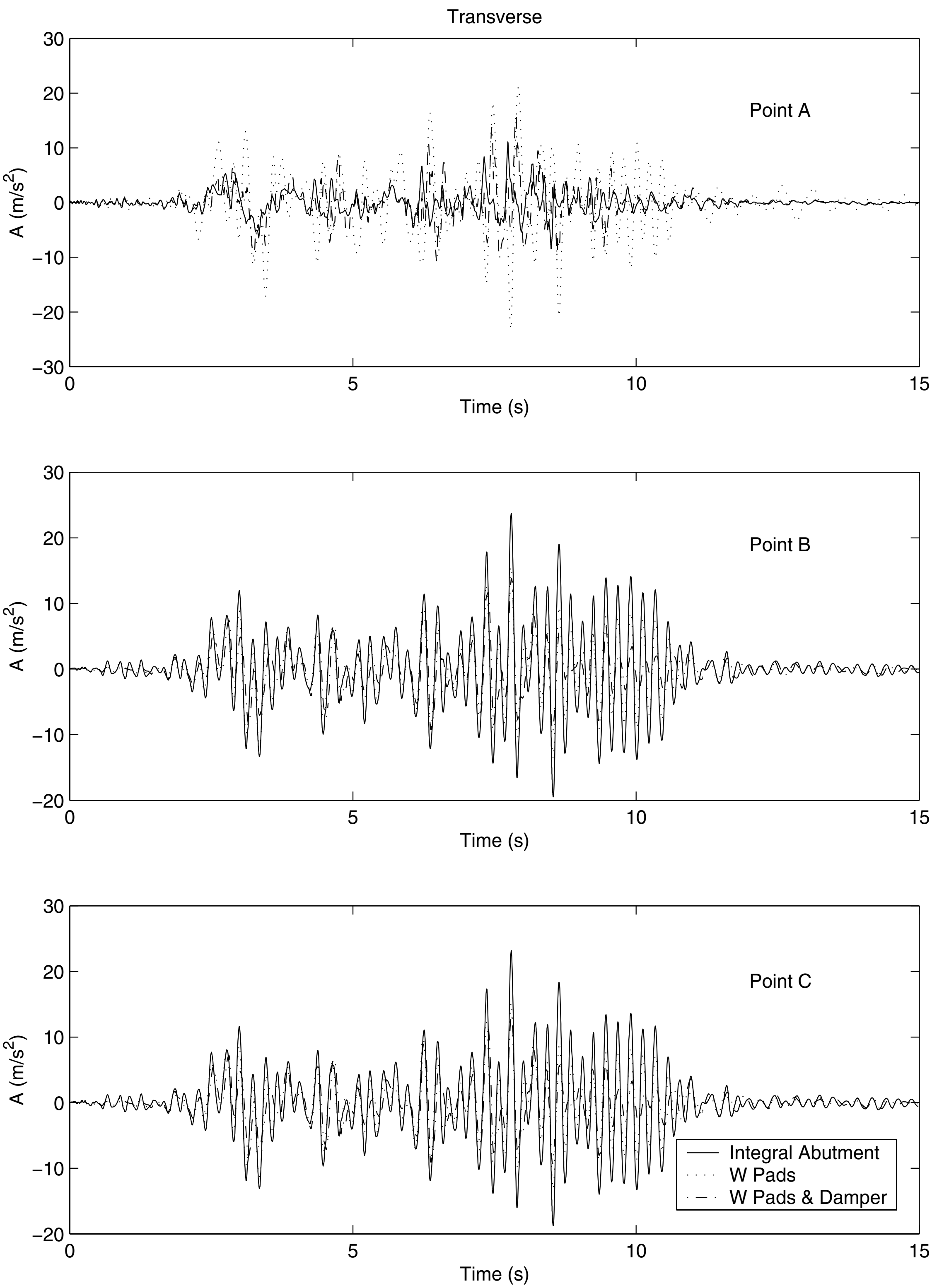

Figure A.10 Transverse acceleration time histories at various locations along bridge subjected to Pacoima Dam records from 1971 San Fernando, California, earthquake. Soil-structure interaction is neglected.

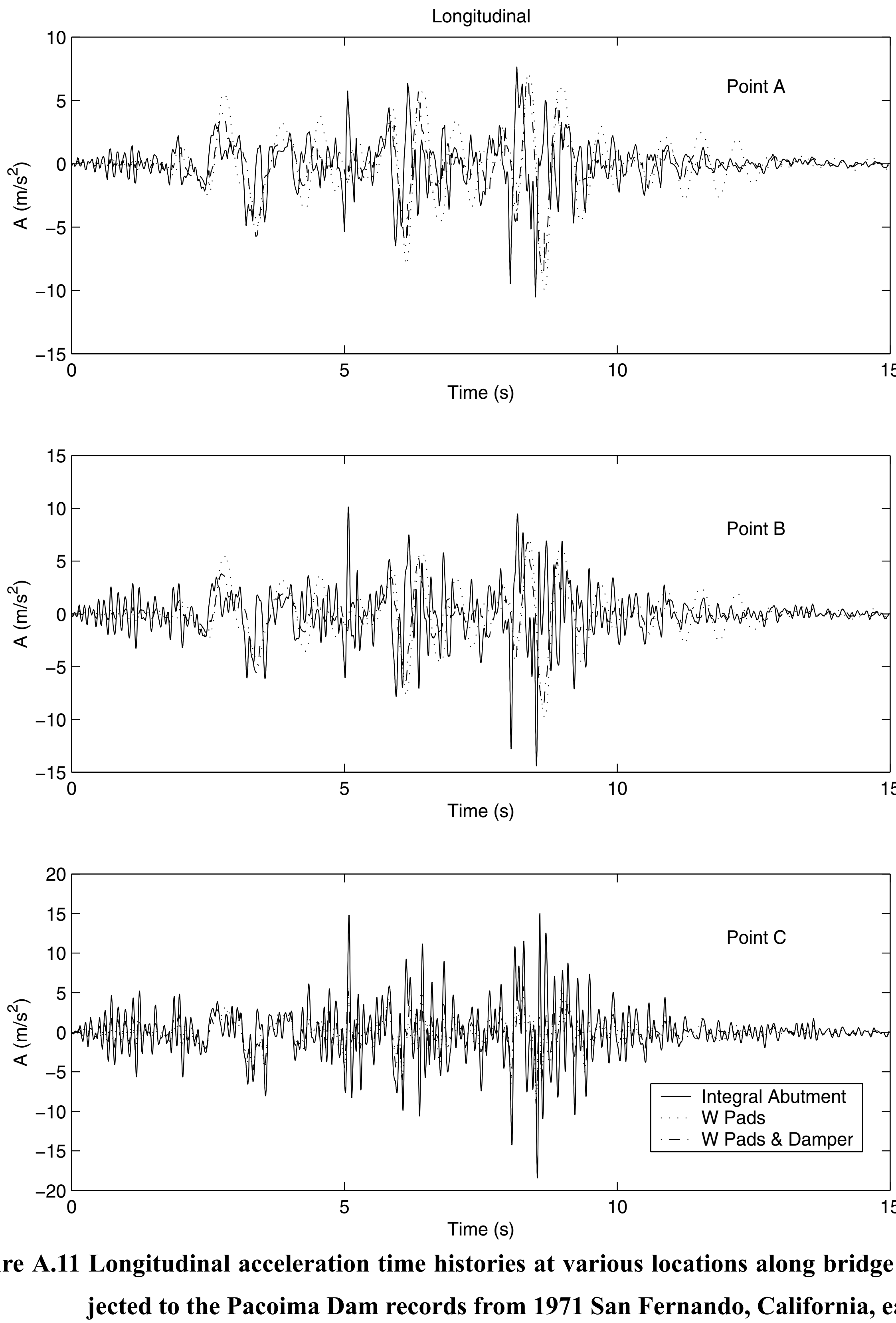

Figure A.11 Longitudinal acceleration time histories at various locations along bridge subjected to the Pacoima Dam records from 1971 San Fernando, California, earthquake. Soil-structure interaction is neglected.

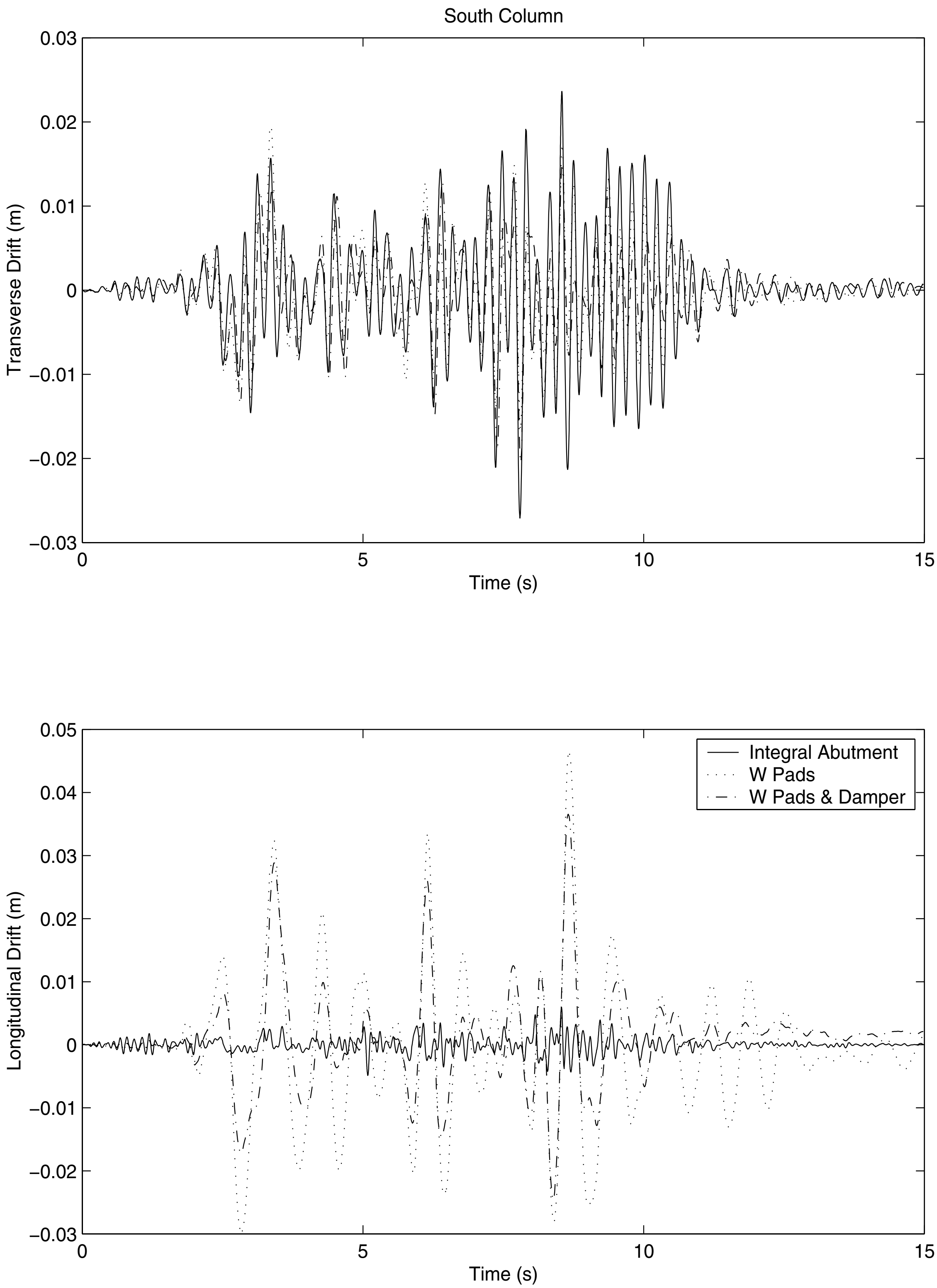

Figure A.12 Drift time histories of south column of 91/5 bridge subjected to Pacoima Dam records from 1971 San Fernando, California, earthquake. Soil-structure interaction is neglected.

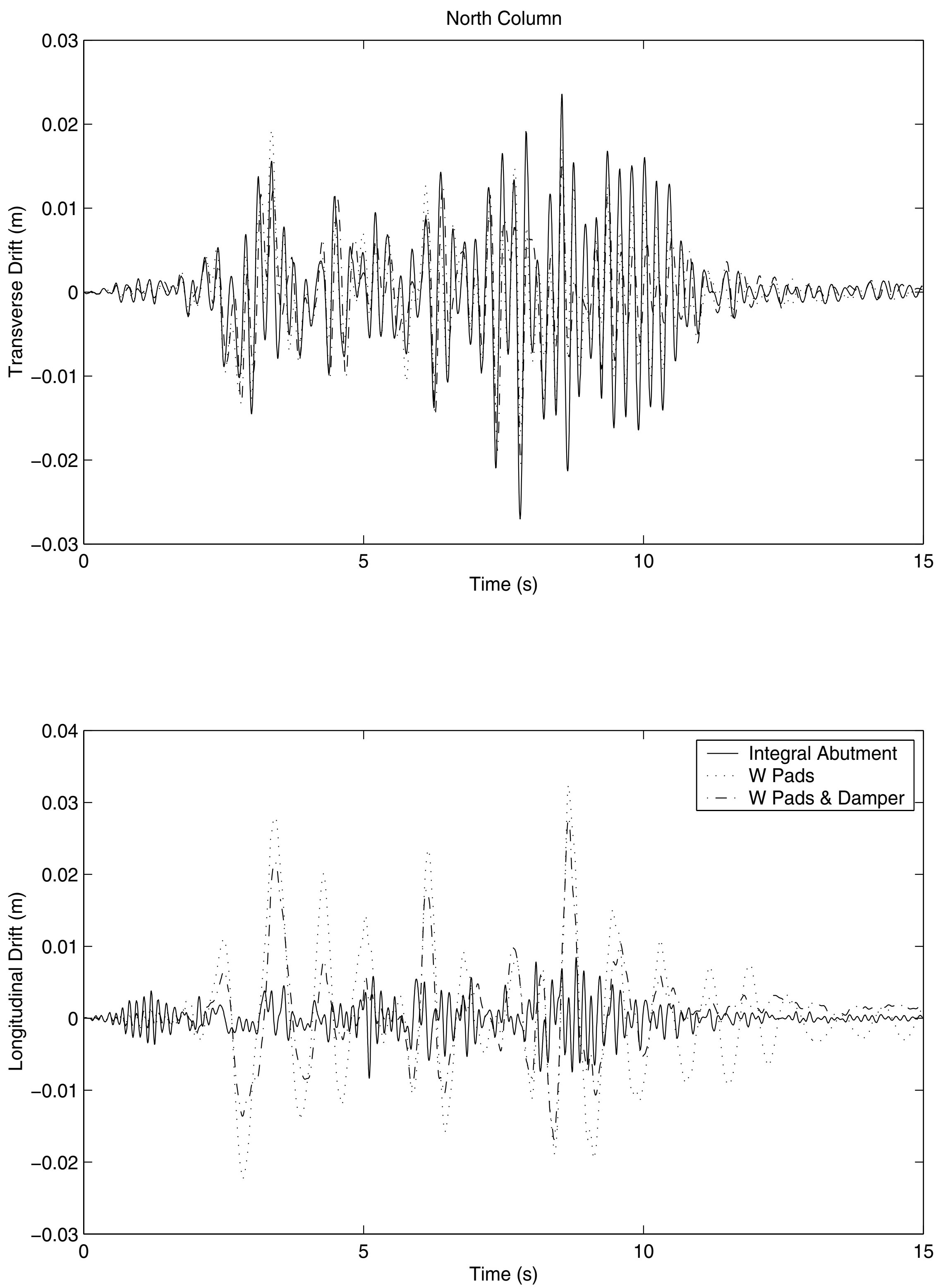

Figure A.13 Drift time histories of north column of 91/5 bridge subjected to Pacoima Dam records from 1971 San Fernando, California, earthquake. Soil-structure interaction is neglected.

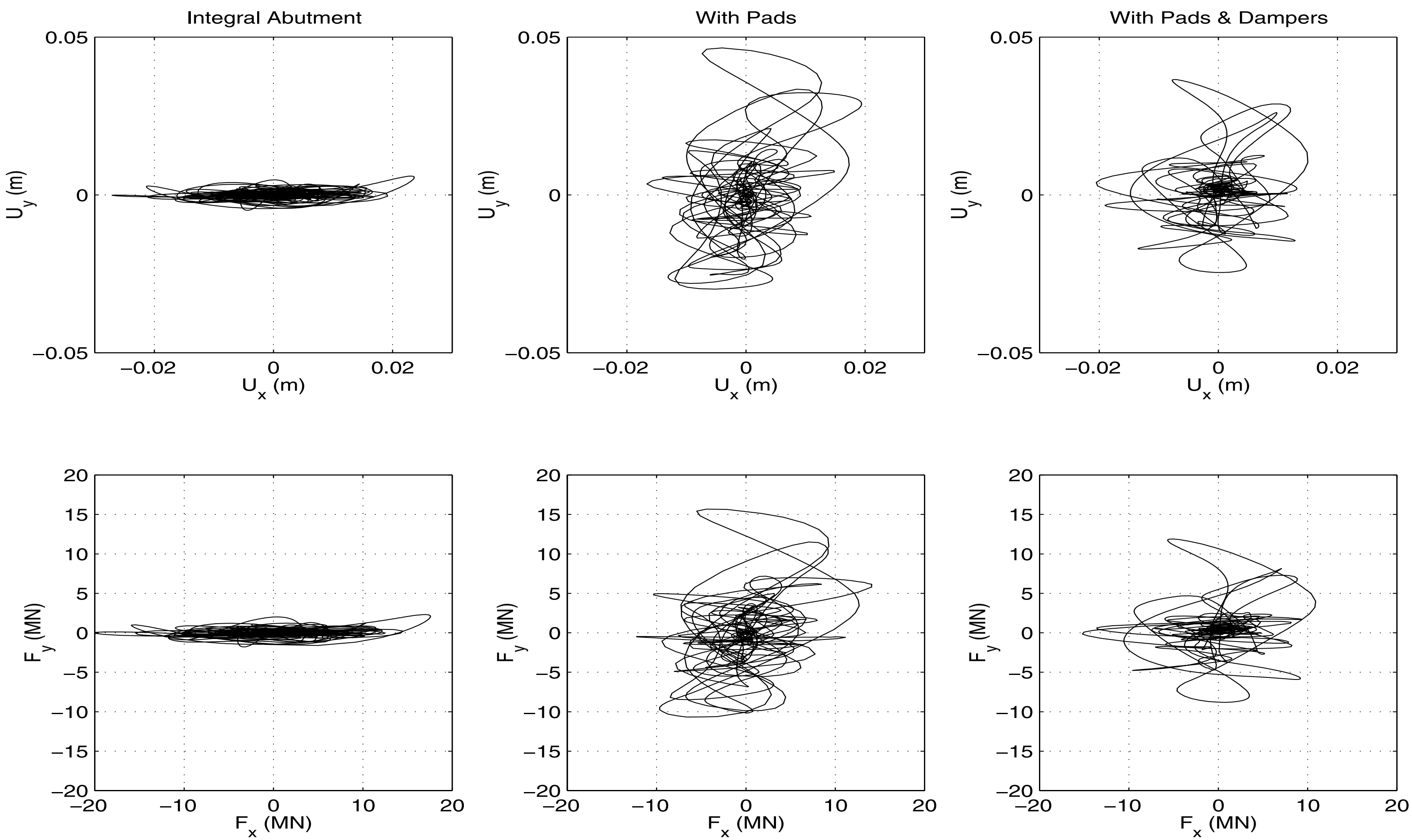

Figure A.14 Displacement and force signatures of south column of 91/5 bridge subjected to the Pacoima Dam records from 1971 San Fernando, California, earthquake. Soil-structure interaction is neglected.

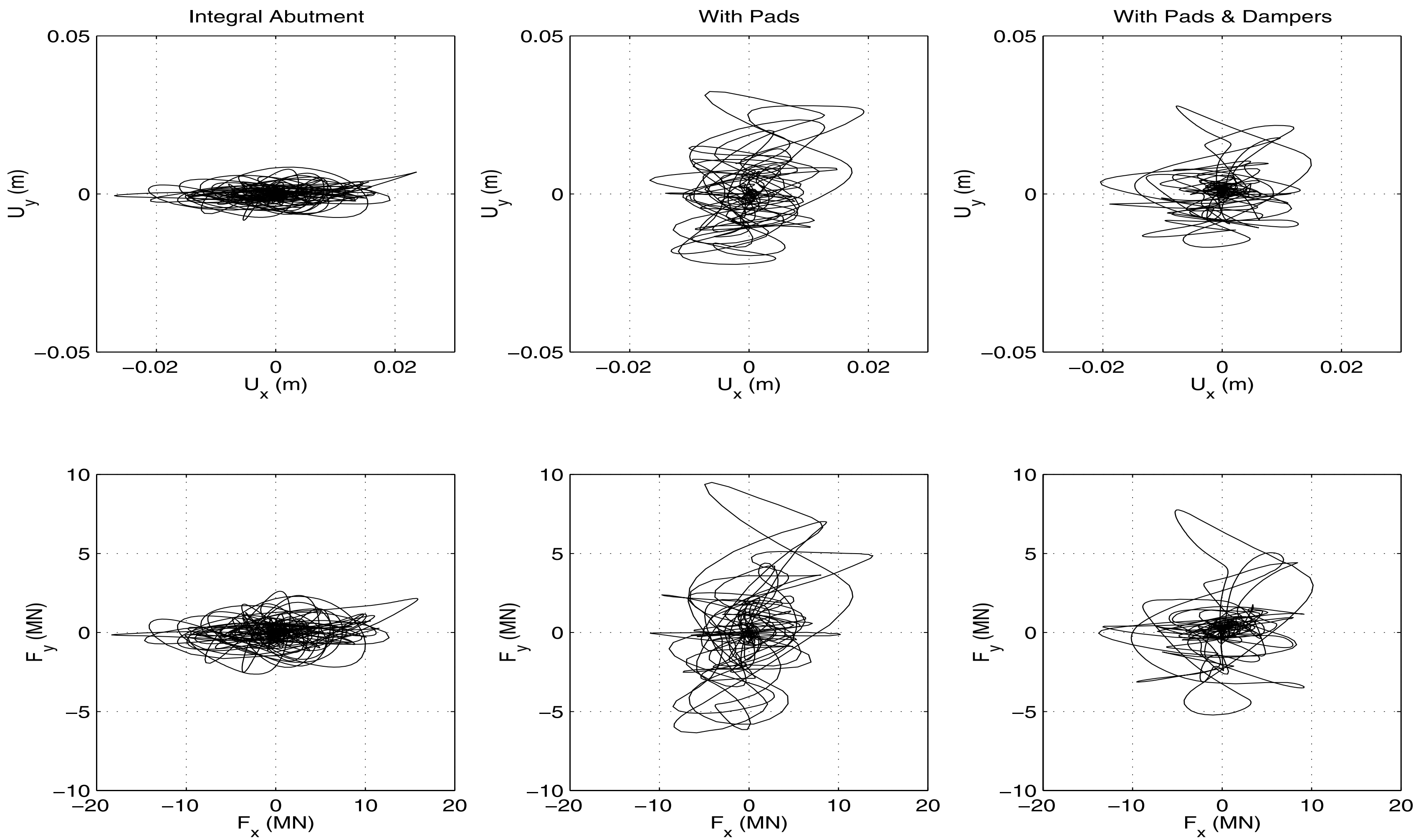

Figure A.15 Displacement and force signatures of north column of 91/5 bridge subjected to the Pacoima Dam records from 1971 San Fernando, California, earthquake. Soil-structure interaction is neglected.

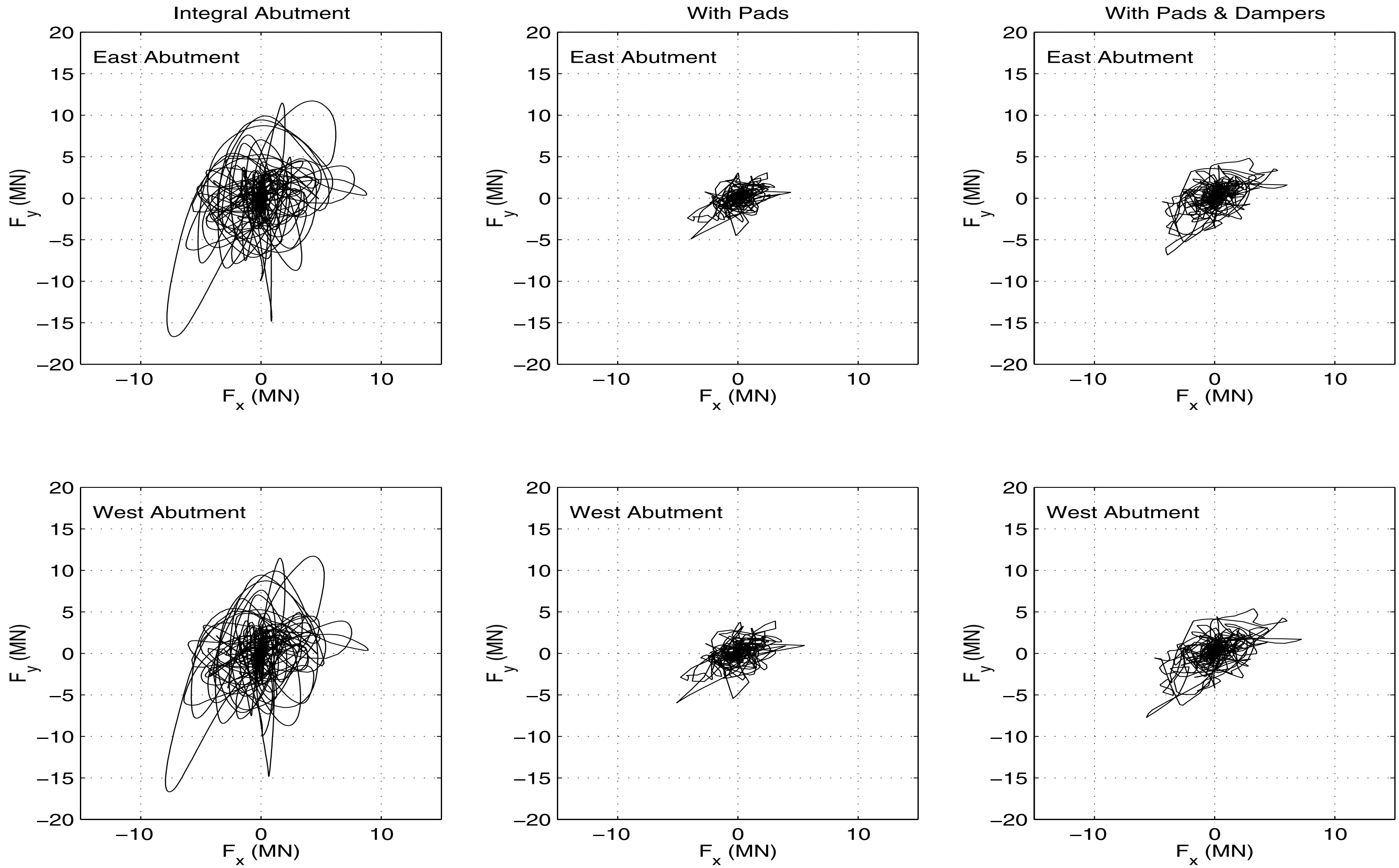

Figure A.16 Force signatures of end abutments of 91/5 bridge subjected to Pacoima Dam records from 1971 San Fernando, California earthquake. Soil-structure interaction is neglected.

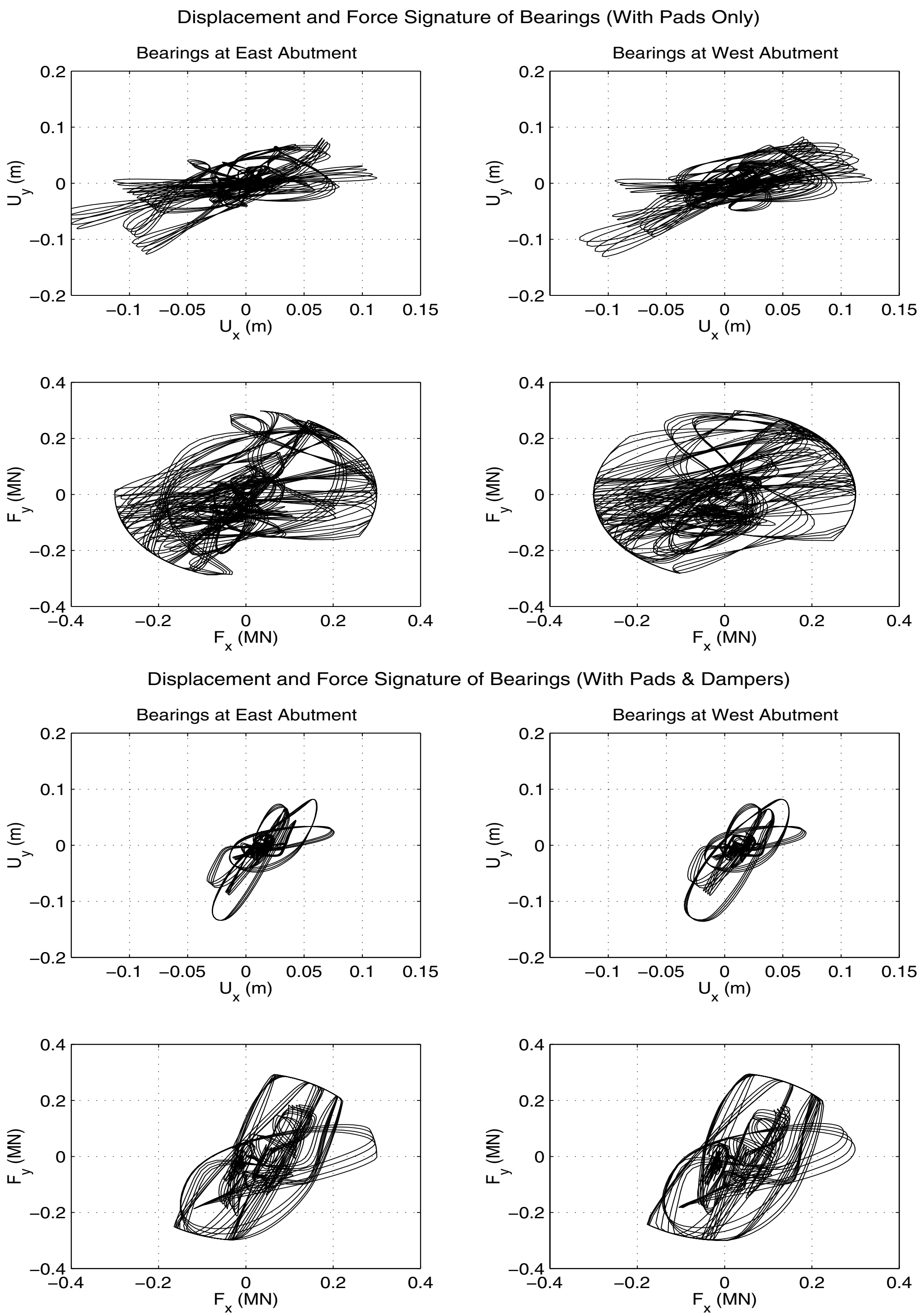

Figure A.17 Displacement and force signatures of elastomeric bearings of 91/5 bridge subjected to Pacoima Dam records from 1971 San Fernando, California, earthquake. Soil-structure interaction is neglected. Top: with pads only; bottom: with pads and dampers.

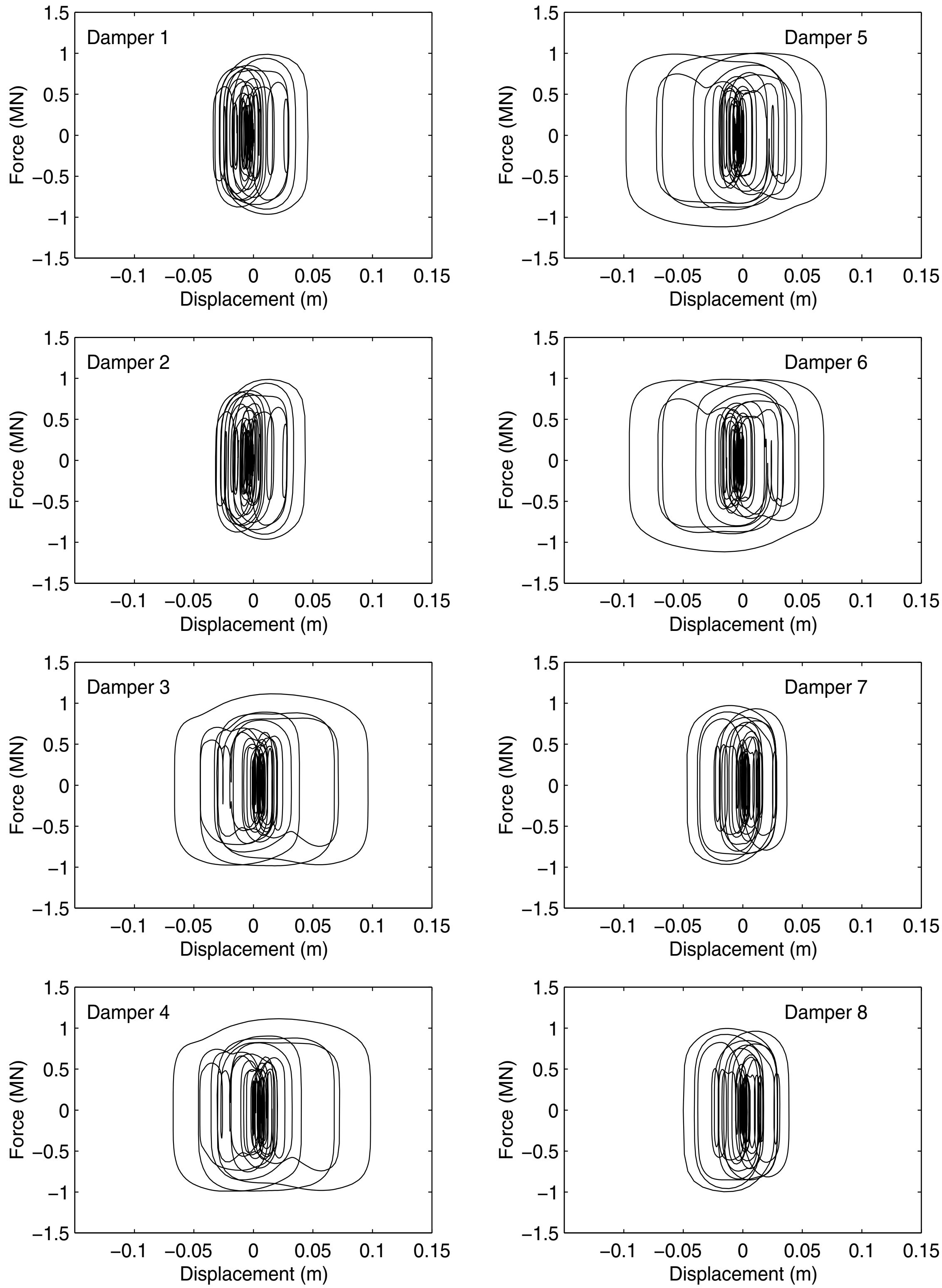

Figure A.18 Force-displacement loops of nonlinear fluid dampers subjected to Pacoima Dam records from 1971 San Fernando, California, earthquake. Soil-structure interaction is neglected.

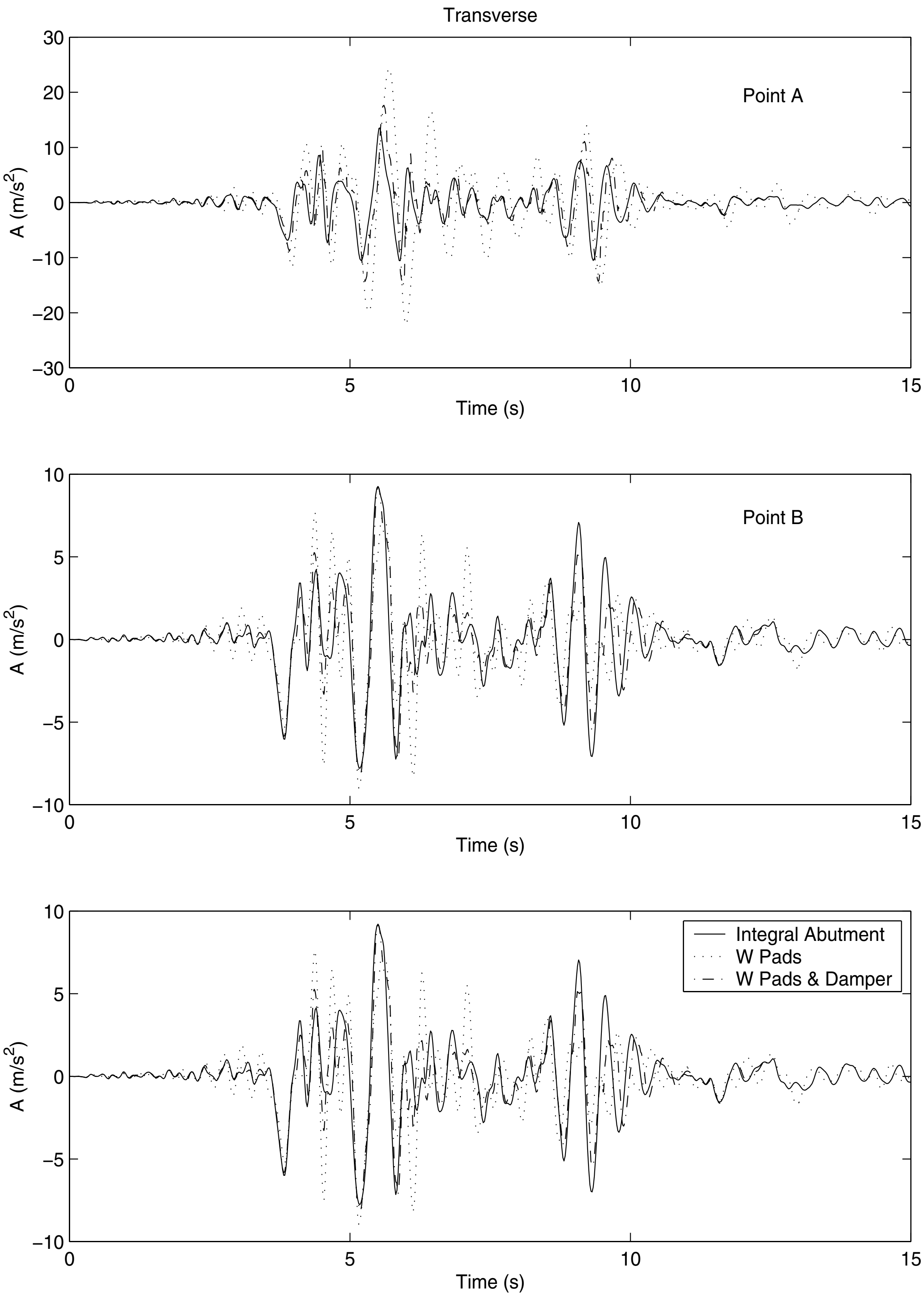

Figure A.19 Transverse acceleration time histories at various locations along bridge subjected to Newhall records from 1994 Northridge, California, earthquake. Soil-structure interaction is included.

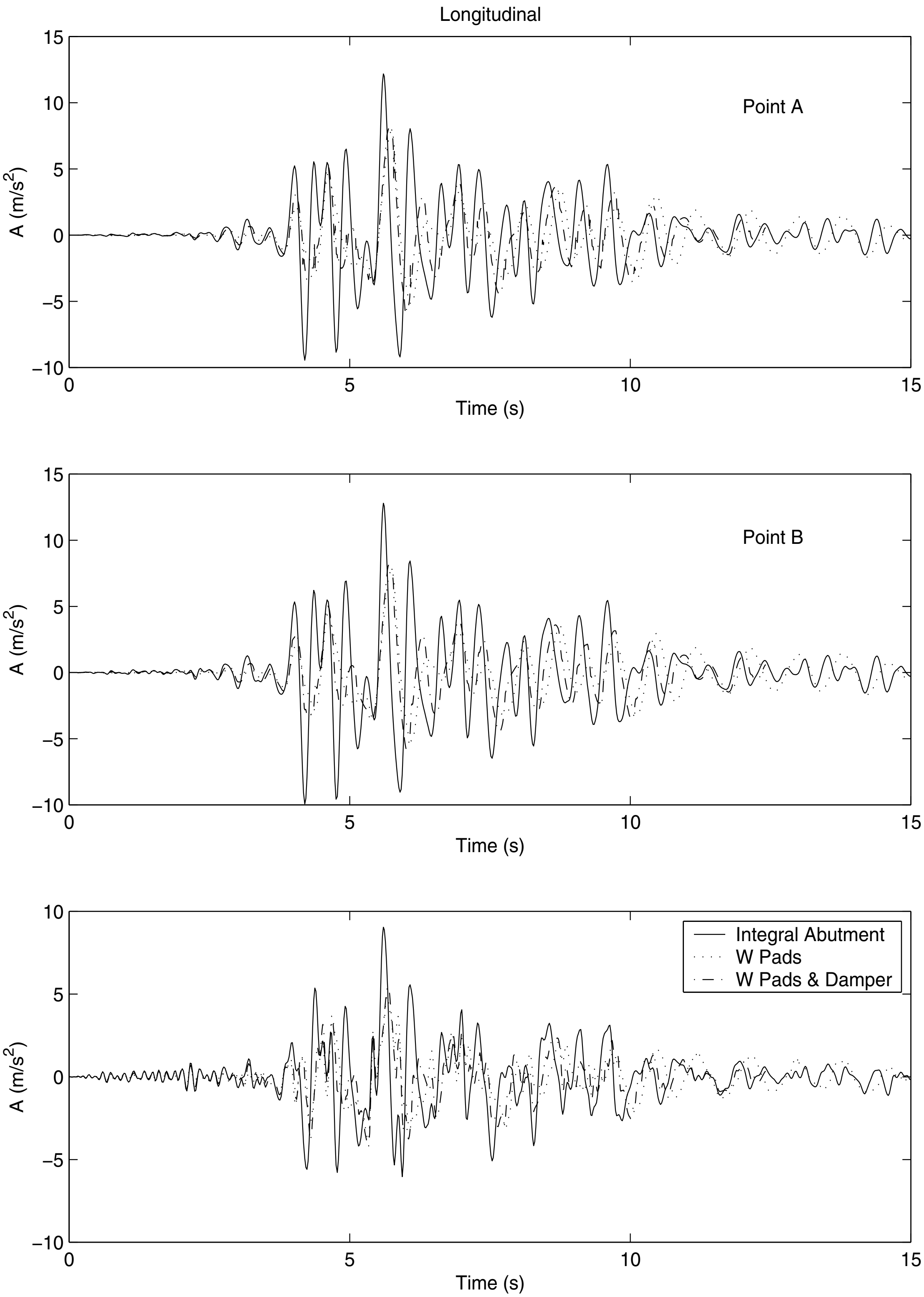

Figure A.20 Longitudinal acceleration time histories at various locations along bridge subjected to Newhall records from 1994 Northridge, California, earthquake. Soil-structure interaction is included.

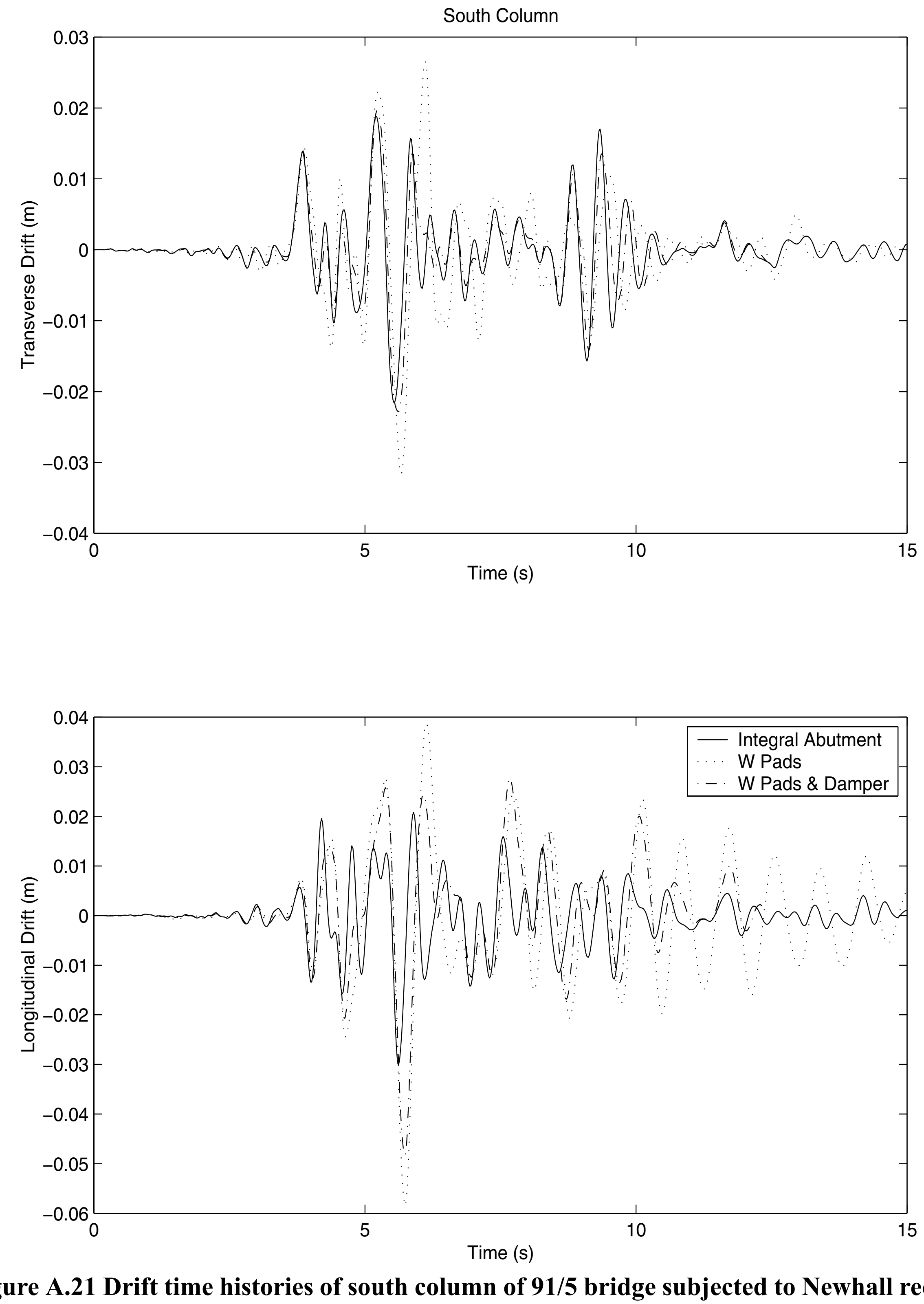

Figure A.21 Drift time histories of south column of 91/5 bridge subjected to Newhall records from 1994 Northridge, California, earthquake. Soil-structure interaction is included.

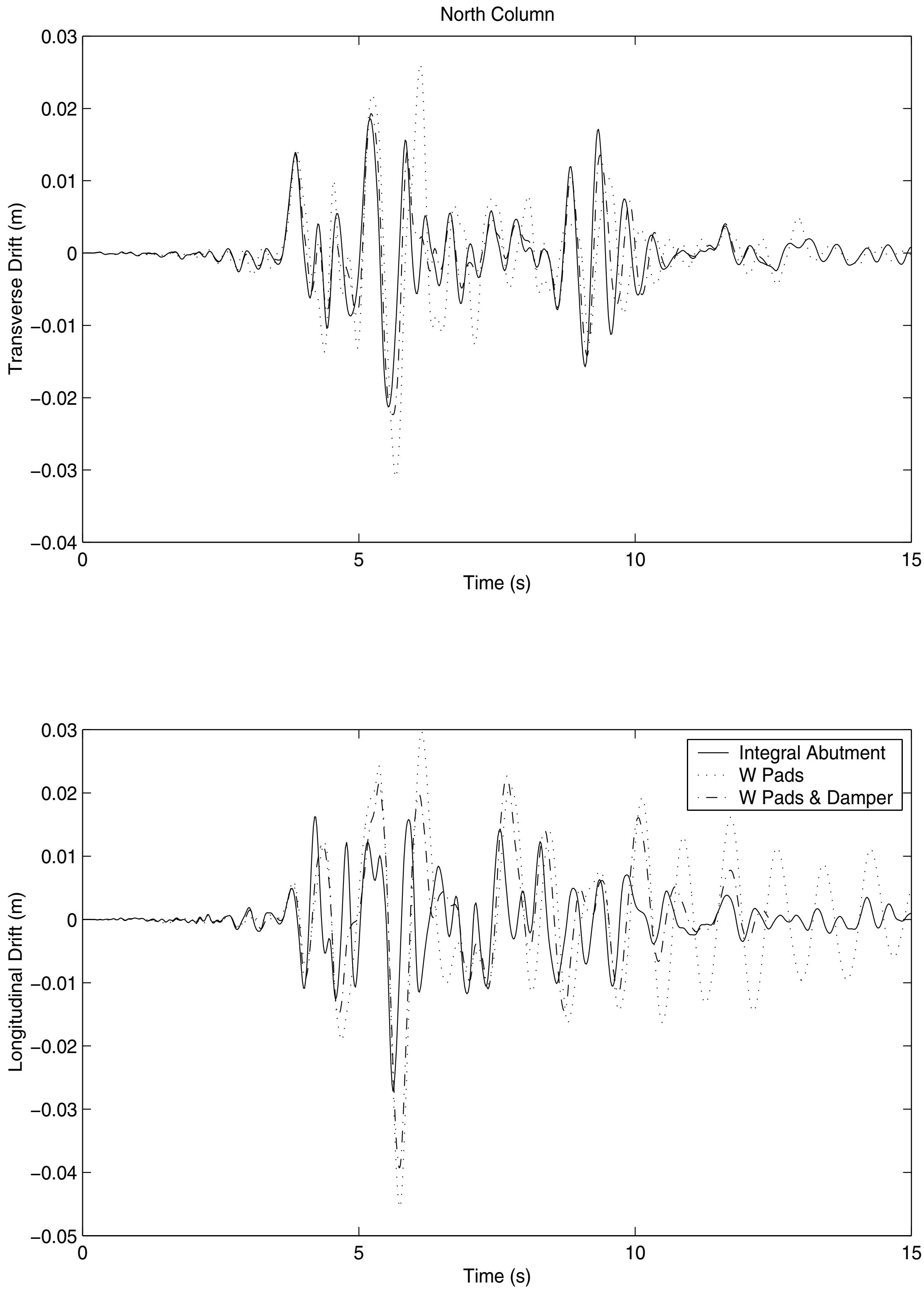

Figure A.22 Drift time histories of north column of 91/5 bridge subjected to Newhall records from 1994 Northridge, California, earthquake. Soil-structure interaction is included.

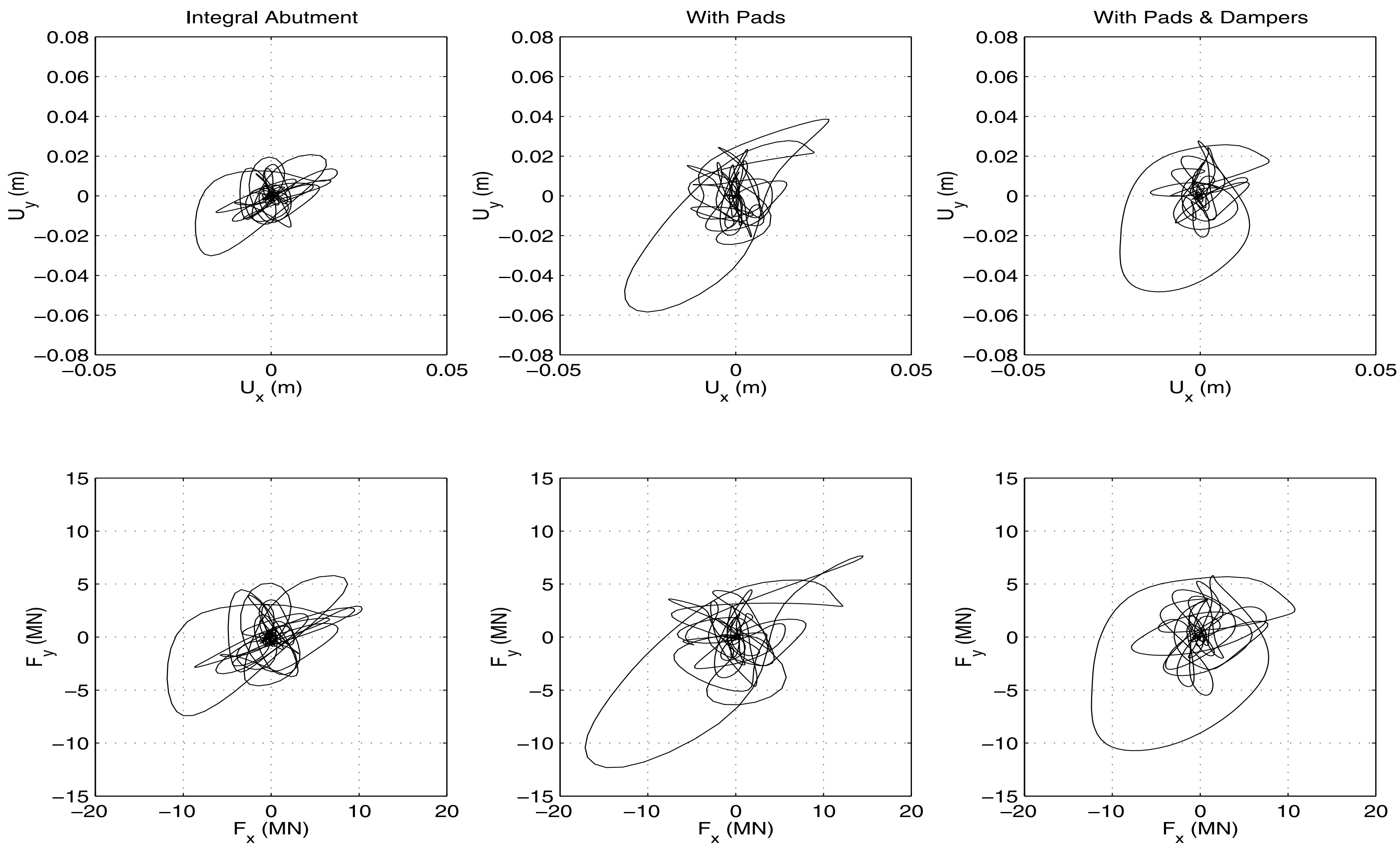

Figure A.23 Displacement and force signatures of south column of 91/5 bridge subjected to Newhall records from 1994 Northridge, California, earthquake. Soil-structure interaction is included.

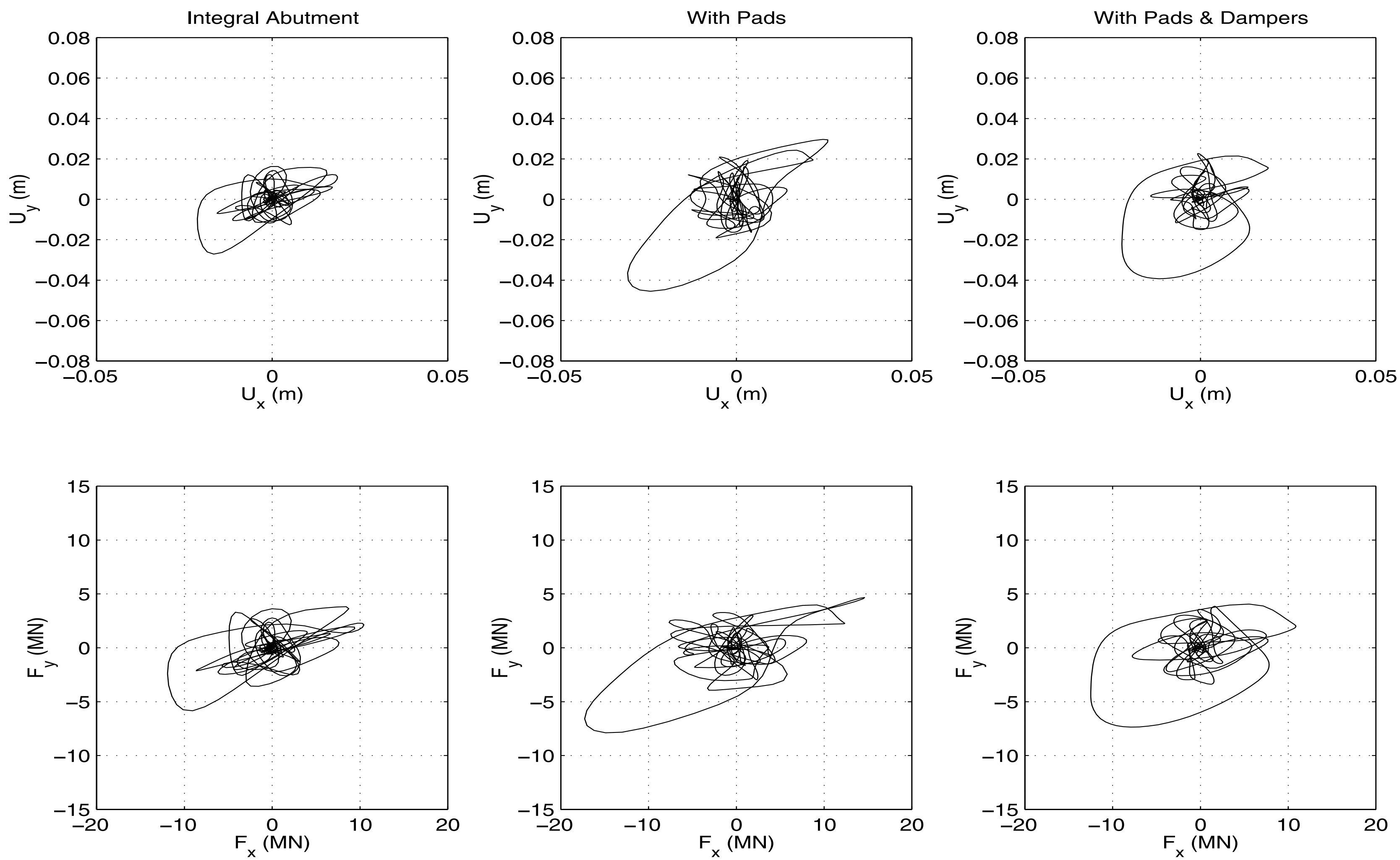

Figure A.24 Displacement and force signatures of north column of 91/5 bridge subjected to Newhall records from 1994 Northridge, California, earthquake. Soil-structure interaction is included.

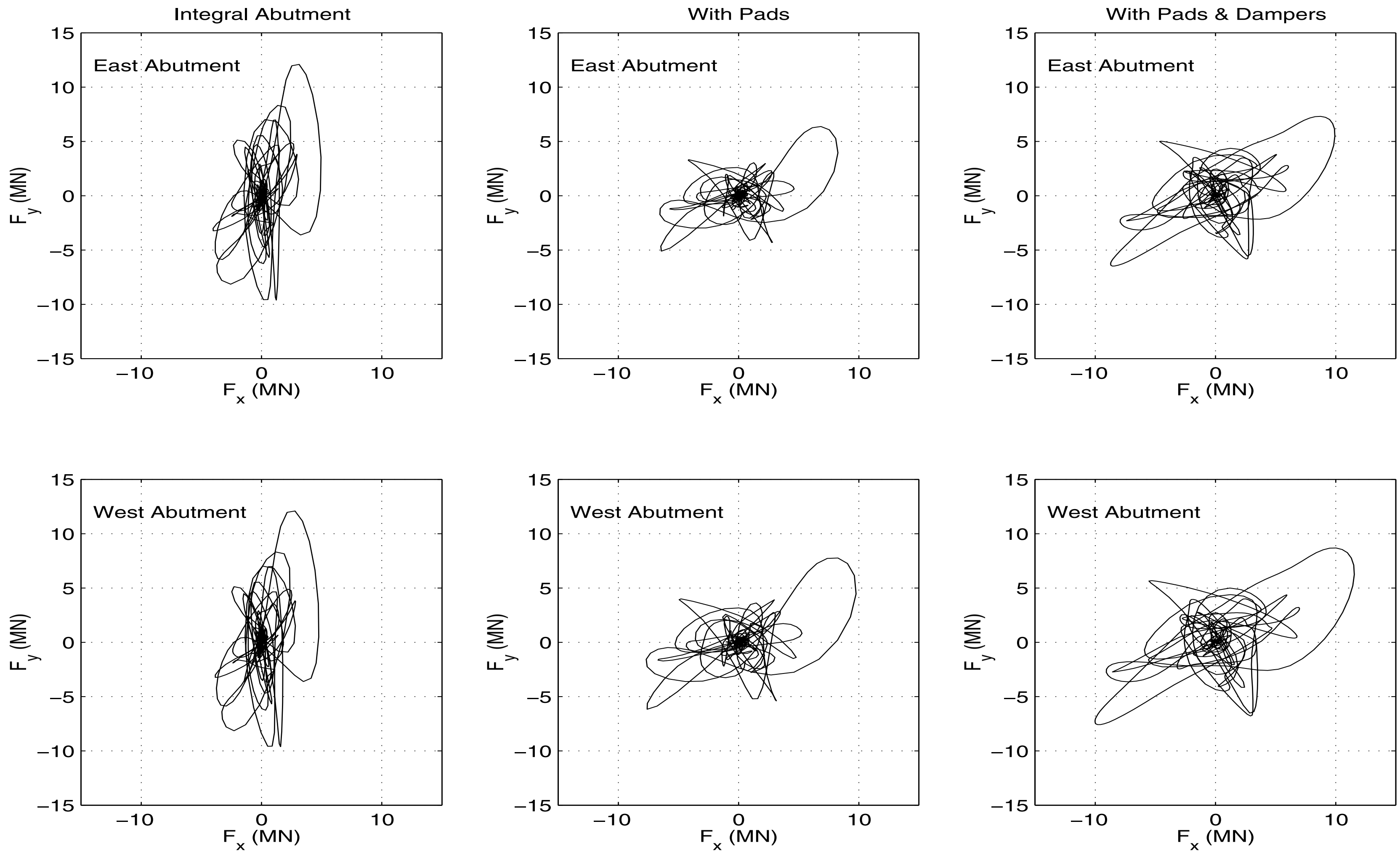

Figure A.25 Displacement and force signatures of end abutments of 91/5 bridge subjected to Newhall records from 1994 Northridge, California, earthquake. Soil-structure interaction is included.

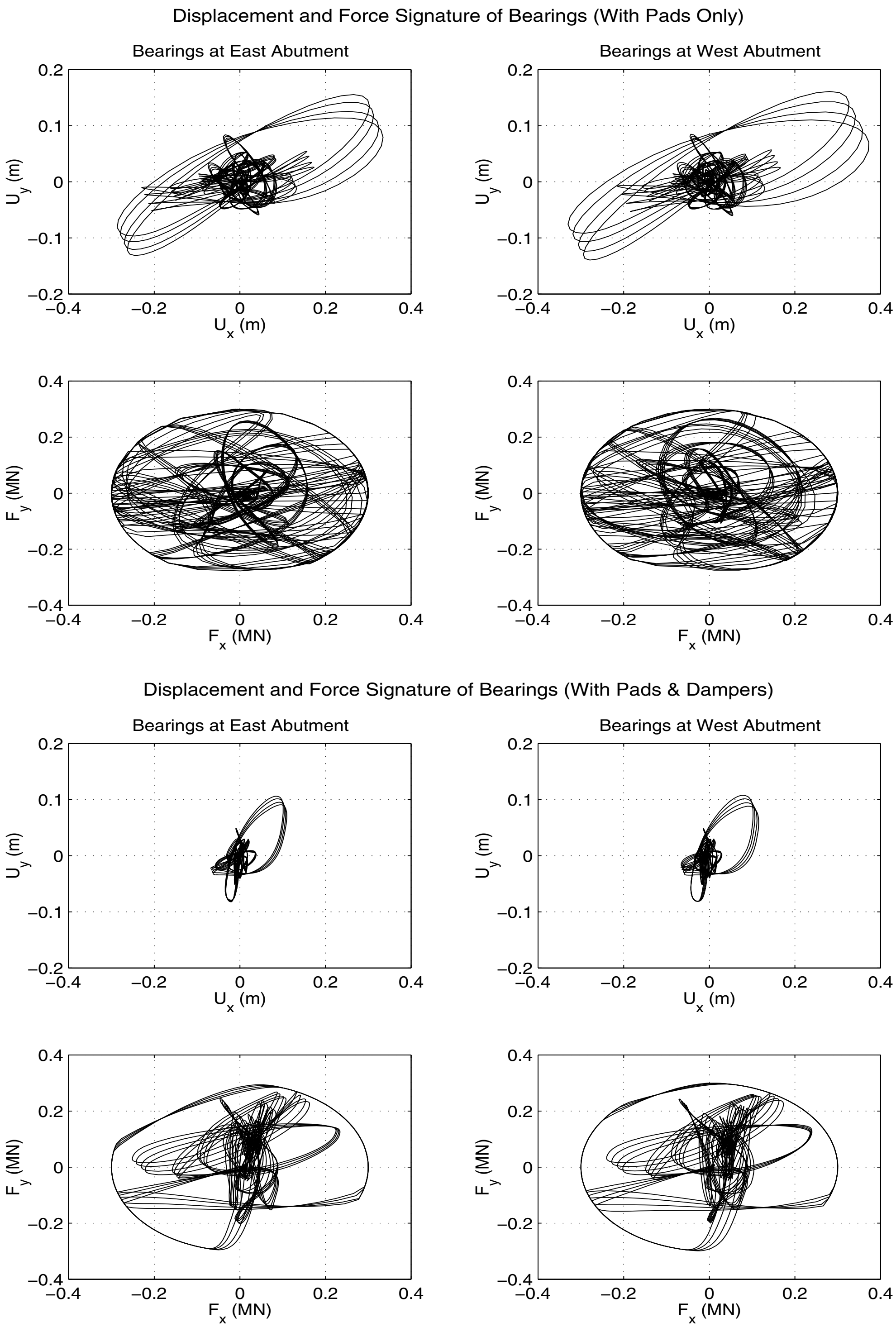

Figure A.26 Displacement and force signatures of elastomeric bearings of 91/5 bridge subjected to Newhall records from 1994 Northridge, California, earthquake. Soil-structure interaction is included. Top: with pads only; bottom: with pads and dampers.

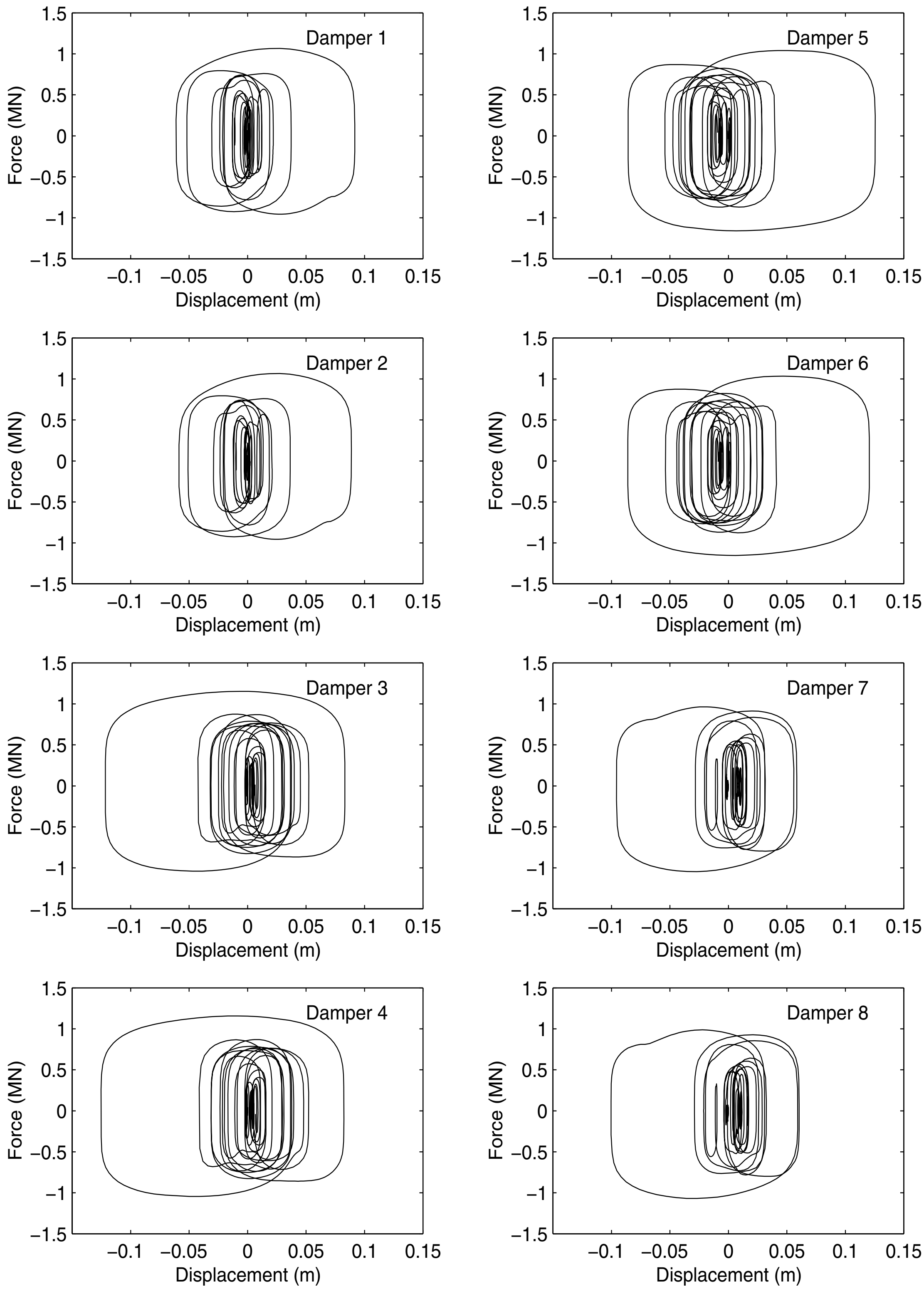

Figure A.27 Force-displacement loops of nonlinear fluid dampers subjected to Newhall records from 1994 Northridge, California, earthquake. Soil-structure interaction is included.

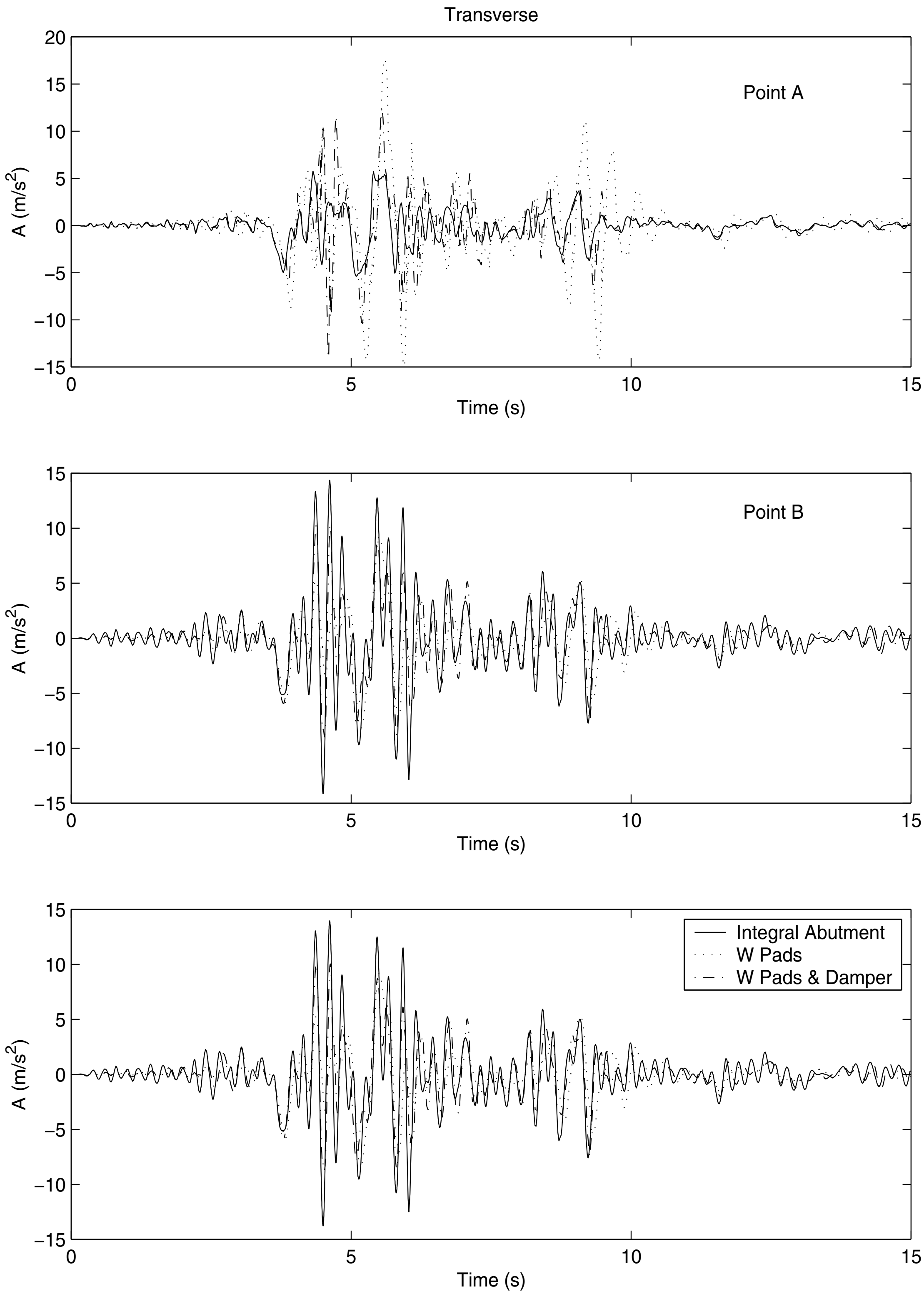

Figure A.28 Transverse acceleration time histories at various locations along bridge subjected to Newhall records from 1994 Northridge, California, earthquake. Soil-structure interaction is neglected.

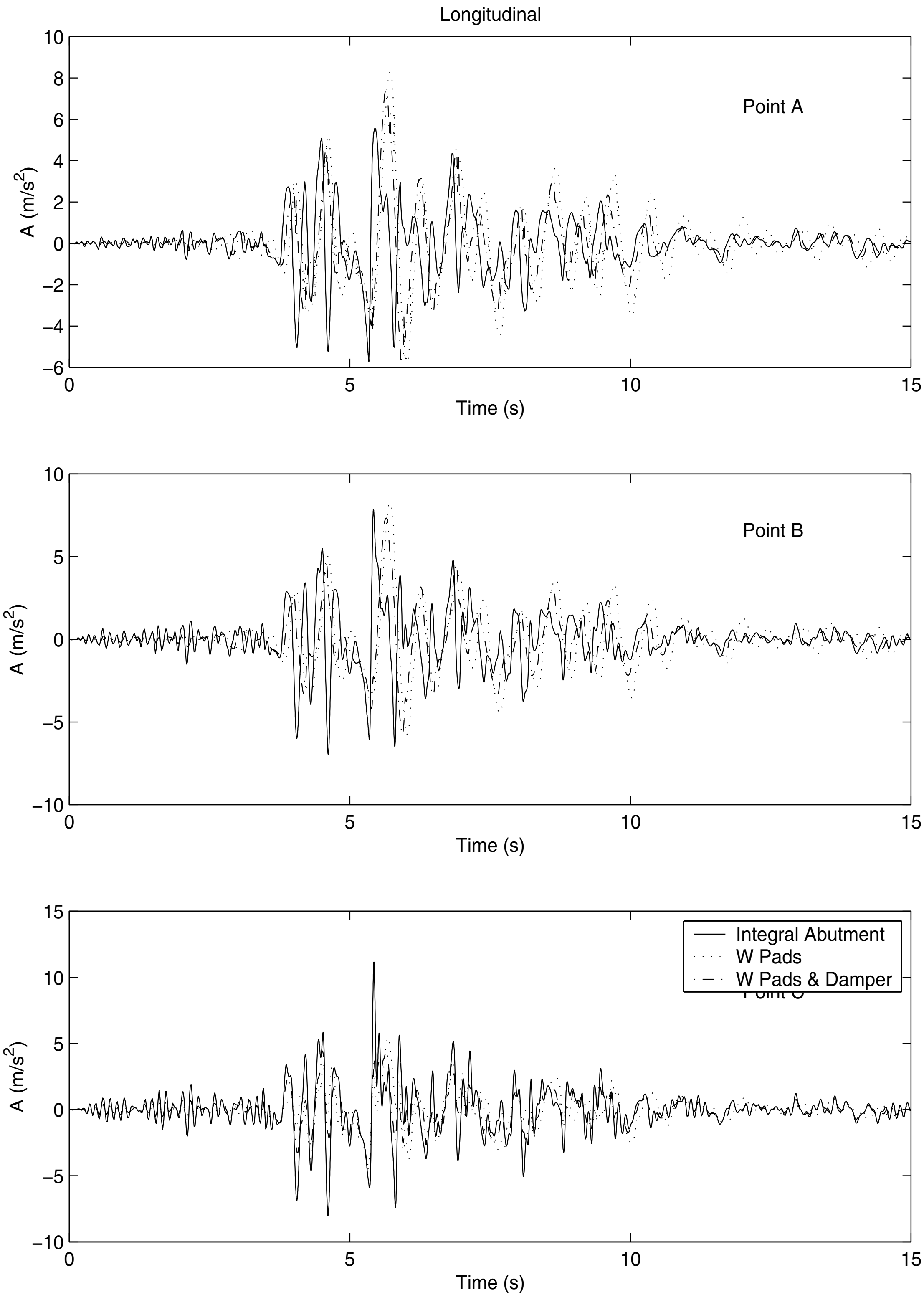

Figure A.29 Longitudinal acceleration time histories at various locations along bridge subjected to Newhall records from the 1994 Northridge, California, earthquake. Soil-structure interaction is neglected.

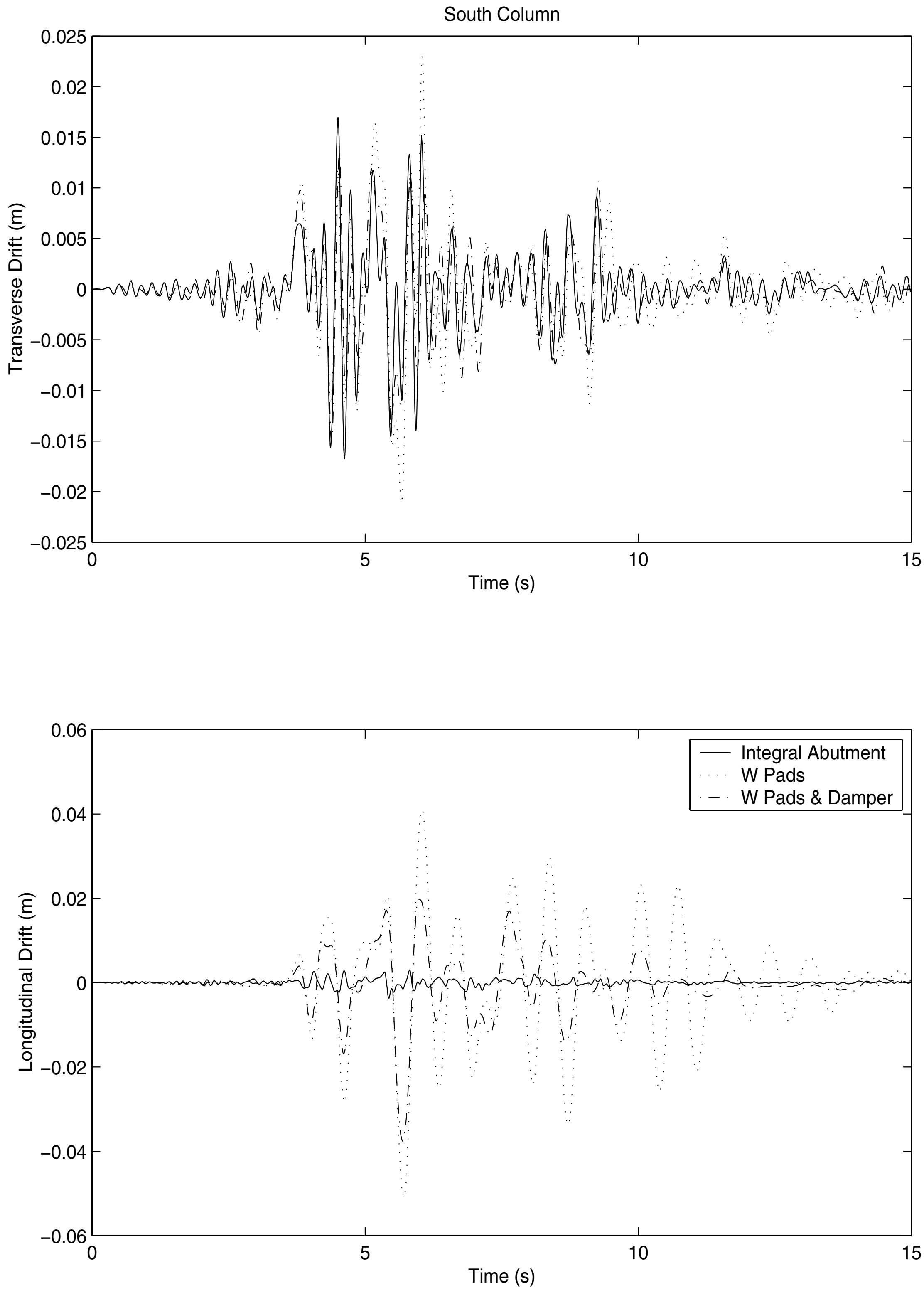

Figure A.30 Drift time histories of south column of 91/5 bridge subjected to Newhall records from 1994 Northridge, California, earthquake. Soil-structure interaction is neglected.

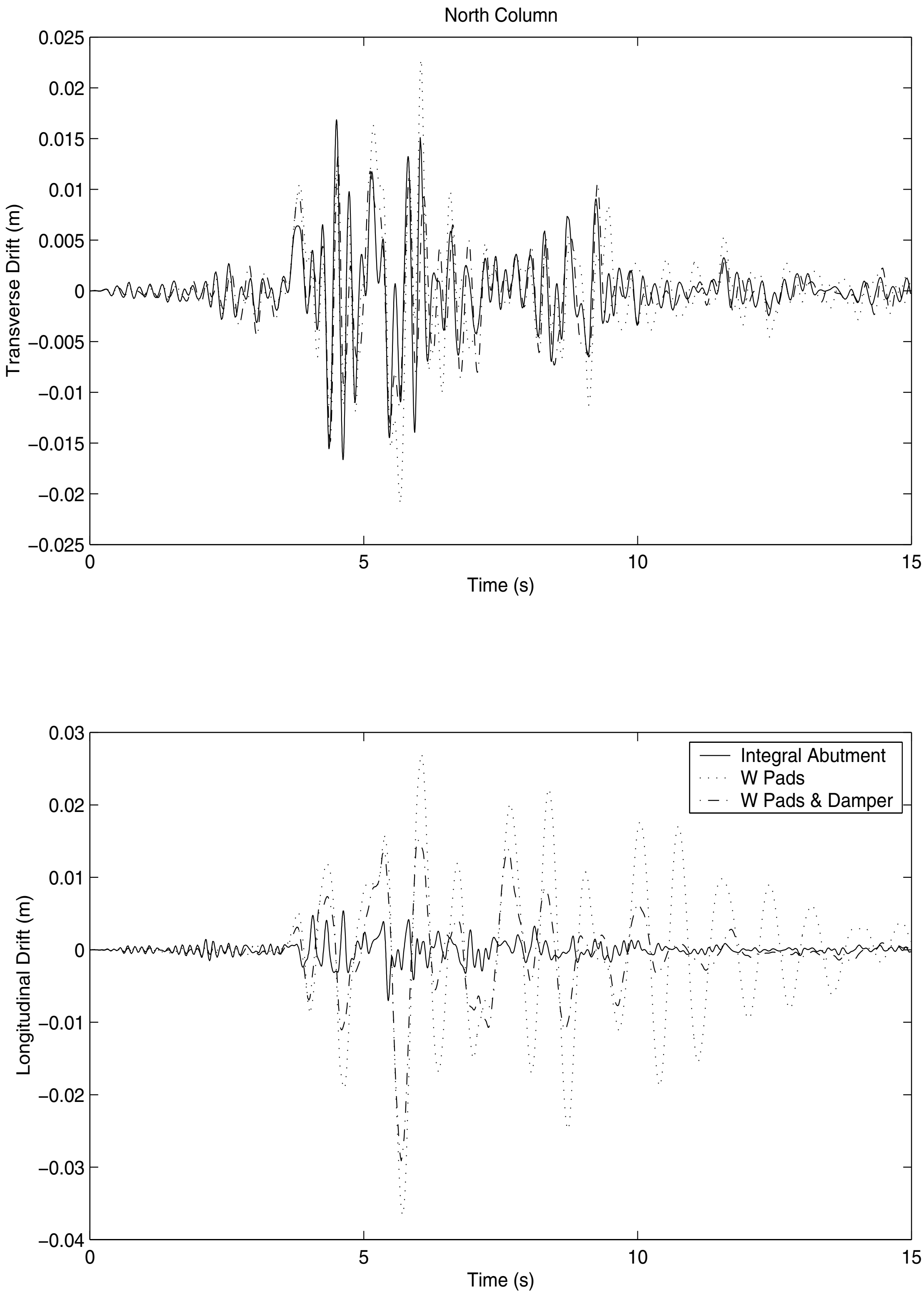

Figure A.31 Drift time histories of north column of 91/5 bridge subjected to Newhall records from 1994 Northridge, California, earthquake. Soil-structure interaction is neglected.

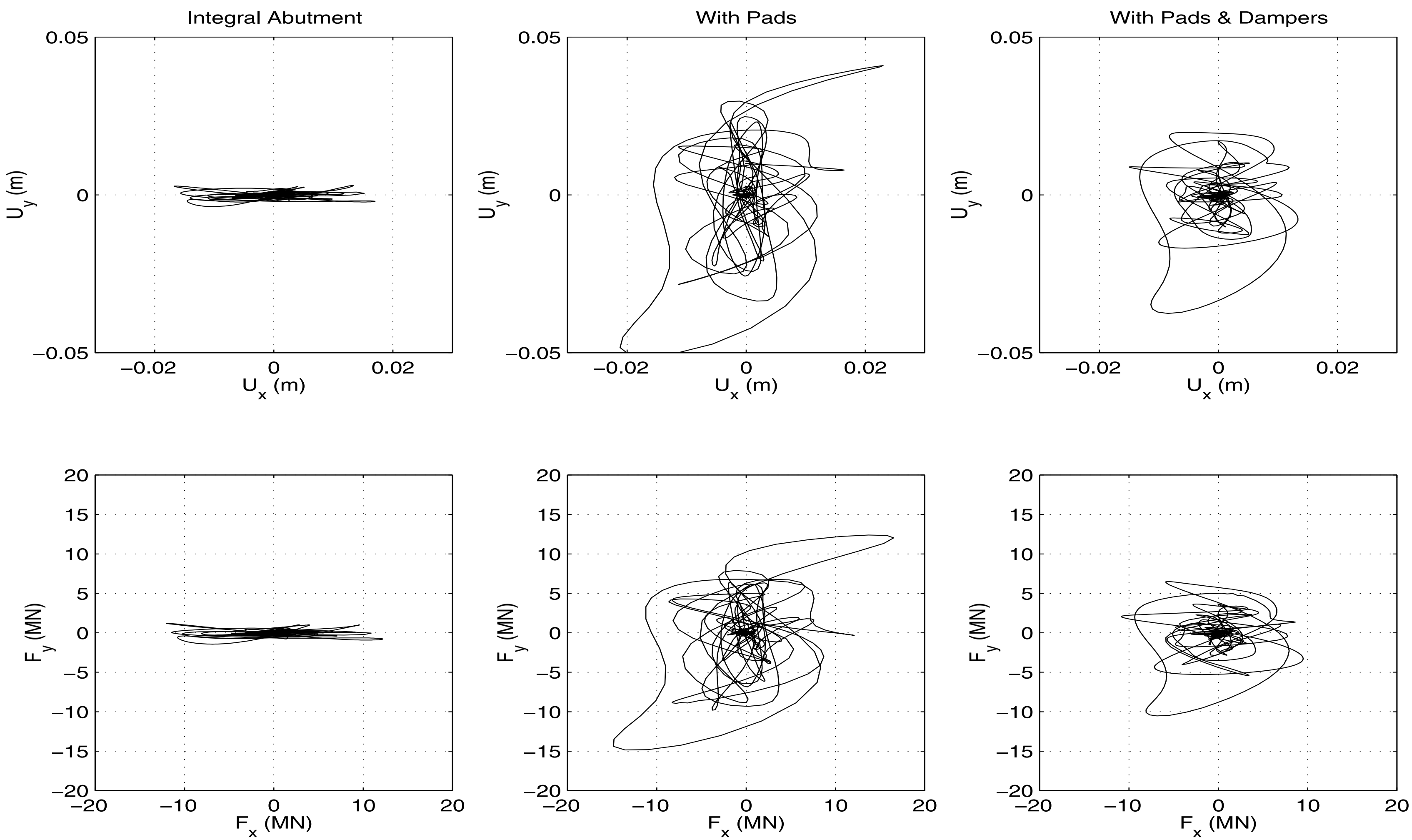

Figure A.32 Displacement and force signatures of south column of 91/5 bridge subjected to Newhall records from 1994 Northridge, California, earthquake. Soil-structure interaction is neglected.

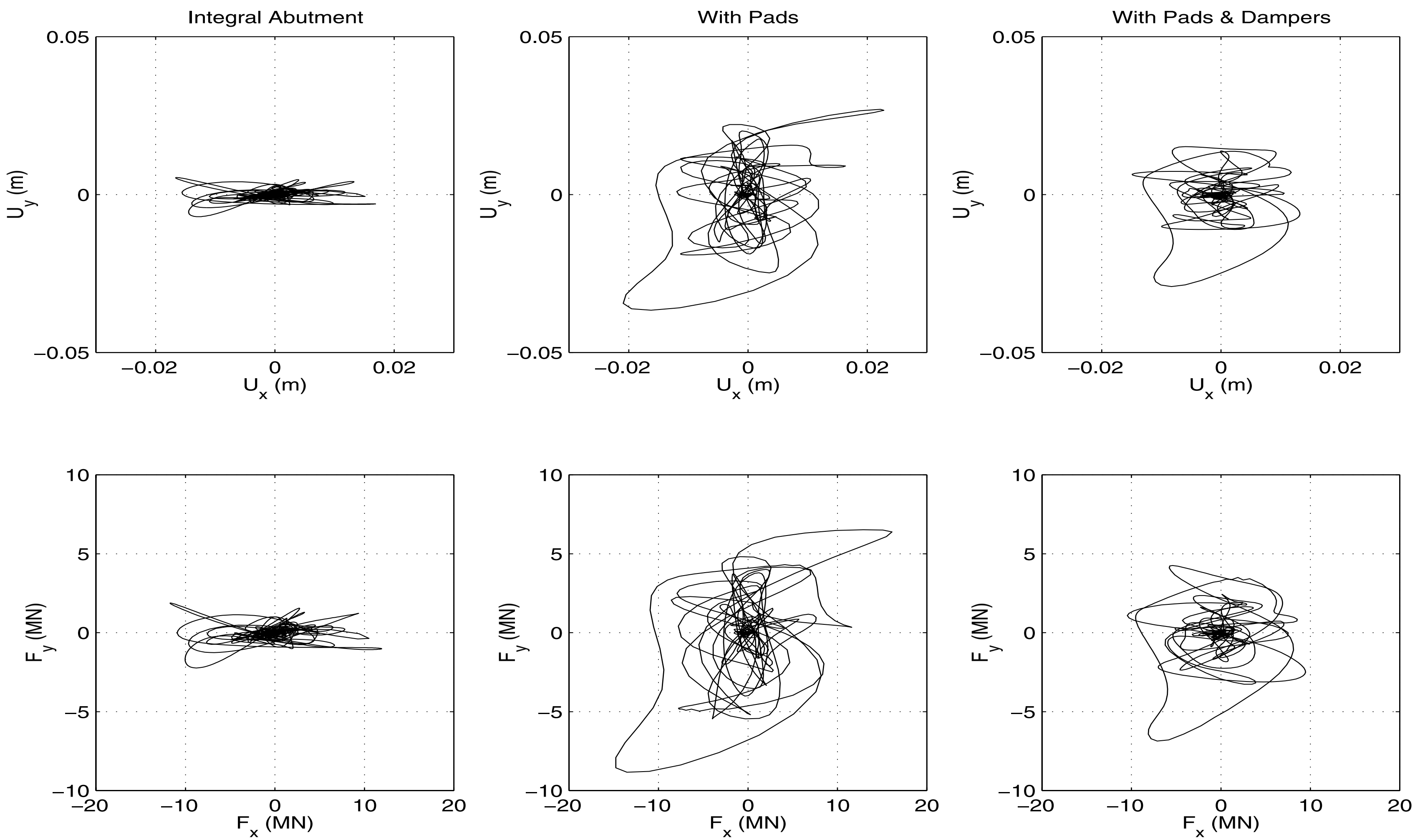

Figure A.33 Displacement and force signatures of north column of 91/5 bridge subjected to Newhall records from 1994 Northridge, California, earthquake. Soil-structure interaction is neglected.

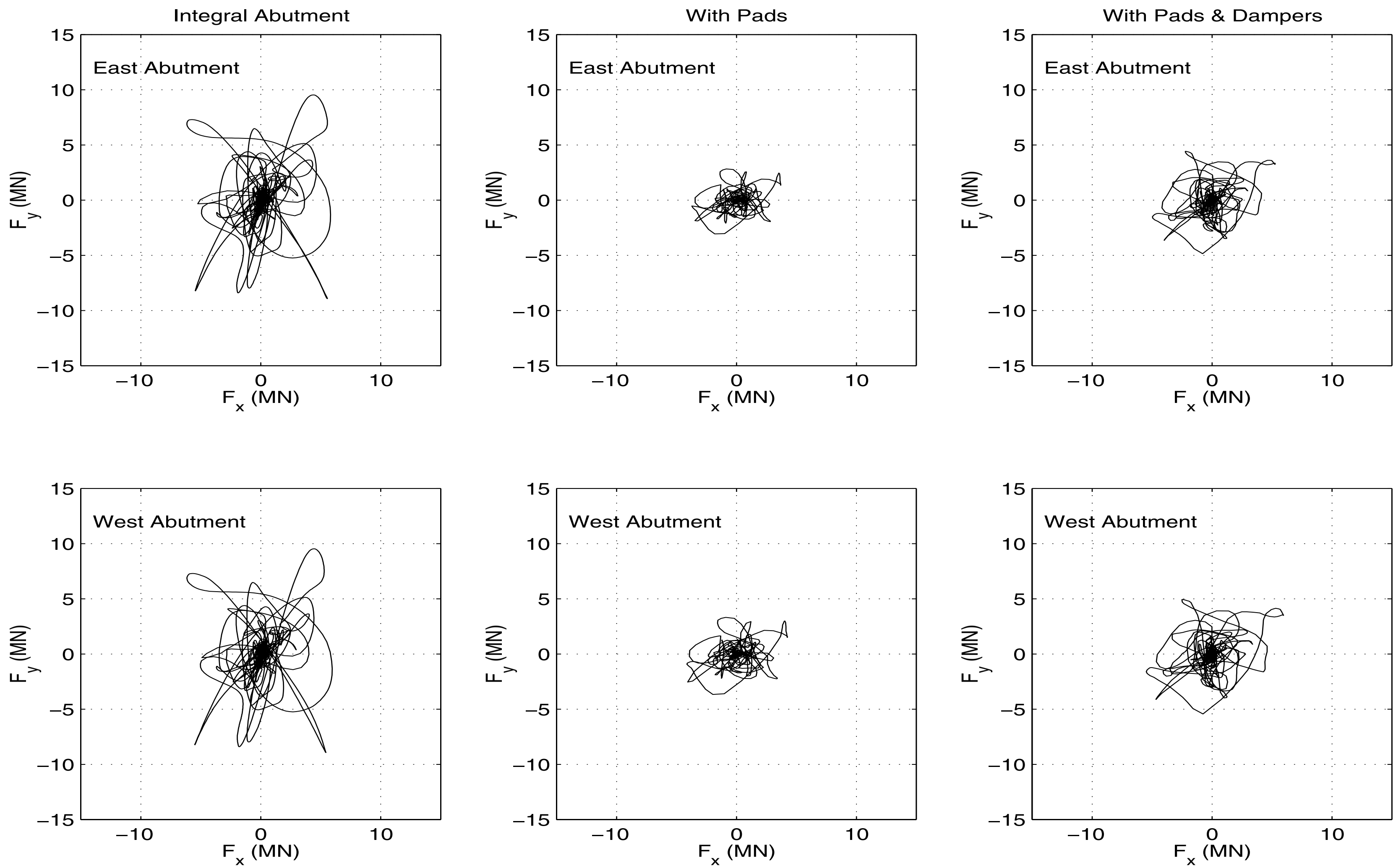

Figure A.34 Force signatures of end abutments of 91/5 bridge subjected to Newhall records from 1994 Northridge, California, earthquake. Soil-structure interaction is neglected.

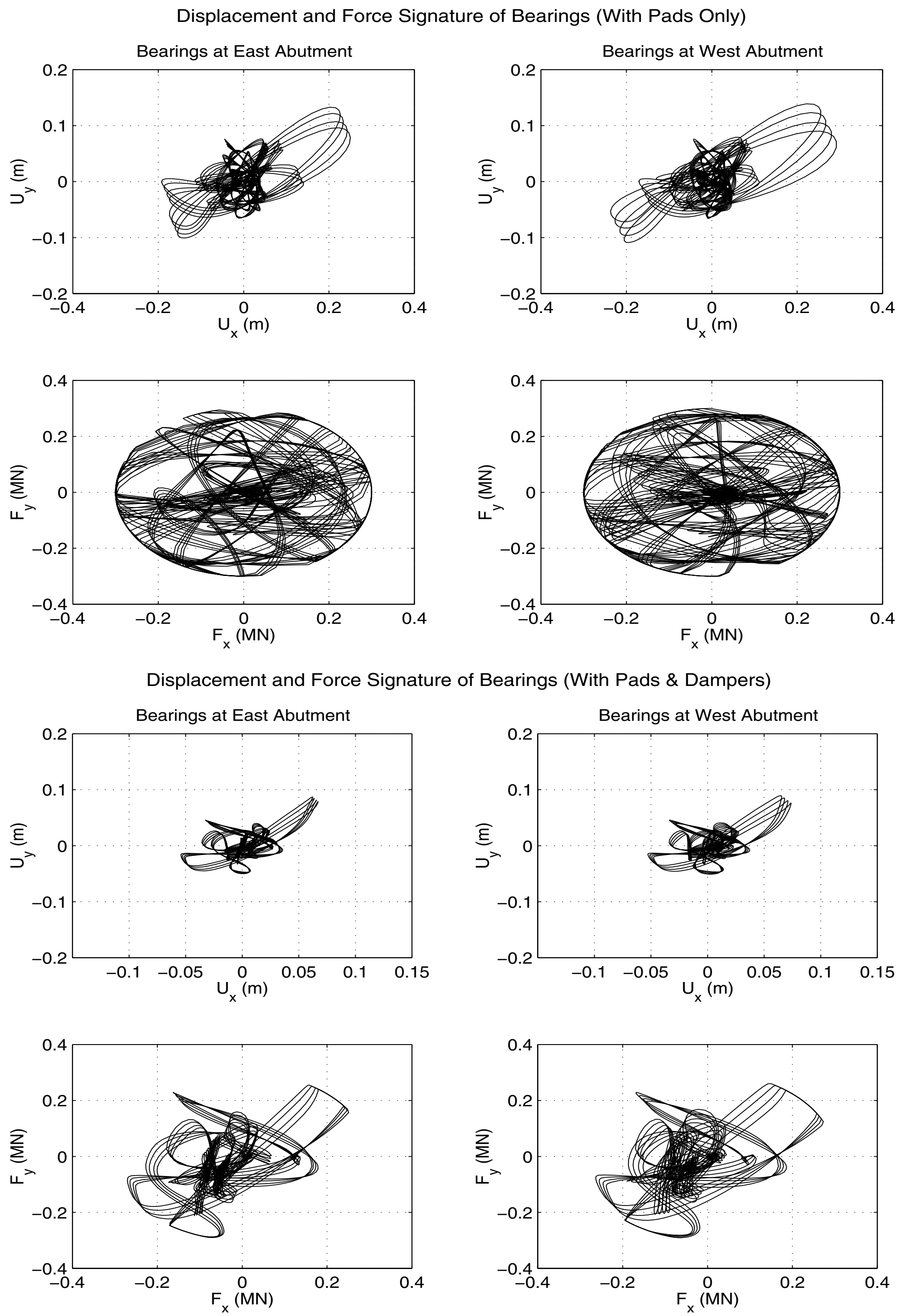

Figure A.35 Displacement and force signatures of elastomeric bearings of 91/5 bridge subjected to Newhall records from 1994 Northridge, California, earthquake. Soil-structure interaction is neglected. Top: with pads only; bottom: with pads and dampers.

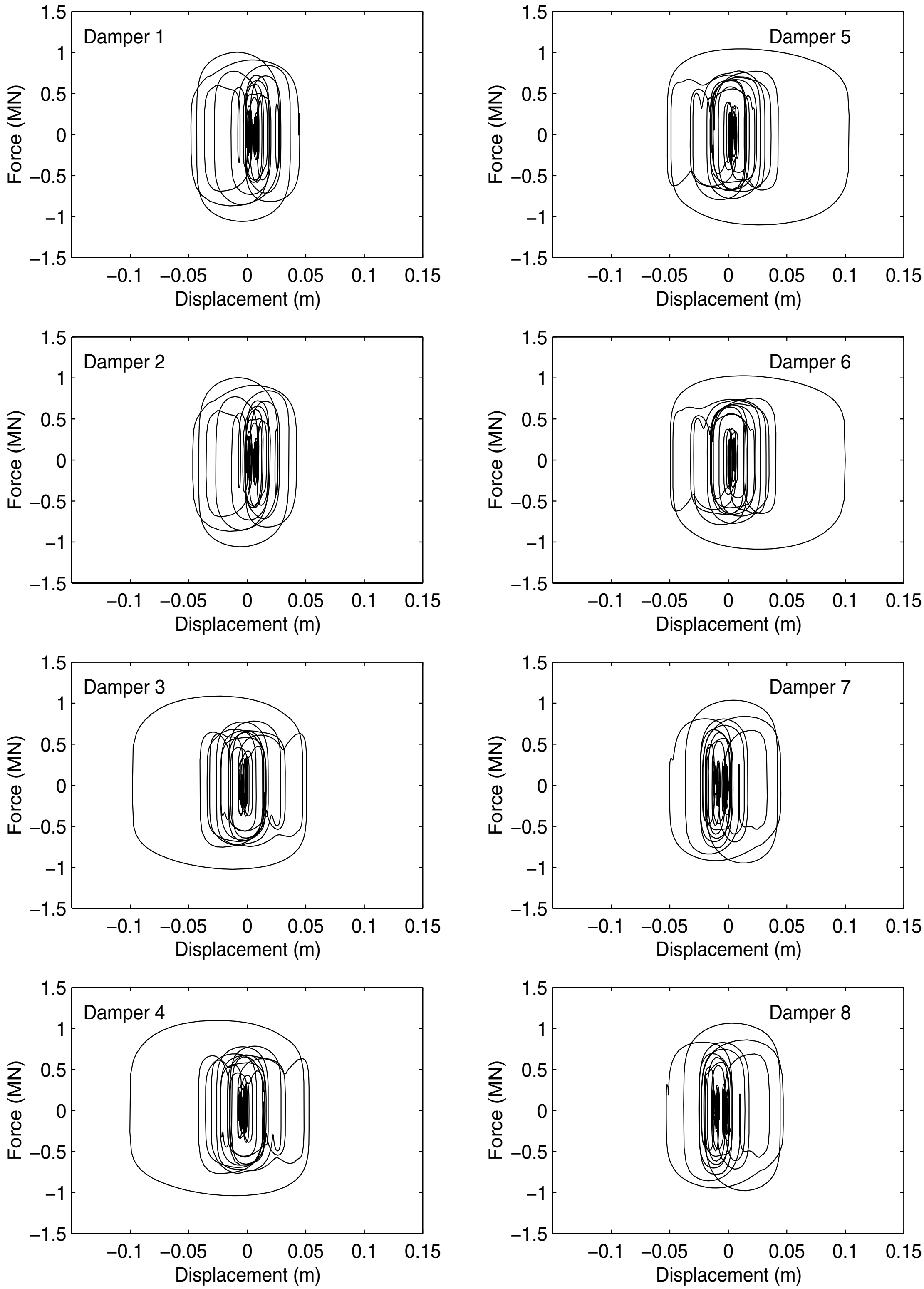

Figure A.36 Force-displacement loops of nonlinear fluid dampers subjected to Newhall records from 1994 Northridge, California, earthquake. Soil-structure interaction is neglected.

PEER REPORTS

PEER reports are available from the National Information Service for Earthquake Engineering (NISEE). To order PEER reports, please contact the Pacific Earthquake Engineering Research Center, 1301 South 46th Street, Richmond, California 94804-4698. Tel.: (510) 231-9468; Fax: (510) 231-9461.

PEER 2002/17 *Structural Characterization and Seismic Response Analysis of a Highway Overcrossing Equipped with Elastomeric Bearings and Fluid Dampers: A Case Study.* Nicos Makris and Jian Zhang. November 2002.

PEER 2002/16 *Estimation of Uncertainty in Geotechnical Properties for Performance-Based Earthquake Engineering.* Allen L. Jones, Steven L. Kramer, and Pedro Arduino. December 2002.

PEER 2002/14 *Inelastic Seismic Response of Extended Pile Shaft Supported Bridge Structures.* T.C. Hutchinson, R.W. Boulanger, Y.H. Chai, and I.M. Idriss. December 2002.

PEER 2002/13 *Probabilistic Models and Fragility Estimates for Bridge Components and Systems.* Paolo Gardoni, Armen Der Kiureghian, and Khalid M. Mosalam. June 2002.

PEER 2002/12 *Effects of Fault Dip and Slip Rake on Near-Source Ground Motions: Why Chi-Chi Was a Relatively Mild M7.6 Earthquake.* Brad T. Aagaard, John F. Hall, and Thomas H. Heaton. December 2002.

PEER 2002/11 *Analytical and Experimental Study of Fiber-Reinforced Strip Isolators*. James M. Kelly and Shakhzod M. Takhirov. September 2002.

PEER 2002/10 *Centrifuge Modeling of Settlement and Lateral Spreading with Comparisons to Numerical Analyses***.** Sivapalan Gajan and Bruce L. Kutter. January 2003.

PEER 2002/09 *Documentation and Analysis of Field Case Histories of Seismic Compression during the 1994 Northridge, California, Earthquake.* Jonathan P. Stewart, Patrick M. Smith, Daniel H. Whang, and Jonathan D. Bray. October 2002.

PEER 2002/08 *Component Testing, Stability Analysis and Characterization of Buckling-Restrained Unbonded Braces™.* Cameron Black, Nicos Makris, and Ian Aiken. September 2002.

PEER 2002/07 *Seismic Performance of Pile-Wharf Connections.* Charles W. Roeder, Robert Graff, Jennifer Soderstrom, and Jun Han Yoo. December 2001.

PEER 2002/06 *The Use of Benefit-Cost Analysis for Evaluation of Performance-Based Earthquake Engineering Decisions*. Richard O. Zerbe and Anthony Falit-Baiamonte. September 2001.

PEER 2002/05 *Guidelines, Specifications, and Seismic Performance Characterization of Nonstructural Building Components and Equipment*. André Filiatrault, Constantin Christopoulos, and Christopher Stearns. September 2001.

PEER 2002/03 *Investigation of Sensitivity of Building Loss Estimates to Major Uncertain Variables for the Van Nuys Testbed.* Keith A. Porter, James L. Beck, and Rustem V. Shaikhutdinov. August 2002.

PEER 2002/02 *The Third U.S.-Japan Workshop on Performance-Based Earthquake Engineering Methodology for Reinforced Concrete Building Structures*. July 2002.

PEER 2002/01 *Nonstructural Loss Estimation: The UC Berkeley Case Study. Mary C. Comerio and John C. Stallmeyer.* December 2001.

PEER 2001/16 *Statistics of SDF-System Estimate of Roof Displacement for Pushover Analysis of Buildings.* Anil K. Chopra, Rakesh K. Goel, and Chatpan Chintanapakdee. December 2001.

PEER 2001/15 *Damage to Bridges during the 2001 Nisqually Earthquake.* R. Tyler Ranf, Marc O. Eberhard, and Michael P. Berry. November 2001.

PEER 2001/14 *Rocking Response of Equipment Anchored to a Base Foundation.* Nicos Makris and Cameron J. Black. September 2001.

PEER 2001/13 *Modeling Soil Liquefaction Hazards for Performance-Based Earthquake Engineering.* Steven L. Kramer and Ahmed-W. Elgamal. February 2001.

PEER 2001/12 *Development of Geotechnical Capabilities in OpenSees.* Boris Jeremic. September 2001.

PEER 2001/11 *Analytical and Experimental Study of Fiber-Reinforced Elastomeric Isolators*. James M. Kelly and Shakhzod M. Takhirov. September 2001.

PEER 2001/10 *Amplification Factors for Spectral Acceleration in Active Regions.* Jonathan P. Stewart, Andrew H. Liu, Yoojoong Choi, and Mehmet B. Baturay. December 2001.

PEER 2001/09 *Ground Motion Evaluation Procedures for Performance-Based Design.* Jonathan P. Stewart, Shyh-Jeng Chiou, Jonathan D. Bray, Robert W. Graves, Paul G. Somerville, and Norman A. Abrahamson. September 2001.

PEER 2001/08 *Experimental and Computational Evaluation of Reinforced Concrete Bridge Beam-Column Connections for Seismic Performance*. Clay J. Naito, Jack P. Moehle, and Khalid M. Mosalam. November 2001.

PEER 2001/07 *The Rocking Spectrum and the Shortcomings of Design Guidelines.* Nicos Makris and Dimitrios Konstantinidis. August 2001.

PEER 2001/06 *Development of an Electrical Substation Equipment Performance Database for Evaluation of Equipment Fragilities*. Thalia Agnanos. April 1999.

PEER 2001/05 *Stiffness Analysis of Fiber-Reinforced Elastomeric Isolators.* Hsiang-Chuan Tsai and James M. Kelly. May 2001.

PEER 2001/04 *Organizational and Societal Considerations for Performance-Based Earthquake Engineering.* Peter J. May. April 2001.

PEER 2001/03 *A Modal Pushover Analysis Procedure to Estimate Seismic Demands for Buildings: Theory and Preliminary Evaluation.* Anil K. Chopra and Rakesh K. Goel. January 2001.

PEER 2001/02 *Seismic Response Analysis of Highway Overcrossings Including Soil-Structure Interaction.* Jian Zhang and Nicos Makris. March 2001.

PEER 2001/01 *Experimental Study of Large Seismic Steel Beam-to-Column Connections.* Egor P. Popov and Shakhzod M. Takhirov. November 2000.

PEER 2000/10 *The Second U.S.-Japan Workshop on Performance-Based Earthquake Engineering Methodology for Reinforced Concrete Building Structures.* March 2000.

PEER 2000/09 *Structural Engineering Reconnaissance of the August 17, 1999 Earthquake: Kocaeli (Izmit), Turkey.* Halil Sezen, Kenneth J. Elwood, Andrew S. Whittaker, Khalid Mosalam, John J. Wallace, and John F. Stanton. December 2000.

PEER 2000/08 *Behavior of Reinforced Concrete Bridge Columns Having Varying Aspect Ratios and Varying Lengths of Confinement.* Anthony J. Calderone, Dawn E. Lehman, and Jack P. Moehle. January 2001.

PEER 2000/07 *Cover-Plate and Flange-Plate Reinforced Steel Moment-Resisting Connections.* Taejin Kim, Andrew S. Whittaker, Amir S. Gilani, Vitelmo V. Bertero, and Shakhzod M. Takhirov. September 2000.

PEER 2000/06 *Seismic Evaluation and Analysis of 230-kV Disconnect Switches.* Amir S. J. Gilani, Andrew S. Whittaker, Gregory L. Fenves, Chun-Hao Chen, Henry Ho, and Eric Fujisaki. July 2000.

PEER 2000/05 *Performance-Based Evaluation of Exterior Reinforced Concrete Building Joints for Seismic Excitation.* Chandra Clyde, Chris P. Pantelides, and Lawrence D. Reaveley. July 2000.

PEER 2000/04 *An Evaluation of Seismic Energy Demand: An Attenuation Approach.* Chung-Che Chou and Chia-Ming Uang. July 1999.

PEER 2000/03 *Framing Earthquake Retrofitting Decisions: The Case of Hillside Homes in Los Angeles.* Detlof von Winterfeldt, Nels Roselund, and Alicia Kitsuse. March 2000.

PEER 2000/02 *U.S.-Japan Workshop on the Effects of Near-Field Earthquake Shaking.* Andrew Whittaker, ed. July 2000.

PEER 2000/01 *Further Studies on Seismic Interaction in Interconnected Electrical Substation Equipment.* Armen Der Kiureghian, Kee-Jeung Hong, and Jerome L. Sackman. November 1999.

PEER 1999/14 *Seismic Evaluation and Retrofit of 230-kV Porcelain Transformer Bushings*. Amir S. Gilani, Andrew S. Whittaker, Gregory L. Fenves, and Eric Fujisaki. December 1999.

PEER 1999/13 *Building Vulnerability Studies: Modeling and Evaluation of Tilt-up and Steel Reinforced Concrete Buildings.* John W. Wallace, Jonathan P. Stewart, and Andrew S. Whittaker, editors. December 1999.

PEER 1999/12 *Rehabilitation of Nonductile RC Frame Building Using Encasement Plates and Energy-Dissipating Devices.* Mehrdad Sasani, Vitelmo V. Bertero, James C. Anderson. December 1999.

PEER 1999/11 *Performance Evaluation Database for Concrete Bridge Components and Systems under Simulated Seismic Loads.* Yael D. Hose and Frieder Seible. November 1999.

PEER 1999/10 *U.S.-Japan Workshop on Performance-Based Earthquake Engineering Methodology for Reinforced Concrete Building Structures.* December 1999.

PEER 1999/09 *Performance Improvement of Long Period Building Structures Subjected to Severe Pulse-Type Ground Motions*. James C. Anderson, Vitelmo V. Bertero, and Raul Bertero. October 1999.

PEER 1999/08 *Envelopes for Seismic Response Vectors.* Charles Menun and Armen Der Kiureghian. July 1999.

PEER 1999/07 *Documentation of Strengths and Weaknesses of Current Computer Analysis Methods for Seismic Performance of Reinforced Concrete Members.* William F. Cofer. November 1999.

PEER 1999/06 *Rocking Response and Overturning of Anchored Equipment under Seismic Excitations.* Nicos Makris and Jian Zhang. November 1999.

PEER 1999/05 *Seismic Evaluation of 550 kV Porcelain Transformer Bushings.* Amir S. Gilani, Andrew S. Whittaker, Gregory L. Fenves, and Eric Fujisaki. October 1999.

PEER 1999/04 *Adoption and Enforcement of Earthquake Risk-Reduction Measures.* Peter J. May, Raymond J. Burby, T. Jens Feeley, and Robert Wood.

PEER 1999/03 *Task 3 Characterization of Site Response General Site Categories*. Adrian Rodriguez-Marek, Jonathan D. Bray, and Norman Abrahamson. February 1999.

PEER 1999/02 *Capacity-Demand-Diagram Methods for Estimating Seismic Deformation of Inelastic Structures: SDF Systems*. Anil K. Chopra and Rakesh Goel. April 1999.

PEER 1999/01 *Interaction in Interconnected Electrical Substation Equipment Subjected to Earthquake Ground Motions.* Armen Der Kiureghian, Jerome L. Sackman, and Kee-Jeung Hong. February 1999.

PEER 1998/08 *Behavior and Failure Analysis of a Multiple-Frame Highway Bridge in the 1994 Northridge Earthquake.* Gregory L. Fenves and Michael Ellery. December 1998.

PEER 1998/07 *Empirical Evaluation of Inertial Soil-Structure Interaction Effects.* Jonathan P. Stewart, Raymond B. Seed, and Gregory L. Fenves. November 1998.

PEER 1998/06 *Effect of Damping Mechanisms on the Response of Seismic Isolated Structures.* Nicos Makris and Shih-Po Chang. November 1998.

PEER 1998/05 *Rocking Response and Overturning of Equipment under Horizontal Pulse-Type Motions.* Nicos Makris and Yiannis Roussos. October 1998.

PEER 1998/04 *Pacific Earthquake Engineering Research Invitational Workshop Proceedings, May 14–15, 1998: Defining the Links between Planning, Policy Analysis, Economics and Earthquake Engineering.* Mary Comerio and Peter Gordon. September 1998.

PEER 1998/03 *Repair/Upgrade Procedures for Welded Beam to Column Connections.* James C. Anderson and Xiaojing Duan. May 1998.

PEER 1998/02 *Seismic Evaluation of 196 kV Porcelain Transformer Bushings.* Amir S. Gilani, Juan W. Chavez, Gregory L. Fenves, and Andrew S. Whittaker. May 1998.

PEER 1998/01 *Seismic Performance of Well-Confined Concrete Bridge Columns.* Dawn E. Lehman and Jack P. Moehle. December 2000.